

Department of Spatial Sciences

**Application of high resolution remote sensing to detect and
map the pasture weed Paterson's curse (*Echium
plantagineum*) in Western Australia**


Daniel Lester McIntyre

**This thesis is presented for the Degree of
Doctor of Philosophy
of
Curtin University**

July 2014

Declaration

To the best of my knowledge and belief this thesis contains no material previously published by any other person except where due acknowledgment has been made. This thesis contains no material which has been accepted for the award of any other degree or diploma in any university.

Signature: 

Date: 17/09/2015

ABSTRACT

Maps of the location and density of weeds have an important role in management programs. Remote sensing has the potential to map weed infestations over regional scales; however this potential has not been fully realised in the past for many species, due to inadequate spatial/spectral resolution, poor timing of acquisition, and inadequate methods. In recent years, new sensors and techniques have been developed, which can potentially overcome past limitations. This thesis investigated the utility of high spectral and spatial resolution remotely sensed datasets for detecting and mapping the pasture weed Paterson's curse (*Echium plantaginium*) in the Wheatbelt Region of Western Australia. Three types of remote sensing data were used: field spectroscopy, high spatial resolution airborne multispectral, and satellite hyperspectral. Using these datasets, as well as different classification, statistical, and quantitative validation approaches, the thesis found that spectral resolution and timing of image capture were the most important factors for discriminating Paterson's curse and producing acceptable levels of mapping accuracy.

The characteristic reflectance peak of Paterson's curse flowers in the blue region of the electromagnetic spectrum resulted in a good relationship between percentage floral cover of Paterson's curse and a Normalised Difference Blue Index (NDBI) derived from field spectroscopy ($R^2 = 0.75$). Paterson's curse was mapped from high spatial resolution airborne multispectral imagery using two non-parametric classifiers: artificial neural networks (multi-layer perceptron) and k-nearest neighbour. A low user's accuracy (23–70%), producer's accuracy (40–73%) and per-class Kappa (0.2–0.4) for Paterson's curse from the two classifiers was due to spectral confusion with pasture and crop. Satellite hyperspectral imagery (EO-1 Hyperion) and a matched filter classification mapped Paterson's curse with good accuracy: 81% user's accuracy, 83% producer's accuracy and a Kappa statistic of 0.64. The most likely reason for the accuracy was that Paterson's curse was mapped later in the season when co-occurring pasture was senescent. Despite the promising results from the field spectroscopy and satellite hyperspectral data, field survey remains the most reliable method for mapping Paterson's curse. Future satellite hyperspectral sensors with high-signal-to-noise ratios and increased area coverage have the potential to provide accurate maps of Paterson's curse at regional scales.

ACKNOWLEDGEMENTS

This PhD has been a long journey—a flowing but sometimes stuttering narrative, filled with trials, tribulations and the occasional but wonderful Eureka moment. Over the years, numerous people have directly or indirectly contributed. Of those whose names I have unintentionally omitted below, you are still gratefully acknowledged.

This research was partially funded by an Australian Research Council Linkage grant (LP0454890) awarded to Professor Graciela Metternicht. Graciela was my supervisor for the first two and a half years of this PhD and I warmly thank her for the valuable direction and advice. An Australian Postgraduate Award scholarship provided personal funding.

Thanks to my supervisor Dr Robert Corner, and my associate supervisor Dr Tom Schut. Tom in particular provided valuable advice on the more technical aspects of the thesis. I am grateful to Mrs Lori Patterson from the Curtin Spatial Sciences Department for proof-reading this thesis and assisting with formatting.

Thanks to my former PhD lab-mates from the Curtin Spatial Sciences Department: Dr Todd Robinson, Dr Georgina Warren, and Dr Deavi Purnomo. In particular, I would like to acknowledge Todd for those valuable exchanges of ideas over the years about remote sensing of weeds. Thanks also to the student volunteers from Curtin: Paula, Roman and Alberto, who assisted at various times in the field.

Thanks to the PhD students and staff from the Tropical Spatial Sciences Group at Charles Darwin University in Darwin, in particular Dr Guy Boggs, Dr Diane Pearson and the late Dr Frank van der Sommen.

My former work colleagues at Energy Resources of Australia were encouraging and helpful along the way, especially Dr Philippe Puig, Dr Matthew Daws, Dr Geoffrey Tsang, Ms Cherie Gellert, and Ms Linda Pugh.

Thanks to the Specterra team in Perth, in particular the managing director Mr Andrew Malcom, and Mr Craig Baldacchino who provided valuable logistic support in the field at a crucial time in the project.

Thanks to Dr David Jupp (CSIRO) for kindly providing the ENVI Hyperion toolkit.

Mr Jeff Watson from the Department of Agriculture and Food, Western Australia, was very accommodating of my numerous requests for spatial data over the years.

The Catholic Agricultural College Bindoon was very supportive of the project from the initial contact. Thanks to the former principal Mr Brad Hall and the farm manager Mr Kevin Marshall who gave unrestricted access to the property during the fieldwork in 2005 and 2006. The College provided comfortable accommodation, hearty meals and friendly hospitality during my stay.

Thanks to Mr Ranford and Mr Huppennen, owners of Morden Downs and Bindarie respectively, for permission to access and conduct fieldwork on their properties. Thanks also to the managers of Bindarie: Mr Dudley Lewis and Mr Norman Lewis for the tour of the property prior to the fieldwork.

My parents Michael and June McIntyre always appreciated the value of education, and those 'little bits of paper' that open up exciting opportunities in life.

My wife Laila and sons Benjamin and Alexander were very patient and understanding over the years, especially of those Sunday absences and the leave from work that didn't involve recreation or holidays.

'It is good to have an end to journey toward; but it is the journey that matters in the end'.

Ursula K. Le Guin

TABLE OF CONTENTS

ABSTRACT	i
ACKNOWLEDGEMENTS	ii
TABLE OF CONTENTS	iv
LIST OF FIGURES	x
LIST OF TABLES	xiii
1 INTRODUCTION	1
1.1 Agricultural Weeds in Australia.....	1
1.2 Case Study: Paterson’s Curse	1
1.3 Weed Management.....	3
1.4 Problem Statement	4
1.5 Research Objectives	5
1.6 Benefits of the Research.....	6
1.7 Research Methods	6
1.8 Thesis Structure.....	7
2 METHODOLOGICAL AND LITERATURE REVIEW	9
2.1 Introduction	9
2.1.1 Definition and scope of remote sensing.....	9
2.2 Analysis of Remotely Sensed Data	9
2.3 Selection of Appropriate Data.....	10
2.3.1 Spatial resolution.....	10
2.3.2 Spectral resolution.....	11
2.3.3 Radiometric resolution	13
2.3.4 Temporal resolution	14
2.4 Selection of Appropriate Method.....	15
2.4.1 Vegetation indices	15
2.4.2 Field spectroscopy.....	16
2.4.3 Classification.....	18
2.4.3.1 Per-pixel classifiers.....	21
2.4.3.1.1 Parametric unsupervised: ISODATA.....	22
2.4.3.1.2 Parametric supervised: maximum likelihood	22
2.4.3.1.3 Non-parametric supervised: minimum distance to means.....	22
2.4.3.1.4 Non-parametric supervised: parallelepiped.....	23

2.4.3.1.5	Non-parametric supervised: support vector machines	23
2.4.3.1.6	Non-parametric supervised: k-nearest neighbour.....	24
2.4.3.1.7	Non-parametric supervised: decision tree classification	24
2.4.3.1.8	Non-Parametric supervised: artificial neural networks	25
2.4.3.1.9	Non-parametric supervised: spectral angle mapper	26
2.4.3.1.10	Non-parametric supervised: Fuzzy c-means	27
2.4.3.1.11	Non-parametric supervised: Linear spectral unmixing	27
2.4.3.1.12	Non-parametric supervised: Matched filtering and mixture tuned matched filtering	29
2.4.3.2	Per-field classification	30
2.4.3.3	Contextual classification.....	31
2.5	Validation.....	32
2.5.1	Sampling and validation data.....	33
2.5.2	Error matrix approach	34
2.5.3	Kappa	34
2.5.4	Soft classification validation.....	36
2.6	Remote Sensing of Weeds	39
2.6.1	Remote sensing of vegetation	40
2.6.2	Properties of vegetation for remote sensing detection.....	40
2.6.3	Characteristics of weeds for detection using remote sensing.....	42
2.6.3.1	Foliage properties	43
2.6.3.1.1	Orientation.....	43
2.6.3.1.2	Colour.....	43
2.6.3.1.3	Density.....	44
2.6.3.1.4	Timing	45
2.6.3.2	Floral properties.....	45
2.6.4	Spectroscopy	46
2.6.5	Aerial photography.....	49
2.6.6	Airborne videography	49
2.6.7	Airborne digital imagery	50
2.6.8	Satellite multispectral imagery.....	52
2.6.9	Airborne hyperspectral.....	57
2.6.10	Satellite hyperspectral	59
2.7	Remote Sensing of Paterson’s Curse	60
2.8	Summary	62
3	STUDY AREA, STUDY SPECIES, AND DATASETS.....	65
3.1	Introduction.....	65

3.2	Characteristics of the Study Area.....	65
3.2.1	Selection and rationale.....	65
3.2.2	Physical features.....	66
3.2.3	Vegetation and soils.....	68
3.2.4	Topography.....	68
3.2.5	Climate.....	69
3.3	Paterson’s Curse.....	70
3.3.1	Description.....	70
3.3.2	Impacts and benefits.....	70
3.3.2.1	Negative impacts.....	71
3.3.2.2	Benefits.....	72
3.3.3	Management.....	72
3.4	Remote Sensing Data.....	73
3.4.1	Digital Multi-spectral Imagery (DMSI).....	73
3.4.2	EO-1 Hyperion satellite hyperspectral imagery.....	75
3.4.2.1	Description and background.....	75
3.4.2.2	Acquisition of EO-1 Hyperion data.....	78
3.4.3	Field spectroscopy data.....	79
3.5	Validation and Field Data.....	80
3.6	Software and Hardware.....	80
3.6.1	Remote sensing and GIS software.....	80
3.6.2	Statistical software.....	81
3.6.3	Global Positioning System (GPS).....	81
3.7	Summary.....	81
4	IDENTIFYING OPTIONS TO DETECT PATERSON’S CURSE USING FIELD SPECTROSCOPY.....	83
4.1	Introduction.....	83
4.2	Methods.....	84
4.2.1	Data collection.....	85
4.2.2	Data processing.....	88
4.2.3	Comparison of spectra.....	88
4.2.4	Derivative analysis.....	88
4.2.5	Relationships between spectra and floral cover.....	89
4.2.5.1	Derivation of band ratios and indices.....	89
4.2.5.2	Spectral unmixing.....	89
4.2.5.3	Correlation and regression analysis.....	90
4.3	Results.....	90

4.3.1	Comparison of spectra.....	90
4.3.2	Derivative analysis.....	91
4.3.3	Relationships between spectra and floral cover.....	92
4.3.3.1	Derivation of band ratios and indices.....	92
4.3.3.2	Correlation and regression analysis.....	96
4.4	Discussion and Conclusion.....	98
5	MAPPING PATERSON'S CURSE WITH MULTISPECTRAL AIRBORNE IMAGERY.....	101
5.1	Introduction.....	101
5.2	Methods.....	102
5.2.1	Image acquisition.....	102
5.2.2	Image pre-processing.....	103
5.2.3	Training area selection.....	103
5.2.4	Training area analysis.....	104
5.2.5	Image classification.....	105
5.2.5.1	Multi-layer perceptron classifier.....	105
5.2.5.2	k-nearest neighbour classifier.....	107
5.2.6	Accuracy assessment.....	107
5.2.6.1	Field survey.....	107
5.2.6.2	Quantitative accuracy assessment.....	109
5.3	Results.....	111
5.3.1	Training area analysis.....	111
5.3.2	Accuracy assessment.....	113
5.3.2.1	Hard classification results.....	113
5.3.2.1.1	Multi-layer perceptron.....	113
5.3.2.1.2	k-nearest neighbour.....	117
5.3.2.2	Soft classification results.....	120
5.3.2.2.1	Multi-layer perceptron.....	120
5.3.2.2.2	k-nearest neighbour.....	122
5.4	Discussion and Conclusion.....	123
6	DISCRIMINATING PATERSON'S CURSE WITH SATELLITE HYPERSPPECTRAL IMAGERY.....	127
6.1	Introduction.....	127
6.2	Methods.....	128
6.2.1	Processing.....	129
6.2.1.1	Specialised Hyperion pre-processing.....	130

6.2.1.2	Standard hyperspectral processing.....	132
6.2.2	Classification.....	134
6.2.2.1	Spectral sampling.....	135
6.2.2.2	Matched filter classification.....	135
6.2.2.3	Analysis of band ratios and indices	136
6.2.3	Validation.....	136
6.2.3.1	Data collection	136
6.2.3.2	Quantitative accuracy assessment.....	139
6.3	Results.....	140
6.3.1	Processing	140
6.3.2	Classification.....	141
6.3.2.1	Spectral sampling.....	141
6.3.2.2	Matched filter classification.....	145
6.3.2.3	Analysis of band ratios and indices	146
6.3.3	Validation.....	148
6.3.3.1	Matched filter threshold independent	148
6.3.3.2	Matched filter threshold dependent	151
6.3.3.3	Band ratio/index threshold independent	152
6.3.3.4	Band ratio/index threshold dependent	154
6.4	Discussion and Conclusion	155
7	SUMMARY AND RECOMMENDATIONS.....	161
7.1	Introduction.....	161
7.2	The Optimum Spatial and Spectral Resolution.....	161
7.2.1	Recommendations	162
7.3	The Optimum Timing of Remote Sensing.....	163
7.3.1	Recommendations	164
7.4	Suitable Image Processing and Classification Techniques	164
7.4.1	Recommendations	166
7.5	Methods of Integrating Remotely Sensed Data and Field Data.....	167
7.5.1	Recommendations	168
7.6	Contribution to Knowledge.....	168
7.7	Conclusion	169
	REFERENCES.....	171
	APPENDIX A.....	196
	APPENDIX B	206
	APPENDIX C	216

APPENDIX D	226
APPENDIX E	228
APPENDIX F	230
APPENDIX G	240
APPENDIX H	251
APPENDIX I	254
APPENDIX J	260
APPENDIX K	262

LIST OF FIGURES

Figure 1.1	Examples of dense infestations of Paterson’s curse in the Chittering Shire, Western Australia.	2
Figure 2.1	Summary of the major classification approaches.....	18
Figure 2.2	Spectral angle mapper concept (adapted from Campbell, 2008).	27
Figure 2.3	Example of a hyper-plane triangle (Adapted from Mather and Koch 2011).	28
Figure 2.4	Example of two ROC plots showing false positive and false negative values.....	38
Figure 2.5	Reflectance spectra for green and senescent vegetation (sourced from Chapter 4). Parts of the electromagnetic spectrum: B = blue, G = green, R = red, RE = red-edge, NIR = near infrared, and MIR = mid infrared.	41
Figure 3.1	Location of properties used as study sites: 1) Catholic Agricultural College Bindoon; 2) Morden Downs; and 3) Bindarie.	66
Figure 3.2	Land use on the three study area properties, and the general area around the town of Bindoon (from Beeston, <i>et al.</i> 2001).	67
Figure 3.3	Extent of DMSI mosaic image (outlined in white) at the Catholic Agricultural College Bindoon property (outlined in yellow).....	75
Figure 3.4	EO-1 and Landsat 7 ground tracks. Adapted from Ungar, <i>et al.</i> (2003).	76
Figure 4.1	Flowchart outlining the methodology for the spectroscopy analysis... ..	84
Figure 4.2	Location of sampling sites A and B at the Catholic Agricultural College Bindoon. Site A: Systematic sampling grid; B: Horse paddock where dense Paterson’s curse spectra were measured.	87
Figure 4.3	Spectral reflectance curves for components of Paterson’s curse and other cover types across the full spectral range (351-2400 nm).	91
Figure 4.4	First order derivatives for Paterson’s curse and green vegetation spectra.	92

Figure 4.5	Spectral response difference between spectra from green vegetation (GV), Paterson’s curse flowers (PCF), Dense Paterson’s curse (DPC), and senescent vegetation (SV) spectra.....	93
Figure 4.6	Scatter plot, regression line ($R^2 = 0.829$), and 95% upper and lower confidence intervals for the NDBI and Paterson’s curse floral cover (proportion).	97
Figure 4.7	Scatter plot, regression line ($R^2 = 0.75$), and 95% upper and lower confidence intervals for Paterson’s curse floral cover (proportion) and estimated floral abundance from linear unmixing.	97
Figure 5.1	Training classes used and representative oblique photographs: a) crop; b) pasture; c) fallow; d) Paterson’s curse.....	104
Figure 5.2	Location of stratified random points at Catholic Agricultural College Bindoon that were surveyed in the field.	109
Figure 5.3	Mean DN spectral plot values for final DMSI training signatures. ...	112
Figure 5.4	Hard classification output for the 3-class MLP classification.	115
Figure 5.5	Oblique photograph of an area of pasture in a field (background) that was misclassified by the 3-class MLP classification (labelled as ‘G’ in Figure 5.4) as crop and Paterson’s curse.....	115
Figure 5.6	Hard classification output from the 2-class MLP classification.	117
Figure 5.7	Hard classification output from 2-class, 3-band classification ($k = 45$).	120
Figure 5.8	Logistic regression model output (probability of presence) of Paterson’s curse from the two-class MLP classification.....	121
Figure 5.9	Oblique photograph of Area ‘A’ on Figure 5.8 showing the Paterson’s curse infestation south of the dam that was identified with a probability of 0.75–1.	122
Figure 5.10	Logistic regression model output (probability of presence) of Paterson’s curse from two-class kNN classification (4-band, $k = 5$). ...	123
Figure 6.1	Flowchart of methodology for 1) processing and 2) classifying and validating Hyperion data.	129

Figure 6.2	Location of sample sites for Paterson’s curse, non-Paterson’s curse. Bands 8 (428 nm), 20 (550 nm), and 30 (652 nm) are represented as blue, green, and red.	138
Figure 6.3	Examples of field plots representing the five density classes of Paterson’s curse.....	139
Figure 6.4	a) Before and b) after de-striping and noise removal was applied to VNIR band 8 (428 nm). Bands 25 (601 nm) and 55 (906 nm) shown for comparison where no striping effect was apparent.	140
Figure 6.5	Location of Paterson’s curse non-Paterson’s curse spectral samples.	141
Figure 6.6	Spectral samples of dense Paterson’s curse and the derived mean end-member spectrum.	142
Figure 6.7	Spectra of the dense Paterson’s curse end-member and co-occurring vegetation types.....	143
Figure 6.8	Reflectance differences between the dense Paterson’s curse end-member spectrum (PC) and spectral samples representing green vegetation (GV), senescent vegetation (SV) and Eucalypt woodland (EW).....	144
Figure 6.9	Spectra of the Paterson’s curse density classes from the field validation plots, with green and senescent vegetation spectra shown for comparison.	145
Figure 6.10	Matched filter image derived from Paterson’s curse end-member. ...	146
Figure 6.11	ROC plots for the matched filter validation result, with cut-off value indicated by arrow.....	149
Figure 6.12	Paterson’s curse model (probability of presence) derived from logistic regression.	150
Figure 6.13	Threshold image showing Paterson’s curse (purple) at a) Bindoon Catholic Agricultural College b) Morden Downs, and c) Bindarie. ..	151
Figure 6.14	ROC plots for three best performing indices, with cut-off values indicated by arrows.	153

LIST OF TABLES

Table 2.1	Spatial resolution of currently available multispectral and hyperspectral remote sensing data.	12
Table 2.2	Spectral resolution of currently available multispectral and hyperspectral remote sensing data.	13
Table 2.3	Temporal resolution of currently available multispectral and hyperspectral remote sensing data.	15
Table 2.4	ROC contingency table (Adapted from Eastman 2006).	38
Table 2.5	Summary of field spectroscopy studies for weeds, with application type (AT) (P: prediction, C: calibration, M: modelling), and instrument type (IT) (S: spectrometer, R: radiometer).....	48
Table 3.1	Mean monthly rainfall data for Gingin Airport from 1996-2010: (Source: Bureau of Meteorology 2010).	69
Table 3.2	Mean temperature and humidity data for Gingin Airport from 1996-2010 (Source: Bureau of Meteorology 2010).	69
Table 3.3	Spectral band centres and spectral feature properties for DMSI bands. Modified from Canci, <i>et al.</i> (2006).	74
Table 3.4	Characteristics of Hyperion, with ALI, and Landsat 7 ETM+ for comparison. Adapted from Ungar, <i>et al.</i> (2003).	77
Table 3.5	Properties of acquired Hyperion image (from product metadata).	79
Table 3.6	Summary of the field datasets used in the research by chapter.....	80
Table 4.1	Summary statistics for Paterson’s curse floral proportion cover from the systematic field grid at Catholic Agricultural College Bindoon....	86
Table 4.2	List of band ratios and indices used to determine a relationship with floral cover.	95
Table 4.3	Pearson correlation coefficient (r) and coefficient of determination of regression (R ²) for first order (a) or second order (b) polynomial relationships between abundance estimates using linear unmixing and selected indices, with percentage floral cover of Paterson’s curse.	96

Table 5.1	Summary statistics of Paterson's curse random sampled locations on the Bindoon Agricultural College study site.....	109
Table 5.2	Training area statistics for each band (B), including number of pixels (N) with mean and standard deviation (SD). Key: C = crop, P = pasture, F = fallow, PC = Paterson's curse.	112
Table 5.3	Transformed divergence results for the final classes.	113
Table 5.4	Summary of accuracy assessment of the MLP classification.	116
Table 5.5	Summary of accuracy assessment of the k-nearest neighbour (kNN) classification. Key: C = class, B = bands.....	119
Table 5.6	Logistic regression and ROC (AUC) results for MLP classifications.	121
Table 6.1	Centre wavelengths of the 158 band image produced by spectral sub-setting for the visible/near infrared (VNIR) and the short-wave infrared (SWIR).	131
Table 6.2	Band centre wavelengths and full width half maximum (FWHM) for the 49 band subset.	134
Table 6.3	Density classes and description of Paterson's curse assessed from random field plots.	137
Table 6.4	Hyperion indices derived from equivalent indices from Chapter 4. ..	147
Table 6.5	Comparison of peak spectral differences of green vegetation/Paterson's curse spectra derived from Hyperion image, and field spectroscopy in Chapter 4.	148
Table 6.6	Chi-square results and ROC statistics from logistic regression of the matched filter classification output.	148
Table 6.7	Threshold dependent accuracy results of matched filter classification with validation dataset (n = 184).....	152
Table 6.8	Chi-square, AUC and accuracy statistics from logistic regression of band ratios and indices with validation dataset (n = 184).....	153
Table 6.9	Threshold dependent accuracy results of band ratios and indices with validation dataset (n = 184).....	155

1 INTRODUCTION

1.1 Agricultural Weeds in Australia

Australia has a long history of introduced plant species becoming weeds. These species have either been deliberately introduced e.g. for ornamental value or agricultural benefit, or arrived unintentionally e.g. from ships and cargo (Adair and Groves 1998). The unintended consequence for many of these species is that they became successful colonisers and invaders, resulting in significant economic, environmental, and social impacts. The Australian agriculture sector in particular has been adversely impacted by weeds. The most recent estimate of the financial impact of agricultural weeds in Australia is between \$3.4 to \$4.4 billion per year (Sinden, *et al.* 2004). The cost of weed impacts on winter crops alone in Australia is estimated by Jones *et al.* (2000) to be \$1.2 billion. In Western Australia's agricultural regions, weed control costs have been estimated to comprise twenty percent of production costs (State Weed Plan Steering Group 2001). The costs associated with pasture weeds in Australia have been estimated at \$792 million per year. The impacts of agricultural weeds include loss of production due to weeds outcompeting desired species, loss of value of products due to contamination (e.g. seeds in cotton), control costs, loss of value of products due to herbicide residue, and new production methods that are required in heavily affected weed areas (Jones, *et al.* 2000; Nordblom, *et al.* 2001).

1.2 Case Study: Paterson's Curse

Paterson's curse or Salvation Jane (*Echium plantagineum*) is an agricultural weed of particular concern in agricultural regions of Australia. The species is an erect winter annual or biennial herb that can grow to 1.5 m in height, although the average is between 30 to 60 cm (Piggin and Sheppard 1995). Paterson's curse originates from the Mediterranean region and was introduced to Australia as an ornamental plant in the mid-19th century on account of its attractive flowers (Piggin and Sheppard 1995) and was intentionally distributed (Sheppard and Smyth 2012). Since then, Paterson's curse has invaded approximately 33 million hectares in southern Australia (Sheppard, *et al.* 2001). The cost of Paterson's curse to Australia is estimated to be \$90 million per year: a figure based on the loss of the carrying capacity of livestock in areas affected by the weed (Nordblom, *et al.* 2001). Paterson's curse has invaded

approximately 220,000 hectares in Western Australia (Parsons and Cuthbertson 2001), mostly in the northern and central Wheatbelt Regions, and the South West Region (Dodd, *et al.* 1993), with particularly dense infestations in the vicinity of Northampton and in the Avon and Swan Valley regions (Hussey, *et al.* 1997). The purple flowers of Paterson's curse can produce a 'blanket' appearance in areas of dense infestation (Figure 1.1). This feature makes Paterson's curse one of the most conspicuous weeds of roadsides, pastures and disturbed lands in Western Australia (Dodd, *et al.* 1993).



Figure 1.1 Examples of dense infestations of Paterson's curse in the Chittering Shire, Western Australia.

The main characteristics of Paterson's curse that favour it as a pasture weed can be summarised as follows (Piggin 1976):

- (i) High productivity in autumn and winter compared with other pasture species;
- (ii) Remaining green in late spring and early summer, when other pasture species have already matured;
- (iii) Seedling establishment and survival that are suited to a Mediterranean-type climate;
- (iv) Seeds that retain viability after passing through the alimentary tract of grazing herbivores (Parsons and Cuthbertson 2001); and
- (v) A lack of natural enemies and competing pasture species in Australia (Piggin and Sheppard 1995).

Paterson's curse is a declared noxious weed in all Australian states and territories (Piggin and Sheppard 1995). In Western Australia, Paterson's curse has been declared as category P1 (introduction of the plant into, or movement of the plant within, an area is prohibited) for the entire state, and Category P3 (Plant to be controlled by reduction in number or distribution of the plant or both) and P4 (Spread of plant beyond where it currently occurs to be prevented) for selected municipal districts (Government of Western Australia 1976). Section 49 of the Agriculture and Related Resources Protection Act (1976) states that private landowners in Western Australia with Paterson's curse (or any other declared plant species) are under a legislative obligation to control it on their property (Government of Western Australia 1976).

1.3 Weed Management

The three main strategies for managing weeds are: prevention and exclusion; early detection and rapid assessment; and control, containment and eradication (Rejmánek 2000). Weed surveys are essential for containment and eradication to be successful, and early detection is vital, as smaller satellite infestations have the potential to spread more rapidly than large infestations (Moody and Mack 1988), and can make the difference between being able to contain and/or eradicate a species, or having to invest in the long term management of the species (Rejmánek 2000). The main benefits of surveys to weed management are:

- (i) Empowering weed management plans and enabling control measures to be planned and funded appropriately (Casady, *et al.* 2005; McGowen 1998);
- (ii) The spread of a weed species can be documented by repeat surveys (McGowen 1998);
- (iii) The economic impact of a weed species can be assessed (McGowen 1998);
- (iv) Studies of the biology and ecology of the species based on the survey data can assist with its control (Casady, *et al.* 2005);
- (v) Public awareness of a particular species can be increased (Casady, *et al.* 2005) which benefits weed management at a community level; and

- (vi) Information on the location of a weed species at a given time can be used to predict the potential distribution of the species (Lawes and Wallace 2008).

Survey methods can be simple questionnaires directed to land managers or interviews on-site (McGowen 1998), or complex regional scale ground surveys involving large teams. There are several approaches to ground survey, which involve varying degrees of complexity: recording presence/absence of a species; ordinal ranking of weed density through visual estimation; sampling grids, transects or randomly generated locations; or conducting a complete census of weeds within weed management zones or districts. Ground based surveys have several advantages, including a higher level of detail on cover and spatial variability when smaller areas are surveyed; they can be the sole source for historical and contemporary description of land use, which are valuable for deriving associated land cover; and information can be provided on other related features such as hydrology and soil type (Wyatt 2000). Ground survey however is typically expensive, labour intensive and logistically difficult, especially over large areas, rough terrain, or remote areas (Pitt and Miller 1988; Wyatt 2000). A minimum standard of skills and training is required for personnel, and there can be issues with consistency and accuracy if quality control is lacking (Wyatt 2000). Large areas usually require a sampling approach, rather than a census of all weeds infestations present, and revisiting sites on a regular (e.g. annual) basis is commonly not feasible (Wyatt 2000).

1.4 Problem Statement

Reliable and cost effective methods for mapping agricultural weeds like Paterson's curse can play an important role in the success of management strategies. Previous survey methods for Paterson's curse in Western Australia were on-ground visual assessments of the approximate area of Paterson's curse on a property by property basis, with no information on the density of an infestation or the spatial distribution. This approach involved a significant investment in time and resources to survey all affected properties in the south-west of Western Australia at a regional scale. Regularly updating a database of Paterson's curse distribution is likely to be time consuming and costly. In addition to the requirement to map Paterson's curse at a regional scale, there is also a need for data to assess the density of Paterson's curse

on each affected property, in order to make an assessment of the success of control measures.

Remote sensing is a possible alternative means of surveying Paterson's curse, given the limitations and cost of other survey methods. Remote sensing can provide data with a synoptic coverage of large areas, with a repetitive and consistent data collection protocol. This protocol allows regional scale distributions of weeds to be mapped with significant savings in cost and time over conventional methods. Remote sensing has not been widely accepted as an operationally based tool for weed management due to several limitations: the spatial and/or spectral resolution of sensors have not been adequate in many past applications for resolving a target species (particularly for Paterson's curse); data processing methods have been too specialised or inadequate; and remotely sensed data were expensive and/or unavailable. In the past decade, many of these problems have been addressed by new sensors with improved spatial/spectral resolution (e.g. high spatial resolution and hyperspectral satellite sensors), improvements in computer architecture and processing power, availability of computer software, and reductions in operational costs of acquiring remotely sensed data.

For remote sensing to be a successful tool for detecting and mapping weeds, a number of important criteria have to be met: the difference between the spectral reflectance of a weed infestation and background cover (e.g. soil, vegetation) must be sufficient. Therefore, the spectral resolution (number of bands and bandwidth) of the sensor must also be sufficient to detect these differences. The timing of remote sensing acquisition must align with an optimum stage of growth that allows the weeds to be discriminated. Finally, remote sensing must provide information to management agencies that is cost effective and in a readily interpretable format (Lamb 1998; Lawes and Wallace 2008; McGowen 1998).

1.5 Research Objectives

From the Problem Statement described above, the overall objective of the research is to investigate suitable remote sensing tools for mapping and monitoring Paterson's curse in the Wheatbelt Region of Western Australia. Ideally, these tools will have the

capability to be used in an operational setting. The following objectives will be addressed in the research:

- (i) Determine the optimal spectral and spatial resolution, and the optimal time of remote sensing data acquisition, based on the phenological and structural characteristics of Paterson's curse. This includes detection limits with regards to spectral and spatial resolution with different sensors, and the threshold of weed density that can be detected (such as floral density) according to the resolution of the data.
- (ii) Investigate suitable image processing and classification techniques for mapping Paterson's curse. This objective will include the development of a quantitative method that can relate floral density to the spectral information of a sensor.
- (iii) Investigate methods for successfully integrating remotely sensed data and field data to map Paterson's curse. The research will determine the most suitable sampling strategies for integrating these data at different scales and image resolution.

1.6 Benefits of the Research

- (i) Explore previously untested remote sensing data and techniques to Paterson's curse, and provide a critical review of the limitations;
- (ii) The research will be the first application of airborne and satellite remote sensing to Paterson's curse in Western Australia;
- (iii) The remote sensing methodology developed in this research may be appropriate for mapping Paterson's curse in other regions of Australia;
- (iv) The research will make a contribution to addressing the problem of matching the correct resolution of remotely sensed data to mapping weeds.

1.7 Research Methods

The major aspects of the research are:

- (i) The application of high spectral resolution hyperspectral satellite and high spatial resolution multi-spectral data to detect Paterson's curse;

- (ii) A comparative analysis of a range of remote sensing image classifiers applied to airborne digital imagery and
- (iii) Investigating methods of integrating field data with remote sensing data classification, including field spectroscopy and appropriate validation approaches.

1.8 Thesis Structure

This thesis is comprised of seven chapters. Chapter 1 outlines the research problem and the background information for the development of remote sensing methods for mapping and monitoring Paterson's curse. Following this, the research objectives are defined, as well as the expected outcomes and benefits of the research. Finally, the research methods are presented, and the thesis structure is outlined.

Chapter 2 reviews the relevant literature and methodologies in order to select the most appropriate approach for detecting and mapping Paterson's curse. The chapter first examines the remote sensing properties that are relevant to weed detection and mapping, including selecting the appropriate imagery for the task (incorporating spatial, spectral, radiometric, and temporal resolution, and scale issues), and appropriate classification and validation methods. The literature that pertains to remote sensing of weeds is reviewed, including the properties of weeds that are applicable to detection with remote sensing. Lastly, the remote sensing literature for Paterson's curse is reviewed, and the most relevant findings are discussed.

Chapter 3 describes the study area, the study species (Paterson's curse), and datasets used in the research. The chapter includes the rationale for selecting the study area, the physical and climate conditions, and the characteristics of the remotely sensed datasets and field data.

Chapter 4 uses field spectroscopy to investigate the spectral properties of Paterson's curse which may allow it to be discriminated from co-occurring cover types with remote sensing, and which can be up-scaled to airborne and satellite sensors. The spectral properties of Paterson's curse flower, stem, and plant material with co-occurring cover types such as green and senescent vegetation is examined; and the relationship between Paterson's curse density (through floral percentage cover

measured in the field) with band ratios/indices and proportion cover estimated from linear spectral unmixing is investigated.

Chapter 5 presents a comparative analysis of two different classification methods for discriminating Paterson's curse using airborne high spatial resolution multispectral imagery. Both hard and soft classification outputs are produced from the non-parametric multilayer perceptron and k-nearest neighbour classifiers. The classifications are validated using the quantitative statistical methods of receiver operating characteristic (ROC) analysis and Kappa statistics.

Chapter 6 presents the results of the application of satellite hyperspectral imagery (EO-1 Hyperion) for mapping Paterson's curse. Matched filter classification outputs are produced; and the relationship between band ratios/indices and Paterson's curse presence/absence is investigated using logistic regression. As with Chapter 6, both hard and soft classification outputs are produced and validated using ROC analysis and Kappa statistics.

Chapter 7 presents a summary of the research, based on the objectives in Section 1.5, and includes recommendations for further research against each objective.

2 METHODOLOGICAL AND LITERATURE REVIEW

2.1 Introduction

This chapter reviews the role of remote sensing for detecting and mapping invasive plants, in order to select the most appropriate approach for detecting and mapping Paterson's curse. The first section examines the remote sensing properties that are relevant to weed detection and mapping, including selecting the appropriate imagery for the task (incorporating spatial, spectral, radiometric, and temporal resolution, and scale issues), and the appropriate classification and validation methods. The second section reviews the literature pertaining to remote sensing of weeds, including the properties of weeds that are applicable to detection with remote sensing. The third section reviews previous remote sensing work relating to Paterson's curse. The final section outlines the most relevant findings of the review that could be applied to Paterson's curse.

2.1.1 Definition and scope of remote sensing

Remote sensing is defined as the art and science of recording information about objects without being directly in contact with those objects (Campbell 2008). It has been successfully applied in many different fields, including geology, seismology, meteorology and ecology. Data can be recorded from satellites, aircraft, boats, unmanned aerial vehicles, and by human operators. In the context of the research presented in this thesis, the definition of remote sensing will pertain to information about vegetation, using the visible and infrared parts of the electromagnetic spectrum, and using data from satellite, aircraft, and field spectroscopy.

2.2 Analysis of Remotely Sensed Data

There are five major stages in deriving information from remote sensing data (Lu and Weng 2007):

- (i) Selection of appropriate remote sensing data;
- (ii) Processing;
- (iii) Selection of appropriate method (e.g. classification);
- (iv) Post-processing; and
- (v) Validation.

Of the five stages, (i), (iii), and (v) will be described in sections 2.3, 2.4, and 2.5 respectively, with examples of applications from the literature. Processing and post-processing are described in detail in reference texts such as Mather and Koch (2011) and Campbell (2008).

2.3 Selection of Appropriate Data

The utility of imagery from a particular sensor for an earth observation application is determined by the type of sensor used (e.g. multi-spectral, hyperspectral, radar), and the resolution properties of the sensor (spatial, spectral, radiometric, and temporal). In order for different features to be extracted from an image and discriminated from each other, the user must carefully consider the attributes of the features of interest, and match these with the appropriate resolution. In most remote sensing applications, a favourable combination of resolution types is required for success, with some more critical than others. There are also trade-offs between increasing one resolution type over another. The following section will examine the four types of resolution, as well as the scale considerations of the target species or object type to be mapped using remote sensing.

2.3.1 Spatial resolution

A pixel (picture element) is the fundamental unit of measure from a remotely sensed image. A pixel is the smallest object in the image, and can be considered as a subdivision of the study area (Fisher 1997). Pixel size is dependent on the instantaneous field of view (IFOV) of a particular sensor i.e. the area on the ground where the sensor receives energy at a particular moment (Tso and Mather 2001). The IFOV is largely fixed for satellite sensors, but not for airborne sensors, where the IFOV can be modified by varying the altitude of capture (Atkinson 1997). Spatial resolution has direct bearing on the area that an image covers; high resolution sensors generally are used to capture smaller areas due to cost, whereas sensors with a coarser spatial resolution can cover continental scales. Sensors can broadly be classified into high spatial resolution (< 10 m pixel size), medium resolution (10–30 m), and coarse (> 30 m). A list of common sensors and the spatial resolution and area covered is shown in Table 2.1.

The value (or digital number) for a given pixel is determined by the average brightness from features contained within the area of that pixel. A homogeneous land cover class within a pixel will contribute consistent brightness values, whereas if a pixel contains multiple land cover classes, the average brightness value may not represent any of the land cover classes (Campbell 2008). The problem of mixed pixels has been widely discussed in the remote sensing literature (e.g. Atkinson and Aplin 2004; Fisher 1997; Woodcock and Strahler 1987). The main factors that influence mixed pixels were identified by Fisher (1997): 1) The degree of sharpness or fuzziness between classes; 2) the presence of eco-tones between classes, which are especially common between vegetation communities in natural environments, where a mixture of each class occurs; 3) the presence of linear objects within pixels (e.g. roads, streams) that have a high contrast to the surrounding features in a pixel, and can be more easily discerned; 4) the presence of sub-pixel objects (e.g. tree crowns, houses) that are smaller than the area covered by a pixel, but can still be discriminated due to a high contrast with the background.

2.3.2 Spectral resolution

The spectral resolution of a sensor is defined by the total number of bands, and the width of the bands. The position of the bands in the electromagnetic spectrum influences the type of materials or cover types that can be sensed. Sensors used in remote sensing can be divided into two types based on the number of bands: hyperspectral and multi-spectral (Table 2.2). Hyperspectral sensors contain large numbers of bands, but also encompass small sections of the electromagnetic spectrum, and therefore have a high spectral resolution. A sensor is generally regarded as being hyperspectral when it has more than 48 bands, and a bandwidth of 20 nm or less (Aspinall, *et al.* 2002). Multi-spectral sensors contain fewer bands (usually less than 20) and the band-width is usually wide, especially with satellite sensors. For multi-spectral airborne sensors with limited bands (e.g. < 5), filters can be applied to selected narrow areas of the electromagnetic spectrum that area of most interest in detecting features of interest. Both the width of bands and the spatial resolution (Section 2.3.1) determine how much energy is received by the sensor.

Table 2.1 Spatial resolution of currently available multispectral and hyperspectral remote sensing data.

Sensor	Type	Pixel Size (m)	Scene Size
Landsat 8 (Operational Land Imager)	Satellite	30	185 x 185 km (full)
IKONOS	Satellite	3.2	11 km swath width
Quickbird	Satellite	2.4	16.5 km swath width
GeoEye-1	Satellite	2	15.2 km swath width
WorldView-2	Satellite	2.4	16.4 km swath width
MODIS	Satellite	250 - 1000	2330 km (length) x 10 km (width)
NOAA AVHRR	Satellite	1001	2600 km swath width
EO-1 Hyperion	Satellite	30	185 x 45 km
SPOT 5	Satellite	20	60 x 60 km
SPOT 6	Satellite	6	60 x 60 km
ASTER	Satellite	15–30	60 km swath width
ALOS (AVNIR-2)	Satellite	10	70 x 70 km
Airborne (analogue and digital)	Airborne	Varies according to altitude	Varies according to altitude
AVIRIS	Airborne	20	Varies
CASI	Airborne	0.25–1.5	Varies
HYMAP	Airborne	3–12	Varies
AISA	Airborne	1–4 (typical)	Varies

Table 2.2 Spectral resolution of currently available multispectral and hyperspectral remote sensing data.

Sensor	Type	No. of Bands	Spectral Coverage (nm)
Landsat 8 (Operational Land Imager)	Satellite	6	430–450; 450–510; 530–590; 640–670; 850–880; 1570–1650; 2110–2290; 1360–1380
IKONOS	Satellite	5	445–516; 506–595; 632–698; 757–853
Quickbird	Satellite	5	450–520; 520–600; 630–690; 760–900
WorldView-2	Satellite	8	400–450; 450–510; 510–580; 585–625; 630–690; 705–745; 770–895; 860–1040
GeoEye-1	Satellite	4	450–510; 510–580; 655–690; 780–920
MODIS	Satellite	19	438–2155
NOAA AVHRR	Satellite	3	580–680; 725–1000; 1580–1640
EO-1 Hyperion	Satellite	220 (196 unique)	400–2500
SPOT 5	Satellite	4	500–590; 610–680; 780–890; 1580–1750
SPOT 6	Satellite	4	450–525; 530–590; 625–695; 760–890)
ASTER	Satellite	9	520–2430
ALOS (AVNIR-2)	Satellite	5	420–500; 520–600; 610–690; 760–890
Airborne (analogue and digital)	Airborne	Variable	Variable
AVIRIS	Airborne	224	400–2500
CASI	Airborne	288	400–1000
HYMAP	Airborne	128	400–2450
AISA	Airborne	20–70	430–1000

2.3.3 Radiometric resolution

The radiometric resolution of a sensor is denoted by the number of grey (or brightness) levels that can be recorded. For digital sensors, the number of levels is dependent on the number of bits, which are binary (base 2) digits (Mather and Koch 2011). For example, 8-bit sensors record 256 levels of brightness, whereas contemporary 16-bit sensors record 65536 levels. Increased radiometric resolution provides greater contrast in parts of the electro-magnetic spectrum where the separability between feature and background/others features is greatest. The radiometric resolution of sensor is also influenced by the spatial resolution. A smaller

pixel size (or IFOV) will result in less energy being received by a sensor, thereby reducing the signal-to-noise ratio, and the sensor may be less sensitive to minor differences in energy levels (Tso and Mather 2001). There is a trade-off between increasing band widths to improve radiometric resolution, and reducing band widths to focus on specific regions of the electromagnetic spectrum (Tso and Mather 2001).

2.3.4 Temporal resolution

Temporal resolution is defined as the period required by a given sensor to re-image the same location on the Earth's surface. For satellite mounted sensors, the orbital characteristics (e.g. altitude) determine the revisit frequency. The revisit frequency for common satellite systems are shown in Table 2.3. For airborne mounted sensors, the revisit capability is far greater than satellite sensors. For example aircraft can be deployed at short notice to take advantage of favourable meteorological conditions. The temporal resolution of some satellites (e.g. SPOT, IKONOS, Quickbird, and Geoeye) can be increased due to their ability to be pointed off-nadir to increase revisit frequency. However these off-nadir images do not have the same viewing geometry as an image captured at nadir. Some satellite sensors such as Landsat 8 and the Moderate Resolution Imaging Spectroradiometer (MODIS) generally capture data during every overpass, whereas other sensors like GeoEye, WorldView, and Earth Observing 1 (EO-1) require specific tasking. The availability of imagery is dependent on factors such as cloud cover, haze, and smoke over the capture area.

Table 2.3 Temporal resolution of currently available multispectral and hyperspectral remote sensing data.

Sensor	Type	Revisit Period
Landsat 8	Satellite	16 days
IKONOS	Satellite	~ 3 days
Quickbird	Satellite	4.1 days
WorldView-1	Satellite	3.8 days
WorldView-2	Satellite	2.7 days
GeoEye-1	Satellite	~ 3 days
MODIS	Satellite	1–2 days
NOAA AVHRR	Satellite	Daily
EO-1 Hyperion	Satellite	16 days
SPOT 5	Satellite	2–3 days
SPOT 6	Satellite	1–2 days
ASTER	Satellite	16 days
ALOS (AVNIR-2)	Satellite	2 days
Airborne (analogue and digital)	Airborne	Variable

2.4 Selection of Appropriate Method

2.4.1 Vegetation indices

A vegetation index is a combination of two or more bands from a remotely sensed image that represents a quantitative measurement of the vigour of vegetation (Bannari, *et al.* 1995). Vegetation indices can focus on specific regions of the electromagnetic spectrum where differences exist between vegetation species or types. The large difference in the spectral response of vegetation in the near infrared and red was a particular focus for developing vegetation indices, and one of the first studies to use a ratio of the two bands from these regions was Jordan (1969), for mapping tropical rainforest canopy. Since the early applications, a large number of vegetation indices have been developed for different applications and environmental conditions. A comprehensive review of the history of the development of vegetation indices in the field of remote sensing is provided by Bannari, *et al.* (1995), including a summary of the more common vegetation indices. One of the most widely used

vegetation indices has been the Normalised Difference Vegetation Index (NDVI), represented in Equation 2.1 (Rouse, *et al.* 1973):

$$NDVI = \frac{NIR-Red}{NIR+Red} \quad (2.1)$$

The NDVI has an advantage over simple ratios (non-normalised) as it is able to account for variable illumination across an image (Jones and Vaughan 2010). However NDVI is less effective where vegetation is sparse, and modified indices such as the Soil Adjusted Vegetation Index (SAVI) have been developed to account for the soil background (Haboudane, *et al.* 2004). Other indices have been developed for detecting water stress (Hunt and Rock 1989), and monitoring the health of vegetation using the red-edge (Cloutis, *et al.* 1996).

Vegetation indices have been widely used in calibration models (e.g. using linear or non-linear regression) in conjunction with information on the biophysical properties of vegetation measured in the field, such as leaf area index, biomass, and cover to estimate those properties over large areas (Chen and Cihlar 1996). Vegetation indices derived from multi-spectral satellite imagery from Landsat TM, SPOT, AVHRR, and MODIS have been used to estimate vegetation biophysical attributes for agricultural areas (e.g. Houborg, *et al.* 2007; Salazar, *et al.* 2008; Wiegand, *et al.* 1991); forested environments (e.g. Chen and Cihlar 1996; Fassnacht, *et al.* 1997); and rangeland (e.g. Purevdorj, *et al.* 1998). Indices derived from hyperspectral sensors such as CASI and HyMap have been used to estimate leaf area index (LAI) and crown volume from forests (Schlerf, *et al.* 2005) and LAI and chlorophyll content from agricultural areas (e.g. Haboudane, *et al.* 2004; Haboudane, *et al.* 2002).

2.4.2 Field spectroscopy

Field spectroscopy is defined by Milton (1987) as ‘the study of the interrelationships between the spectral characteristics of objects and their biophysical attributes in the field environment’ (pg. 1808). Quantitative measurements of radiance, irradiance, reflectance or transmission (from ambient solar illumination) for vegetation are recorded by an instrument and calibrated with attributes such as LAI, biomass, or cover (Curtiss and Goetz 1994). The two main types of instrument used in field spectroscopy are spectroradiometers and radiometers, in which the former measure

spectral information over a continuous range of spectral bands and the latter over a limited number of discrete bands (Milton 1987). The sampling interval of spectrometers is usually smaller than the spectral resolution (bandwidth), which results in oversampling and less degradation when re-sampling spectra to match other hyperspectral instruments (Curtiss and Goetz 1994). The three main remote sensing applications for field spectroscopy are defined by Milton (1987) as prediction, calibration, and modelling. Each of these terms has a particular meaning in the context of field spectroscopy.

Prediction is an approach in which field spectra are collected from cover types and target materials to determine their suitability (i.e. predicting success) for up-scaling and detection using airborne and satellite remote sensing sensors (Curtiss and Goetz 1994). Field spectroscopy can be used to locate optimum spectral bands for a certain application, the best conditions (e.g. time of day, look angle), and the best time of year (Milton 1987).

Calibration involves using spectra of invariant surfaces collected on the ground by spectrometers in order to correct aerial or satellite imagery for atmospheric effects and convert the data from at-sensor radiance to at-surface reflectance (Milton, *et al.* 2009). There are two main types of calibration: reflectance, and radiance. For the former, the reflectance of a large flat and bare homogeneous area (near Lambertian surface) is measured with a spectrometer or radiometer, used in a radiative transfer model with atmospheric information to predict the radiance at the top of the atmosphere for each image band (Milton, *et al.* 2009; Slater, *et al.* 1987). The latter is similar to reflectance calibration, except measurements are taken for a helicopter or plane, rather than from the ground (Slater, *et al.* 1987).

In the context of field spectroscopy, modelling is an approach to determining relationships between the biophysical properties of vegetation and spectral properties. Band ratios and indices, in conjunction with a statistical approach such as linear or non-linear regression have been used to determine relationships between vegetation properties such as leaf area index, biomass, leaf chlorophyll, and leaf water content (Milton 1987). Studies have measured small scale features in the field such as individual leaves, as well as scaling up leaf measurements to that of a

vegetation canopy (Milton, *et al.* 2009). Spectra from vegetation species have been modelled from a variety of environmental settings, including agricultural (e.g. Broge and Mortensen 2002; Thenkabail, *et al.* 2000; Tucker 1979), tropical forests (Cochrane 2000), and greenhouse experiments for various plant species (e.g. Gitelson and Merzlyak 1994; Slaton, *et al.* 2001). In particular, the technique has been used extensively in precision agriculture, generating a large body of literature pertaining to field spectroscopy of crop and pasture biophysical attributes (Hatfield, *et al.* 2008).

2.4.3 Classification

Classification in a remote sensing context can be defined as the process of assigning pixels in an image to categories (e.g. land cover types) by means of a mathematical algorithm (Mather and Koch 2011). Producing thematic maps by image classification is one of the most common procedures in remote sensing (Foody 2004). Another term commonly used for image classification is pattern recognition, in which the pattern is a group of pixels in multi-dimensional feature space, and the recognition is of a set of one or more features about that pattern, such as brightness, elevation, or texture (Tso and Mather 2001). Image classification techniques can be divided into a general hierarchy (Figure 2.1), where the main classification types are per-pixel, per-field and contextual. Each type is discussed in the following sections, with examples of individual classification algorithms.

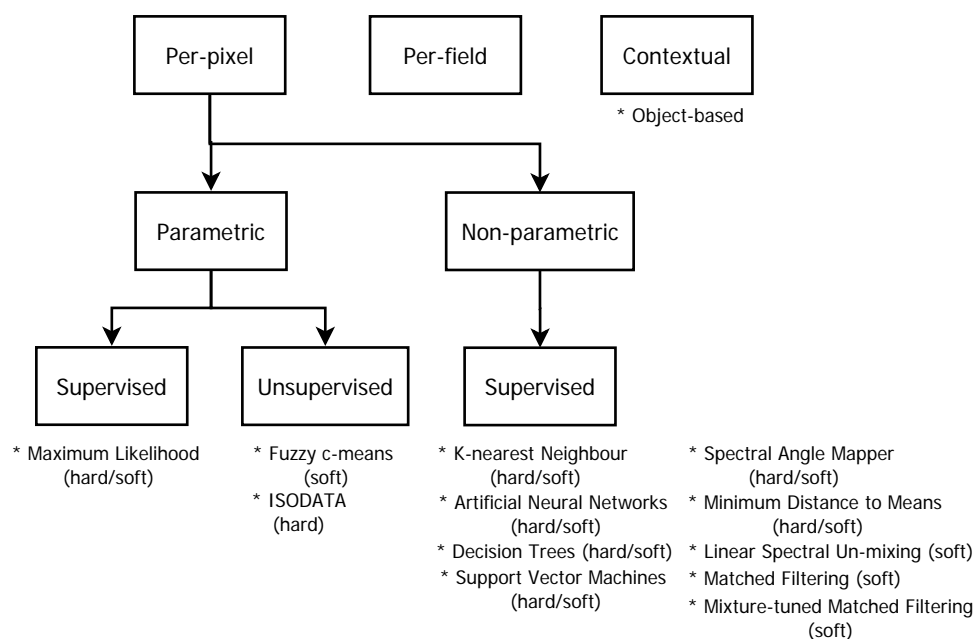


Figure 2.1 Summary of the major classification approaches.

Classification algorithms are broadly divided into parametric and non-parametric. Parametric algorithms have an assumption of normally distributed training data sets, which incorporates statistical parameters such as mean and covariance (Lu and Weng 2007). It can be common for the normality assumption of parametric classifiers not to be met (especially with heterogeneous environments), due to training samples lacking in size, having multi-modal distributions, and not representing the full spectral properties of the classes of interest (Lu and Weng 2007). Non-parametric algorithms lack the requirement of normally distributed data and can incorporate ancillary data, such as texture and elevation (Lu and Weng 2007).

Parametric algorithms can be either supervised or unsupervised, whereas non-parametric classifiers are only supervised. Unsupervised classification is a parametric approach that uses an algorithm to generate clusters in multi-dimensional feature space, based on statistical information (e.g. mean) from the image (Lu and Weng 2007; Tso and Mather 2001). The clusters, or spectral classes are areas of similar brightness across two or more image bands (Campbell 2008). Most unsupervised classifiers are cluster based, in which a pixel is assigned to a class (cluster) in image feature space based on the shortest distance to the cluster mean (Mather and Koch 2011). Initial clusters in feature space are randomly selected, and the mean pixel value of each cluster around the mean changes until a convergence threshold (proportion of unclassified pixels remaining) or iteration limit is reached (Tso and Mather 2001). At the completion of the classification, the spectral classes are labelled by the analyst (Tso and Mather 2001).

The advantages of unsupervised classification are: no prior knowledge is required of land cover classes or the environment in the area to be classified; error is reduced by the automated computer algorithm and minimal interference by the analyst during the process; the output classes are more spectrally homogeneous than those from a supervised classification approach; and there is a greater potential to delineate smaller clusters that would be otherwise be mixed with larger classes (Campbell 2008; Mather and Koch 2011). The disadvantages of unsupervised classification are: the spectral classes may not adequately represent the land cover classes of interest; the analyst has no control over the algorithm once started; the spectral properties of clusters (and labelled classes) are fixed for a particular image and classification, and

classifications cannot be applied directly across images and/or dates (Campbell 2008). Unsupervised classification is rarely used as a stand-alone classifier, and is more typically used as an exploratory method to ascertain the spectral properties of an image and how they relate to land cover classes of interest (Mather and Koch 2011), and to create spectrally homogenous and normally distributed classes to input into other algorithms, especially parametric supervised classifiers (Tso and Mather 2001).

Supervised classification is a parametric or non-parametric approach in which the analyst has some prior knowledge of the environment and land cover classes from the image to be classified (Lu and Weng 2007). 'Training area' samples are collected from representative areas of the image in order to train the classifier to determine the decision boundaries in feature space and assign class labels to pixels (Tso and Mather 2001). The training samples representing each class need to be homogeneous, and not contain mixtures of other classes. (Campbell 2008). In order to avoid bias in a classification, training areas should not be included in the validation dataset used to assess accuracy (Congalton and Green 1999). Training areas can be chosen at random (and subsequently removed) from a validation data set (Mather and Koch 2011), or located away from validation sites.

The advantages of supervised classification are that the classes created by the analyst may better represent a particular application or region; classifications can be more readily compared between geographic areas or between dates; training data can be analysed prior to the classification to determine statistical validity (e.g. for a parametric approach) and whether classes are properly represented (Campbell 2008). The disadvantages of the approach are that the training samples of classes may not adequately represent their spectral properties (non-homogeneous), especially in complex landscapes; smaller sized classes may not be represented; and creating representative training areas can be challenging and time consuming (Campbell 2008).

A 'hard' classification is where there is a one-to-one relationship between pixels and class labels, and a pixel is assigned to a single class (Tso and Mather 2001). The success of a hard classifier depends on the algorithm used and the variability between

classes in feature space. Where cover types are mixed, there can be significant mixing of the spectral signal recorded within a pixel. The problem of mixing is worse when the cover type of interest occurs in low proportions in a study area. Hard classifiers are most effective where spectral variability is minimal in the image to be classified, and in the associated land cover classes or types. Hard classifiers have limited effectiveness where there are numerous boundary pixels, where there are ecotones, or the image has a large amount of spectral variation (Foody 1996; Settle and Drake 1993).

‘Soft’ classification is a method to determine the degree to which a pixel belongs to a particular class, and the overall mixture of classes within that pixel (Eastman 2006) It is in essence a one-to-many relationship between pixels and class labels (Tso and Mather 2001). Where the decision boundaries in feature space are fixed in hard classifiers, in soft classification these boundaries can overlap (Tso and Mather 2001). Some common hard classification methods have the option to output soft classification equivalents (e.g. artificial neural networks, maximum likelihood and k nearest neighbour).

Soft classification has several distinct advantages over hard classification: i) they can assess the uncertainty of a classification; ii) additional knowledge can be incorporated into a classification prior to the individual class memberships being included in a decision rule, to produce a hard classification containing the most suitable class; iii) classes can be considered that are only partially represented in a pixel; and iv) the areal extent of a particular class can be more accurately estimated (Eastman 2006; Eastman and Laney 2002; Foody 1996). A limitation with soft classifiers is that the accuracy is difficult to quantify, compared to the error matrix approach (Section 2.5.2) of hard classifiers (Lu and Weng 2007). An overview of methods to assess the accuracy of soft classifiers is provided in Section 2.5.4.

2.4.3.1 Per-pixel classifiers

Per-pixel (or per-point) classification approaches consider each pixel as an independent entity, and a class is assigned to that pixel based only on its spectral properties (Jones and Vaughan 2010; Mather and Koch 2011). A brief description of the main per-pixel classification methods is provided in the following sections.

2.4.3.1.1 Parametric unsupervised: ISODATA

The most common unsupervised clustering algorithm has been the Iterative Self Organising Data Analysis Technique (ISODATA). The technique is described in detail in Ball and Hall (1967) but can be summarised as follows:

- (i) The initial cluster locations are randomly chosen by the algorithm, based on a user defined number of pixel coordinate pairs. The locations can also be defined from training data;
- (ii) Pixels are assigned to a cluster based on the shortest distance (e.g. Euclidian);
- (iii) The location of the cluster means change with each iteration based on the pixels assigned to them; and
- (iv) The algorithm stops when a certain condition is reached – for example if the cluster means remain unchanged from one iteration to the next, or the change is below a certain threshold (Campbell 2008; Mather and Koch 2011; Tso and Mather 2001).

2.4.3.1.2 Parametric supervised: maximum likelihood

Maximum likelihood is one of the most common supervised classification algorithms. It is based on Bayesian probability theory, in which each training class has a probability density function, derived from the mean and co-variance, and represented in three dimensions as a bell shaped surface (Campbell 2008; Lillesand and Kiefer 2000). Each pixel is assigned to the class to which it has the highest probability of membership (Tso and Mather 2001). The classifier is computationally more complex than minimum distance to means and parallelepiped, but can account for variability between classes more effectively. There is an assumption that training classes have a multivariate normal (Gaussian) distribution and that they are homogeneous in representing a particular land cover type (Campbell 2008). If the training classes do not meet these assumptions, the classifier can result in low accuracy (Eastman 2006).

2.4.3.1.3 Non-parametric supervised: minimum distance to means

This classifier is based on the distance of pixels in feature space to a mean (vector) from a set of training classes (Campbell 2008). The similarity of the mean vector and

the value of an unclassified pixel in feature space increases at smaller distances, based on a dissimilarity coefficient (Tso and Mather 2001). Although the classification is computationally faster than maximum likelihood, the accuracy is limited where there is high variance between classes. A pixel can be misclassified into a class with low variance and a smaller distance in feature space, rather than the correct class - with high variance and a longer distance in feature space (Lillesand and Kiefer 2000).

2.4.3.1.4 Non-parametric supervised: parallelepiped

The parallelepiped classifier is based on range of upper and lower threshold values (or standard deviation) in a training class, which are bound within a rectangular region (parallelepiped) in n-dimensional feature space (Lillesand and Kiefer 2000). Although the method is faster than minimum distance to means or maximum likelihood, classification results can be poor where there is high co-variance between classes. A pixel located on the boundary of two classes (parallelepipeds) can be assigned to both classes, and large areas of an image can remain unclassified due to pixels being located outside the parallelepipeds in feature space. The classifier is not widely used, due to the emergence of superior methods such maximum likelihood and artificial neural networks; the absence of computing power limitations which once made the method popular; and the high potential for low accuracy.

2.4.3.1.5 Non-parametric supervised: support vector machines

Support vector machines (SVM) are a supervised non-parametric classification approach that uses an algorithm to find the optimal boundary between training classes in multi-dimensional feature space (Huang, *et al.* 2002). The boundary is a hyper-plane with a margin of two parallel lines. The hyper-plane can be linear or non-linear, where a mapping function (kernel) is used to separate classes (Mather and Koch 2011). The support vectors are the pixels within the margin that determine the margin size that results in maximum separability of the two classes (Mountrakis, *et al.* 2011). The main advantages of SVM are the non-parametric assumption about the input data, and that smaller training samples are required, which represent the support vector pixels on class boundaries (Mather and Koch 2011). SVM have been demonstrated to produce similar or higher classification accuracy than other classifiers (e.g. Dixon and Candale 2008; Foody and Mathur 2004; Su, *et al.* 2007).

The disadvantages of SVM are that the algorithms can be complex and difficult to understand compared to other classifiers; the choice of kernel can have a big influence on the classification result; and SVM can be affected by noisy data or hyperspectral data with high dimensionality (Mountrakis, *et al.* 2011).

2.4.3.1.6 Non-parametric supervised: k-nearest neighbour

The k-nearest neighbour (kNN) classifier is a non-parametric supervised approach. For each image pixel, kNN calculates the k-nearest pixels in feature space (which is always an odd number to avoid ties), and the pixel is assigned to the class that has the majority of its training pixels within the k-neighbours (Campbell 2008). kNN can produce both hard and soft classification output. The soft classification produces an output image that contains the degree of membership of each pixel to a class based on the proportion of k-nearest neighbours (Eastman 2006). The advantages of kNN are that it is a relatively simple algorithm, and it is a suitable classifier for non-Gaussian multi-modal training data (Campbell 2008). The disadvantages are that large training classes may overshadow smaller ones (Eastman 2006); selecting a k-value requires cross-validation; and individual bands cannot be weighted (Campbell 2008).

The kNN method has been extensively used in national forest inventory mapping in North America and northern Europe, for estimating basal area, volume, and cover type based on training data from field plots (e.g. Franco-Lopez, *et al.* 2001; McRoberts 2008; Tokola, *et al.* 1996; Tomppo and Halme 2004). The technique was also used for mapping tropical rainforest in South America (Thessler, *et al.* 2008).

2.4.3.1.7 Non-parametric supervised: decision tree classification

Decision tree classification (DTC) is an approach where an image is progressively divided into homogeneous spectral regions based on decision criteria (Friedl and Brodley 1997). The process is analogous to the hierarchical top-down method in the fields of environmental and life sciences for classifying organisms (Tso and Mather 2001). A decision tree contains a root node, which comprises the complete data set (e.g. an image), which is divided into splits (internal nodes) and finally leaves (terminal nodes) which are given a class label (Friedl and Brodley 1997). The four types of decision tree are manual, univariate, multivariate, and hybrid. The manual

method or manual design approach (Swain and Hauska 1977) utilises a user created hierarchy and information on class separability from class statistics and spectral plots to create decision boundaries (Tso and Mather 2001). The manual method can be difficult to implement when the image data and the environment are complex, and in that case an algorithmic approach is required (Friedl and Brodley 1997; Tso and Mather 2001). Univariate decision trees split the input data into two or more subsets based on a single feature (e.g. a band ratio), whereas multivariate decision trees split the data into two or more subsets based on more than one feature in the input data (Friedl and Brodley 1997). Hybrid decision trees combine different classification algorithms and have the advantage of being used for complex classifications, and can be applied to different subsets of a larger dataset that may have different properties or characteristics (Friedl and Brodley 1997).

DTC has several advantages over other pixel based classification methods by being flexible, less complex, computationally faster, and being non-parametric, makes no statistical assumptions about the data (Friedl and Brodley 1997). The output of decision trees is easier to interpret than complex classifiers like artificial neural networks and requires less training time (Pal and Mather 2003). The decision tree approach has been compared with other classification methods, and has produced higher classification accuracy (e.g. Friedl and Brodley 1997; Otukei and Blaschke 2010); or similar accuracy (e.g. Duro, *et al.* 2012; Pal and Mather 2003). Pal and Mather (2003) reported that DTC produced lower classification accuracy than other methods when used with image data with high dimensionality (greater than 20 bands), thereby potentially limiting its utility in classifying hyperspectral data.

2.4.3.1.8 Non-Parametric supervised: artificial neural networks

Artificial neural networks (ANN) started to be used in the late 1980s for classifying remotely sensed images (Kanellopoulos and Wilkinson 1997). They are based on a simplified model of the human brain that applies artificial intelligence to pattern recognition (Tso and Mather 2001), with the premise that the human brain is effective in processing large volumes of data from different sources (Atkinson and Tatnall 1997). The main advantage of ANN classifiers for remote sensing is that they are non-parametric and subsequently do not require normally distributed training data. This means that multi-source data can be integrated into classifiers more

effectively (Benediktsson, *et al.* 1990), and training areas can be distributed in feature space as separate clusters (Atkinson and Tatnall 1997).

ANN classifiers are structured in a similar way to statistical classifiers, having a training stage and classification stage (Paola and Schowengerdt 1995). ANNs ‘learn’ about the data during the training phase, and subsequent decision rules are applied during the classification phase (Tso and Mather 2001). The most common algorithm used for training ANNs is back-propagation, where the network is trained until a minimum error threshold is reached between the desired and actual output values of the network (Paola and Schowengerdt 1995). Once the network has been trained, it is fed forward to produce an image classification. The most commonly used back-propagation algorithm has been the multi-layer perceptron (MLP). Artificial neural networks are generally more accurate than statistical classifiers, and can process large image datasets more quickly once the network has been trained (Atkinson and Tatnall 1997). The disadvantages of ANNs are that they require larger training samples than other classification methods (Benediktsson, *et al.* 1990) in order to properly train the network and are more complex and difficult to interpret than other classifiers.

2.4.3.1.9 Non-parametric supervised: spectral angle mapper

Spectral angle mapper (SAM) is a classification method most commonly used for hyperspectral, and sometimes multi-spectral data. The method determines the spectral similarity between two spectra (a pixel and reference) in feature space along vectors (Campbell 2008). The reference spectra can be derived from an image or a spectral library. The size of the angle between the two vectors determines the degree of similarity (from 0 to 1) between the pixel and the reference spectra (Figure 2.2). The strength of SAM is that the vector angles are not affected by differences in vector length caused by factors such as illumination differences in an image (Kruse, *et al.* 1993). The disadvantage of the method is that SAM requires training (end-member) classes to be comprised of pure spectra, with no mixed pixels (Campbell 2008).

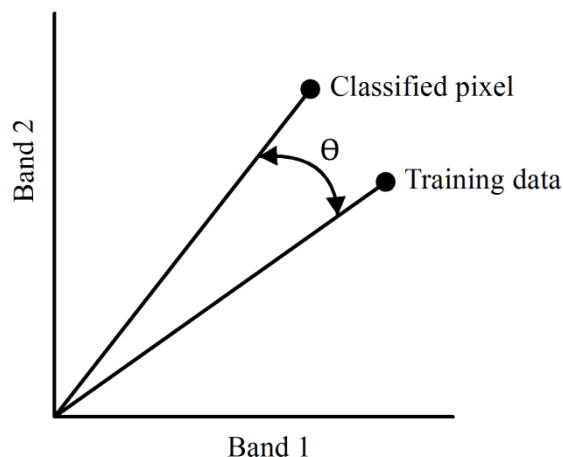


Figure 2.2 Spectral angle mapper concept (adapted from Campbell, 2008).

2.4.3.1.10 Non-parametric supervised: Fuzzy c-means

The fuzzy c-means algorithm (Bezdek, *et al.* 1984) has been a commonly used soft classifier (e.g. Canon, *et al.* 1986; Foody 2000). The algorithm assigns a fuzzy membership grade (from 0 to 1) to a given pixel based on its Mahalanobis or Euclidian distance to a set of clusters in feature space (Mather and Koch 2011). The clusters can be user-defined or randomly generated, and the outcome of the classification is not dependent on the initial cluster location, as is the case with ISODATA (Tso and Mather 2001).

2.4.3.1.11 Non-parametric supervised: Linear spectral unmixing

Linear spectral unmixing (LSU) is a method which estimates the proportion of each cover type within a pixel (Settle and Drake 1993). Each cover type is represented as a spectrally ‘pure’ end-member that contains pixels with 100% abundance of that cover. The weighted linear sum of all the end-members for a given pixel determines the total energy that reaches a sensor, and is represented in Equation 2.2 (Mather and Koch 2011):

$$r_i = \sum_{j=1}^n a_{ij}f_j + e_i \quad (2.2)$$

Where r_i is the reflectance of a pixel of band i , j is the number of end-member components, f_j is the value of the j th fractional component that constitutes r , and a_{ij} is the reflectance of end-member j in band i .

Each end-member is a point in n -dimensional features space, where the number of dimensions is determined by the number of bands (Settle and Drake 1993). Where two end-members are used, the mixture of those two materials for a given pixel will be somewhere along a two-dimensional line joining the two end-members. For three or more end-members, the mixture will be within a triangle (Figure 2.3) or a multi-dimensional shape, in which the number of dimensions will be determined by the number of image bands.

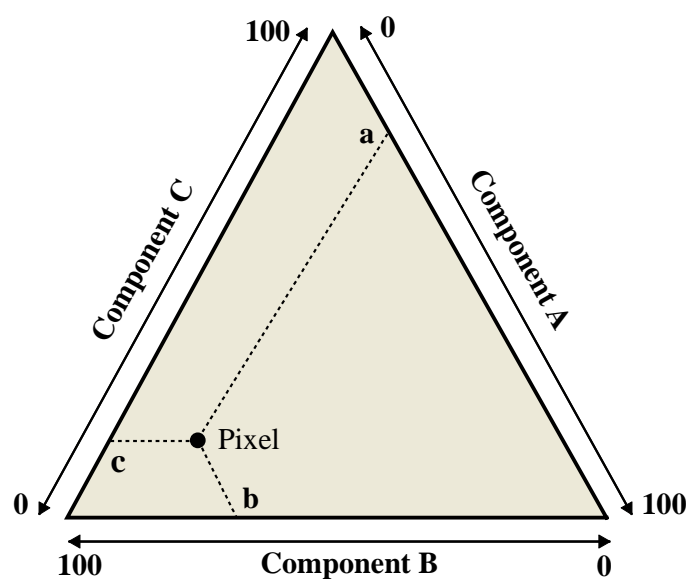


Figure 2.3 Example of a hyper-plane triangle (Adapted from Mather and Koch 2011).

There are two variations of linear unmixing: constrained/partially constrained, and un-constrained. For the former, the fractional abundances for individual cover types must be between 0 and 1, and the sum of all cover types must be less than or equal to 1 (Mather and Koch 2011). For the latter, the fractional abundances can be greater than 1 ('overshoots') or be negative ('undershoots'), and the sum of cover types does not need to sum to 1 (ITT Visual Information Solutions 2006a; Mather and Koch 2011).

Linear spectral unmixing has two main assumptions: i) the number of end-members must be less than the number of image bands (ITT Visual Information Solutions 2006a), which is why LSU has been mainly used with hyperspectral data, as there are usually too few bands with multispectral data to satisfy the assumption; and ii) the

linear mixing occurs when photons interact with more than one cover type before being received by a sensor (Tso and Mather 2001), and the problem is particularly prevalent with heterogeneous cover types with dispersed patterns, where there is a multiple scattering and subsequent mixing of photons (Campbell 2008; Tso and Mather 2001). The other limitation with LSU that can affect model fit, is that all materials or land cover types present in an image must be included as end-members (Mather and Koch 2011). This can present particular problems when only a small number of cover types are of interest, or not all land cover types within a particular scene are known (Tso and Mather 2001).

2.4.3.1.12 Non-parametric supervised: Matched filtering and mixture tuned matched filtering

The matched filter technique was developed for electrical engineering applications for detecting signals amongst mixed backgrounds (e.g. radio and radar) and introduced to remote sensing in the late 1980's (Boardman 1998). The matched filter maximises the contrast between an end-member and the background by suppressing the background (Boardman 1998). The advantage of matched filter over LSU is that only one end-member at a time is input into the classifier, which is valuable where a material type is present in the scene in lower abundances or there is a lack of knowledge of other materials in the scene (Boardman 1998). The disadvantage of matched filter is the instance of false positives that occur, particularly where image datasets are noisy or where a particular material is uncommon (ITT Visual Information Solutions 2006a).

Mixture tuned matched filtering (MTMF) is a combination of LSU and matched filtering but does not have the disadvantages of each (Boardman 1998). The output of MTMF is a matched filter score, and an image of infeasibility (noise sigma units) that can reduce the number of false positives (Boardman 1998). Plots of the matched filter score against infeasibility can be produced in two dimensional feature space, allowing the end-user to manually threshold the image based on low infeasibility values and corresponding matched filter scores above background values of zero (ITT Visual Information Solutions 2006a).

2.4.3.2 Per-field classification

Per-field classification is a method developed for agricultural regions, to overcome the limitations of per-pixel classifiers where there is high spectral variability between similar land cover types, such as crop and pasture (Lobo, *et al.* 1996). The method integrates vector and raster data types, in which spectral information from a remote sensing image is obtained from within a core area of a vector parcel shape, and a buffer area on the outside is excluded from the statistics to reduce mixed pixel effects; the final class label is assigned to the entire shape, including the buffer area (Dean and Smith 2003).

The main strengths of per-field classification over a per-pixel approach are that it is repeatable and operational, and existing classification maps can be updated based on new vector information for land cover (Smith and Fuller 2001). The method also eliminates the problem from per-pixel classifiers where misclassification can occur within areas of homogeneous classes e.g. grass in cropped areas (Smith and Fuller 2001). The per-field approach has been found to improve classification accuracy over the per-pixel approach (e.g. Aplin and Atkinson 2001; Dean and Smith 2003; Erol and Akdeniz 2005; Lloyd, *et al.* 2004; Lobo, *et al.* 1996; Smith and Fuller 2001; Turker and Ozdarici 2011).

There are several disadvantages with the per-field classification method: the process can be hampered by the differences in the data types of vector and raster information; (Lu and Weng 2007); up-to-date vector data of land parcels is required, which may not be available in many regions (Smith and Fuller 2001); and the landscape to be classified needs to be comprised of land cover parcels that are homogeneous and represent pure examples of cover types (Smith and Fuller 2001). Dean and Smith (2003) suggested that per-pixel classification may be a better alternative if multiple land cover types occur within parcels. The method has been shown to be effective in agricultural areas (crop and grassland) where one cover type tends to dominate, but less so in natural or semi-natural areas where a mosaic of cover types can occur (e.g. Dean and Smith 2003; Smith and Fuller 2001).

2.4.3.3 Contextual classification

A limitation of per-pixel classifiers is that each pixel is considered as a separate entity, with no association with neighbouring pixels (Blaschke and Strobl 2001). Per-pixel approaches were very effective with coarse and medium resolution satellite imagery (e.g. Landsat) where objects or features were of a similar size to the pixels (Blaschke 2010), but were shown to be less effective when high spatial resolution imagery like IKONOS and Quickbird became available (Blaschke and Strobl 2001). At high spatial resolution, a single pixel is smaller than single features or objects (e.g. buildings and tree canopies), which are represented as multiple pixels (Blaschke 2010). Pixel based classification of high spatial resolution imagery can result in a 'salt and pepper' appearance which has limited value for some applications and is not readily transferable into a usable format (e.g. for a geographic information system (GIS)). Spectral information used in isolation therefore only conveys a limited amount of information from a remote sensing image (Daniels 2006).

Contextual classification is an approach that assumes pixels in the neighbourhood of a given pixel share similar spatial information and hence are likely to be the same cover type (Magnussen, *et al.* 2004). There are three main categories of contextual classification: morphological and textural; Markov Random Fields and Bayesian and neural networks; and object based classification (Thoonen, *et al.* 2012).

Morphological information in the form of spatial datasets derived from a GIS can be incorporated into a contextual classification, such as slope, rainfall, location, land use, and any other additional information that might improve classification accuracy (e.g. Daniels 2006; Magnussen, *et al.* 2004). Textural information, in the form of filters can be applied pre-or post-classification to remove the 'salt and pepper' appearance of a classification, particularly in heterogeneous environments, and produce improvements in classification accuracy (Luo and Mountrakis 2011). Texture filters can also be used to produce additional layers to incorporate into a classifier, for example the grey level co-occurrence matrix of Haralick, *et al.* (1973). Contextual classification approaches such as Markov Random Fields (e.g. Kasetkasem, *et al.* 2005; Melgani and Serpico 2003; Zhao, *et al.* 2007), Bayesian (Aspinall and Veitch 1993; Osborne, *et al.* 2001), Dempster Shafer decision theory

(Momani, *et al.* 2006) and neural networks have been used extensively for incorporating additional information into image classification.

Object based classification—or object based image analysis (OBIA) is a contextual classification approach that uses an algorithm to simulate the way the human brain interprets and classifies the patterns of features observable in an image (Blaschke 2010; Blaschke and Strobl 2001; Harris 1980). The basic procedure of object classification is to first divide (or segment) an image into objects based on spectral and spatial properties. These generated objects are considered analogous to pixels, and may be further classified using a range of properties including spectral, spatial, association, context and the inclusion of ancillary (GIS) data. Object classification emerged in the 1970's, starting with segmentation algorithms that generated objects from scenes. These early algorithms were essentially texture based (e.g. Haralick, *et al.* 1973), and provided input layers to classifiers, rather than being a classifier in their own right. In the early 2000s a software package called eCognition (Definiens Imaging) emerged and resulted in a major increase in object based applications (Benz, *et al.* 2004). The program integrated a segmentation algorithm, a decision tree hierarchical structure with fuzzy class boundaries, and a collection of object properties that include spatial, spectral, and context. A thorough review of the development and application of object based classification is presented in Blaschke (2010).

2.5 Validation

Accuracy assessment is an essential procedure for ratifying the quality of maps and other products derived from remote sensing (Congalton and Green 1999). Prior to the availability of satellite remotely sensed imagery and computer based classification techniques, the accuracy of what were mostly photo-interpreted map products was not assessed. Early maps from satellite remote sensing were assessed using a single accuracy value that was non site-specific i.e. spatially located samples on the map were not used (Congalton 1991). It was also common to use the same dataset to both train and validate the classification, which violated the assumption of independence of the validation data (Congalton 1991). The main components of an accuracy assessment are the type of data used to validate the classification; the method used to assess the accuracy (whether it is quantitative or qualitative); and where applicable,

the statistical approach used. These components are discussed in the following sections.

2.5.1 Sampling and validation data

The concept of sampling for training, and in particular validation, of remotely sensed data has been discussed in depth in the remote sensing literature (e.g. Atkinson and Aplin 2004; Curran and Williamson 1985; 1986; Dungan, *et al.* 2002; Stehman 2009). Sample data are used to determine the accuracy of an output classification product based on reference data (Tso and Mather 2001). The reference data can be obtained from field survey or from other remote sensing data (e.g. aerial photography). Discrete (or statistical) sampling is the most common method, in which a portion of the study area is sampled (Curran and Williamson 1986), given that remote sensing accuracy assessment is costly in time and money (Congalton 1988).

Curran and Williamson (1985) identified five aspects to consider when designing a field sampling program for validating remote sensing products: 1) number of sites; 2) number of samples per site; 3) area of each sample; 4) how the samples are processed or classified; and 5) competency of field staff. There are three additional aspects to consider: the design of the sampling scheme (e.g. simple random, stratified random, cluster, and systematic); the distance between samples (to minimise spatial autocorrelation); and the method for collecting the samples. Stehman (2009) outlined the major criteria for designing a sampling program for validating remotely sensed data: 1) the sampling should be probability based to allow for quantitative statistical analysis; 2) it should be realistic and cost effective; 3), there should be an even distribution of samples across the classification area; 4) there should be a small sampling error, which can be addressed through random rather than systematic sampling; 5) the standard error should be minimised by collecting a large sample size.; and 6) the sampling design should incorporate some flexibility to change the sample size and distribution to account for changing conditions during the survey (e.g. to reduce the original sample size or collect extra samples).

2.5.2 Error matrix approach

The error matrix, also known as a confusion matrix or contingency table (Story and Congalton 1986) was used increasingly from the late 1970's and became the most common method for assessing the accuracy of a classification derived from remotely sensed imagery (Congalton 1991). An error matrix is comprised of a square array of rows and columns, where the rows typically represent the classification data, and the columns the reference data (Congalton and Green 1999). The advantages of the error matrix approach are that descriptive and analytical statistical tests can be used to compare the performance of one or more classifications (Congalton 1991), and the accuracy of individual classes and overall accuracy can be quantified (Congalton and Green 1999).

The overall accuracy of an error matrix is calculated by dividing the sum of the correctly classified samples (diagonal), by the total number of samples in the matrix (Congalton and Green 1999). There are two measures of accuracy for individual classes: producer's and user's accuracy. Both are calculated by dividing the number of samples correctly allocated into a particular class (on the diagonal) by the number of reference samples for that class. The reference samples are derived from the column total for producer's accuracy, and from the row total for user's accuracy (Congalton 1991). The user's accuracy describes the quality of a map for representing a particular class on the ground (i.e. reality), whereas the producer's accuracy describes the effectiveness of a classification for mapping a particular class (Foody 2004; Story and Congalton 1986). User's accuracy is also known as commission error and producer's accuracy as omission error. These two error types are proportionally linked, as a misclassification will not only omit a given sample from the correct category, but include that sample into another category (Story and Congalton 1986).

2.5.3 Kappa

A statistical approach (rather than a direct comparison of accuracy) is required if the significance of the results of one or more classifications are compared (Foody 2004). The most common approach is Kappa - a discrete multivariate analysis technique (Congalton, *et al.* 1983). Kappa was first described by Cohen (1960), for the medical sciences, and the first published account of Kappa in the remote sensing literature was Congalton, *et al.* (1983). A KHAT statistic is produced from Kappa, which is the

difference between the actual agreement in the error matrix (major diagonal), and the chance agreement which is denoted by the row and column totals (Congalton and Green 1999). The equation for Kappa is provided below in Equation 2.3 (Congalton, *et al.* 1983):

$$\widehat{K} = \frac{\sum_{i=1}^r n_{ii} - \sum_{i=1}^r (n_{i+} n_{+i})}{n^2 - \sum_{i=1}^r (n_{i+} n_{+i})} \quad (2.3)$$

Where n is the total number of samples for all classes, n_{ii} is the number of correctly assigned samples for class i , n_{i+} is the row total for class i , and n_{+i} is the column total for class i .

In addition to overall kappa, conditional kappa (per-class) can be calculated to determine agreement in individual categories. The equations for conditional Kappa from user and producer perspective are given below in equations 2.4 and 2.5 (Congalton and Green 1999):

$$\widehat{K}_i = \frac{nn_{ii} - n_{i+}n_{+i}}{nn_{i+} - n_{i+}n_{+i}} \quad (2.4)$$

$$\widehat{K}_i = \frac{nn_{ii} - n_{i+}n_{+i}}{nn_{+i} - n_{i+}n_{+i}} \quad (2.5)$$

The parameters in the equations are described for Equation 2.3.

The large sample variance for the user's class i is given in Equation 2.6 (Congalton and Green 1999):

$$\widehat{var}(\widehat{K}_i) = \frac{n(n_{i+} - n_{ii})}{[n_{i+}(n - n_{+i})]^3} [(n_{i+} - n_{ii})(n_{i+}n_{+i} - nn_{ii}) + nn_{ii}(n - n_{i+} - n_{+i} + n_{ii})] \quad (2.6)$$

The parameters in the equation are as described for Equations 2.3 and 2.4. The producer's large sample variance is calculated by reversing the row and column totals (n_{i+} and n_{+i}).

The equations for testing the statistical significance of one classification and for a statistically significant difference between two classifications are shown in Equations 2.7 and 2.8 respectively (Congalton, *et al.* 1983):

$$Z = \frac{\hat{K}_1}{\sqrt{\hat{\sigma}_1^2}} \quad (2.7)$$

$$Z = \frac{\hat{K}_1 - \hat{K}_2}{\sqrt{\hat{\sigma}_1^2 + \hat{\sigma}_2^2}} \quad (2.8)$$

Where \hat{K}_1 and \hat{K}_2 refer to the Kappa statistic of classification 1 and 2, and $\hat{\sigma}_1^2$ and $\hat{\sigma}_2^2$ refer to the large sample variance derived from Equation 2.6 (Congalton and Green (1999)).

2.5.4 Soft classification validation

The error matrix approach for assessing accuracy and the corresponding Kappa statistic described in the previous sections are only applicable to the output from hard classifiers (Lu and Weng 2007). In contrast, the output from soft classifiers comprises a continuum of membership values for each class, and the approaches used for hard classification are therefore not applicable. A soft classification can be hardened by retaining the class with the highest probability (mixed classes excluded) in order to use error matrices and Kappa, but the accuracy of the original soft classification may not be properly assessed (Foody 1996). There have been different methods proposed in the literature for assessing soft classifiers with mixed classes such as fuzzy error matrices (Silván-Cárdenas and Wang 2009), measures of closeness (Foody 1996), and entropy (Maselli, *et al.* 1994), however no single method has yet been able to properly account for confusion between classes (Silván-Cárdenas and Wang 2009).

For classification methods that produce a single continuous output, such as matched filtering, there are two assessment methods that can find an optimum threshold and provide a quantitative measure of accuracy: density dependent and density independent. For the density dependent approach, the continuous classification output is divided into sections, Kappa values are then calculated for each section and the optimum cut-off point (based on the highest Kappa value) is used to produce a hard classification (Fielding and Bell 1997). This technique was used by Aspinall

(2002) to determine the optimum threshold value for a matched filter score from a MTMF classification of large woody debris from a CASI hyperspectral image.

For the density independent approach, the most common method used has been the receiver operating characteristic (ROC), which provides a quantitative measure of the predictive accuracy of a model (Fielding and Bell 1997; Pontius Jr. and Schneider 2001; Zweig and Campbell 1993). The approach been widely used for validating spatial predictive models in the environmental sciences (Osborne, *et al.* 2001; Pontius Jr. and Schneider 2001). For example Aspinall (2002) used ROC to assess the accuracy of a matched filter classification of large woody debris, and to determine the optimum cut-off point for hardening the classification. In other examples, Bradley and Mustard (2005) used ROC to determine the accuracy of a threshold NDVI classification of Landsat TM and AVHRR imagery for detecting the weed Cheatgrass (*Bromus tectorum*); Ishii and Washitani (2013) used ROC to validate generalised linear models of the relationship between the weed *Solidago altissima* and MNF bands and to produce a binary classification map.

ROC compares the values from a probability dataset with a corresponding validation dataset, made up of presence and absence records. The probability values are divided into percentile groups (e.g. 1%), where the top 1% of all records with the highest suitability are assigned to that class. The process continues until there are 100 groups, each containing 1% of the total records. A table (Table 2.5) is produced that shows the proportion of pixels in each suitability group that are classified as present/absent (Pontius Jr. and Schneider 2001). The true positive value is derived from $A/(A + C)$ while the false positive value is derived from $B/(B + D)$, where A, B, C and D are record counts in the contingency table for each threshold (Eastman 2006). The false positive and true positive are also referred to as 1-specificity and sensitivity respectively (Fielding and Bell 1997). ROC plots the false positive/true positive values from the range of decision thresholds over the range of the results (Zweig and Campbell 1993) (Figure 2.4).

Table 2.4 ROC contingency table (Adapted from Eastman 2006).

		Validation Data	
		In class of interest (1)	Not in class of interest (0)
Classified Image	In class of interest	A (true positive)	B (false positive)
	Not in class of interest	C (false negative)	D (true negative)

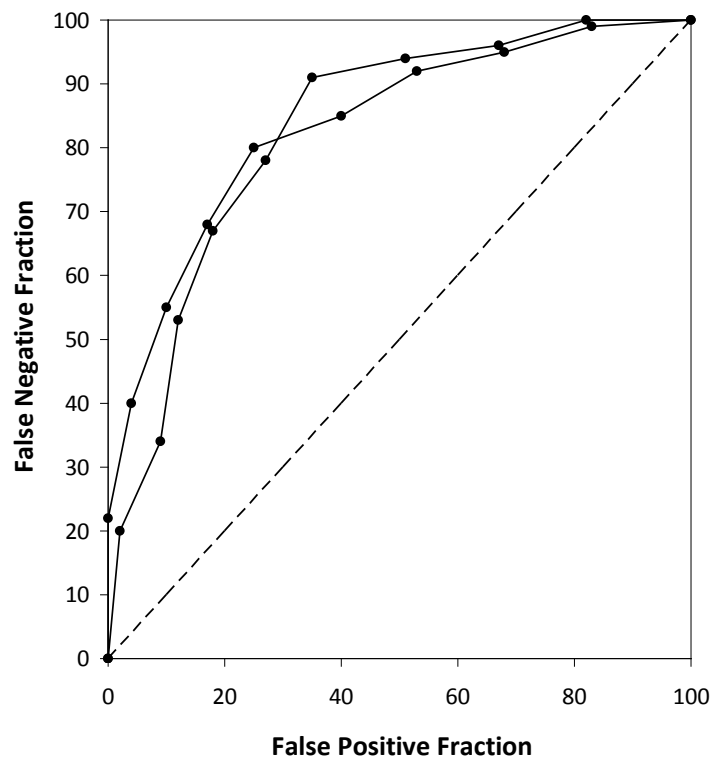


Figure 2.4 Example of two ROC plots showing false positive and false negative values.

The ROC index statistic (Equation 2.9) is determined by the area under the curve (AUC) that connects the plotted points (Pontius Jr. and Schneider 2001).

$$AUC = \sum_{i=1}^n [x_{i+1} - x_i] [y_i + y_{i+1} - y_i/2] \quad (2.9)$$

Where x_i is the rate of false positives, y_i is the rate of true positives, and n is the number of suitability groups.

The AUC value denotes the probability that a presence site will have a higher probability value than an absence site when the two are selected at random from a population (Elith, *et al.* 2006). An AUC value of 1 denotes a perfect match between the probability and validation data sets. Tests with higher accuracy (and corresponding AUC value) will have a curve that is close to the upper left corner of the plot, whereas tests with no discrimination ability (i.e. completely random) will be similar to a 45 degree line running from the lower left corner to the upper right corner, and have an AUC value of 0.5 (Pontius Jr. and Schneider 2001; Zweig and Campbell 1993).

For assessing the accuracy of band ratios and indices, most studies have used calibration methods such as linear and non-linear regression, due to the independent variable being a continuous data type. In an example where the independent variable was categorical (presence/absence), Apan, *et al.* (2004) used discriminant analysis to assess the accuracy of indices and band ratios derived from EO-1 Hyperion imagery to detect rust disease in sugarcane.

2.6 Remote Sensing of Weeds

In Chapter 1, remote sensing was identified as a potentially valuable source of information to assist with managing Paterson's curse, by providing regional scale information on the distribution and density of the species. The first part of this chapter reviewed the literature for appropriate methods of remote sensing for detecting and mapping invasive species and vegetation in general. The next part of this chapter will: 1) briefly describe the role of remote sensing for detecting vegetation, and briefly describe the properties of vegetation related to detection; 2) highlight the characteristics of weeds from previous applications of remote sensing that allowed them to be discriminated from surrounding vegetation and land cover; and 3) review previous applications of remote sensing to weeds, in order to determine what methods were used, what imagery types, and what level of success was obtained. The scope of this section will be agricultural environments, including pastures, rangelands, as well as weeds in natural environments, including riparian areas, and forests. Site specific weed management applications involving remote sensing will not be reviewed, as they are more relevant to precision agriculture in

croplands, where automated control of weeds is done through mechanised means (e.g. robotic vision).

2.6.1 Remote sensing of vegetation

Vegetation has physical and chemical properties that make it especially amenable to being detected with remote sensing. These properties are covered in Section 2.6.2. Remote sensing of vegetation has a long history, and there are a diverse range of successful examples in the literature including:

- (i) Long term vegetation cover trends (> 40 years) obtained from historical aerial photography (e.g. Bowman and Dingle 2006; Fensham, *et al.* 2005; Kadmon and Harari-Kremer 1999; Sharp and Bowman 2004), and satellite imagery (e.g. Furby, *et al.* 2008; Liangyun, *et al.* 2013);
- (ii) Monitoring changes in the structure and composition of Northern Hemisphere forests (Song and Woodcock 2003); deforestation in tropical rainforests (Arai, *et al.* 2011), and the impact of fire on savanna vegetation in sub-tropical Australia (Edwards, *et al.* 2001) and Africa (Archibald, *et al.* 2010);
- (iii) Satellite imagery has been used on a continental and global scale to determine vegetation health and vigour, and for inclusion in global climate change models (e.g. Zhang, *et al.* 2006);
- (iv) Emerging high spatial resolution satellite sensors and high spectral resolution airborne digital sensors are being used to map vegetation communities in increasing detail, including Light Detection and Ranging (LiDAR) that can detect the height of individual trees and species (e.g. Cho, *et al.* 2012; Whiteside, *et al.* 2011).

2.6.2 Properties of vegetation for remote sensing detection

The way in which light interacts with vegetation, and the proportion of light that is reflected, absorbed, and transmitted from vegetation, is wavelength dependent (Jones and Vaughan 2010). The spectral information received by a particular sensor from a canopy (or plant) is a mixture of the spectral response from individual leaves, stem and trunk material, multiple interactions with leaves, and the soil or water background (Jones and Vaughan 2010; Knipling 1970). Each species of plant has

leaves with a varying type of surface, thickness, internal architecture, and pigment content (Knippling 1970) which results in different proportions of reflected, absorbed, or emitted energy. The overall reflectance from a dense vegetation canopy will be less than that from a single leaf, due to a greater number of reflectance interactions; similarly the contribution of soil or water will be greater in sparser vegetation (Jones and Vaughan 2010).

A typical reflectance spectrum for green plant material is shown in Figure 2.5. Leaf reflectance in the visible wavelengths (400–700 nm) is determined by photosynthetic pigments like chlorophyll and carotenoids (Gates, *et al.* 1965). Absorption of light (70-90%) by leaves for photosynthesis is strong in the blue and red parts of the spectrum, but low in the green (500-600 nm) (Gates, *et al.* 1965; Mather and Koch 2011). In the near infrared (700-1350 nm), absorption of light is low, and reflectance is mainly determined by leaf structure (Gates, *et al.* 1965; Mather and Koch 2011). In the mid infrared (1350-2500 nm) wavelengths, reflectance is determined by water content, with water absorption troughs occurring at 1450 and 1950 nm (Gates, *et al.* 1965).

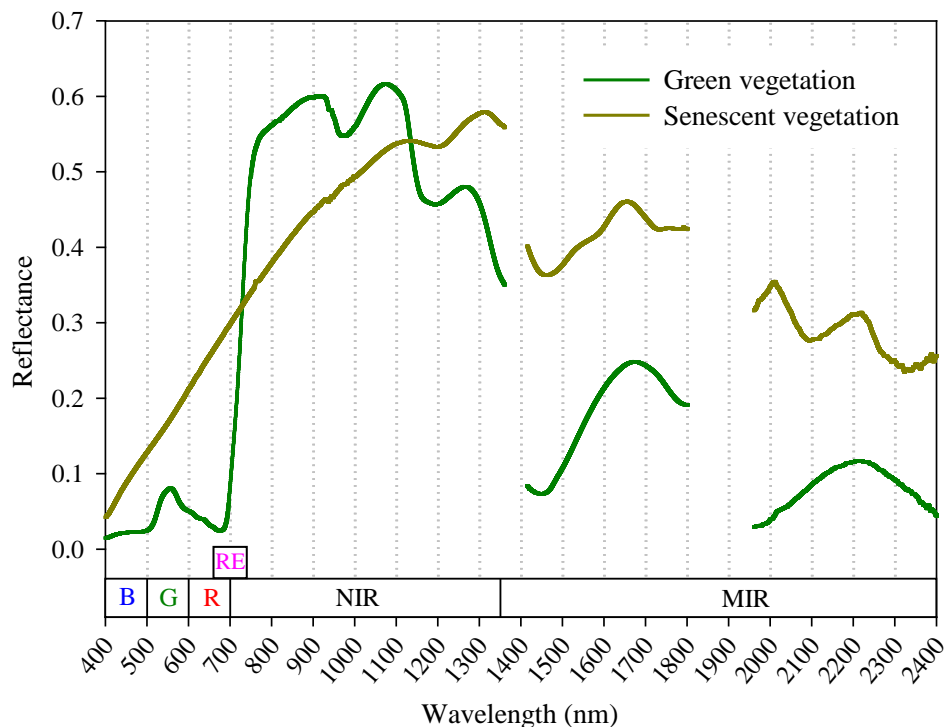


Figure 2.5 Reflectance spectra for green and senescent vegetation (sourced from Chapter 4). Parts of the electromagnetic spectrum: B = blue, G = green, R = red, RE = red-edge, NIR = near infrared, and MIR = mid infrared.

One of the strengths of remote sensing is the ability to detect stress in plants, even if the stress is not readily apparent to the human eye, which is restricted to the visible part of the electromagnetic spectrum. Carter (1993) found that spectral reflectance differences between stressed and healthy leaves were most likely to occur between 535 to 640 nm and 685 to 700 nm, and are characterised by low absorption by Chlorophyll a. Carter (1993) observed that even a small decrease in Chlorophyll-a from stress could result in decreased absorption and higher reflectance in stressed leaves. Infrared reflectance did not show a consistent or significant change as a result of stress, and was only significantly affected when leaves became dehydrated (Carter 1993). The spectrum of senescent vegetation (Figure 2.5) is distinct from green vegetation and shows a lower reflectance in the near infrared and a consistently higher reflectance in the visible wavelengths.

The red-edge feature has been demonstrated to be important for determining the health and condition of vegetation. The red-edge is defined as the transition between the red region of the spectrum and the near infrared (680-740 nm), where the reflectance of green vegetation shows a rapid increase (Dawson and Curran 1998; Slaton, *et al.* 2001). This property is unique to vegetation, and is caused by high internal leaf scattering producing high near infrared reflectance, and chlorophyll absorption in the red part of the spectrum (Horler, *et al.* 1983). Gates, *et al.* (1965) observed that the red-edge shifted towards longer wavelengths in the leaves of white oak (*Quercus alba*) during a growth cycle, and proposed that it may be a good indicator of the amount of chlorophyll in a plant. A number of studies have either confirmed the relationship (e.g. Curran, *et al.* 1990; Horler, *et al.* 1983), or have shown that red-edge differences can be used to detect plant stress, and differences in the spectral properties of plants at different growth stages (e.g. Broochs, *et al.* 1990; Filella and Penuelas 1994; Smith, *et al.* 2004).

2.6.3 Characteristics of weeds for detection using remote sensing

An understanding of the characteristics of a target weed species is important for making an informed decision about the type of sensor, and the classification and analysis methods to be employed in a remote sensing application. A ground-up approach to weed detection with remote sensing can minimise the likelihood of the wrong sensor or method being employed, and a potential erroneous conclusion being

drawn about the utility of a sensor and/or method (Aspinall, *et al.* 2002). A review of the remote sensing literature (summarised in Appendix A) shows that differences in foliage and floral characteristics were the dominant mechanisms for discriminating weed species from the background vegetation and soil. However there were other characteristics which were unrelated to floral and foliage, including form (e.g. shrub, herb, grass, tree), spatial characteristics (e.g. density, patchiness), and life history (e.g. annual or perennial). Examples of these characteristics from the literature are described below.

2.6.3.1 Foliage properties

2.6.3.1.1 Orientation

Orientation relates to how foliage in a vegetation canopy is arranged, for example vertical (erectophile) or horizontal (planophile). These differences in canopy arrangement affect the way in which electromagnetic energy interacts within the canopy. For example the erectophile canopy structure of false broomweed (*Ericameria austrotexana*) was distinctive from co-occurring vegetation due to more gaps and shadowing, which resulted in a lower reflectance in the near infrared (Everitt, *et al.* 1984). In a similar study, Everitt, *et al.* (1987) reported lower near infrared reflectance from the erectophile canopy of Spiny aster (*Aster spinosus*), which made it spectrally distinctive from co-occurring vegetation. In contrast, when the species was flowering, it was not distinctive from co-occurring vegetation. A combination of small leaves and an erectophile canopy allowed Everitt, *et al.* (2007b) to discriminate Ashe juniper (*Juniperus ashei*) from co-occurring vegetation in the near infrared due to the lower reflectance from shadowing and reduced canopy density. In instances where Ashe juniper had similar near infrared reflectance to co-occurring vegetation, it could be discriminated in the visible wavelengths.

2.6.3.1.2 Colour

Foliage colour is determined by the composition of pigments and other chemicals in leaves. Colour can vary within and between species, due to factors such as the health and stress of a plant and the time of year. For example, the bright red leaves of Chinese tallow (*Sapium sebiferum*) in autumn produced a distinct spectral contrast to green woodlands and scrublands, and brown grasslands in the visible wavelengths (Ramsey III, *et al.* 2002). In a similar example, the yellow orange foliage of the

deciduous shrub tamarisk (*Tamarix* spp.) had higher visible reflectance in late autumn-early winter (550 and 650 nm) compared to the surrounding native vegetation (Evangelista, *et al.* 2009; Everitt and Deloach 1990; Frazier and Wang 2011; Wang, *et al.* 2013). Another species with different coloured foliage to native vegetation in winter was the evergreen shrub/small tree Redberry juniper (*Juniperus pinchotii*), with dark green leaves (Everitt, *et al.* 2001). In an aquatic environment, the floating macrophyte water lettuce (*Pistia stratiotes*) had light green foliage which produced higher reflectance in the green and red wavelengths than darker co-occurring vegetation (Everitt, *et al.* 2003). In contrast, the submersed macrophyte Hydrilla (*Hydrilla verticillata*) had dark green foliage with lower green and red reflectance than lighter co-occurring vegetation (Everitt, *et al.* 1999).

2.6.3.1.3 Density

The density of foliage in a canopy is related to the number and size of leaves per unit area. The higher the density of green vegetation in a canopy, the higher the corresponding near infrared reflectance and associated chlorophyll absorption in the red wavelengths (Gates, *et al.* 1965). The density of vegetation stands has some bearing of the density of canopies, for example whether they grow in clumps, or are dispersed into single trees or shrubs. Big bend loco (*Astragalus mollissimus var. earlei*) and Wooton loco (*Astragalus wootonii*) on west Texas rangelands had consistently higher near infrared reflectance than co-occurring vegetation due to a higher density canopy (Everitt, *et al.* 1994). Similarly, redberry juniper (*Juniperus pinchotii*) on northwest Texas rangelands had higher vegetation density and higher near infrared reflectance than co-occurring vegetation, which was in winter dormancy (Everitt, *et al.* 2001). In temperate forests, the evergreen tree glossy privet (*Ligustrum lucidum*) had a denser canopy and higher NIR reflectance than native forest species (Gavier-Pizarro, *et al.* 2012). The dense green foliage in the crowns of blackberry (*Rubus fruticosus* sp. agg.) was reported by Ullah, *et al.* (1989a) and Dehaan, *et al.* (2007) to be a good cue for discriminating the species, especially when it occurred in mono-specific patches in the landscape. However Ullah, *et al.* (1989a) found that there was spectral confusion with mixed vegetation types when blackberry was not in mono-specific stands.

2.6.3.1.4 Timing

The life history of a weed species can be an important factor to determine its suitability for detection with remote sensing. It relates to whether a species is annual or perennial, the timing of foliage and flowering, and the spectral and spatial relationship between the weed species and co-occurring vegetation. The foliage of the introduced perennial pasture species para grass (*Urochloa mutica*) had higher near infrared reflectance than senescent co-occurring vegetation on a floodplain in the mid-dry season (July) (Boyden, *et al.* 2013; Catt and Thirarongnarong 1992). In a similar example, Lass, *et al.* (2002) found that the success of detecting the annual herb spotted knapweed (*Centaurea maculosa*) was also dependent on the co-occurring vegetation being sparse and in a senescent stage. The combination of new blue-green stems and residual red-brown stems produced a higher reflectance in the near infrared compared with co-occurring vegetation. The understory shrub Amur honeysuckle could be detected at the time of year when it retained its foliage while the over-story was senescent (Wilfong, *et al.* 2009). The understory herb late goldenrod (*Solidago altissima*) could be detected in spring as understory before overstory grass species were dominant (Ishii and Washitani 2013). Two other understory species - Common (*Frangula alnus*) and glossy buckthorn (*Rhamnus cathartica*) produced foliage earlier in the growing season than the overstory forest species and retained it for longer (Becker, *et al.* 2013).

2.6.3.2 Floral properties

The floral characteristics of a weed species pertains to the colour of the flowers, the density of the flowers, and the timing and duration of flowering. There are examples in the literature where the spectrally distinct flowers of weed species provided the dominant spectral cue for discrimination, and other examples where species were not detectable in the non-flowering phase. For example the dense bloom of yellow flowers on Mexican palo-verde (*Parkinsonia aculeata*) on south Texas rangelands made the species spectrally separable from co-occurring vegetation in the green wavelengths due to the flowers, but was not separable when not flowering (Everitt and Villarreal 1987). The dense canopy coverage of orange-yellow flowers of huisache (*Acacia farnesiana*) was found by Everitt and Villarreal (1987) to have higher reflectance in 550 and 650 nm than other co-occurring vegetation species in March, but huisache could not be distinguished from co-occurring vegetation outside

of the flowering period. Other species with distinctive flowers that were only detectable during flowering included common goldenweed (*Isocoma coronopifolia*) and Drummond goldenweed (*Isocoma drummondii*) on south Texas rangelands (Everitt, *et al.* 1992), leafy spurge (*Euphorbia esula*) on rangelands in North Dakota and Montana (Everitt, *et al.* 1995), and broom snakeweed (*Gutierrezia sarothrae*) on rangelands in New Mexico and Texas (Everitt, *et al.* 1987).

The duration and timing of flowering has been shown to be important for detecting weed species. For example during the two week peak flowering period of yellow hawkweed (*Hieracium pratense*) in mountain meadows of the northwest United States of America, the bright yellow flower heads were spectrally distinctive from co-occurring pasture species, with reflectance differences in the yellow-green and yellow-red wavelengths (Lass and Callihan 1997). The species could be discriminated from pasture species at different stages of flowering, but not during the non-flowering phase. Andrew and Ustin (2006) found that during peak flowering for perennial pepperweed (*Lepidium latifolium*) in California (USA), the numerous small white flowers produced higher visible and near infrared reflectance compared to co-occurring vegetation. Similarly the woody legume Mexican palo-verde (*Parkinsonia aculeata*) had a limited flowering period, but produced a dense bloom of yellow flowers which produced a distinctive tone on colour infrared aerial photography (Everitt and Villarreal 1987).

2.6.4 Spectroscopy

In section 2.4.2, spectroscopy was highlighted as a valuable technique for remote sensing of vegetation. There were three main applications: 1) measuring the spectral properties of a plant species to determine the most suitable areas of the spectrum to discriminate and to relate those properties to airborne and satellite sensors (prediction); 2) Collecting ground spectra to calibrate airborne and satellite sensors (calibration); and 3) Determining the relationship between the spectral and biophysical properties of plants (modelling).

There are numerous examples in the literature where spectra of a target weed species have been captured with radiometers or spectrometers in the field, and compared with airborne and satellite remote sensing data collected on similar dates (Table 2.5).

In applications using multispectral imagery, the bands of the radiometers were similar to the bands from the airborne or satellite remote sensing sensors, which allowed a better assessment of the capabilities of the sensor. Spectroradiometers have been used in studies to examine the spectral properties of target weeds based on discrete areas of the electromagnetic spectrum that allows discrimination from other cover types. (e.g. Glenn, *et al.* 2005; Parker-Williams and Hunt 2002; Yang and Everitt 2007).

Several studies have used the reflectance from invariant targets captured with a spectroradiometer to calibrate imagery and perform atmospheric correction (Bradley and Mustard 2005; Underwood, *et al.* 2003; Yang and Everitt 2007). A particularly innovative study by Ramsey III and Nelson (2005) calibrated a EO-1 Hyperion hyperspectral satellite image using reflectance spectra from Chinese tallow (*Triadica sebifera*) in order to detect the species at low density.

Some studies have used band ratios and indices derived from field spectroscopy to map a weed species, or to determine the relationship between the band ratios/indices and the biophysical properties of the weed. For example Andrew and Ustin (2006) used band ratios within decision tree models to map perennial pepperweed (*Lepidium latifolium*) in California's San Francisco Bay/Sacramento–San Joaquin River Delta. In another example, Mirik, *et al.* (2006) investigated the relationship between the biophysical properties of Musk thistle (density, percent ground cover, height, and flower head density) and band ratios/indices using data from three sources: a spectroradiometer, radiometer and airborne hyperspectral imagery.

Table 2.5 Summary of field spectroscopy studies for weeds, with application type (AT) (P: prediction, C: calibration, M: modelling), and instrument type (IT) (S: spectrometer, R: radiometer).

Reference	Common Name	AT	IT
Everitt, <i>et al.</i> (1984)	False broomweed (<i>Ericameria austrotexana</i>)	P	R
Everitt and Villarreal (1987)	Huisache & Mexican palo-verde (<i>Acacia farnesiana</i> & <i>Parkinsonia aculeata</i>)	P	R
Everitt, <i>et al.</i> (1987)	Broom snakeweed & spiny aster (<i>Gutierrezia sarotbrae</i> & <i>Aster spinosus</i>)	P	R
Everitt and Deloach (1990)	Chinese tamarisk (<i>Tamarix chinensis</i>)	P	R
Everitt, <i>et al.</i> (1992)	Common & Drummond goldenweed (<i>Isocoma coronopifolia</i> & <i>Isocoma drummondii</i>)	P	R
Everitt, <i>et al.</i> (1994)	Big bend loco & Wooton Loco (<i>Astragalus mollissimus</i> var. <i>Earlei</i> & <i>Astragalus wootonii</i>)	P	R
Everitt, <i>et al.</i> (1995)	Leafy spurge (<i>Euphorbia esula</i>)	P	R
Lass, <i>et al.</i> (1996)	Yellow starthistle (<i>Centaurea solstitialis</i>)	P	S
Lass and Callihan (1997)	Yellow hawkweed & oxeye daisy (<i>Hieracium pratense</i> & <i>Chrysanthemum leucanthemum</i>)	P	S
Everitt, <i>et al.</i> (2001)	Redberry juniper (<i>Juniperus pinchotii</i>)	P	R
Parker-Williams and Hunt (2002)	Leafy spurge (<i>Euphorbia esula</i>)	P	S
Underwood, <i>et al.</i> (2003)	Iceplant & jubata grass (<i>Carpobrotus edulis</i> & <i>Cortaderia jubata</i>)	P/C	S
Parker-Williams and Hunt (2004)	Leafy spurge (<i>Euphorbia esula</i>)	P	S
Andrew and Ustin (2006)	Perennial pepperweed (<i>Lepidium latifolium</i>)	P/M	S
Everitt, <i>et al.</i> (2007b)	Ashe juniper (<i>Juniperus ashei</i>)	P	R
Dehaan, <i>et al.</i> (2007)	Blackberry (<i>Rubus fruticosus</i> sp. agg.)	P	S
Mitchell and Glenn (2009)	Leafy spurge (<i>Euphorbia esula</i>)	P	S
Yang, <i>et al.</i> (2009)	Ashe juniper (<i>Juniperus ashei</i>)	P	S
Martin, <i>et al.</i> (2011)	<i>Avena sterilis</i> & <i>Lolium rigidum</i>	P/M	S
Ramsey III, <i>et al.</i> (2005c)	Chinese tallow (<i>Triadica sebifera</i>)	P/C	R
Yang and Everitt (2007)	Waterhyacinth (<i>Eichhornia crassipes</i>)	P/C	S
Bradley and Mustard (2005)	Cheatgrass (<i>Bromus tectorum</i>)	C	S
Everitt, <i>et al.</i> (1999)	Waterhyacinth, hydrilla (<i>Eichhornia crassipes</i> & <i>Hydrilla verticillata</i>)	P	R
Everitt, <i>et al.</i> (2003)	Waterlettuce (<i>Pistia stratiotes</i>)	P	R
Everitt, <i>et al.</i> (2004)	Giant reed (<i>Arundo donax</i>)	P	R
Mirik, <i>et al.</i> (2006)	Musk thistle (<i>Carduus nutans</i>)	M	S/R

2.6.5 Aerial photography

Aerial photography was the most common source of remotely sensed data for weed mapping prior to the widespread availability of digital airborne and high resolution satellite imagery (e.g. Everitt, *et al.* 1992; Everitt, *et al.* 1995; Everitt and Deloach 1990; Everitt, *et al.* 1993; Everitt, *et al.* 1984; Everitt, *et al.* 1994; Everitt and Villarreal 1987; Everitt, *et al.* 2001; Ramsey III, *et al.* 2002). An advantage of an aerial platform (for either aerial photography or digital imagery) is that the altitude of the aircraft can be set to capture photographs at a high spatial resolution, which enables small infestations of weeds to be detected. Aerial photography has been used to detect weed infestations down to the level of individual plants, such as for leafy spurge (*Euphorbia esula*) (Everitt, *et al.* 1995), big bend loco (*Astragalus mollissimus var. Earlei*) (Everitt, *et al.* 1994) and shin oak (*Quercus havardii*) (Everitt, *et al.* 1993). The large number of aerial photography applications in the literature provides a useful means to predict the success of newer high resolution satellite sensors and aerial digital imagery. These new high resolution image sources can also be combined with historic aerial photography to map weed species at a similar spatial scale (Müllerová, *et al.* 2013).

2.6.6 Airborne videography

Aerial videography was another common remote sensing data source from the 1980s to 2000s for vegetation mapping, prior to the availability of cost effective digital aerial imagery (e.g. Everitt, *et al.* 1991; Everitt and Nixon 1985; Menges, *et al.* 2001; Nixon, *et al.* 1985). It has several advantages over aerial photography: it does not require chemical processing, and is quickly available after capture for analysis (Everitt, *et al.* 1992; Everitt, *et al.* 1993; Everitt, *et al.* 1994); the cost of aerial video imagery is lower than an equivalent area captured by aerial photography (Everitt, *et al.* 1992) and is considered a low cost means of assessing the accuracy of medium resolution satellite imagery, such as Landsat and SPOT (Everitt, *et al.* 1993). Even with a lower cost factor compared to aerial photography and aerial digital imagery, the cost of using airborne video to detect weeds over similar large areas to Landsat and SPOT is considered too high for most applications (Everitt, *et al.* 1994).

The spatial resolution of airborne video imagery is typically coarser than conventional film, and has been shown in some examples to be less effective than the

latter for detecting individual plants or small patchy infestations (Everitt, *et al.* 1992). For example Everitt, *et al.* (1992) found that that classified video imagery with a 0.15-0.2 m spatial resolution could not be used to map small patches and individual plants of common and Drummond goldenweed, and Everitt, *et al.* (1993) using imagery at a spatial resolution of 1.3-2.6 m, could only detect small stands of shin oak, in contrast to individual plants with aerial photography.

For non-woody weeds, the coarser spatial resolution of video may be more appropriate when the spectral reflectance of the target weeds species dominates a pixel. For example giant salvinia (*Salvinia molesta*) was mapped by Fletcher, *et al.* (2010) with 3 m spatial resolution CIR video imagery to a similar level of accuracy to CIR photography (Everitt, *et al.* 1999) due to high NIR reflectance from dense mono-specific mats of giant salvinia in the study area.

2.6.7 Airborne digital imagery

Airborne digital sensors record information from visible and near-IR bands at high spatial resolution. This high spatial resolution allows features as small as individual trees and shrubs to be detected, and the information is in a digital format which facilitates computer classification. Other advantages of digital aerial sensors include: a spatial resolution that can vary according to the flying height of the aircraft, which allows the end user to choose the pixel size, and the size of a given scene; a flexible deployment capability compared to satellite sensors, to take advantage of favorable meteorological conditions or limited periods in which weed species may be most detectable; and (for recent scanners and cameras), a high radiometric resolution of 12 or 16 bits, allowing tens of thousands of grey levels to be utilised by image classification algorithms. The disadvantages of airborne imagery include a potentially high cost of acquisition, and many images may be required to cover a large area.

High spatial resolution airborne imagery has been used in several applications to detect weeds in pasture. Carson, *et al.* (1995) used four band (blue, green, red, near infrared) Airborne Data Acquisition and Registration (ADAR) imagery at 1 m spatial resolution to map yellow hawkweed (*Hieracium pratense*) in pasture and meadow in Northwest Idaho. The omission error for maximum likelihood and

unsupervised classification ranged from 20 to 60% and 60 to 95% respectively when density classes were greater than 30%. Lass and Callihan (1997) used similar density classes to Carson, *et al.* (1995) to map yellow hawkweed (*Hieracium pratense*) with four band 1 m spatial resolution ADAR imagery. Yellow hawkweed could be discriminated from co-occurring vegetation species at > 20% cover, however the 20 to 60% class had a 30% omission error, which was attributed to spectral overlap between hawkweed and grass/forb mixes. Lass, *et al.* (1996) applied an unsupervised algorithm to four band imagery at a range of spatial resolutions (0.5–4 m) for yellow starthistle (*Centaurea solstitialis*) and common St. John's wort (*Hypericum perforatum*). The detection threshold for the two species was higher than Carson, *et al.* (1995), with density classes that ranged from 30% to 100%. The lack of a weed density class below 20 to 30% was a common theme across all three studies, and highlights the potential limitations of multi-spectral airborne data for mapping low densities of weed species in pastures.

High resolution airborne imagery has been used to detect shrubs in rangelands and semi-arid environments. For example Everitt and Yang (2007b) mapped broom snakeweed in Southern Texas rangeland using 0.5 m spatial resolution digital airborne imagery (Kodak Megaplus1.4i digital camera) and ISODATA unsupervised classification. Broom snakeweed could be discriminated from co-occurring vegetation with > 80% user's and producer's accuracies (overall Kappa 0.76–0.82). A notable weakness of that study was that no density classes or minimum patch sizes for detection were used. In a Western Australian rangeland study, Robinson, *et al.* (2008) reported an R^2 of 0.98 between field and image derived canopy cover of Mesquite (*Prosopis sp*) from 1.4 m spatial resolution digital multispectral imagery (DMSI). The minimum estimated canopy cover for detection of Mesquite shrubs was 3 m. In another semi-arid application to woody vegetation, Stow, *et al.* (2000) mapped invasive *Acacia* in native shrub-land in South Africa using 0.5 m spatial resolution imagery from a DCS 420 camera. Individual shrubs and trees (down to 1.5 m canopy diameter) could be visually identified on the imagery prior to classification, but within canopy variation in shadow and illumination caused spectral confusion when classified, although an accuracy assessment was not conducted to quantify it. All three previous rangeland studies (Everitt and Yang 2007b; Robinson, *et al.* 2008; Stow, *et al.* 2000) were more suited to an object

classification approach, given the spatial arrangement of woody vegetation was in clusters or patches.

2.6.8 Satellite multispectral imagery

The first commercial land resource satellites were launched in the early 1970s, and they provide a valuable time series of land monitoring data across the globe. Satellite based sensors have a number of advantages over aircraft, including geometric consistency over an entire image (less distortion at the periphery of imagery); regular capture (overpass) times; and lower cost than airborne imagery, especially over large areas.

In 1972, the Landsat 1 satellite was launched, carrying the Multi-spectral Scanner (MSS). Landsat 1 was the first of the Landsat series of satellites, and was typical of the series by having spatial and regular temporal coverage that made it suitable for monitoring vegetation at the landscape scale (Lawes and Wallace 2008). The first study to use data from Landsat MSS for weed detection was McDaniel, *et al.* (1975) who mapped areas of treated brush cover in Malheur County, Oregon, USA. Other studies to use Landsat MSS include Martinko (1982) and Boyd (1986). The main limitation with Landsat MSS from these early studies was the coarse spatial resolution (80 x 80 m), which meant that weed infestations had to be very large and at high density.

An opportunity to discriminate weeds at finer spatial scales and lower densities than Landsat MSS was provided by Landsat 4 and 5 Thematic Mapper (TM) and Landsat 7 Enhanced Thematic Mapper Plus (ETM+). These sensors had improved spectral and radiometric resolution, and a higher spatial resolution (30 m) than Landsat MSS. The relatively coarse spatial resolution of Landsat TM and ETM+ (compared to aerial imagery) still presented problems with classification accuracy due to mixed pixels and spectral overlap between weeds and co-occurring vegetation. For example Somodi, *et al.* (2012) used two dates of Landsat ETM+ and a four-band CIR orthophoto to predict the occurrence of *Robinia pseudacacia* in lowland forest in north-east Slovenia. A generalised linear model used image bands as predictor variables and presence of *Robinia pseudacacia* as response variable. The Landsat images did not perform well as an 4-band CIR orthophoto due to the mixing of

Robinia with other vegetation species within the pixels. Peterson (2005) addressed the issue of spectral overlap between cheatgrass (*Bromus tectorum*) and native grasses on Nevada rangelands by using the difference between two Landsat ETM+ images where cheatgrass and native grass were both green in the first image, and where cheatgrass was in senescence and native grass was green in the second image. Using such an approach, they obtained a R^2 of 0.71 from stepwise regression of cheatgrass cover in the field and vegetation indices and ancillary data (e.g. elevation).

Other studies using Landsat TM and ETM+ were successful due to the target weed species retaining its spectral distinctiveness when co-occurring vegetation was senescent, in early stages of growth or had experienced leaf fall. For example Wilfong, *et al.* (2009) reported an R^2 of 0.77 between NDVI derived from TM and ETM+ images, and percentage cover of Amur honeysuckle (*Lonicera maackii*). At the time of image acquisition, the overstory was in a senescent stage and the leaves of Amur honeysuckle in the understory were still green. In a similar example, Cuneo, *et al.* (2009) applied a maximum likelihood classifier to ETM+ imagery to map African olive with low commission and omission errors of 5.4% and 7.7% respectively. The detectability of African olive (*Olea europaea* L. *ssp.* *Cuspidata*) was enhanced by being spectrally distinct from co-occurring vegetation; being present as a mono-specific closed forest canopy (> 80%) or as a dominant understory beneath a sparse Eucalypt canopy; and the slow growing (10 years to maturity) habit of the species made it easier to collect representative ground validation data. Saltcedar (*Tamarisk*) was accurately mapped (Kappa 0.79–0.94) by Frazier and Wang (2011) and Evangelista, *et al.* (2009) along riparian zones in the Rio Grande and Lower Arkansas River, due to the species having distinctive yellow brown leaves when most co-occurring native vegetation species had shed their leaves.

In one example, a weed species was detected from Landsat TM imagery due to a year-round lack of co-occurring vegetation that could otherwise cause spectral confusion. Lawes and Wallace (2008) used Landsat TM mosaics from 8 dates from 1989 to 2004 to map prickly Acacia (*Acacia nilotica*) on the Mitchell grass plains of Northern Queensland. A discriminant analysis between vegetation indices and prickly Acacia tree density found the weed could be discriminated from the native

grassland species, but the authors noted that the success of the method was due to a lack of perennial woody species causing spectral confusion with prickly Acacia.

Some studies have combined a multi-temporal coverage of Landsat TM and ETM+ to include all relevant phenological stages of the weed species to enhance detection. For example Becker, *et al.* (2013) combined 49 Landsat TM/ETM+ images from 2007-2011 to map common (*Frangula alnus*) and glossy (*Rhamnus cathartica*) buckthorn in mixed prairie and forest in the Oak Openings Region in north-west Ohio and south-east Michigan. A parallelepiped classification was performed on separate image stacks comprised of tasseled cap greenness index, enhanced vegetation index and NDVI, of which the greenness index had the best accuracy (overall accuracy 83%, Kappa 0.73). Using a similar approach, Gavier-Pizarro, *et al.* (2012) mapped glossy privet (*Ligustrum lucidum*) on temperate to semi-arid slopes of the Sierras Chicas of Córdoba Argentina, using a stack of Landsat TM/ETM+ images from 1983 to 2006. From the stack, eight classes that included individual dates (1983 and 2006) and various periods of expansion were input into a Support Vector Machines classification. The best accuracy result for glossy privet was from the 2006 image (overall Kappa of 0.76 and per-class Kappa 0.88).

The first commercial satellite alternative to Landsat was SPOT 1, which launched in 1986. The main feature of SPOT was the 20 m spatial resolution, which was finer than the 30 m of Landsat TM. Anderson, *et al.* (1993) found that SPOT imagery was inferior to high resolution (0.6 m) aerial video imagery for detecting small stands (> 0.5 ha) of false broomweed (*Ericameria austrotexana*) on native rangeland in South Texas, USA. The SPOT imagery produced low accuracy during non-drought periods, when the spectral signature of false broomweed was confused with co-occurring herbaceous vegetation. They suggested a compromise, where SPOT imagery would be useful to map likely locations of false broomweed, and high resolution imagery for mapping the actual locations of infestations. In another rangeland study in Texas, the spatial resolution of SPOT was found by Everitt, *et al.* (1993) to be too coarse for mapping small stands of shin oak, although the larger area covered by the imagery was an advantage over airborne video and colour infrared photography.

In an study that combined image classification and spatial modelling, Lu, *et al.* (2013) used a temporal series (1988-2007) of SPOT 1 and 2 images to map and predict the distribution of *Leucaena leucocephala* in mixed tropical environments in Taiwan. The mapped expansion of the weed for the preiod 1988–1997 was used in a backward stepwise linear regression against various predictor variabed (e.g. distance to roads, 1988 mapped coverage, slope). The acuracy of the model (93% overall and 0.70 Kappa) was tested using the 2007 classification and showed that the distribution of *Leucaena* in 1988 contributed most to the spread of the species over time. A weakness of the study was that the model was only tested using pixels that contained *Leucaena*. at a density of greater than 50%.

Coarse spatial resolution satellite sensors such as MODIS and NOAA provide scenes that cover thousands of square kilometres. In one of the early applications of coarse resolution imagery to weeds, Peters, *et al.* (1992) found that the 1 km spatial resolution of NOAA-10 satellite imagery was inadequate for discriminating broom snakeweed (*Gutierrezia sarothrae*) in 19 km² plots on New Mexican prairie due to the spectral mixing with co-occurring prairie vegetation. A comparison of field sites containing moderate and light density broom snakeweed with NDVI values showed no significant difference between the sites. Although Peters, *et al.* (1992) suggested that more homogenous training areas and ground truth information were needed to represent the variety of grasslands in the study area, it is unlikely that this would overcome the limitations of mixed pixels for such a coarse spatial resolution.

Despite the coarse resolution of sensors such as MODIS and NOAA, they do have the advantage of providing data from daily overpasses which provide a much greater opportunity to take advantage of favourable meteorological conditions, or plan field validation. For example Huang, *et al.* (2009) utilized the capability of the MODIS sensor to acquire a time series of images to map the tufted perennial grass Lehmann lovegrass (*Eragrostis lehmanniana*) in semi-desert grassland. A regression coefficient (R^2) of 0.23 was obtained between NDVI and biomass, with over 20 images being used for each year between 2000 and 2004. The lack of success in detecting the weed was not due to spatial resolution, but the spectral limitation of the sensor. Field verification showed that Lehmann lovegrass during its growing season did not have a higher spectral response than native vegetation during summer due to

bright inflorescences and litter suppressing the green signal in the near infrared, and the spectral response being diluted by a bright soil background.

The era of high spatial resolution commercial satellite sensors started with the launch of IKONOS in 1999, followed by QuickBird in 2001, and then a further series including Worldview 1 and 2. The imagery from these sensors have the advantages of being captured from a stable platform; provided to end users in a ready to use format (e.g. geometrically corrected); a lack of deployment costs; and the ability to cover large areas without the need to mosaic large numbers of small photo frames. High resolution satellite imagery has similar drawbacks to aerial high resolution data such as being more expensive compared to medium or coarse resolution data to cover similar sized areas. The high cost factor means that frequent recapture for monitoring may not be feasible for most research/management agencies. Another disadvantage is that a higher level of geometric correction is required to align field validation sites with the imagery (e.g. requires differential GPS).

High spatial resolution satellite imagery can detect smaller weed infestations in a similar manner to aerial photography and aerial imagery. Everitt, *et al.* (2007b) compared the results of a Quickbird image and scanned colour infrared photography for detecting Ashe juniper. An ISODATA classification of a Quickbird image resulted in user's and producer's accuracy from 93% and 90% compared to the 89 % and 90% for colour infrared photography. Casady, *et al.* (2005) reported that IKONOS imagery had a similar detection ability for leafy spurge to airborne videography and colour infrared photography. When leafy spurge patches were < 200 m² or < 30% cover, they were not reliably detected by a maximum likelihood classification method, which was similar to findings by Everitt, *et al.* (1995) where videography and colour infrared (CIR) aerial photography could not detect leafy spurge when the canopy cover was < 25%, even with a spatial resolution of 0.3 m. Everitt, *et al.* (2004) achieved similar accuracy results from an unsupervised classification of Quickbird imagery and CIR videography and photography for mapping giant reed (*Arundo donax*). User's and producer's accuracy for giant reed were 100% and 78 to 83% respectively, with Kappa at 0.72 for the Quickbird classification and 0.78 for the videography and CIR aerial photography. In another study, Everitt, *et al.* (2007a) used the same distinctive dark tone (spectral response)

of spiny aster on Quickbird imagery to discriminate it from co-occurring vegetation as was reported by Everitt, *et al.* (1987) for CIR and colour photography.

2.6.9 Airborne hyperspectral

Airborne hyperspectral sensors (airborne spectroscopy) have been used since the early 1980s for detecting and mapping vegetation (e.g. Goetz, *et al.* 1985). Some benefits of airborne hyperspectral remote sensing are analogous to aerial photography and airborne digital imagery: a high spatial resolution, flexible temporal capture, and a choice in the spatial resolution based on flying height. The advantage of airborne hyperspectral over airborne and satellite multispectral sensors is that spectral information is recorded over hundreds of narrow bands rather than several wide bands. This increases the likelihood of detecting a weed species that is spectrally distinct from co-occurring cover types in discrete areas of the electromagnetic spectrum. As a consequence, airborne hyperspectral sensors have been increasingly utilised in recent years for mapping weeds (e.g. Andrew and Ustin 2008; Atkinson, *et al.* 2014; Cheng, *et al.* 2007; Dehaan, *et al.* 2007; Glenn, *et al.* 2005; Ishii and Washitani 2013; Mirik, *et al.* 2013; Silván-Cárdenas and Wang 2009; Wang, *et al.* 2013).

A particular emphasis of hyperspectral applications for weeds has been to improve on previous multi-spectral applications that have had less success in accurately mapping weed infestations, especially in cases where there were lower density or patchy distributions. For example Glenn, *et al.* (2005) detected Leafy spurge with HyMap imagery at a spatial resolution of 3.5 m down to 40% cover with a user's and producer's accuracy of 78% and 68% respectively, and in some instances to less than 10% cover with a lower accuracy level. The outcome was similar to Everitt, *et al.* (1995) who found that small patches of Leafy spurge could be reliably detected down to 25% canopy cover with 0.3 m spatial resolution aerial photography, and 1.2 m spatial resolution airborne video imagery. Dehaan, *et al.* (2007) mapped blackberry (*Rubus fruticosus*) with a high classification accuracy (81% and 92% user and producer accuracy) with 3.5 m spatial resolution Hymap imagery, compared to the 79% overall accuracy of Frazier (1998) with 1m spatial resolution multispectral video airborne imagery. Miao, *et al.* (2006) found that yellow star thistle could be mapped at densities of < 10% cover with 3 m spatial resolution CASI-2 data, which

was a significant improvement in the detection of yellow starthistle compared to the airborne multispectral classification of Lass et al. (1996).

Even high spatial resolution hyperspectral data are heavily influenced by the environment type in terms of maximising spectral differences between the weed and co-occurring cover types. For example, Andrew and Ustin (2008) found that variations in environmental complexity and in particular the presence of co-occurring vegetation affected the accuracy of mapping perennial pepperweed (*Lepidium latifolium*) with Hymap data at three different sites. The user's accuracy (86–93%) and producer's accuracy (86–74%) at two sites was high, but low at the third site (18% and 23%), where perennial pepperweed could not be distinguished from sparse vegetation. In a study that proved to be an exception, Cheng, *et al.* (2007) achieved user's and producer's accuracy of 83% and 73% for mapping kudzu (*Pueraria Montana*) with AVIRIS imagery. The weed was difficult to detect when mixed with oak hardwood forest, but a noise reduction prior to the classifications enhanced the difference between oak and kudzu spectral signatures. The ability to detect kudzu was attributed to the combined high spatial and spectral resolution of the AVIRIS imagery, even when spectrally similar to co-occurring vegetation. Brazilian waterweed (*Egeria densa*) and water hyacinth (*Eichhornia crassipes*) were mapped by Underwood, *et al.* (2006) with 3 m spatial resolution HyMap imagery over the entire Sacramento-San Joaquin Delta and at smaller 50 ha site, with user's accuracies of 73% and 65% for the former, and 93% and 29% for the latter. The low mapping accuracy of Brazilian waterweed was attributed by Underwood, *et al.* (2006) to variability in water levels across the larger delta, particularly when the species was partially submerged, and also to higher levels of turbidity and algae in some areas of the delta.

In a rare example of remote sensing of a weed species with prominent purple flowers, Mirik, *et al.* (2013) mapped musk thistle (*Carduus Nutans*) in semi-arid grassland in Palmer County, Texas. Two images at 1 m spatial resolution from the Airborne Imaging Spectrometer for Applications (AISA) were classified using Support Vector Machines: one from pre-flowering in April and one from the peak flowering period in June. The June image had superior classification accuracy (user's

accuracy 90%, producer's accuracy 88%) compared to the April image (72% and 79%), which was variously attributed to lack of co-occurring native vegetation in June as well as spectral differences arising from differences in water content or phenology. Of particular note was that the AISA imagery did not include a blue band, which may have further increased the detectability of musk thistle during peak flowering.

2.6.10 Satellite hyperspectral

In 2001, the era of satellite hyperspectral remote sensing began with the launch of the EO-1 Hyperion sensor (Pearlman, *et al.* 2003). Hyperion imagery has the same 30 m spatial resolution as Landsat 8, but with the advantage of being a hyperspectral sensor with 198 bands and a 10 nm bandwidth (Pearlman, *et al.* 2003). This means that hyperspectral imagery can be captured over larger areas than airborne hyperspectral imagery, and without the high cost.

The first applications of the EO-1 Hyperion sensor to weeds were Ramsey III and Nelson (2005), Ramsey III, *et al.* (2005b) and Ramsey III, *et al.* (2005c), who developed an approach to map the low percentage canopy cover of Chinese tallow across a study area that included coastal and upland areas along the Texas and Louisiana borders. The method allowed Chinese tallow to be detected at 10% and 15% cover within pixels at 68% and 85% percent accuracy, which was equivalent to 10 m x 10 m and 15 m x 15 m areas respectively (Ramsey III, *et al.* 2005c).

In an application of EO-1 Hyperion to aquatic weeds, Pengra, *et al.* (2007) used an approach equivalent to the SAM to map the weed *Phragmites australis* at Green Bay, Wisconsin. The accuracy of the classification (user's and producer's accuracy of 61% and 69%) was similar to a previous mapping attempt using high spatial resolution hyperspectral imagery (Bachmann, *et al.* 2002). The spatial arrangement of *Phragmites* along shorelines in strips of 20 m or less precluded it from being represented in pure pixels, but the authors noted that the advantage of Hyperion imagery was that it covers large areas, and is a means of locating hotspots of the species, which could then be surveyed in the field.

In a recent study, Somers and Asner (2013) mapped the weed *Morella faya* and a co-occurring native tree *Metrosideros polymorpha* in montane rainforest on the island of Hawaii using a time series of Hyperion images and Multiple End-member Spectral Mixture Analysis (MESMA). A feature selection approach was used to select the optimum bands and maximise separability between end-members in order to highlight small spectral and phenological differences between *Morella faya* and *Metrosideros polymorpha*. A threshold independent approach identified the optimum threshold (Kappa) for single band images ranged from 0.51 to 0.69 and 0.78 for a multiple image dataset. The results indicate that the feature selection approach could produce acceptable accuracy results even when a temporal series of images did not cover all phenological stages (e.g. due to cloud cover).

2.7 Remote Sensing of Paterson's Curse

The first application of remote sensing to Paterson's curse was Ullah, *et al.* (1989b) at a study site east of Albury-Wodonga near Lake Hume, New South Wales. Contrast enhancement and de-correlation stretches were applied to two 1988 Landsat TM sub-scenes (5th and 29th of November) in order to map medium to dense Paterson's curse infestations in areas of pasture. The de-correlation stretches highlighted dense Paterson's curse infestations on the imagery, but also forest cover types. The value of the study was in identifying possible instances of spectral overlap between Paterson's curse and co-occurring vegetation, but was comprised by the lack of a formal accuracy assessment, and no description of the dense and medium classes mapped on the imagery (e.g. percentage cover).

In a later study at the same location, Bulman (2004) used Landsat TM and high spatial resolution (1.2 m) CASI hyperspectral imagery. An index called the Paterson's Curse Index (PCI) was derived from the spectral differences of CSIRO laboratory spectra of Paterson's curse flowers and whole plant material. Using the same 1988 Landsat TM images as Ullah, *et al.* (1989b), Bulman (2004) tested a range of techniques including principal component analysis, decorrelation stretch, ISODATA unsupervised classification, and maximum likelihood classification. Paterson's curse was mapped from the CASI image from a SAM classification and the PCI. The Landsat TM imagery over-estimated the spatial extent of Paterson's curse in adjacent forested areas, while less dense infestations went undetected due to

spectral overlap with pasture species. In contrast, the CASI imagery was more effective in discriminating smaller infestations, and the greater number of spectral bands was superior over Landsat TM for highlighting the spectral differences between Paterson's curse and surrounding land cover. As with the work of Ullah, *et al.* (1989b), no formal accuracy assessment was performed. The classification results were visually assessed and evaluated through field knowledge of the study area.

Bulman (2004) quantitatively modelled the floral proportion cover of Paterson's curse with remotely sensed imagery. The percentage cover of Paterson's curse flowers in 1 m² quadrats was visually estimated from vertical field photographs and band-combinations and indices from CASI hyperspectral data were modelled with floral percentage using linear regression. No significant relationships between image and field data were reported, and the floral density estimates were too low to show any meaningful relationship with image pixel values. Bulman (2004) acknowledged the limitations of visual estimation for deriving floral cover estimates, and recommended the development of a method to quantitatively extract the floral percentage of Paterson's curse from field photography.

Bulman (2004) identified three aspects for further work that were relevant for the current research, and could make a contribution towards determining the utility of remote sensing for mapping and monitoring Paterson's curse:

- (i) The development of a quantitative method that can relate floral density to a sensor. Bulman (2004) suggested a 'Floral Area Index', analogous to the common Leaf Area Index (LAI) used in many quantitative studies linking remotely sensed data to field data. A method of deriving such estimates from photographs collected in the field was an idea worth further investigation;
- (ii) The relationship between floral density and plant density of Paterson's curse in the field. Bulman (2004) proposed that floral density could be a surrogate for plant (infestation) density; and

- (iii) The detection limits of Paterson's curse with regards to spectral and spatial resolution from different sensors. The detection limit defines the threshold of weed density that can be detected (e.g. floral density) according to the resolution of the data.

The spectral properties of Paterson's curse and other cover types were investigated by Schut and McIntyre (2009) at two study sites in south west Western Australia. Spectra of Paterson's curse flower and plant material were recorded with a spectroradiometer, and concurrent digital field photographs of Paterson's curse floral cover were captured. Linear unmixing was applied to end-members, and increasing abundance of Paterson's curse was simulated by producing linear mixtures from the flower and green stem material of Paterson's curse, and senescent vegetation material. Linear regression of the spectral unmixing and floral cover resulted in R^2 values of 0.67 and 0.54 for the two study sites. An index called the Normalised Difference Blue Index (NDBI) was derived from the spectral differences at 430 and 490 nm. The R^2 values from the NDBI for the two sites were 0.71 and 0.46. The blue peak from Paterson's curse flowers of the modelled spectra at 430 nm was 'diluted' when mixed with green or dead material, and flower fraction was difficult to extract when mixed, and was dependent on the ratio of green and dead material.

2.8 Summary

The following section summarises the key findings from the methodological and literature review, and links them to the following chapters in the thesis.

Vegetation has been particularly amenable to detection with remote sensing, due to chemical and physical properties that make it spectrally different to other materials, especially in the red-edge region. Applying remote sensing to weeds requires a consideration of the properties of the weed species that makes it distinct from co-occurring vegetation and land cover types. Successful examples of remote sensing for a weed species have utilised features that maximise differences, such as timing of flowering and flower colour, foliage density and colour, structure, and spatial patterning. For example the purple flowers of Paterson's curse and the dense coverage are a particularly distinctive feature, and have been the impetus for previous remote sensing applications to detect and map the species.

The resolution of a sensor is an important consideration for any remote sensing application to weeds. The spatial, spectral, radiometric, and temporal resolution has to be considered in the light of which combination will maximise the ability of the sensor to discriminate the weed species. Often a compromise between the different resolution types is necessary. Three types of remote sensing data with different resolution will be considered in this thesis: field spectroscopy in Chapter 4, airborne high spatial resolution multispectral imagery in Chapter 5, and satellite hyperspectral imagery in Chapter 6. Field spectroscopy has been another valuable technique for determining the utility of remote sensing for detecting weeds, and for calibrating field and image data. Medium resolution satellite remote sensing has been shown to be inadequate for detecting Paterson's curse due to spectral confusion with other vegetation types. Therefore, in this thesis, high spatial resolution multi-spectral data will be investigated. Satellite hyperspectral data with medium spatial resolution could be useful for detecting Paterson's curse, given the limited area coverage and higher cost of airborne hyperspectral data. EO-1 Hyperion was used in Chapter 6, as it covers a larger area than airborne, but has a spectral resolution similar to airborne hyperspectral sensors.

The literature review highlighted the advantages and limitations of various image classification algorithms and approaches. Traditional non-parametric classifiers were shown to be inferior to non-parametric classifiers, and per-pixel classification approaches were not as effective as contextual or per-area approaches. In Chapter 5, two non-parametric approaches - ANN and kNN are used to classify DMSI imagery. The review showed that matched filtering and mixture tuned matched filtering were both effective for classifying hyperspectral imagery when not all end-members or cover types were known. The matched filter approach is used in Chapter 6 for classifying satellite hyperspectral imagery.

A quantitative approach to accuracy assessment is important for the current research, given the inadequacies in past weed remote sensing work, especially for Paterson's curse. For hard classification output, the error matrix and Kappa statistic provide a quantitative and robust method of assessing the accuracy, and is utilised in the digital multispectral imagery (DMSI) classification in Chapter 5. For soft classification,

density dependent (Kappa threshold) and density independent (e.g. ROC) methods have been shown to be robust approaches. These approaches will be used in Chapters 5 and 6 for assessing the accuracy of the DMSI and Hyperion soft classification output.

The next chapter describes the study area, study species (Paterson's curse) and the datasets used in the research (remote sensing and field data). The software and hardware used in the research are also described.

3 STUDY AREA, STUDY SPECIES AND DATASETS

3.1 Introduction

The following chapter describes the characteristics of the study area and the datasets used in the research. Section 3.2 describes the rationale for selecting the study area, and then describes the general characteristics such as climate, topography, and land use. Section 3.3 provides a general description of Paterson's curse, followed by its impacts and benefits, and management strategies. Sections 3.4 to 3.7 describe the datasets used for the research, including the remotely sensed datasets, the field data used to validate the analyses, and a brief description of the software and hardware used.

3.2 Characteristics of the Study Area

3.2.1 Selection and rationale

Potential study sites were selected from a database of Paterson's curse infestation records provided by the Department of Agriculture and Food, Western Australia. The database records were overlaid on property boundaries in a GIS, and properties located within 150 km of Perth, and containing more than 100 ha of Paterson's curse were short-listed. Some properties located at a distance greater than 150 km north of Perth had very large infestations, but the logistics of travelling that far from Perth for fieldwork was considered to be too restrictive, and permission to conduct fieldwork on these properties was not forthcoming. Based on the initial study area selection process, the Chittering Shire was found to have some of the largest infestations of Paterson's curse within a reasonable distance (less than a 1.5 hour drive) from Perth.

The chosen study area was located approximately 100 km north of Perth, within 10 km of the town of Bindoon (Figure 3.1), and comprised three properties: Catholic Agricultural College Bindoon (CACB) (3643 ha), Morden Downs (664 ha), and Bindarie (1163 ha). The study area was located within an hour's drive of the Perth metropolitan area. This was an important issue when considering short windows of opportunity for collecting field data concurrently with image data. In general, property sizes closer to Perth are smaller, and hence the management of Paterson's curse and other pasture weeds tends to be more active.

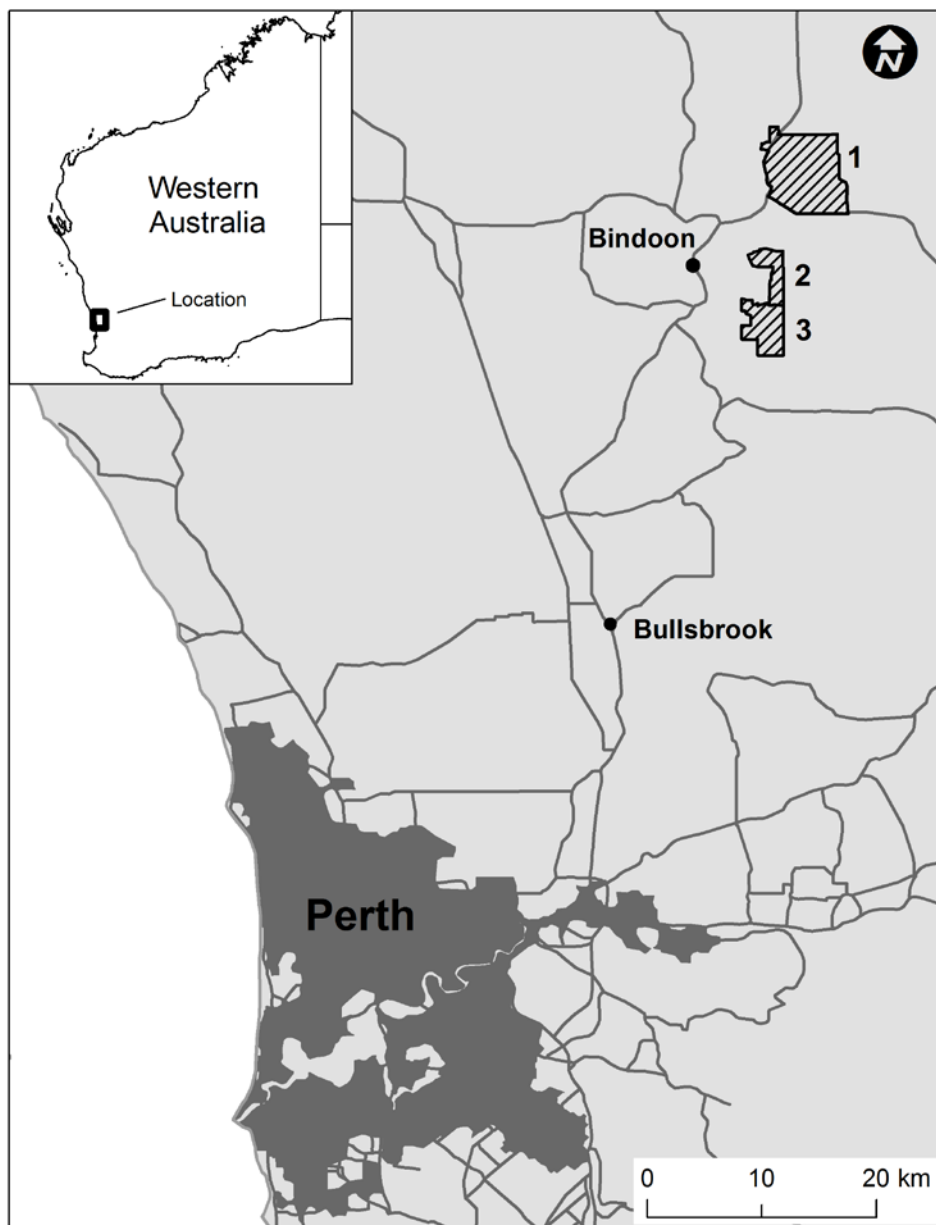


Figure 3.1 Location of properties used as study sites: 1) Catholic Agricultural College Bindoon; 2) Morden Downs; and 3) Bindarie.

3.2.2 Physical features

The primary land use in the area around Bindoon is dominated by dry-land agriculture (mainly cropping) and conservation and natural environments (Figure 3.2). In the vicinity of the Bindoon township, the land use is described as ‘intensive use’, which includes residential, recreational, and manufacturing and industrial, and animal production (Beeston, *et al.* 2001). There are also smaller areas of irrigated agriculture (e.g. horticulture). The CACB property is comprised of similar proportions of dry-land agriculture and conservation and natural environments, as

well as small area of intensive animal production. The conservation and natural environment is characterised by areas of remnant vegetation dominated by Eucalypt woodland (Department of the Environment and Water Resources 2007). The property has a fully functional farm as part of an educational institution, which includes approximately 300 head of cattle, 6000 sheep, a piggery, poultry and horses (Catholic Agricultural College Bindoon 2007). The land use of the Bindarie and Morden Downs properties is mostly comprised of dry-land agriculture and small areas of remnant Eucalypt woodland.

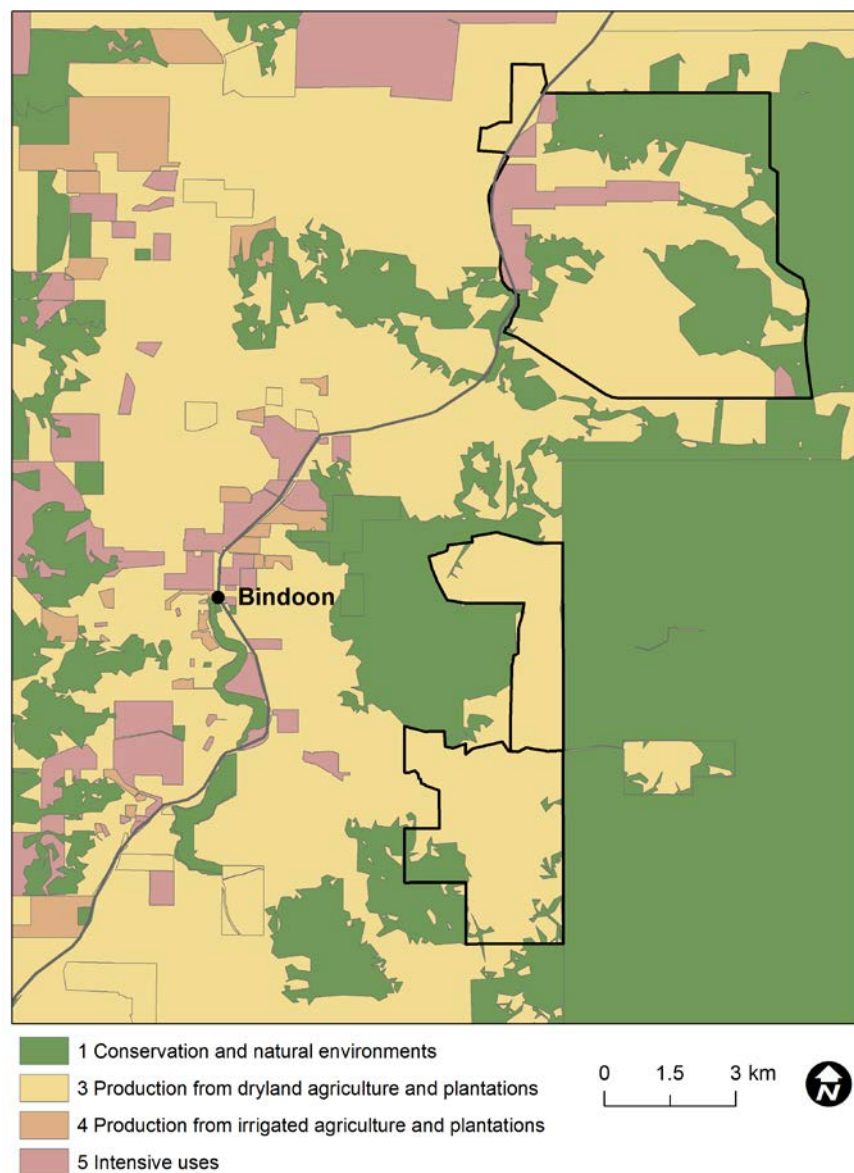


Figure 3.2 Land use on the three study area properties, and the general area around the town of Bindoon (from Beeston, *et al.* 2001).

3.2.3 Vegetation and soils

The vegetation and soils described for the study sites are based on the landscape unit descriptions from Schoknecht, *et al.* (2004).

A summary table and map of the landscape units for the CACB property are shown in Appendix B (Table B.1 and Figure B.1). The dominant unit for the property (253Ju_2c) comprises 39% of the area, and is comprised of very gentle to moderate hill slopes, with red and yellow duplex soils, which cover most of the areas on the property that are utilised for cropping and pasture. Three other units (253Ju_2a, 253Bn_2x, and 253WnYa6) comprise 10 to 12% of the property area each, with the remaining units comprising less than 5% each. The 253Ju_2a unit is characterised by remnant *Eucalyptus* spp. woodland, particularly on some steeper slopes and knolls not suitable for pasture or cropping. The property is intersected by gentle to moderately sloping valleys with alluvial soils (253Ju_3an and 253Ju_3a). These areas are moderately saline, and are comprised of lower lying areas prone to inundation.

A summary table and map of the landscape units for Bindarie and Morden Downs properties are shown in Appendix B (Table B.2 and Figure B.2). The properties are dominated by gentle to moderate hill slopes (1–15%), with dominant *Eucalypt* spp. woodland, and some saline prone areas. The soil types are highly variable, with duplexes (red, yellow), sandy loams, clay, shallow gravels, sands and laterite.

3.2.4 Topography

Topographic information for the three properties was derived from a high spatial resolution 1 m Digital Elevation Model (DEM) supplied by the Department of Agriculture and Food Western Australia: the mean elevation of the CACB property is 234 m (Australian Height Datum) with a range of 164 to 291 m (35 m standard deviation); the mean elevation of the Morden Downs property is 275 m with a range of 237 to 307 m (11 m standard deviation); and the mean elevation over Bindarie is 223 m with a range of 162 to 285 m (26 m standard deviation).

3.2.5 Climate

The climate in the study area is hot-summer Mediterranean, characterised by long warm dry summers and winter dominant rainfall (Bureau of Meteorology 2010). The nearest rain gauge station to the Bindoon study sites is located approximately 50 km away at Gingin Airport (31.46° S, 115.86° E). Climate data were available from Bureau of Meteorology records collected between 1996 and 2010 (Table 3.1). The average annual rainfall for Gingin Airport for the period was 661 mm, with most of the annual rainfall occurring in the winter/spring months of May to September, as well as the highest number of rain days (> 10 days per month).

Table 3.1 Mean monthly rainfall data for Gingin Airport from 1996-2010: (Source: Bureau of Meteorology 2010).

	J	F	M	A	M	J	J	A	S	O	N	D
Mean monthly rainfall (mm)	16	5	16	30	79	119	128	106	84	39	18	7
Highest monthly rainfall (mm)	96	26	52	70	139	236	214	141	126	93	51	32
Mean number of rain days	2	2	4	7	11	14	17	15	14	8	5	3

The mean temperature and humidity data for Gingin Airport is shown in Table 3.2. The number of days above 30°C increases from 2.9 to 9.1 from October to November (spring to summer transition). The mean maximum daily temperature increases incrementally through spring (August-October), and increases significantly from November to a maximum of 33°C in February.

Table 3.2 Mean temperature and humidity data for Gingin Airport from 1996-2010 (Source: Bureau of Meteorology 2010).

	J	F	M	A	M	J	J	A	S	O	N	D
Mean daily max temp (°C)	33	33	31	27	23	20	18	19	20	24	28	30
Mean daily min temp (°C)	16	17	15	12	9	7	6	6	7	9	12	14
Mean number of days temp > 30°C	20	19	16	6	1	0	0	0	0	3	9	13
Mean daily 9 am rel. humidity (%)	48	51	55	65	71	78	80	77	70	59	51	48
Mean daily 3 pm rel. humidity (%)	33	33	35	43	49	56	58	55	54	46	39	35

3.3 Paterson's Curse

3.3.1 Description

The distinctive flowers of Paterson's curse are 18 to 30 mm long, funnel shaped, usually purple in colour but can be blue, pink or (rarely) white (Piggin and Sheppard 1995). The normal flowering period for Paterson's curse plants is between two to five months, but can be reduced by drought conditions (especially in shallow soils), or increased by moisture availability, and defoliation (Piggin and Sheppard 1995). Under Australian conditions, seedlings usually emerge in late summer/early autumn (February to April), flower in late winter/early spring, then die in summer (Piggin and Sheppard 1995). Those plants growing near areas of higher moisture availability (e.g. drains, rivers, dams, and roadsides) can flower into summer, and die in late summer/early autumn (Piggin and Sheppard 1995).

Paterson's curse is a prolific seed producer, with a single mature plant capable of producing up to 10,000 seeds in a year (Piggin and Sheppard 1995). A consequence of the high seed production is a large seed bank in the soil. In New South Wales, the seed bank in un-grazed pasture has been as high as 30,000 seeds m², and 2000–18,000 seeds m² in grazed areas (Piggin and Sheppard 1995). Although the seeds are small and heavy, and subsequently not easily spread by wind, other seed vectors include ants, water birds, and anthropogenic activities. Seeds can be spread between farms and districts by transport in soil, animal fodder and grain (especially during drought), movement of livestock, and by vehicle (Parsons and Cuthbertson 2001).

3.3.2 Impacts and benefits

Paterson's curse has been listed as a noxious weed Australia-wide for its numerous negative impacts on the agricultural industry. However, the species does possess productive or positive values which make it valuable. This apparent ambiguity between positive and negative outcomes of the species was the reason behind a senate enquiry in the 1980's in light of proposed introduction of biological control vectors (Delfosse 1985). The negative and positive aspects of Paterson's curse are described below.

3.3.2.1 Negative impacts

Paterson's curse plant material contains pyrrolizidine alkaloids, which have been demonstrated to have deleterious effects on animals and livestock. Pigs and horses (non-ruminants) are most susceptible to alkaloid poisoning as they lack the necessary micro-organisms in the stomach to break down the alkaloids, and suffer damage to the liver tissue (Parsons and Cuthbertson 2001). Ruminants such as sheep, goats, and cattle are less affected by the toxins (Parsons and Cuthbertson 2001). Culvenor et al. (1984) found that sheep were not adversely affected by the toxins, but subsequent work by Seaman et al. (1989) and Seaman and Dixon (1989) found that Merino weaners died from poisoning when fed a sole diet of Paterson's curse, and lost health and condition when grazing on a mixed diet. Smyth et al. (1997) advocated that careful grazing management of Paterson's curse on a paddock by paddock basis during the flowering period can reduce the exposure of livestock to the toxicity of the plants, especially if the more toxic resistant Merino wethers were used (Piggin 1979).

Paterson's curse can reduce the productivity of pastures by replacing more desirable pasture species. For example the nitrogen content of soils can be reduced when nitrogen fixing species are outcompeted (Parsons and Cuthbertson 2001). The seedling density of Paterson's curse can dominate other species and the large broad rosette leaves shade and smothers other species (Parsons and Cuthbertson 2001). Other impacts of Paterson's curse include: the pollen affecting human health and causing hay fever (Parsons and Cuthbertson 2001); irritation to livestock and humans by the hairy stems and leaves (Parsons and Cuthbertson 2001); a reduction in economic value of hay and grain contaminated with Paterson's curse seeds (Sheppard and Smyth 2012); and the reduced market value of properties infested with the species (Sheppard and Smyth 2012).

Anecdotal accounts from farmers in Western Australia, particularly those in high rainfall areas show a general consensus that it is a competitive weed in pastures which excludes beneficial plants and does not improve the forage value of the pastures (Dodd, *et al.* 1993). However a contrasting set of attitudes has emerged between Australian farmers who lack Paterson's curse on their properties and are serious about enforcing control measures to ensure their property is not infested, versus other farmers who already have the weed on their property, and have adopted

a 'leave it be' attitude towards the weed and its control (Parsons and Cuthbertson 2001).

3.3.2.2 Benefits

Paterson's curse is an important plant to the honey industry in Australia. The large amounts of pollen and nectar produced by the species enables bee populations to increase early in the flowering season, which allows both plentiful honey to be produced and a better harvest of plant species that flower later in the season (Parsons and Cuthbertson 2001). Piggin (1977) demonstrated that Paterson's curse remained a useful pasture species due to its nutritive value and high productivity in autumn and winter, when other pasture species are less productive. Some farmers in marginal and semi-arid lands in Australia value the species for increasing pasture production and as a drought resistant fodder (Dodd, *et al.* 1993; Parsons and Cuthbertson 2001).

3.3.3 Management

A variety of control methods for Paterson's have been proposed, but the effectiveness of the methods has largely gone unreported (Piggin 1979). The methods include burning, hand pulling, herbicide treatment, grazing, and cultivation (Piggin and Sheppard 1995). These methods can be costly, and have a negative impact on other pasture species, soil, and livestock (Smyth, *et al.* 1997). Spray grazing is a control technique in which a moderate amount of herbicide is applied to Paterson's curse seedlings in autumn, followed by a short intense period of grazing by ruminants (Piggin 1979; Smyth, *et al.* 1997). The method has shown to significantly reduce the cover of Paterson's curse, while reducing herbicide costs and the environmental impact (Piggin 1979). Another method is 'graze topping', where flowering Paterson's curse infestations are grazed by livestock, resulting in a reduction of seed production in the short term, and a long term impact on the seed bank (Dowling and Wong 1993; Smyth, *et al.* 1997).

Sheppard and Smyth (2002) observed that the seed bank of Paterson's curse under normal pasture conditions declined rapidly in cultivated and grazed (simulated) pastures. In cultivated areas, Paterson's curse can be controlled more effectively, due to a reduction in seed germination in hot bare soil, and control methods such as herbicide application are more effective (Sheppard and Smyth 2012). The presence

of perennial grasses can benefit the control of Paterson's curse by occupying recruitment space, but have no impact on the decline of the underground seed bank (Sheppard and Smyth 2012). The control of Paterson's curse relies on a long term strategy of eliminating the seed bank by controlling emergent seedlings (Sheppard and Smyth 2002). Sheppard and Smyth (2002) highlighted the risky nature of strategies to reduce the seeding capacity of Paterson's curse populations: without a long term management strategy of the pastures, any remaining plants after short to medium term treatment have the capacity to return the seed bank to pre-control conditions.

Australia is the presently the only country to use biological control on Paterson's curse (Sheppard and Smyth 2012). In 1972 CSIRO investigated a range of possible agents from Europe. After subsequent trials, eleven insects were tested, starting in 1981 with a moth (*Dialectica scaliella*), followed between 1988 and 1994 by two root weevils (*Morgulones larvatus* and *M. geographicus*), two flea beetles (*Longitarsus echii* and *L. aencus*), a cerambycid beetle (*Phytoecia coerulesems*), and a pollen beetle (*Meligethes planiusculus*) (Sheppard and Smyth 2012). Of the introduced insects, *M. larvatus* and *L. echii* have been shown by field to studies to cause mortality in plants prior to flowering and have led to a large decline of Paterson's curse where introduced (Sheppard and Smyth 2012).

3.4 Remote Sensing Data

3.4.1 Digital Multi-spectral Imagery (DMSI)

DMSI imagery was provided by Specterra Services, a Perth-based remote sensing company. The DMSI is a frame transfer type-imaging sensor designed for mapping and monitoring vegetation at high spatial, spectral, and radiometric resolution (Canci, *et al.* 2006). The sensor is made up of four 12-bit digital charge-coupled device cameras, recording 1024 x 1024 pixels per frame. Four inter-changeable narrow (20 nm width) band-pass interference filters are standard (Table 3.3). The band centres are located in close proximity to the prominent vegetation reflectance features in the electromagnetic spectrum.

Table 3.3 Spectral band centres and spectral feature properties for DMSI bands. Modified from Canci, *et al.* (2006).

Band	Wavelength (nm)	Bandwidth (nm)	Features
1	450	20	Plant pigment absorption
2	550	20	High transmission and reflectance
3	675	20	Chlorophyll absorption
4	780	20	High scattering and transmission

Airborne digital imagery such as DMSI has a number of advantages over satellite remotely sensed imagery: imagery can be captured during optimum periods at relatively short notice, which presents an opportunity for researchers to take advantage of breaks in the weather, and also allowing field data collection and image capture times to be co-incident; the aircraft platform allows variable spatial resolution to be chosen, decided by the altitude of the aircraft at time of capture; the DMSI sensor has a small base-to-height ratio compared to other airborne photogrammetric cameras, which allows images to be captured at high solar angles and illumination levels, whilst minimising view angle and illumination angle effects; DMSI has narrow field of view, which minimises the look angle, and produces a more consistent spectral response across an image (Canci, *et al.* 2006).

DMSI data was captured over the Catholic Agricultural College Bindoon on October 14 2005 at noon on a clear dry day. A Cessna 182 flew at an altitude of 5500 feet to capture image data with a spatial resolution of one metre. The spatial resolution of one metre was considered optimum for the study for the following reasons: a higher spatial resolution was possible (e.g. 0.5 m) but considered redundant for the purpose of mapping non-woody vegetation and would increase the costs associated with increased flying time; the pixel size allowed a substantial area to be captured, and the resulting dataset was of a size that was manageable on an average personal computer.

Image processing was performed in-house by SpecTerra Services. Each image frame was registered to ortho-rectified aerial photography using first order polynomial warping and nearest-neighbour re-sampling. A final mosaic of 4534 columns by 5475 rows (4.5 x 5.5 km) was produced using cut-line feathering over three pixels. The mosaic was radiometrically corrected by SpecTerra using in-house software. The

effects of the BRDF were minimised by an algorithm (developed by SpecTerra) which was applied to the imagery (Roujean, *et al.* 1992). The algorithm reduces BRDF from 20% of the dynamic range of individual frames to less than 5%, producing a radiometrically seamless image mosaic containing a significant reduction in BRDF and solar hotspot effects (Canci, *et al.* 2006). The location of the mosaic image at the Catholic Agricultural College Bindoon property is shown in Figure 3.3.

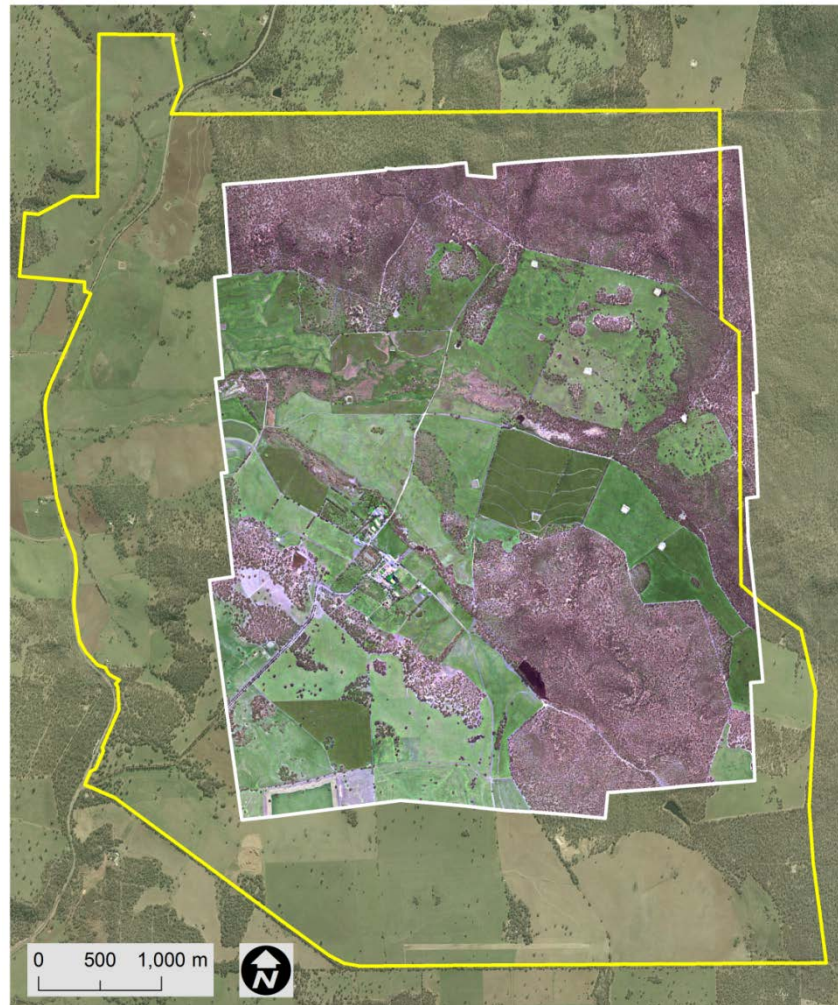


Figure 3.3 Extent of DMSI mosaic image (outlined in white) at the Catholic Agricultural College Bindoon property (outlined in yellow).

3.4.2 EO-1 Hyperion satellite hyperspectral imagery

3.4.2.1 Description and background

The Earth Observing 1 (EO-1) satellite was launched on November 21 2000 as part of the NASA New Millennium Program (NMP). The purpose of the program was to showcase new technologies and strategies for improved earth observations (Ungar, *et*

al. 2003). The EO-1 mission would evaluate experimental earth observation sensors by directly measuring performance with a diverse range of applications (Ungar, *et al.* 2003). The EO-1 satellite contains three sensors: Hyperion, Advanced Land Imager (ALI), and the Linear Etalon Imaging Spectral Array (LEISA) Atmospheric Corrector (LAC) (Ungar, *et al.* 2003). The EO-1 sensors were assembled under time constraints using backup components from the Lewis HyperSpectral Imager (HSI), which failed to achieve a stable orbit after launch and never captured any imagery (Jupp and Datt 2004). The orbit path of EO-1 is the same as Landsat 7 (Figure 3.4) in order to provide direct comparison between the data types, but crosses the equator one minute later (Ungar, *et al.* 2003).

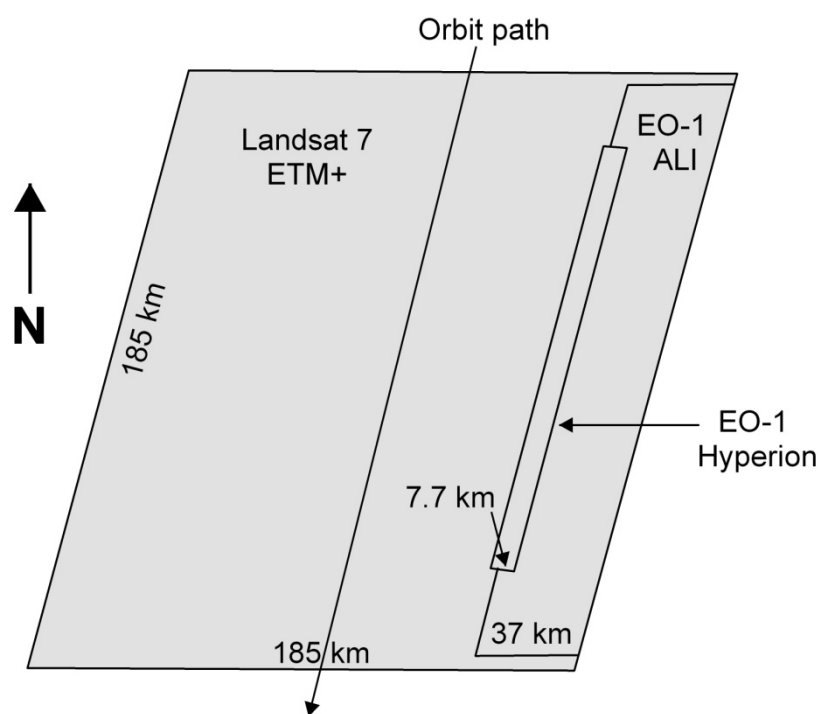


Figure 3.4 EO-1 and Landsat 7 ground tracks. Adapted from Ungar, *et al.* (2003).

The main characteristics of the Hyperion sensor are shown in Table 3.4. Hyperion has a single telescope and two spectrometers; a visible/near infrared (VNIR) and a short-wave infrared (SWIR) spectrometer (Pearlman, *et al.* 2003). Hyperion has a total of 220 bands (bandwidth = 10 nm), but only 198 bands are unique due to non-functioning detectors on the array (Pearlman, *et al.* 2003). Hyperion is a push-broom sensor, with a swath width of 7.7 km, and an along-track length of 185 km.

Table 3.4 Characteristics of Hyperion, with ALI, and Landsat 7 ETM+ for comparison. Adapted from Ungar, *et al.* (2003).

	Landsat 7 ETM+	EO-1 ALI	EO-1 Hyperion
Spectral range (μm)	0.4–2.4	0.4–2.4	0.4–2.5
Spatial resolution (m)	30	30	30
Swath width (km)	185	37	7.7
Spectral resolution (nm)	variable	variable	10
Spectral coverage	discrete	discrete	continuous
Number of bands	7	10	220

Following launch and establishment of a stable orbit by the EO-1 satellite, a NASA Science Validation Team (SVT) was established to provide validation and scientific evaluation. A quantitative validation approach was used, in conjunction with Landsat 7 imagery, airborne imagery, and field data (Ungar, *et al.* 2003). The SVT for the Southern Hemisphere campaign was represented by an Australian component of 23 principal and co-investigators (Jupp and Datt 2004). Three sites in Australia were used (Lake Frome, Mount Fitton, and Coleambally) to assess performance against specifications (Jupp and Datt 2004). Two years were spent on validating different applications from sites in Argentina, North America, and Australia. Many of the validation studies were reported in the Earth Observing 1 Special Issue of IEEE Transactions in Geoscience and Remote Sensing in June 2003. Some examples of the validation studies conducted in Australia include agriculture at Coleambally (Datt, *et al.* 2003); forestry at Tumbarumba (Coops, *et al.* 2003); water quality at Moreton Bay and Lake Argyle (Brando and Dekker 2003); coral reefs at the Great Barrier Reef; rangelands at Kunoth; and minerals at Mounts Fitton and Panorama.

During the two years of validation, there were no reported failures of the spacecraft or the sensor components, and the original EO-1 mission objectives were all satisfied (Ungar, *et al.* 2003). Some issues with Hyperion imagery did emerge during the validation phase including a low signal-to-noise ratio, reduced performance from atmospheric interference and noise in the regions below 500 nm, 950-1000 nm, and > 2300 nm, streaking from malfunctioning detectors, and the requirement for specialised atmospheric correction software (Jupp and Datt 2004).

The demand from users for EO-1 imagery after the validation period prompted NASA to start the 'Extended Mission' in February 2002, making it possible to task the satellite for specific data acquisitions (Ungar, *et al.* 2003). The EO-1 mission was extended to take into account the lack of satellite hyperspectral platforms, after the OrbView-4 mission failed in September 2001 (Jupp and Datt 2004). EO-1 (ALI and Hyperion) data were available via the Australian Centre for Remote Sensing (ACRES) and the United States Geological Survey (USGS) for users in Australia and overseas. The Hyperion sensor has been utilised during the Extended Mission for a number of applications, including invasive plant mapping (Pengra, *et al.* 2007; Ramsey III and Nelson 2005; Ramsey III, *et al.* 2005a), discriminating different sugar cane species (Galvao, *et al.* 2005); (Galvao, *et al.* 2006), classifying vegetation and crop species (Thenkabail, *et al.* 2004), and detecting rust disease in sugarcane (Apan, *et al.* 2004).

3.4.2.2 Acquisition of EO-1 Hyperion data

Hyperion data for this research was obtained from a Data Acquisition Request (DAR) that was lodged with ACRES. The DAR consisted of the geographic coordinates of the area of interest and a time period (or capture window) over which the capture of an image was desired. During any particular window, the EO-1 satellite makes a limited number of overpasses. On each overpass date during the window, image data will be captured and inspected at NASA for cloud cover. If a particular image contains less than 25% cloud cover, the acquisition is considered to be successful, and the image is processed and sent to the user. If a capture is not successful, then further attempts are made on subsequent overpasses. The individual overpass dates were sourced from the USGS EO-1 website acquisition schedule (United States Geological Survey 2014). This schedule was used for this research to plan fieldwork and a ground truth data collection campaign to coincide with the date (s) of the satellite overpass.

The capture window for the research was from October 10 to November 10 2006. This window was chosen as it coincided with the peak flowering period of Paterson's curse, and there was a reduced likelihood of cloud cover over the study area from the end of spring (mid-October). Images were captured during overpasses on October 23 and 28, but most of the study area contained cloud and associated shadow, so the

images from those dates were not used. A suitable image was captured on Thursday November 2nd 2006 (Table 3.5). Conditions during the time of overpass (10:30 am Western Standard Time) were clear and cloud free. The Hyperion product was supplied as a Level 1R radiometric corrected image in 16-bit signed radiance values. The dimensions of the image were 45 km in the along-track direction (length) and 7.65 km in the across-track direction (width).

Table 3.5 Properties of acquired Hyperion image (from product metadata).

Acquisition Date	November 2, 2006
NW Corner	31°01'41.25"S, 116°12'54.73"E
NE Corner	31°02'38.74"S, 116°17'39.26"E
SW Corner	31°52'04.25"S, 115°59'01.19"E
SE Corner	31°53'02.20"S, 116°03'48.31"E
Image Cloud Cover (%)	0-9
Scene Start Time (GMT)	2006:306:01:54:27.019
Scene Stop Time (GMT)	2006:306:01:54:42.019
Path	112
Row	82
Sun Azimuth	66.63°
Sun Elevation	56.97°
Satellite Inclination	98.16°
Look Angle	-5.93°

3.4.3 Field spectroscopy data

Radiance spectra of Paterson's curse and other cover types were collected in the field using an Analytical Spectral Devices (ASD) Fieldspec Pro Jr. spectroradiometer (Analytical Spectral Devices Inc. 1999). This instrument captures data from 2150 bands between 350 nm and 2500 nm. In the 350 to 1100 nm range, the sampling interval is 1.4 nm between spectral samples (full width half maximum FWHM = 3 nm) and 2 nm interval between spectral samples (FWHM = 10–12 nm) in the 1000 to 2500 nm range. Data from the spectroradiometer was output into a raw digital number (16 bit) reflectance or radiance values in a binary and ASCII file. The procedure for processing the field spectroscopy data from this research is described in Chapter 4.

3.5 Validation and Field Data

Chapter 2 highlighted the importance of validation data for assessing the accuracy of maps derived from remotely sensed data. The Paterson's curse validation datasets used in the thesis were derived from on-ground field survey, and non-Paterson's curse classes were derived from a combination of field survey and random selection from a GIS, based on field knowledge. Validation using other remotely sensed data (e.g. aerial photography) was not possible due to the lack of high resolution imagery close to the DMSI and Hyperion image capture dates. Field data provided a detailed and flexible approach to providing training data for image classification algorithms, and for validating the accuracy of a classification.

Table 3.6 provides a summary of the field data used in the thesis. Random point data were collected in October 2005 to validate the classification of DMSI imagery discussed in Chapter 5. Field data were recorded from a systematic grid in October 2006 for determining relationships between the floral density of Paterson's curse and field spectroscopy data from the CACB study site discussed in Chapter 4. Random plot data were recorded in October 2006 at different properties in the Bindoon area for the purpose of providing validation data for indices and a matched filter classification of EO-1 Hyperion data. A description of these data is provided in Chapter 6.

Table 3.6 Summary of the field datasets used in the research by chapter.

Date collected	Type	Chapter	No. PC records	Mean floral cover (%)
October 2006	Systematic (grid)	4	69	2.05
October 2005	Stratified random	5	115	1.28
October 2006	Random	6	84	N/A

3.6 Software and Hardware

3.6.1 Remote sensing and GIS software

Several remote sensing and GIS software packages were used for the research. The remote sensing software packages used were: eCognition v. 4.0 (Baatz, *et al.* 2004), ERDAS Imagine v. 8.7 (Leica Geosystems 2005), ENVI v. 4.5 (ITT Visual Information Solutions 2006c), and IDRISI Andes (Clark University 2006). For GIS

analysis, ESRI ArcGIS v. 9.x (ESRI 2004) was mostly used, although IDRISI Andes was used for some analyses due to its integrated GIS/remote sensing functionality.

3.6.2 Statistical software

The statistical software used for the research was SPSS for Windows v. 15 (SPSS Inc. 2007). The software was used for the correlation and regression analyses in Chapters 4 and 5, and logistic regression and receiver operating characteristic (ROC) analysis in Chapters 5 and 6.

3.6.3 Global Positioning System (GPS)

A handheld GPS (Lowrance iFinder H²O) was used to collect validation data in Chapters 5 and 6. This GPS used the Global Navigation Satellite System (GNSS) common to all handheld GPS units in Australia. The location accuracy of the unit depends on the quality of the line-of-site between receiver unit and the satellites. The GPS had a location accuracy of approximately 5–10 m in open areas away from tree canopies, which was typical of the pasture areas sampled during the field surveys in Chapters 5 and 6.

A differential GPS (DGPS) was used to mark out transects for a survey at the CACB property to measure the floral cover of Paterson's curse (reported in Appendix C). The DGPS Max (CSI Wireless Inc.) is a real-time DGPS, using the OmniSTAR Wide Area DGPS Service. Network stations are located in selected geographic locations around Australia, and they produce GPS correction data for a particular region, and transfer the data to an L-band receiving geostationary satellite. The corrected data is then transmitted over a large area to the DGPS Max L-band receiver, where the spatial coordinates are processed using Virtual Base Station (VBS) algorithms. The location accuracy of the receiver is approximately one metre, and depends on the quality of the line-of-sight between the GPS receiver and the satellite.

3.7 Summary

In this chapter, the properties selected for the study, and the general Bindoon area were described in terms of the physical and climatic properties, and the rationale for choosing them for the current research. The target weed species Paterson's curse was described in terms of its physical characteristics, negative and positive impacts, and

management. The datasets selected for the research (DMSI and EO-1 Hyperion) are described, as well as the supporting field data, software and hardware.

4 IDENTIFYING OPTIONS TO DETECT PATERSON'S CURSE USING FIELD SPECTROSCOPY

4.1 Introduction

Field spectroscopy was highlighted in Chapter 2 as a valuable method for determining the utility of airborne and satellite remotely sensed imagery for mapping weed species. In that regard, it has been employed to: 1) determine the spectral separability of a target weed species from co-occurring vegetation and other cover types, according to parts of the electromagnetic spectrum that correspond to attributes of the target weed species, such as leaf and flower colour and canopy density; and 2) examine the effects of seasonality on the spectral properties of both a weed species and co-occurring vegetation, to determine the optimum period of the season to use remote sensing (e.g. Dehaan, *et al.* 2007; Everitt, *et al.* 1995; Everitt, *et al.* 1984; Everitt, *et al.* 1994; Everitt and Villarreal 1987; Lass and Callihan 1997; Martin, *et al.* 2011; Mitchell and Glenn 2009; Underwood, *et al.* 2003). Another advantage of field spectroscopy, as identified in Chapter 2, is that data are recorded over hundreds of narrow discrete bands, which allows band ratios and indices to be derived that exploit the maximum spectral differences between weeds and co-occurring vegetation. These derived band ratios and indices can be related to bio-physical attributes of weeds, such as foliage and flower cover (e.g. Bulman 2004; Martin, *et al.* 2011; Mirik, *et al.* 2006).

The spectral properties of Paterson's curse flowers have been investigated in several previous studies using spectroscopy (Bulman 2004; McGowen 1998; Mitchell, *et al.* 2006; Schut and McIntyre 2009). The flowers have been shown to have distinct spectral differences to whole plants in two regions of the spectrum: 1) a shift in the red-edge to shorter wavelengths; and 2) a distinctive reflectance peak in the blue (400-500 nm) region. There has been previous work on the spectral properties of pigments in flowers, in which the reflection properties for flowers are related to pigment content, and has been measured spectrally (Hunt, *et al.* 2004). However there is no prior knowledge about the detection of Paterson's curse by means of the spectral properties of the pigments in the purple flowers. In addition it is not clear how accurately pigment signatures from Paterson's curse sampled in the field can be measured. In the absence of knowledge of the pigments in Paterson's curse flowers,

using spectroscopy to detect Paterson’s curse will be based on a statistical relationship between spectral features (e.g. indices) and the percentage cover of flowers.

This chapter analyses the spectral characteristics of Paterson’s curse and co-occurring materials using field spectroscopy. The objectives of the chapter are to: 1) highlight the regions of the electromagnetic spectrum where differences between the spectra of Paterson’s curse and co-occurring materials are greatest; 2) determine if there is a relationship between the floral cover of Paterson’s curse and indices/band ratios and estimated floral cover from linear spectral un-mixing; and 3) assess whether the approach used in this chapter can be up-scaled (Milton, *et al.* 2009) to airborne and satellite multispectral sensors—given that such an approach was not within the scope of this research.

4.2 Methods

An outline of the methodology is shown in Figure 4.1, and the steps are described in the following sections.

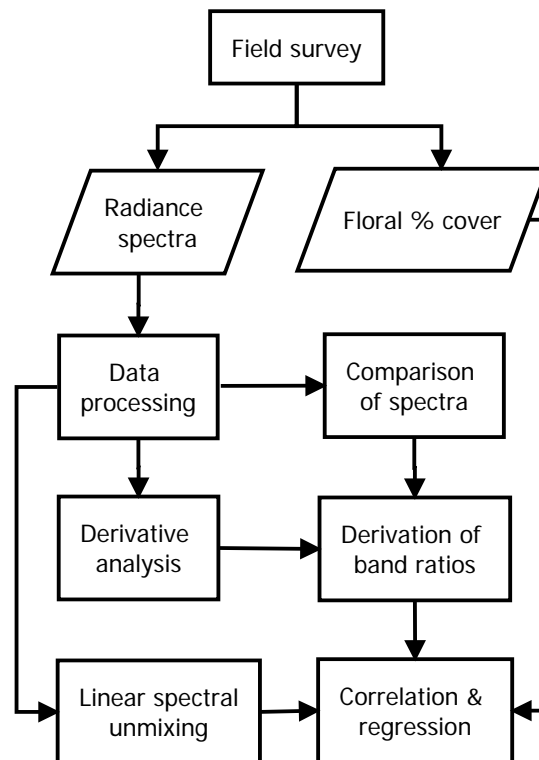


Figure 4.1 Flowchart outlining the methodology for the spectroscopy analysis.

4.2.1 Data collection

A field survey was conducted in late October/early November 2006 to coincide with the acquisition of EO-1 Hyperion satellite data (Chapter 6). Field measurements of Paterson's curse spectra were collected within a systematic sampling grid on the Catholic Agricultural College Bindoon (CACB) property on October 27, 2006. The location of the sampling grid (-31.291° S, 116.198° E) is shown as Site A in Figure 4.2. The grid was located in an area of the CACB property where there was good variation in the floral density of Paterson's curse for generating correlations with spectral information (see Section 4.2.5.3). The grid had dimensions of 150 m x 120 m, and incorporated eight parallel transects located 15 m apart, and each transect included 10 sampling points at 15 m intervals. The 15 m spacing between measurements ensured that spatial variation in Paterson's curse abundance was adequately captured. The sampling grid was marked by four survey poles positioned on the corners, and wooden stakes marked with flagging tape were placed at the beginning and end of each transect. A measuring tape was used to position the wooden stakes, and a compass and pacing were used to determine the locations of the sampling points along each transect.

Radiance measurements were made with a Fieldspec Pro JR spectroradiometer and a fibre optic cable with a 25° field of view fore-optic. Each measurement was recorded at a consistent height of 1.7 m from the ground. In accordance with CSIRO guidelines, the elevation angle of the fore-optic was 58° from the horizontal plane and the azimuth angle was at 90° to the plane of the sun (Phinn, *et al.* 2008). A ground sampling area of approximately 0.45 m^2 was obtained using these parameters. At each location, four spectral measurements were made in a 2 x 2 pattern, separated by 1 m. Dark current and reference measurements were taken after every ten samples, using a 5 x 5 cm pure white Spectralon calibration panel with Lambertian reflectance properties. Spectrum averaging of ten samples was used for the reference and dark current measurements, and twenty-five samples for the field radiance measurements.

All measurements were recorded between the hours of 10:30 and 13:00 to reduce the impact of shadow and low sun-angle on the measurements. Weather conditions

during the sampling were dry and warm: 26–28 degrees C, a relative humidity of 31–39%, with no cloud cover (Bureau of Meteorology 2010). There was no evidence of recent rainfall at the survey site that would influence the spectral response of vegetation. No precipitation was recorded at Gingin Airport in the 48 hours prior to the sampling so it can be assumed that no precipitation occurred at the sampling site for that period due to the close proximity of Gingin Airport to the study area (approximately 50 km).

The influence of other sources of radiance was minimal, as measurements were taken in large open area, separated by at least 50 m from potential sources of interference such as trees. Of the original 80 measurements recorded within the sampling grid, 11 were corrupted and subsequently discarded. The remaining 69 were used in the subsequent analysis.

A digital vertical photograph was captured at each measurement location. A wide-angle lens (28 mm) digital camera (Ricoh Caplio 400G) was positioned approximately 1.7 m above the centre of each quadrat (nadir) on a modified camera tripod/lighting stand (Manfrotto 420b). Floral percentage cover was derived post-survey using the object classification method described in Appendix C. The statistics of the floral cover measured from the grid are summarised in Table 4.1. The mean floral percentage of the 69 measurements was 2.1% with a standard deviation of 1.2%.

Table 4.1 Summary statistics for Paterson’s curse floral proportion cover from the systematic field grid at Catholic Agricultural College Bindoon.

N	Min	Max	Mean	SD
	(%)	(%)	(%)	(%)
69	0.29	5.71	2.05	1.21

Spectral measurements of dense Paterson’s curse were made from a site located on the CACB property, shown as Site B in Figure 4.2 (-31.31°S, 116.17°E). Radiance data were recorded from 30 measurements along a transect at 5 m intervals. At each location a digital photograph was captured. The floral cover from this transect was determined from the photographs using an object classification method described in Appendix C, and had a mean floral cover of 3.5% and a maximum of 8.8%.

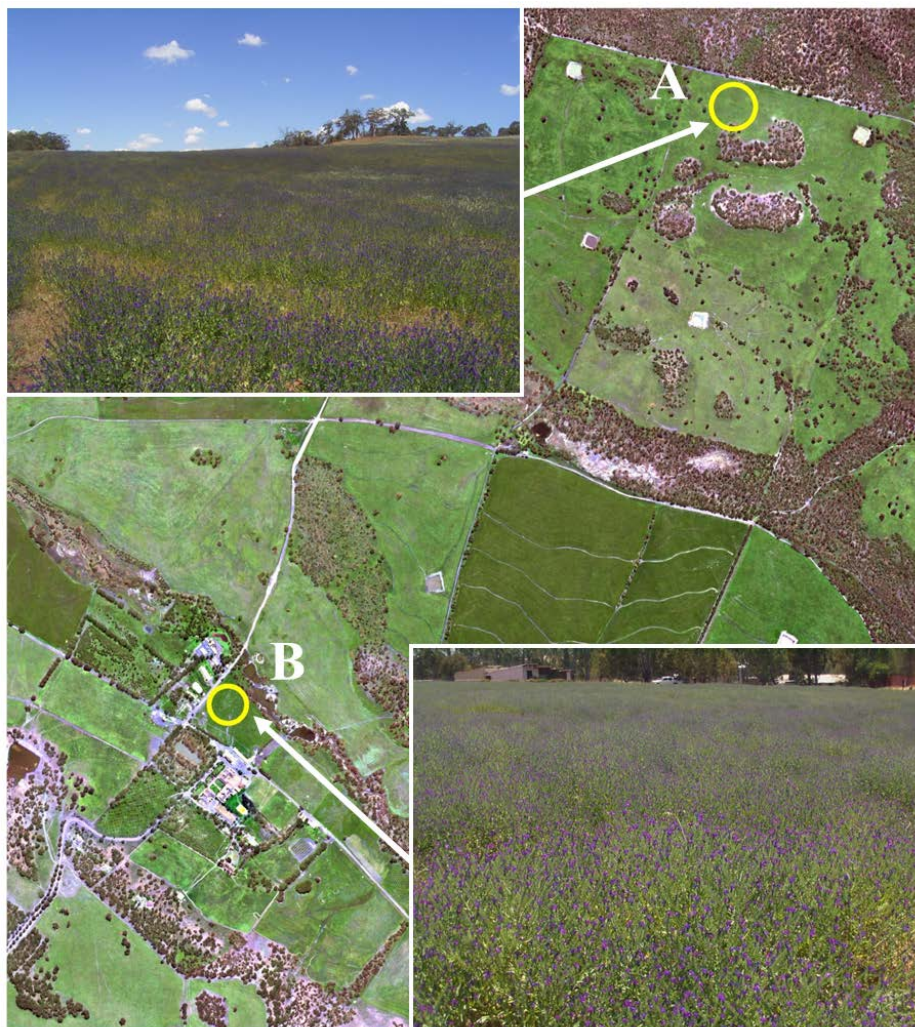


Figure 4.2 Location of sampling sites A and B at the Catholic Agricultural College Bindoon. Site A: Systematic sampling grid; B: Horse paddock where dense Paterson's curse spectra were measured.

Spectra for flowers and green plant material from Paterson's curse were recorded in the field on November 2, 2006 at the CACB. Approximately 20 measurements each were taken from flower and green material from mature Paterson's curse plants. The fore-optic from the fibre optic cable was positioned as close to the target material as possible in order to collect a pure sample and minimise spectral mixing with other materials. Spectra of senescent plant material, green pasture material and soils were sourced from Schut, *et al.* (2010). These spectra represented the mean spectral response of the main cover types expected to co-occur with Paterson's curse at a regional scale.

4.2.2 Data processing

The raw radiance data from the spectrometer were converted to reflectance data using radiance measurements from the Spectralon reference panel. Signals between 1361 and 1414 nm, 1801 and 1959 nm, and above 2401 nm were removed as attenuation of solar radiance by atmospheric water vapour caused high noise levels. For each measurement, a mean and a smoothed spectrum were calculated using a Gaussian filter with a sum of weights equal to one and a standard deviation of 12 nm. These smoothed spectra were subsequently used to calculate the first derivative and the continuum removed spectra (Heinz and Chang 2001; Kokaly and Clark 1999). The continuum was forced to include points at minor peaks around 555, 755, 1300, 1700, 1800, 2020 and 2230 nm.

4.2.3 Comparison of spectra

The spectra of Paterson's curse flowers, green stems, and dense Paterson's curse were compared with reflectance spectra for green and senescent vegetation and common soils in south-west Western Australia from Schut, *et al.* (2010). The purpose of comparing spectra was to determine the general spectral properties of Paterson's curse, relative to other cover types, and to previous studies that have examined the spectral properties of Paterson's curse. The green vegetation spectra represented lush and dense cover and the senescent vegetation spectra represented brown vegetation that was covering the ground.

4.2.4 Derivative analysis

The red-edge position (REP) was calculated for the spectra of green vegetation, Paterson's curse flowers and green stems, and dense (mixed) Paterson's curse. First derivative spectra were derived from a first order difference, shown in Equation 4.1 (Dawson and Curran 1998):

$$D_{\lambda(j)} = \frac{R_{\lambda(j+1)} - R_{\lambda(j)}}{\Delta\lambda} \quad (4.1)$$

Where $D_{\lambda(j)}$ is the first difference transformation at a wavelength i midpoint between bands j and $j+1$; $R_{\lambda(j)}$ is the reflectance at the $j+1$ waveband; and $\Delta\lambda$ is the difference in wavelength between j and $j+1$.

4.2.5 Relationships between spectra and floral cover

4.2.5.1 Derivation of band ratios and indices

Band indices were created by pairing each of the Paterson's curse spectra (dense Paterson's curse or Paterson's curse flowers) with a non-Paterson's curse spectra (senescent vegetation and green vegetation). For each pair, the reflectance values from the Paterson's curse spectrum were subtracted from those of the non-Paterson's curse spectrum and the difference in reflectance was plotted. From each plot, appropriate bands were selected from regions of the electromagnetic spectrum where there were large but opposite spectral differences (i.e. a positive and negative difference). The purpose of the simple spectral difference approach was to produce indices that had the highest sensitivity to Paterson's curse.

Other band ratios and indices were sourced from the literature and included the Normalised Difference Blue Index (NDBI) (Schut and McIntyre 2009), Paterson's Curse Index (PCI) (Bulman 2004), the Red-Edge Normalised Difference Vegetation Index (reNDVI) (Gitelson, *et al.* 1996), the Normalised Difference Red-Edge (NDRE) (Barnes, *et al.* 2000), and the Red-Edge 2 (RE 2) ratio (Cloutis, *et al.* 1996). Also included was a red-edge band ratio derived from a first order derivative analysis of spectra from Paterson's curse flowers and green vegetation (Section 4.2.4).

4.2.5.2 Spectral unmixing

Linear spectral unmixing (Section 2.5.3.2.1) was conducted on the spectra of Paterson's curse from the systematic sampling grid at CACB, using end-members derived from Paterson's curse flowers and stems, soils, and senescent and green vegetation (Section 4.2.1). Fractional coverage of soil, green and floral parts of Paterson's curse plants and dead material was determined for each measurement location with a fully constrained, exhaustive search linear unmixing procedure (Schut and McIntyre 2009). With this procedure, sets of mixtures were created, including various combinations of the pre-defined end-members and four contrasting soil-spectra. Sums of squared differences were calculated between the spectra and the mixtures over all bands between 500 nm and 2250 nm of the continuum removed spectra. The best matching mixture, i.e. the mixture with the smallest sum of squared differences, was subsequently selected. This procedure yielded the abundance of soil, flowers and dead material for each measurement location.

4.2.5.3 Correlation and regression analysis

Relationships between the band ratios/indices and estimated floral cover from the spectral unmixing with Paterson's curse floral cover were investigated using correlation and regression in the SPSS software package (SPSS Inc. 2007). The Spearman rank non-parametric correlation was used, as several of the variables lacked a normal distribution when tested with the Shapiro-Wilk test (Appendix D). A first or second order linear regression was used to fit a relationship between the independent (x) variable (floral cover) and the dependent (y) variable (ratio, index or unmixing).

4.3 Results

4.3.1 Comparison of spectra

The reflectance spectra from the spectroradiometer are shown in Figure 4.3. White sand and grey sand soil spectra were distinctive from the other spectra, due to a consistently higher response in the visible region of the spectrum and a relatively smooth transition through the visible and near infrared. The green vegetation spectra showed a 'textbook' vegetation spectral response (Section 2.1.3).

The spectrum for Paterson's curse flowers had a characteristic peak in the blue (400–500 nm), a higher reflectance than green vegetation from the violet/blue through the blue (400–500 nm) and part of the green wavelength range of the spectrum (500–510 nm). The flower spectrum also showed a distinctive red-edge increase in reflectance at approximately 630 nm, compared to 685 nm for green vegetation and material of Paterson's curse. The spectrum of green Paterson's curse material had similar reflectance to green vegetation throughout the spectral range. The reflectance spectra of dense Paterson's curse had similar reflectance to green vegetation in the blue part of the spectrum (400–500 nm); lower reflectance in the green (500–600 nm) and part of the red (600–620 nm); higher reflectance in the remainder of the red part of the spectrum (620–700 nm); and a lower reflectance in the near infrared (700–1360 nm).

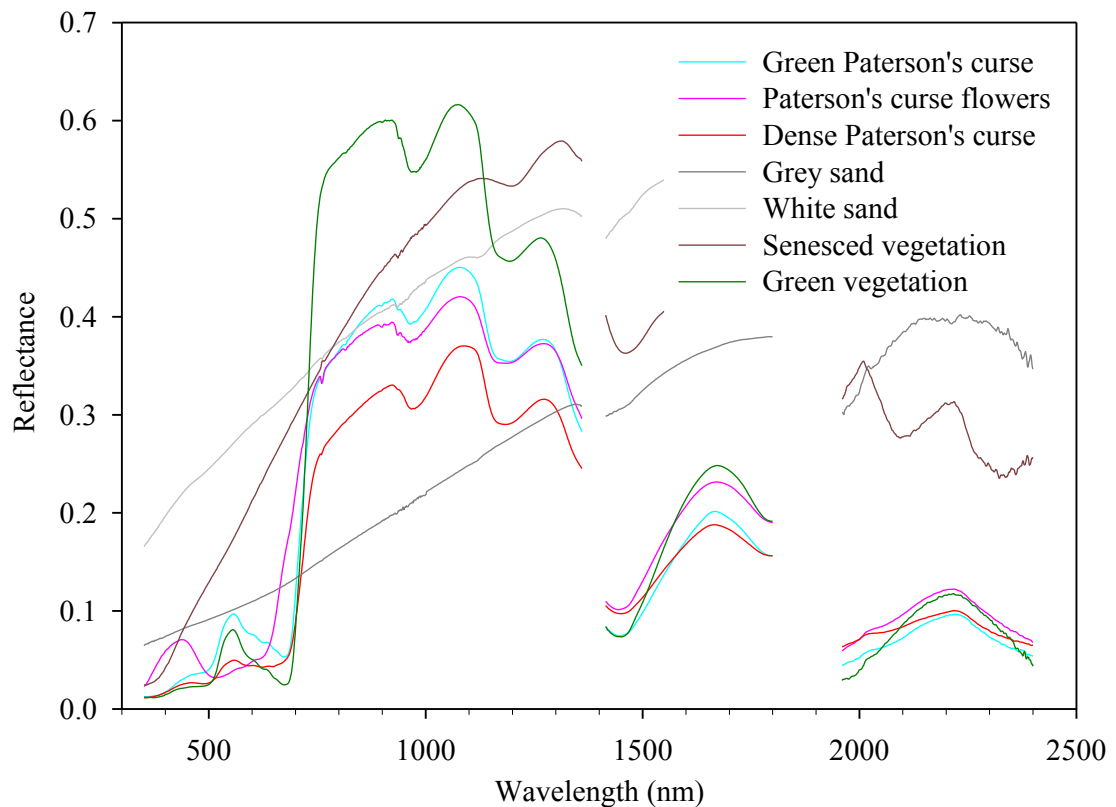


Figure 4.3 Spectral reflectance curves for components of Paterson's curse and other cover types across the full spectral range (351–2400 nm).

4.3.2 Derivative analysis

The first order derivative spectra for Paterson's curse green, flower, dense, and green vegetation are shown in Figure 4.4. The presence of multiple peaks in derivative spectra is common in spectra derived from spectroscopy data with a high spectral resolution (Smith, *et al.* 2004). Subsequently, no smoothing was performed on the derivative spectra, as the peaks were not attributable to sensor noise. Green vegetation had two peaks at 703 nm and 728 nm; Paterson's curse flowers had three peaks at 656 nm, 694 nm and 720 nm; Paterson's curse green had two peaks at 701 nm and 719 nm; and dense Paterson's curse had two peaks at 702 and 718 nm. The REP (Equation 4.1) for green Paterson's curse was 719 nm, 694 nm for Paterson's curse flowers, 718 nm for dense Paterson's curse, and 728 nm for green vegetation.

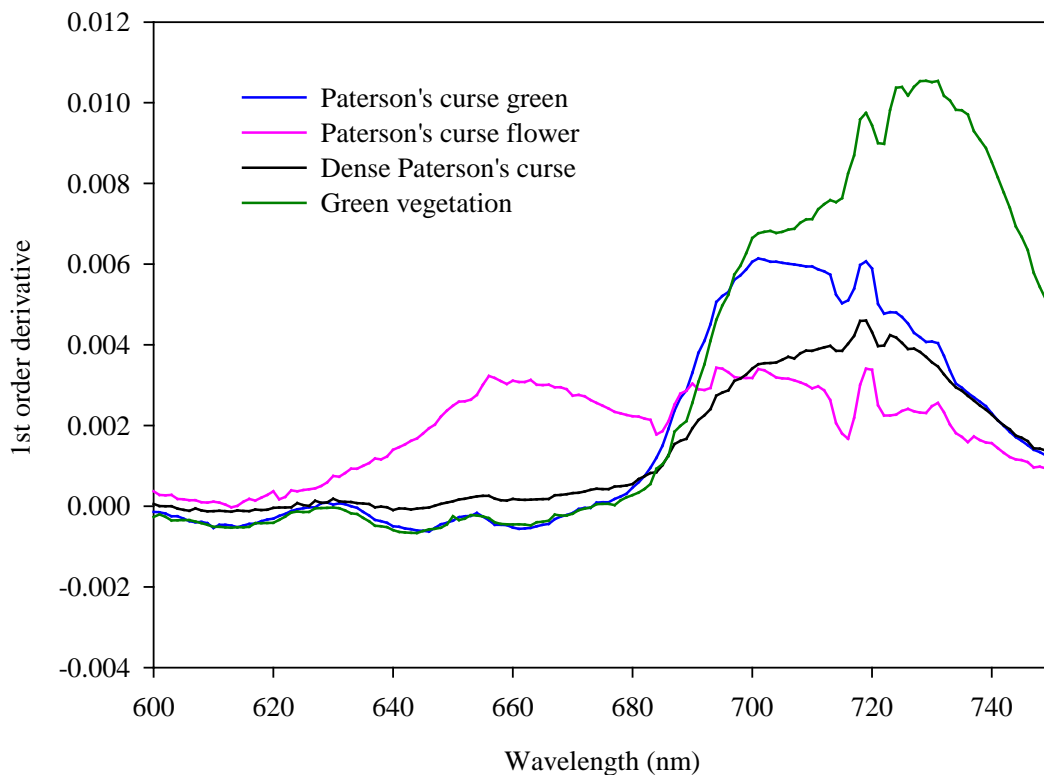


Figure 4.4 First order derivatives for Paterson's curse and green vegetation spectra.

4.3.3 Relationships between spectra and floral cover

4.3.3.1 Derivation of band ratios and indices

The difference plots of Paterson's curse flowers with green vegetation and senescent vegetation are shown in Figure 4.5. For flowers and green vegetation, the greatest differences were at 898 nm, 908 nm and 691 nm. Smaller differences occurred at 553 nm and 438 nm. For flowers and senescent vegetation the greatest differences are at 1415 nm, 2007 nm and 684 nm, with a small difference at 391 nm.

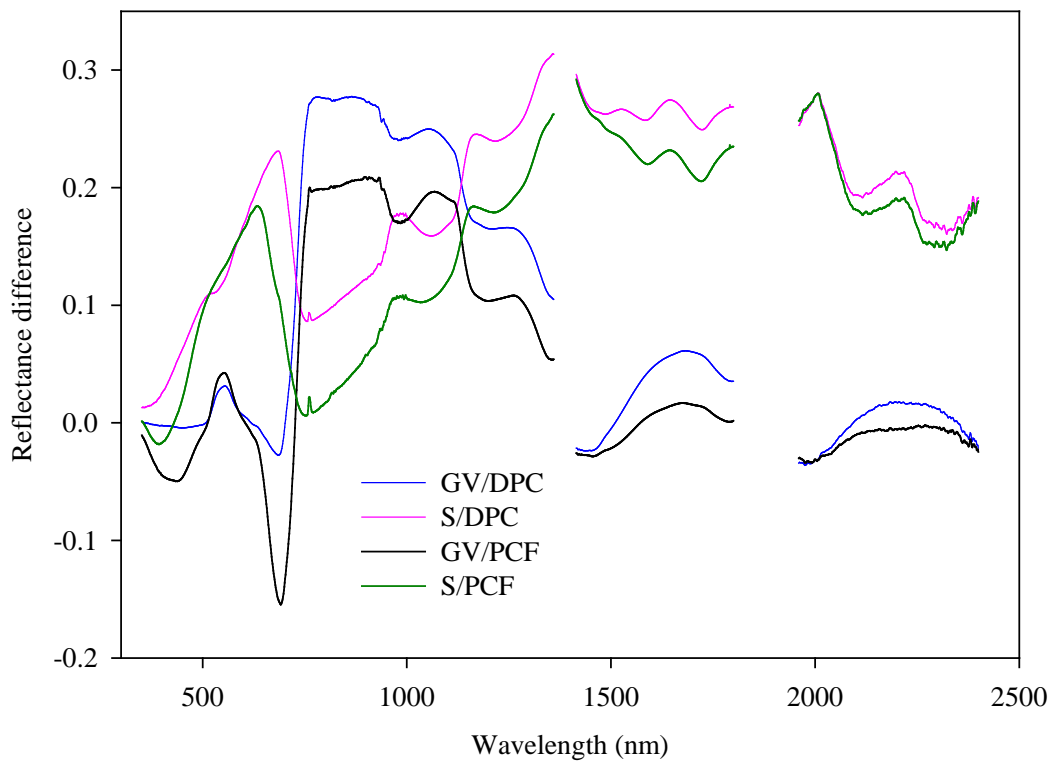


Figure 4.5 Spectral response difference between spectra from green vegetation (GV), Paterson's curse flowers (PCF), Dense Paterson's curse (DPC), and senescent vegetation (SV) spectra.

Four indices were derived from the difference between green vegetation and Paterson's curse flowers, and two indices were derived from the difference between senescent vegetation and Paterson's curse flowers (Table 4.2). For the green vegetation indices, the first index (GVPCF 1) was derived from bands of the visible part of the spectrum; the remaining three indices (GVPCF 2 and GVPCF 3) were derived from visible and near infrared bands, where GVPCF 2 was a Normalised Difference Vegetation Index (NDVI). For the two senescent vegetation indices, the first index (SVPCF 1), highlighted the difference between the red (634 nm) and the violet/blue (391 nm) part of the spectrum and the second (SVPCF 2) index highlighted the difference between the mid infrared (2007 nm) and the near infrared (1415 nm) bands.

The difference plots for dense Paterson's curse with green vegetation and senescent vegetation are shown in Figure 4.5. The largest difference between dense Paterson's curse and green vegetation was at 865 nm, with smaller peak differences at 555 nm and 684 nm. For dense Paterson's curse and senescent vegetation, there were peak

differences in reflectance at 1358 nm, 2007 nm, 685 nm, and 984 nm. Three indices were derived from the difference between dense Paterson's curse and green vegetation and, and two indices were derived from the difference between dense Paterson's curse and senescent vegetation and (Table 4.2). For the green vegetation indices, the first index (GVDPC 1) was derived from bands from the visible portion of the spectrum, while the remaining two indices were derived from bands from the visible and near infrared, with GVDPC 2 being a Normalised Difference Vegetation Index (NDVI), and GVDPC 3 a Normalised Difference Green Index (NDGI). For the two senescent vegetation indices, the first index (SVDPC 1) highlighted the differences between the near infrared (984 nm) and the red-edge (685 nm), and was a Normalised Difference Vegetation Index (NDVI). The second index (SVDPC 2) highlighted the difference between mid-infrared near infrared bands (2007 nm and 1358 nm).

An additional four ratios were included, which utilised spectral information from the red-edge part of the spectrum. Three of the ratios were derived from the literature and represented common red-edge ratios (Table 4.2). The fourth red-edge ratio was identified from the 1st order derivative of the Paterson's curse flower spectra (Section 4.3.2) and highlighted the difference between the first peak at 656 nm and the second peak at 720 nm.

Table 4.2 List of band ratios and indices used to determine a relationship with floral cover.

Ratio/Index	Bands
NDBI (Schut and McIntyre 2009)	$\frac{(490 \text{ nm} - 430 \text{ nm})}{(430 \text{ nm} + 490 \text{ nm})}$
PCI (Bulman 2004)	$\frac{(650 \text{ nm} + 450 \text{ nm})}{(650 \text{ nm} + 550 \text{ nm} + 450 \text{ nm})}$
GVPCF Index 1	$\frac{(553 \text{ nm} - 438 \text{ nm})}{(553 \text{ nm} + 438 \text{ nm})}$
GVPCF Index 2	$\frac{(908 \text{ nm} - 691 \text{ nm})}{(908 \text{ nm} + 691 \text{ nm})}$
GVPCF Index 3	$\frac{(898 \text{ nm} - 438 \text{ nm})}{(898 \text{ nm} + 438 \text{ nm})}$
GVPCF Index 4	$\frac{(691 \text{ nm} - 438 \text{ nm})}{(691 \text{ nm} + 438 \text{ nm})}$
SVPCF Index 1	$\frac{(634 \text{ nm} - 391 \text{ nm})}{(634 \text{ nm} + 391 \text{ nm})}$
SVPCF Index 2	$\frac{(2007 \text{ nm} - 1415 \text{ nm})}{(2007 \text{ nm} + 1415 \text{ nm})}$
GVDPC Index 1	$\frac{(684 \text{ nm} - 555 \text{ nm})}{(684 \text{ nm} + 555 \text{ nm})}$
GVDPC Index 2	$\frac{(865 \text{ nm} - 684 \text{ nm})}{(865 \text{ nm} + 684 \text{ nm})}$
GVDPC Index 3	$\frac{(865 \text{ nm} - 555 \text{ nm})}{(865 \text{ nm} + 555 \text{ nm})}$
SVDPC Index 1	$\frac{(984 \text{ nm} - 685 \text{ nm})}{(984 \text{ nm} + 685 \text{ nm})}$
SVDPC Index 2	$\frac{(2007 \text{ nm} - 1358 \text{ nm})}{(1358 \text{ nm} + 2007 \text{ nm})}$
Red-Edge NDVI (reNDVI) (Gitelson, <i>et al.</i> 1996)	$\frac{(750 \text{ nm} - 710 \text{ nm})}{(750 \text{ nm} + 710 \text{ nm})}$
Normalised Difference Red-Edge (NDRE) (Barnes, <i>et al.</i> 2000)	$\frac{(790 \text{ nm} - 720 \text{ nm})}{(790 \text{ nm} + 720 \text{ nm})}$
Red-Edge 2 (RE 2) (Cloutis, <i>et al.</i> 1996)	$\frac{(712 \text{ nm} - 680 \text{ nm})}{(712 \text{ nm} + 680 \text{ nm})}$
Normalised Flower Red-Edge (NFRE)	$\frac{(720 \text{ nm} - 656 \text{ nm})}{(720 \text{ nm} + 656 \text{ nm})}$

4.3.3.2 Correlation and regression analysis

Table 4.3 shows the correlation and regression coefficients from the relationship between the Paterson's curse floral proportion data from the systematic sampling grid and the band ratios and indices described in Section 4.3.3.1. The correlation coefficients were significant for all variables (at $\alpha = 0.01$) except the non-significant GVPCF 1 index. The NDBI had the highest correlation of all the variables, with a Spearman coefficient of -0.83. A second-order polynomial fitted to the data produced an R^2 of 0.75 (Figure 4.6). The abundance of Paterson's curse flowers estimated with linear unmixing (UNMIX) had the second highest correlation coefficient of 0.73 with an R^2 of 0.68 (Figure 4.7). The remainder of the variables had correlation coefficients from 0.42 (GVPCF 3) to 0.71 (NFRE) and R^2 values from 0.20 to 0.49.

Table 4.3 Pearson correlation coefficient (r) and coefficient of determination of regression (R^2) for first order (a) or second order (b) polynomial relationships between abundance estimates using linear unmixing and selected indices, with percentage floral cover of Paterson's curse.

Variable	r	R^2
NDBI	-0.829	0.745 _b
UNMIX	0.731	0.678 _b
NFRE	0.706	0.487 _b
ReNDVI	0.566	0.434 _a
SVPCF 1	-0.5	0.414 _b
GVDPC 3	0.601	0.401 _b
RE 2	0.595	0.382 _b
PCI	-0.564	0.37 _b
NDRE	0.492	0.37 _a
GVDPC 2	0.546	0.369 _b
GVPCF 2	0.523	0.366 _b
SVDPC 1	0.516	0.336 _b
SVDPC 2	0.546	0.33 _b
GVPCF 4	-0.482	0.32 _b
SVPCF 2	0.481	0.246 _b
GVDPC 1	-0.446	0.24 _b
GVPCF 3	0.416	0.197 _b
GVPCF 1	0.133	-

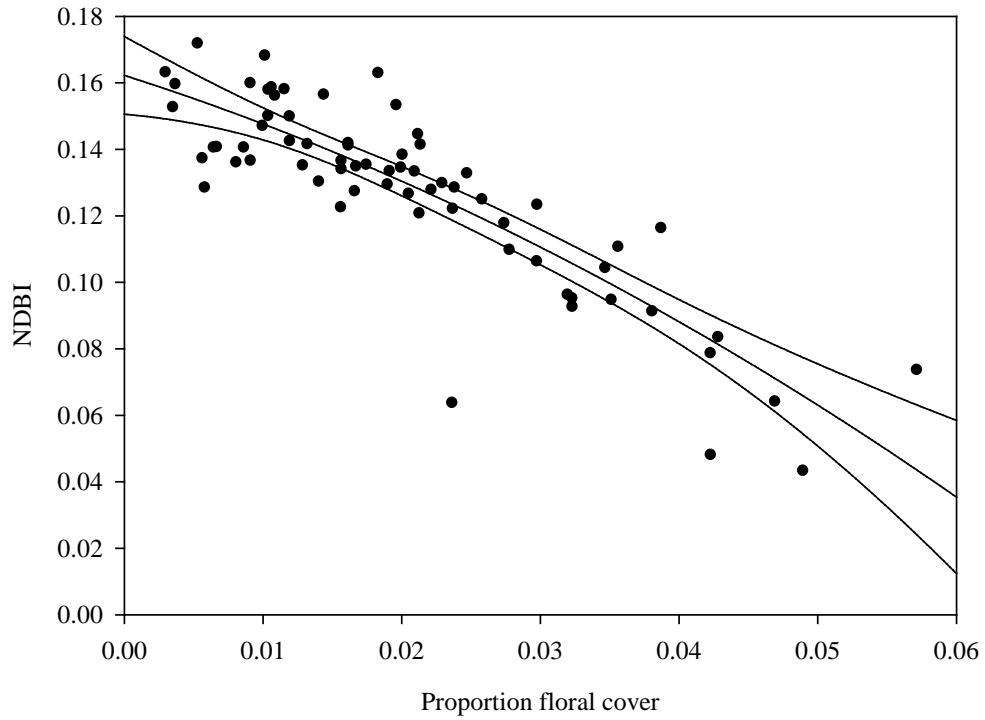


Figure 4.6 Scatter plot, regression line ($R^2 = 0.829$), and 95% upper and lower confidence intervals for the NDBI and Paterson's curse floral cover (proportion).

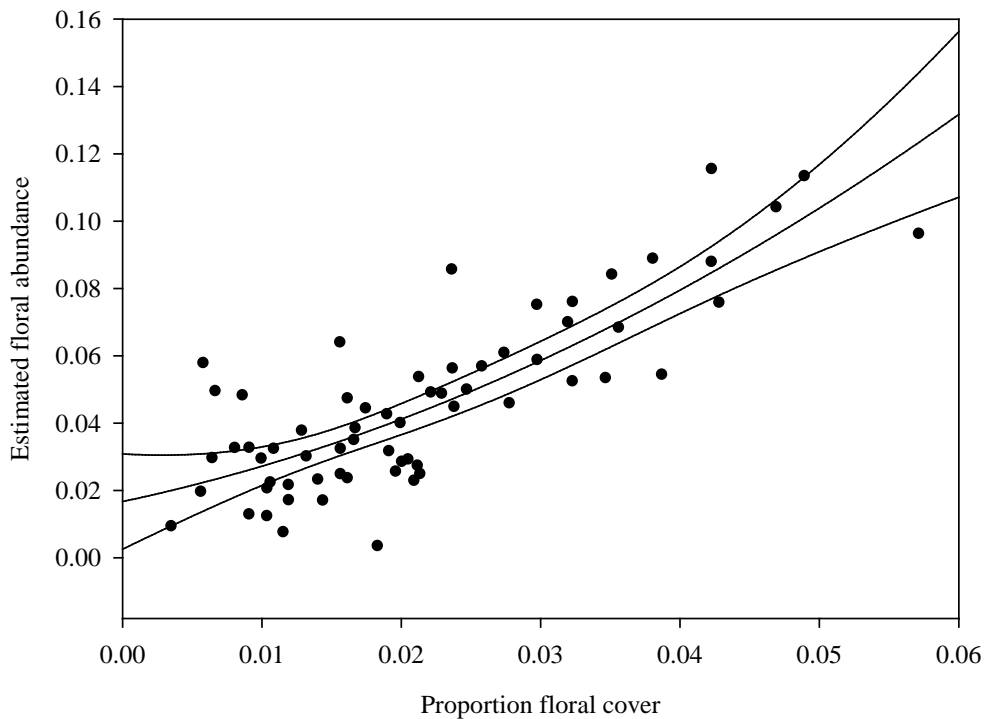


Figure 4.7 Scatter plot, regression line ($R^2 = 0.75$), and 95% upper and lower confidence intervals for Paterson's curse floral cover (proportion) and estimated floral abundance from linear unmixing.

4.4 Discussion and Conclusion

The high spectral resolution of the spectroradiometer data highlighted differences between Paterson's curse and other material types over small discrete regions of the electromagnetic spectrum. There were several strong correlations between some ratios/indices and the floral proportion cover of Paterson's curse. The ratios and indices were not an exhaustive collection, but did represent the areas of the spectrum where there was a large difference between Paterson's curse and other materials, and they provide a good indication of which spectral band combinations could be used if an airborne or satellite hyperspectral sensor is used. For example the Normalised Difference Blue Index ($R^2 = 0.75$) takes advantage of the higher reflectance response of Paterson's curse flowers in the blue region of the spectrum. Similarly, the relationship between spectral unmixing and Paterson's curse floral cover data ($R^2 = 0.61$) demonstrates the potential of spectral unmixing and hyperspectral data to detect Paterson's curse at different densities, and for discriminating it from pasture and crops.

The spectral properties of the Paterson's curse flower, stem and plant spectra from the current research are similar to those reported from other studies. The distinctive peak in the blue portion of the spectrum (400-500 nm) for Paterson's curse flowers, and lack of such a peak for the Paterson's curse (whole) plant spectrum has also been reported by McGowan (1998) and Mitchell et al. (2006). A shift in the red-edge to shorter wavelengths by Paterson's curse flower material relative to plant material (flowers and stems) has also been noted by Bulman (2004) and Mitchell et al. (2006). The REP for the flower, plant, and green vegetation spectra described in this research are not comparable to previous studies which reported the red-edge as being the start of the increase in reflectance towards the red-edge rather than a REP. However the start of the increase in reflectance of the Paterson's curse flower spectrum at 630 nm from this research is similar to the 640 nm observed by Bulman (2004), and similarly the green Paterson's curse spectrum had a similar increase towards the red-edge at 685 nm compared to the 690 nm of Bulman (2004).

The regression results from the spectral unmixing of Paterson's curse flowers ($R^2 = 0.61$) and the NDBI ($R^2 = 0.75$) confirms that the flowers of Paterson's curse are an

important cue for detection. A similar result was reported by Schut and McIntyre (2009) at Muresk with linear spectral unmixing of Paterson's curse flowers ($R^2 = 0.54$), but a lower R^2 of 0.46 was produced by the NDBI. A possible explanation for the poorer relationship was the lower percentage cover range of Paterson's curse flowers at Muresk (2.5%), compared to Bindoon (5.7%). The only other known study to use field spectroscopy to relate the floral properties of weed species to spectral indices was Mirik, *et al.* (2006), who obtained an R^2 of 0.46 for the flower head density of Musk thistle (*Carduus nutans*), and attributed the result to the low density of flower heads. The NDBI result from this research shows that indices for a specific spectral feature of the flowers of a weed (e.g. blue peak), rather than vegetation indices (cf. Mirik, *et al.* 2006) can produce good correlations and if floral density is sufficiently high, the difference can be enough to spectrally discriminate the weed.

The relationship of percentage floral cover with the four red-edge ratios was weak to moderate (R^2 of 0.37 to 0.49), compared to the strong relationship with the NDBI and linear spectral unmixing. The spectra of Paterson's curse from the systematic field grid were comprised of a mixture of flowers (2% mean floral percentage cover), green material from Paterson's curse, and senescent pasture. The poor performance of the red-edge ratios was likely due to a decrease in the magnitude of the red-edge shift in the mixed Paterson's curse spectra, compared to the larger observed shift in the Paterson's curse flower spectra. Infestations of Paterson's curse with a floral proportion cover range of less than 10% are therefore unlikely to show strong relationships with red-edge ratios due to the small difference in the red-edge shift across that range.

Of all the ratios and indices analysed in this section, the NDBI is worth further investigation for up scaling to airborne and satellite multispectral sensors. If this index is to be effectively scaled up, there are three main considerations: First, the spectra of vegetation from a spectroradiometer are derived from a precision instrument with a greater signal-to-noise ratio and a higher spectral resolution than aerial and (especially) satellite multispectral sensors. In particular, noise in the blue region for satellite sensors is pronounced due to atmospheric path scattering (Jones and Vaughan 2010). Therefore, rigorous radiometric and atmospheric correction, and calibration (Milton, *et al.* 2009) will be required to reduce noise from the two blue

bands in the NDBI. Secondly, the sensor needs to contain a blue band with a small bandwidth to capture the reflectance peak at of Paterson's curse flowers at 430 nm. Due to the former criterion, the DMSI data (Section 3.4.1) lacks two blue bands, and the NDBI cannot be applied. Examples of current multispectral satellites with two blue bands are WorldView 2 and Landsat 8 (Table 2.2).

Thirdly, spatial resolution is another important consideration when scaling up to multispectral sensors, given the relationship between increasing pixel size and the likelihood of cover types being mixed (Fisher 1997). At the sub-metre spatial resolution of the spectroradiometer measurements (0.25 m²), the mixture of Paterson's curse with pasture or other cover types within the sample area was minimal. When scaling up to sensors such as a Landsat 8 (900 m² pixel area), it is likely that the problem of spectral overlap of Paterson's curse with other cover types reported by Bulman (2004) and Ullah, *et al.* (1989b) will be encountered. Airborne sensors and satellite sensors with a similar higher spatial resolution to that of WorldView 2 (3.24 m² pixel area) are likely to contain less of a mixture of other cover types, especially for areas of lower density (and patchy) Paterson's curse and along margins with other cover types such as Eucalypt woodland.

5 MAPPING PATERSON'S CURSE WITH MULTISPECTRAL AIRBORNE IMAGERY

5.1 Introduction

The field spectroscopy analysis in Chapter 4 highlighted the spectral differences between Paterson's curse and other cover types, using a high spectral resolution sensor with narrow bands in the visible and near infrared. The next step is to investigate whether the spectral differences between Paterson's curse and the co-occurring cover types are applicable over a larger area, and with a spectral resolution coarser than field spectroscopy. As already highlighted in the literature review in Chapter 2, multi-spectral medium spatial resolution sensors (Landsat 5 and 7) have had limited success in reliably detecting and mapping Paterson's curse (Bulman 2004; Ullah, *et al.* 1989b) due to spectral overlap between Paterson's curse and other cover types. Airborne multispectral imagery therefore is a potentially useful source of remote sensing data for mapping Paterson's curse.

Airborne multispectral data are inexpensive compared to airborne hyperspectral data and do not require specialised processing. Airborne sensors also have a number of advantages over satellite platforms. The new generation of satellite-borne sensors (e.g. World View 2) provide high spatial resolution multispectral imagery, but these sensors have limitations with temporal acquisitions of imagery, due to a limited revisit capability, and the associated problem of cloud cover. Airborne sensors have the flexibility to be deployed at short notice to take advantage of favourable meteorological conditions. This is a particularly important consideration for Paterson's curse, as cloud cover is common over the Bindoon study area during October, which coincides with the short (peak) flowering period.

As shown in the literature review in Chapter 2, high spatial resolution multi-spectral sensors have been successful for detecting weed species in semi-arid regions and rangelands (Everitt and Yang 2007b; Robinson, *et al.* 2008; Stow, *et al.* 2000), and pasture (Carson, *et al.* 1995; Lass and Callihan 1997; Lass, *et al.* 1996). These studies have used supervised and unsupervised classification methods, such as maximum likelihood (Carson, *et al.* 1995) and minimum distance to means (Lass and

Callihan 1997) for the former, and ISODATA (Everitt and Yang 2007b; Robinson, *et al.* 2008; Stow, *et al.* 2000) for the latter. The smaller pixel size reduced the effect of mixed pixels, and allowed smaller infestation sizes and densities to be detected. These mapped species also had distinctive characteristics compared to co-occurring cover types that resulted in higher accuracy from the classifiers. In a similar manner, the purple flowers of Paterson's curse are a potentially good feature for detection with airborne multispectral remote sensing.

This chapter investigates the utility of airborne multispectral imagery to detect and map Paterson's curse at the Catholic Agricultural College Bindoon (CACB) study site. It represents the first application of this type of remote sensing data for Paterson's curse. The objectives of the research reported in this chapter are:

- i) To determine if Paterson's curse can be detected and mapped from airborne multispectral imagery using image classification techniques;
- ii) To produce quantitative measures of classification accuracy for Paterson's curse and associated cover types from each of the classifiers and compare their performance; and
- iii) To highlight the spectral and spatial limitations of the image data and the classifiers for detecting and mapping Paterson's curse.

5.2 Methods

The approach described in this chapter followed a standard remote sensing classification workflow, in which imagery was acquired and processed, and classifications were trained and implemented. Field and ancillary data were used to collect training data and validate the classification results.

5.2.1 Image acquisition

Digital airborne multispectral imagery (DMSI) was acquired over the CACB property by Specterra, a Perth based company. A description of the DMSI image capture and pre-processing is provided in Section 3.3. In summary, DMSI imagery was captured on October 14 2005, at a spatial resolution of 1 m. The imagery was processed in-house by Specterra to produce an ortho-rectified mosaic (see Figure 3.5, Chapter 3).

5.2.2 Image pre-processing

The DMSI mosaic was spatially subset to an area of 1132 ha, with dimensions of 3.19 km x 3.55 km. This area was chosen to restrict the analysis to within the property boundary of the CACB, and to provide a representative area of Paterson's curse and other cover types. Regions of the image not relevant to the analysis were masked, which included Eucalypt woodland, swampland, roads and tracks, buildings and other cleared areas devoid of ground cover. A semi-automated approach was used to create the mask: a segmentation algorithm was applied to the image using the eCognition software package (Baatz, *et al.* 2004) and the resulting objects (polygons) were assigned to the mask based on field knowledge and conventional image interpretation cues.

Atmospheric correction was not performed on the DMSI image prior to classification for the following reasons: (i) a single date of imagery was used; (ii) the capture time was at noon, under clear dry meteorological conditions; (iii) the topographic variation over the study area was minimal; and (iv) atmospheric haze was minimal (Chavez 1988).

5.2.3 Training area selection

Training signatures were created from four land cover classes (crop, pasture, fallow, and Paterson's curse) to be used for supervised classification (Section 5.2.5). The training areas for Paterson's curse and the other classes were derived from locations where field reconnaissance was previously conducted with a digital camera and a handheld GPS. Examples of field photos of the classes are shown in Figure 5.1 and the classes are briefly described below:

- i) Crop: a dense cover of green vegetation, with a bare soil background. Most cropped areas on the CACB property occurred as a dense monoculture of a particular crop species.
- ii) Pasture: green vegetation of varying density of ground cover, which was dependent on the level of grazing. In grazed pastures, the vegetation cover was light, and in un-grazed pastures the cover was typically dense and similar to that of cropped areas.

- iii) Fallow: bare soil and senescent plant material from previous growing seasons.
- iv) Paterson's curse: Paterson's curse at floral cover of up to approximately 15%. Multiple density classes were not used due to the low range (0.1–7%) and mean (< 2%) floral percentage cover from the validation dataset, which represented the general distribution of Paterson's curse in the study area.

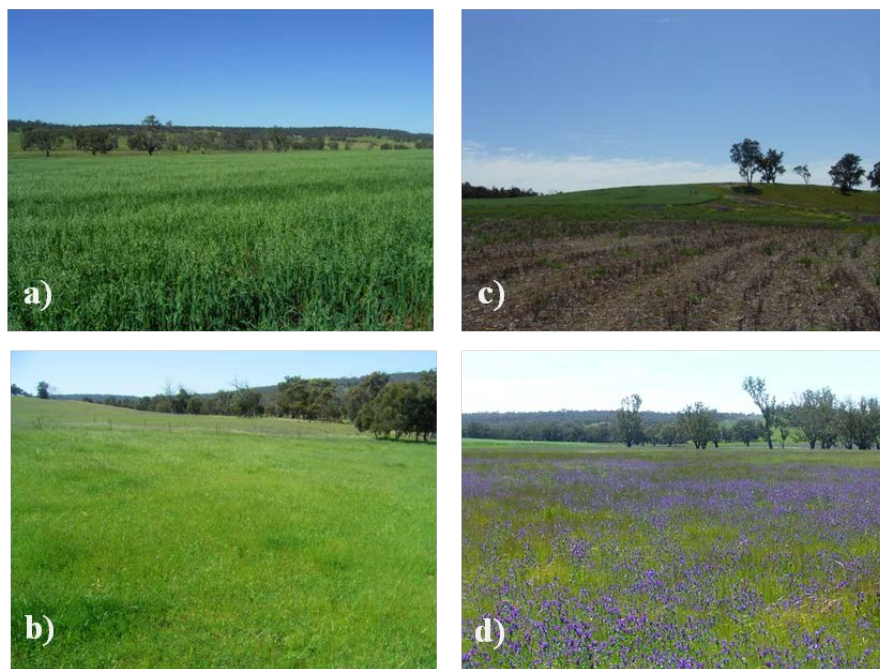


Figure 5.1 Training classes used and representative oblique photographs: a) crop; b) pasture; c) fallow; d) Paterson's curse.

Training areas for all classes were digitised manually on-screen from the DMSI image. Paterson's curse signatures were extracted from several training areas at different floral densities to account for spectral variability. Multiple signatures were created for each class (from 3 to 9) to include as much of the spectral variation present within the particular cover types as possible. Training areas were located at least 10 metres from the nearest validation point to remove bias in the classification results.

5.2.4 Training area analysis

The spectral properties of the training areas were analysed using spectral plots of training classes, and the spectral separability of classes was measured with Transformed Divergence using the ERDAS Imagine software (Leica Geosystems

2005). For the latter method, various band combinations were tested to determine the influence of removing bands on separability. The separability of signatures was assessed according to indicative values from Jensen (1996): separability greater than 1900 was considered good; separability between 1700 and 1900 was fair; and separability below 1700 was poor. The final training signatures for the crop, pasture, fallow and Paterson's curses classes and for each band were also tested for the assumption of normal distribution in the SPSS software package (SPSS Inc. 2007) using a skewness metric and a Shapiro-Wilk test of significance. The results from the normality test are shown in Appendix E.

5.2.5 Image classification

Two non-parametric classification algorithms were used: multi-layer perceptron (MLP) and k-nearest neighbour (kNN). These two classification algorithms were chosen as the training signatures did not satisfy the assumption of normality for parametric classifiers (Campbell 2008), and the two algorithms have been shown to be superior to parametric approaches (e.g. maximum likelihood).

For the MLP and kNN algorithms, separate classifications were run on two separate class sets (A and B). Set A was comprised of crop, pasture and Paterson's curse; and Set B was comprised of pasture and Paterson's curse. Crop was removed in Set B in order to determine if the accuracy of the classification could be improved in the absence of potential spectral overlap between the crop and Paterson's curse classes.

5.2.5.1 Multi-layer perceptron classifier

The MLP classification was performed using the IDRISI Andes software (Eastman 2006). The back-propagating network of the classifier contained one input layer, one output layer, and one or more hidden layers. The input layer consisted of the four DMSI image bands (blue, green, red and near infrared), and the output (classified) layer consisted of the four classified land cover classes from the training areas (Paterson's curse, crop, pasture and fallow). Prior to implementing the classification, the values of pixels from all four bands were scaled from 0 to 1, by dividing the digital number value of each pixel by the band maximum. This was done in order to match the activation function range (percentage) order of magnitude instead of the

range of the sensor (12-bit), to prevent the network from being saturated (Kanellopoulos and Wilkinson 1997).

The MLP network was trained with signatures from Paterson's curse, pasture, crop and fallow. Each input signature was divided into training and validation sets comprised of an equal number of pixels. The purpose of training the network was to obtain the appropriate weights for both for the connection between the input and hidden layer, and between the hidden and the output layer for the classification of the unknown pixels (Eastman 2006). The network learnt the properties of each training class through a series of successive forward and backward passes (Eastman 2006). Each sample (pixel) from a training class was fed by the network into the input layer and the activities of the neurons were updated on the way through to the output layer, according to a mapping function (Tso and Mather 2001). A non-linear sigmoid mapping function was applied to the weighted sum of inputs before the signal was passed to the next layer (Eastman 2006). When the forward pass was completed the activities of the output nodes were compared with their expected activities (Eastman 2006). The network error was the difference between the actual and expected outcomes, and was distributed through the network by means of a backward pass which updated the weights (Tso and Mather 2001).

An adaptive learning rate algorithm (Eastman 2006) was used during training to prevent oscillation from over training, and a local minimum on the error surface from under-training (Mas and Flores 2008). The algorithm decreased the learning rate if the overall training error increased, and increased the learning rate if the overall error decreased (Paola and Schowengerdt 1995). The initial learning rate value was not considered critical, and the classifier was trained faster due to the learning rate being adjusted to the highest value that did not cause instability (Paola and Schowengerdt 1995). A momentum term of 0.5 was used as recommended by Eastman (2006) and Kavzoglu and Mather (2003), which would increase the time to convergence and reduce the likelihood of oscillation problems. A stopping threshold of 80% training accuracy was used, after several training trial iterations found that the training and testing error began to diverge when the training accuracy exceeded 80%. The stopping threshold corresponded to a root mean square error of 0.38.

Following network training, the neural network classifier was run to produce hard and soft output classification images. The hard classification images were comprised of the same classes as the training areas: Paterson's curse, pasture, crop and fallow. The soft classification output was comprised of a set of maps, each map representing one class. The maps were created from the output of the activation levels for each output layer (class), which were 'fuzzified' into a 0–1 range using an activation function (Eastman 2006). The fuzzy range represented the degree of membership of each pixel to a class, with higher values representing higher degrees of membership (Eastman, 2006).

5.2.5.2 k-nearest neighbour classifier

The kNN classifier from the IDRISI Andes software package was applied to a three-class signature set comprised of crop, pasture and Paterson's curse; and a two class set comprised of pasture and Paterson's curse. Both hard and soft classification was applied to each set. The hard classification output consisted of an image containing either three or two classes (Set A and B respectively). The soft classification output produced a soft image for each class, and the proportion among the k-nearest neighbours was assigned to each pixel as a degree of membership to that class (Eastman 2006). For each set, the most separable band combinations identified in the training area analysis in Section 5.2.4 were used. An iterative series of classifications was then performed, to determine if different k-values resulted in a significant difference in accuracy, measured by the Kappa statistic (refer Section 5.2.6.2). Classification output was generated using between 5 and 55 k-neighbours, in increments of 10.

5.2.6 Accuracy assessment

5.2.6.1 Field survey

A stratified random sampling scheme was used to collect validation data to assess classification accuracy (Congalton 1991). The sampling was conducted less than a week after the DMSI imagery was captured. The DMSI image was stratified to include areas of crop, pasture and Paterson's curse, and to exclude areas not relevant to the analysis, which included Eucalypt woodland, swampy areas, and cleared areas such as roads, tracks, and infrastructure. A field reconnaissance was conducted on October 15 2005 to define a stratified area of Paterson's curse. A total of 86 locations

across the property were recorded with a handheld GPS and oblique digital photos were captured. The stratification was performed by segmenting the image into objects using the Definins eCognition software (Baatz, *et al.* 2004). The objects were assigned to one of four general classes: Paterson's curse, pasture, crop and mask. Each image object was manually assigned into an appropriate class based on field knowledge and conventional image interpretation cues.

From the area of Paterson's curse (77 ha) digitized from the DMSI image, 150 random sample locations were generated using a geographic information system (GIS). The points were surveyed in the field from October 17 to 19 2005. A handheld GPS (Lowrance iFinder H²O) was used to navigate to each location. At each location, five vertical photographs and one oblique photograph were captured within a 1 m² quadrat. The vertical photographs were captured at a distance of four metres from the centre of the plot in each of the four cardinal compass directions. This distance was chosen to account for location uncertainty from the GPS and the rectification of the DMSI image. A hand-held compass was used in conjunction with measured pacing to determine the distances and bearings.

From the 150 random points sampled in the field, 115 were Paterson's curse, 11 pasture, 4 crop and 7 fallow. The remaining 13 samples occurred in areas of woodland and land cover types not relevant to the analysis (e.g. swamp, cleared areas). An additional 104 pasture and 111 crop random points were generated within the pasture and crop strata from a GIS to produce the same number of samples as the Paterson's curse class (Figure 5.2). A total of 345 random samples were produced, with the crop, Paterson's curse and pasture classes each comprised of 115 sample points. The fallow samples were subsequently not used for validation due to the small sample size and limited area coverage in the study area.

The percentage cover of Paterson's curse flowers for each quadrat was determined by an object classification approach described in Appendix C. Summary statistics of percentage cover are shown in Table 5.1, and the statistics for all Paterson's curse random samples are listed in Appendix F.

Table 5.1 Summary statistics of Paterson's curse random sampled locations on the Bindoon Agricultural College study site.

N	Minimum (%)	Maximum (%)	Mean (%)	SD (%)
115	< 0.1	7.14	1.28	1.70



Figure 5.2 Location of stratified random points at Catholic Agricultural College Bindoon that were surveyed in the field.

5.2.6.2 Quantitative accuracy assessment

The hard classifications were assessed using an error matrix approach, which included overall accuracy, user's and producer's accuracy for each class, an overall Kappa statistic and conditional (per-class) Kappa. Significant differences in the overall Kappa statistic within and between each classifier were assessed by

comparing z-scores. The classes were extracted from each hard classification image using a 5 x 5 pixel modal filter to address location uncertainty.

The images from the MLP and kNN soft classifications were assessed using binary logistic regression and receiver operating characteristic (ROC) analysis in the SPSS software package (SPSS Inc. 2007). Binary logistic regression was preferred over discriminant analysis, as logistic regression does not require the predictor variables to be normally distributed (Pohar, *et al.* 2004). The advantages of using binary logistic regression were the simplicity in the field validation data required (presence/absence) compared to density class data, and probability maps could be derived from the soft classification output (Aspinall 2002). Logistic regression fits a model of the relationship between the outcome (dependent or response variable) that is categorical (usually dichotomous) and a set of independent (predictor or explanatory) variables which are usually continuous (Pohar, *et al.* 2004). The predicted dependent variable represents a function of the probability that the subject will be present given the value of a predictor variable. The logistic regression model predicts the logit, which is the natural logarithm of the odds of the dichotomous dependent variable. The odds are calculated from the natural logarithm of the variables in the logistic regression equation, which is shown in Equation 5.1:

$$ODDS = e^{a+bX} \quad (5.1)$$

Where a is the constant, b is the slope of the logistic regression equation, and X is the predictor variable

The odds from Equation 5.1 were converted to predicted probabilities (\hat{Y}) using Equation 5.2:

$$\hat{Y} = \frac{ODDS}{1+ODDS} \quad (5.2)$$

The predictor variable was the output from the kNN and MLP soft classifications, and the output probability images were generated from Equations 5.1 and 5.2. The validation datasets were comprised of Paterson's curse records comprising the present (1) set, and crop and pasture comprising the absent (0) set.

A Pearson Chi square statistic was generated from the logistic regression model. The statistic tested the null hypothesis that the independent variable (the output from the soft classification) was not linearly related to the log-odds of the dependent variable (presence/absence of Paterson's curse) (Aspinall 2002).

ROC area-under-curve (AUC) statistics (see Section 2.6.4) were generated from the SPSS software package. Predicted probabilities (Equation 5.2) were applied from the binary logistic regression to the soft outputs of the MLP and kNN classifications. False positive and true positive fractions from progressive 1% thresholds of the predicted probabilities were produced from ROC contingency tables (Table 2.4). The resulting values were plotted on a curve, and an overall ROC statistic (AUC) was calculated using the trapezoidal rule (Equation 2.9).

A qualitative accuracy assessment was conducted to complement the quantitative accuracy assessment of the hard and soft classifiers. Qualitative accuracy assessment has been demonstrated to have an important role in accuracy assessment, as information on the success of a classifier can be obtained from qualitative assessment that may not be obtained through a statistically rigorous quantitative method (Mundt, *et al.* 2005). The assessment was performed by examining the classified images and using field knowledge to ascertain the success of the classifier in regions of the image where such information was available.

5.3 Results

5.3.1 Training area analysis

The statistics for each class, including number of pixels, mean, and standard deviation for each band are listed in Table 5.2. The spectra for the final four classes are shown in Figure 5.3. There was a minimal difference between the means of all classes for band 1 except the fallow class. Pasture and Paterson's curse had very similar means for band 4, with crop having the highest digital number (DN), but there was still overlap at 1 standard deviation (SD). The pasture training area had the highest mean DN in band 2 (green), with fallow and Paterson's curse having a similar mean DN. The means of Paterson's curse, pasture, and crop in band 3 (red) were separable.

Table 5.2 Training area statistics for each band (B), including number of pixels (N) with mean and standard deviation (SD). Key: C = crop, P = pasture, F = fallow, PC = Paterson's curse.

Class	N	Mean (B1)	SD (B1)	Mean (B2)	SD (B2)	Mean (B3)	SD (B3)	Mean (B4)	SD (B4)
C	843	702.58	26.71	1198.06	86.23	431.77	49.55	1667.04	111.19
P	1093	775.30	49.12	1486.45	135.08	681.48	101.95	1549.04	70.93
F	377	907.28	42.10	1298.74	114.45	862.67	111.99	923.26	87.29
PC	956	739.32	32.20	1272.82	117.50	549.59	76.83	1539.91	239.43

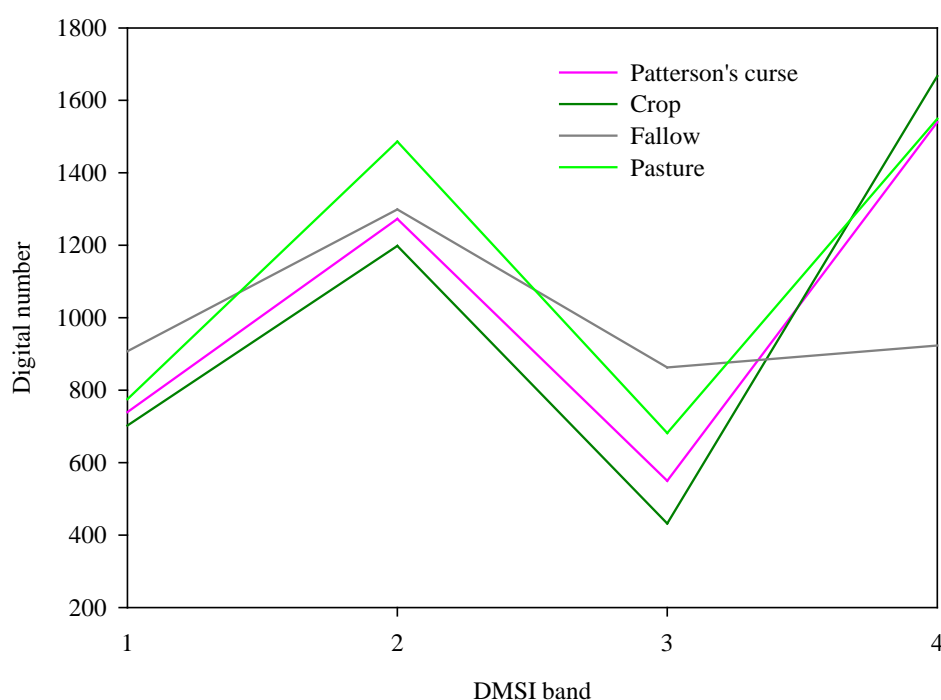


Figure 5.3 Mean DN spectral plot values for final DMSI training signatures.

The results of the transformed divergence measures between Paterson's curse, crop and pasture, and the best band combinations are shown in Table 5.3. The Paterson's curse class had poor separability from crop and pasture (1522 and 1687) in all four bands. The separability improved to fair with band two removed (1764 and 1853), and improved to good with pasture with bands 3 and 4 (1954). Separability remained fair (1732) with crop for these two bands. The separability between crop and Paterson's curse was good (1909) with band 3 and fair (1872) with bands 3 and 4.

Table 5.3 Transformed divergence results for the final classes.

1-4			
	P	C	PC
P		1940	1687
C			1522
PC			

1,3,4			
	P	C	PC
P		2000	1853
C			1764
PC			

3,4			
	P	C	PC
P		2000	1954
C			1732
PC			

3			
	P	C	PC
P		2000	1872
C			1909
PC			

5.3.2 Accuracy assessment

5.3.2.1 Hard classification results

The results of the accuracy assessment for the MLP and kNN classifications are summarised below in Tables 5.4 and 5.5. The results for each classifier are described in detail below. The error matrices for all classifications are in Appendix G.

5.3.2.1.1 Multi-layer perceptron

The overall accuracy, commission and omission error for the 3-class MLP classification are shown in the first row of Table 5.4. Paterson's curse had the highest commission and omission error (0.52 and 0.67) of the three classes. The dominant source of commission error for Paterson's curse was pasture, with 27 of 79 records misclassified, and crop to a lesser extent with 14 of the 79 records misclassified. The errors of omission for Paterson's curse were due to 33 (29%) and 44 (38%) of the 115 records being misclassified by crop and pasture respectively. In the case of pasture, the number of misclassified records was greater than the number of correctly classified Paterson's curse records. The overall Kappa statistic (0.35) and the Kappa per class (user's and producer's) for Paterson's curse were between 0.13 and 0.22, which classified them as poor according to the Monserud and Leemans (1992) Kappa threshold. All of the Kappa statistics were statistically significant at the 5% ($z > 1.96$) level. Across all three classes (crop, pasture and Paterson's curse), the Kappa per-class for user's and producer's were below 0.50.

The hard image for the 3-class MLP classification is shown in Figure 5.4. Crop was correctly classified in the large paddock at 'A', but incorrectly mapped (commission error) in some areas of pasture (e.g. at B and C). There was an occurrence of commission error when crop was misclassified in a paddock known to contain Paterson's curse (D). Another occurrence of commission error occurred where crop was classified in a small area of Paterson's curse surrounding a dam at 'E'. Most of the areas of pasture in the west and south-west of the image were correctly classified as pasture (F). An area of pasture in the field between a road and a tree line (G) was incorrectly classified as Paterson's curse (Figure 5.5). Paterson's curse was mapped correctly at 'H' and some parts of the southern area of the field at 'C', but was incorrectly mapped in a semi-circular crop area at 'I'. A large field containing crop in the east of the image had some areas incorrectly classified as Paterson's curse (J).

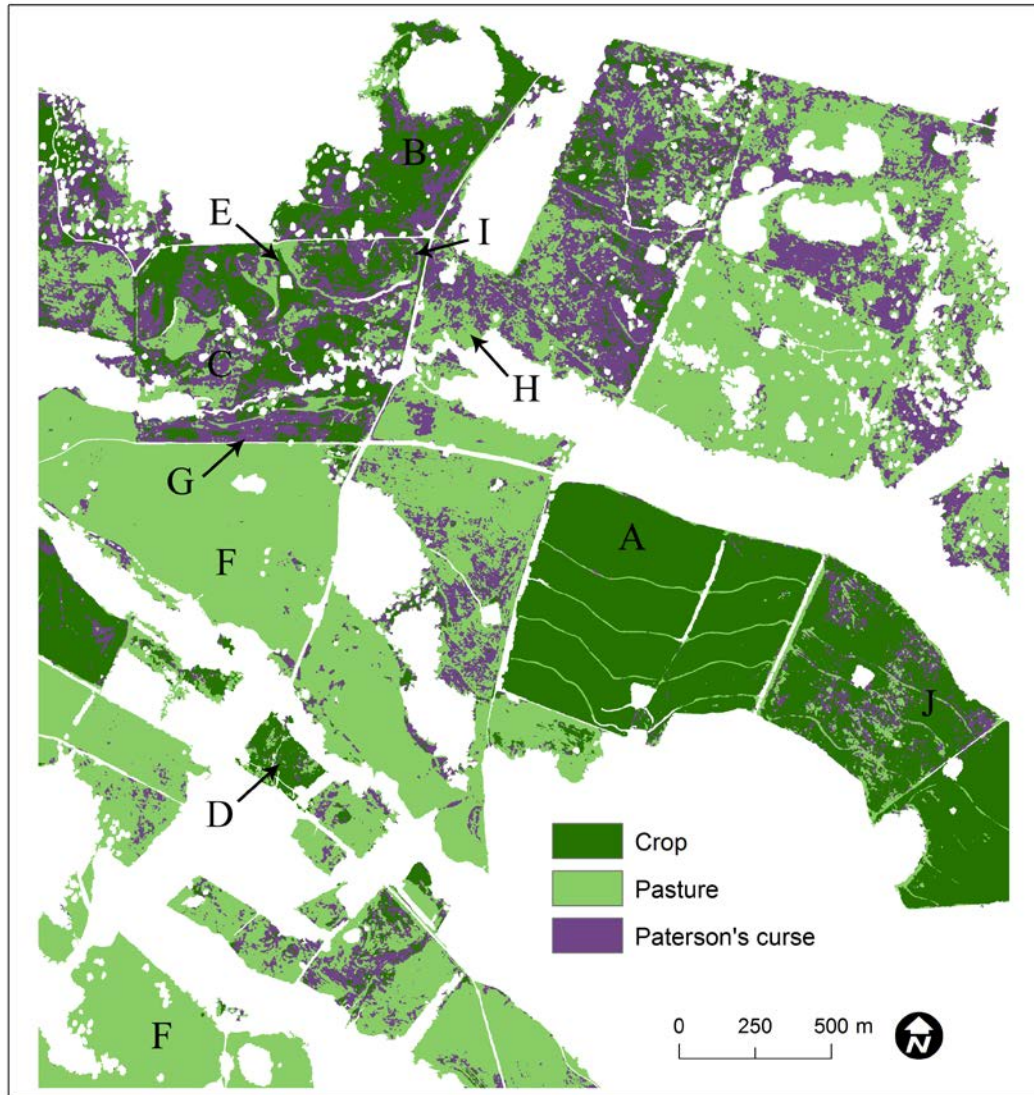


Figure 5.4 Hard classification output for the 3-class MLP classification.



Figure 5.5 Oblique photograph of an area of pasture in a field (background) that was misclassified by the 3-class MLP classification (labelled as 'G' in Figure 5.4) as crop and Paterson's curse.

The overall accuracy, user's accuracy and producer's accuracy for the 2-class MLP classification are shown in the second row of Table 5.4. There was a small increase in the overall accuracy (62%) compared to the 3-class classification (56%). Paterson's curse had a higher producer's and user's accuracy (73 and 42%) compared to the 3-band classification (48 and 33% respectively). The overall Kappa statistic of 0.26 was statistically significant at the five percent ($z > 1.96$) level, but was not statistically different to the 3-class classification (0.35). The per-class Kappa (user's) at 0.46 was statistically different ($z > 1.96$) to the 0.22 of the 3-class classification, but the 0.20 per class Kappa (producer's) was not statistically different to the Kappa of 0.13 for the 3-class classification.

Table 5.4 Summary of accuracy assessment of the MLP classification.

Type	Set	Overall Accuracy (%)	Producer's Accuracy (%)	User's Accuracy (%)	Overall Kappa	User's Kappa	Producer's Kappa
MLP	3-class	56	48	33	0.35	0.22	0.13
MLP	2-class	62	73	42	0.26	0.46	0.20

The hard image for the 2-class MLP classification is shown as Figure 5.6. Previous commission error from crop in the 3-class classification was eliminated in the 2-class classification, particularly in the northern section of the field labelled as 'A', where there was a mixture of Paterson's curse and pasture. Paterson's curse was present in the area around the dam at 'B', whereas in the 3-class image, this area was misclassified as crop. The area of pasture in the field between the road and tree line (C) was misclassified as Paterson's curse, and 'filled in' the areas previously misclassified as crop in the 3-class classification. Paterson's curse was correctly classified in the 'horse paddock' (D) that was misclassified as crop in the 3-class classification (also labelled as 'D' in Figure 5.4).

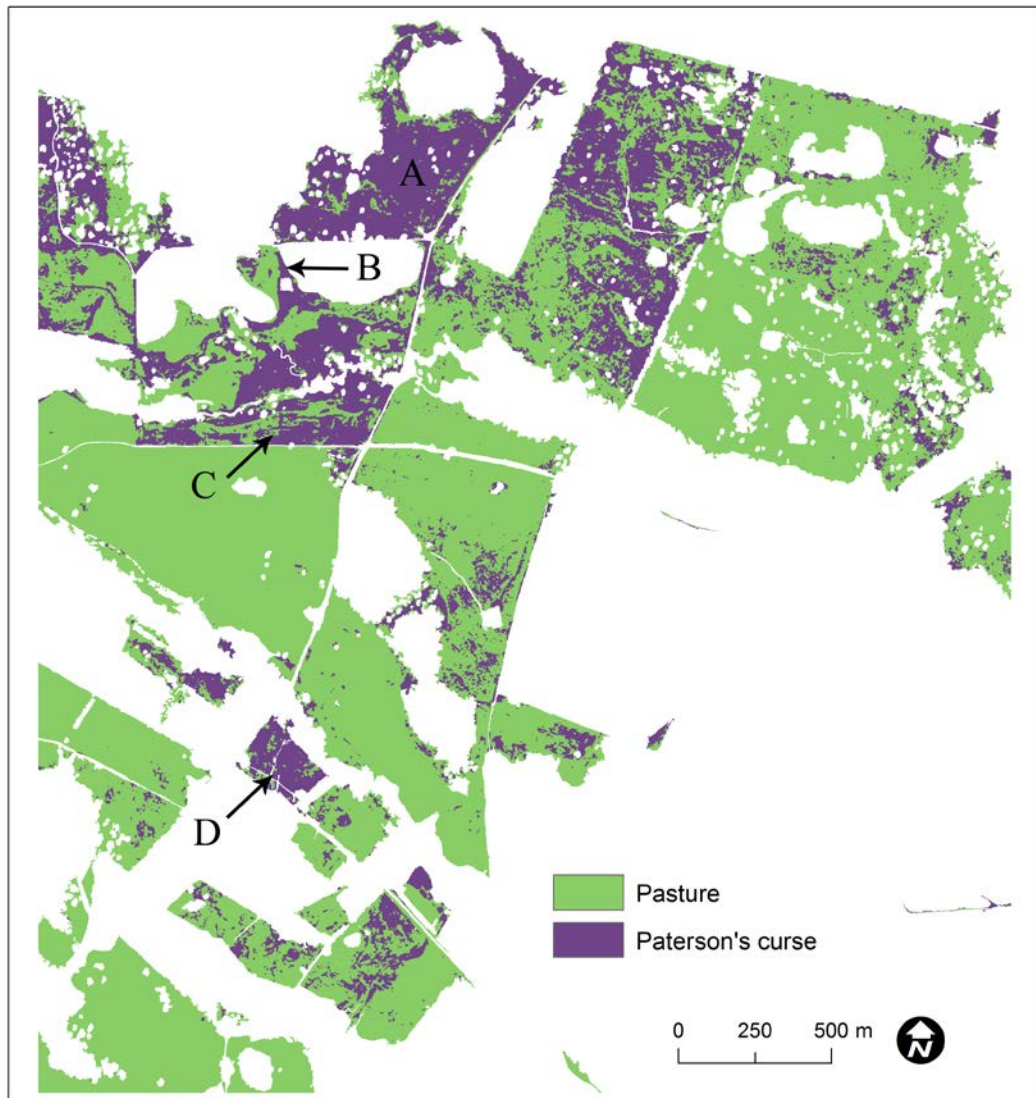


Figure 5.6 Hard classification output from the 2-class MLP classification.

5.3.2.1.2 k-nearest neighbour

The overall accuracy, user's accuracy and producer's accuracy for all classes are summarised in rows 1 to 3 of Table 5.5. The overall accuracy across the full range of band sets and k-neighbours was low, and ranged from 55 to 57%. The best overall accuracy of 57% was shared between 4 classifications (4-band, $k = 5$; 2-band, $k = 5$, 35 and 45). The producer's accuracy for Paterson's curse ranged from 40% (4-band, $k = 25$) to 44% (2-band, $k = 45$), and the user's accuracy ranged from 23% (3-band, $k = 15$) to 49% (3-band, $k = 5$).

The overall Kappa statistics were all significant at the five percent ($z > 1.96$) level. The two- and four-band classifications had the highest overall Kappa statistic (0.348)

at a k-value of 5; however the three-band classification had the most consistently low Kappa statistic across the range of k-values. The Kappa per-class (user's) for Paterson's curse was between 0.10 and 0.16, with a small amount of variation across the range of k-values. The 2-band classification at a k-value of 45 produced the highest per-class Kappa (user's) statistic (0.157). The per-class Kappa (producer's) were between 0.10 and 0.17, and the highest Kappa statistic was the 3-band classification at a k-value of 5, although there was no statistical difference between the 2 and 3-band classifications across the range of k-values. The four-band classifications had the lowest Kappa statistics (overall and per-class), with the k-values of 15 through to 55 being statistically non-significant.

The overall accuracy, user's accuracy, producer's accuracy, overall Kappa and Kappa per-class (user's and producer's) are summarised in rows 4-6 of Table 5.4. The overall accuracy ranged from 62% (4 bands, k = 15) to 66% (2 bands, k = 45). The producer's accuracy for Paterson's curse ranged from 60% (3 bands, k = 35) to 63% (2 bands, k = 45), and the user's accuracy ranged from 61% (4 bands, k = 15, 35, and 45) to 73% (3 bands, k = 5). The overall Kappa statistics were consistently lower than the three-class kNN classifications (all with Kappa of < 0.30), and Kappa increased with the number of k-neighbours in contrast to the 3-band classification. The highest overall Kappa statistic (0.315) was the two-band classification at 45 k-neighbours. The per-class Kappa (user's) results were all higher than the 3-class classifications, and ranged from 0.21 to 0.27, with a gradual trend of increasing Kappa with the number of k-neighbours. The 4-band classification at 65 k-neighbours and the 2-band classification at 45 k-neighbours both had the highest Kappa statistic (0.27). The per-class Kappa (producer's) results were consistently higher than the 3-class classifications (0.10 – 0.17).

Table 5.5 Summary of accuracy assessment of the k-nearest neighbour (kNN) classification. Key: C = class, B = bands.

Type	Set	Overall Acc. (%)	Prod's Acc. (%)	User's Acc. (%)	Overall Kappa	User's Kappa	Producer's Kappa
kNN	3C/4B	56–57	40–42	37–44	0.34-0.35	0.10-0.13	0.10-0.14
kNN	3C/3B	55–56	41–42	23–49	0.33-0.34	0.12-0.14	0.15-0.17
kNN	3C/2B	55–57	41–44	42–46	0.33-0.35	0.12-0.16	0.12-0.16
kNN	2C/4B	62–64	61–63	61–67	0.24-0.27	0.23-0.27	0.23-0.27
kNN	2C/3B	63–65	61–62	72–73	0.27-0.30	0.21-0.25	0.29-0.34
kNN	2C/2B	63–66	61–63	69–71	0.27-0.32	0.22-0.27	0.27-0.31

The hard classification map for the best (Kappa) performing kNN combination (2-class, 3-bands, $k = 45$) is shown in Figure 5.7. A larger number of pixels were classified as Paterson's curse, compared with the MLP 2-class classifier in Figure 5.6, which represents higher commission error for Paterson's curse. For example the field at 'A' was almost completely classified as Paterson's curse, even though the area contained a mixture of pasture and Paterson's curse. The area between the road and tree-line at 'C' was almost completely misclassified as Paterson's curse, however the small paddock at 'D' was classified correctly as Paterson's curse.

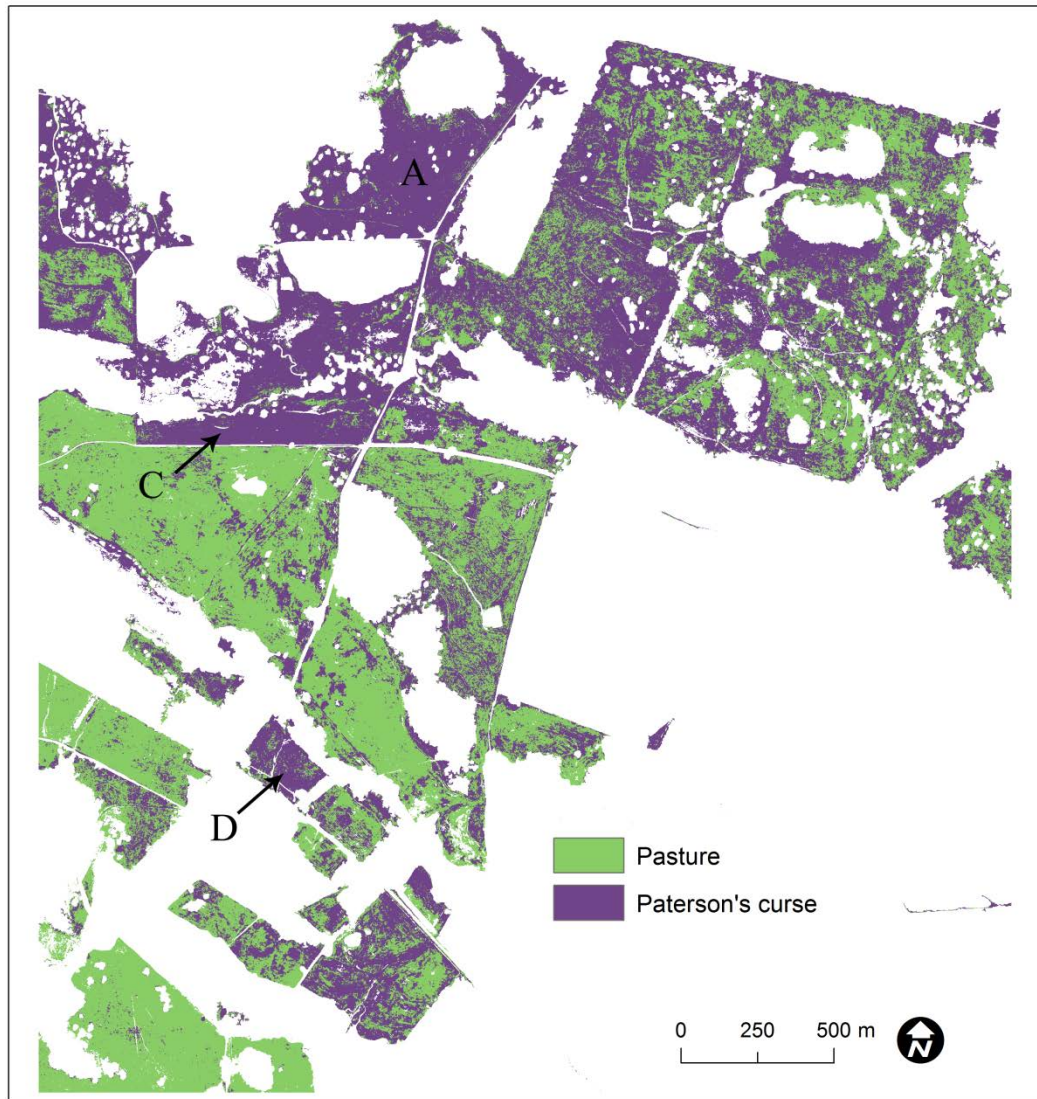


Figure 5.7 Hard classification output from 2-class, 3-band classification ($k = 45$).

5.3.2.2 Soft classification results

5.3.2.2.1 Multi-layer perceptron

The logistic regression and ROC analysis results for the two MLP classifications are shown in Table 5.6. Set B had a Chi-square statistic result that was significant at > 0.01 , whereas the Set A Chi-square result (4.998) was significant at 0.025. The AUC statistic of Set B (0.656) was higher than set A (0.579) and significant at > 0.001 . The probability map (denoting presence of Paterson's curse) from the Set B soft-classification is shown as Figure 5.8. The areas where there was 0.75–1 probability mostly occurred over a small proportion of the study area and tended to be in locations where there were low levels of co-occurring pasture vegetation. For

example an area around the dam labelled in Figure 5.8 as ‘A’ (shown in Figure 5.9) was correctly classified as Paterson’s curse by the 2-class MLP classification (Figure 5.6, label ‘B’). Another example was the ‘horse paddock’ (B) that was also correctly classified in the 2-class MLP classification (Figure 5.6, label ‘D’).

Table 5.6 Logistic regression and ROC (AUC) results for MLP classifications.

Set	Chi-Square	Sig.	AUC	SE	Lower Bound	Upper Bound	Sig.
A	4.998	0.025	0.579	0.031	0.519	0.640	0.017
B	19.036	0.01	0.656	0.036	0.585	0.727	0.000

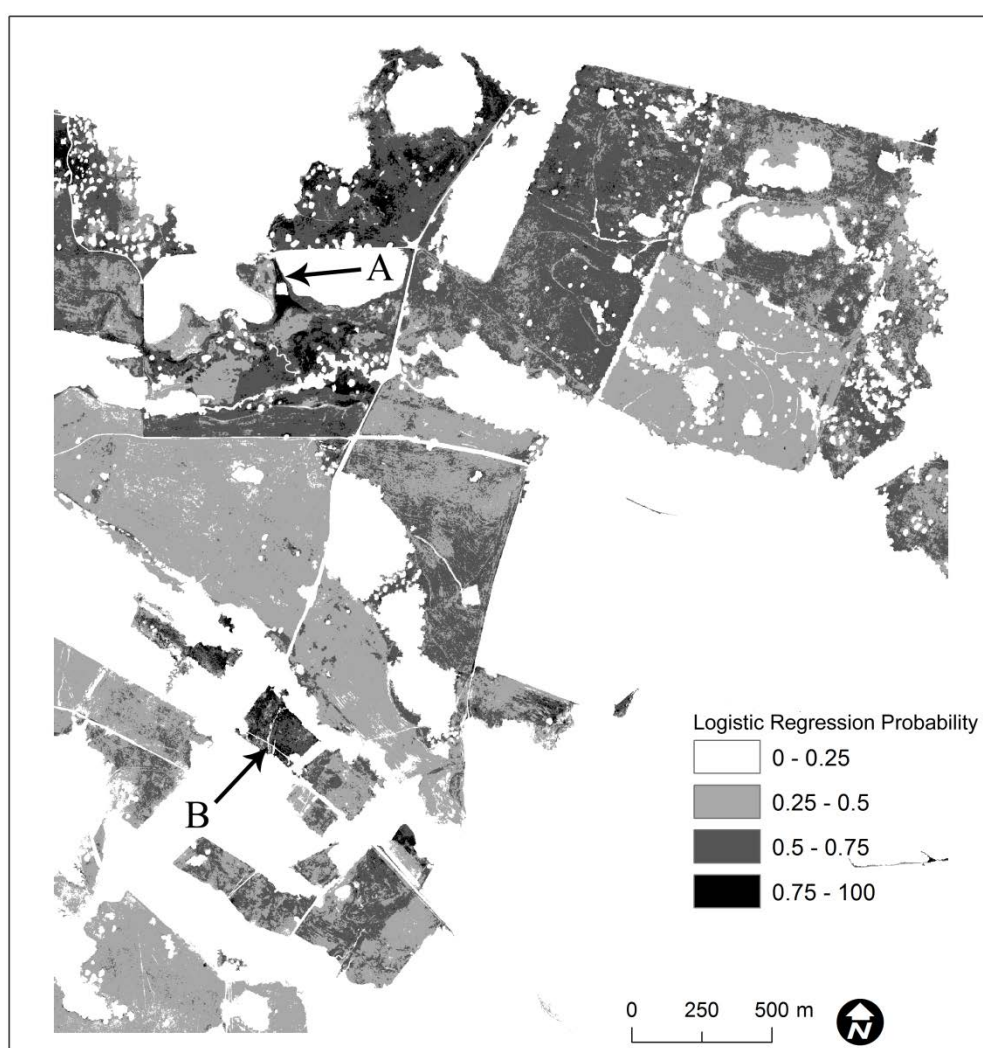


Figure 5.8 Logistic regression model output (probability of presence) of Paterson’s curse from the two-class MLP classification.



Figure 5.9 Oblique photograph of Area 'A' on Figure 5.8 showing the Paterson's curse infestation south of the dam that was identified with a probability of 0.75–1.

5.3.2.2.2 k-nearest neighbour

The logistic regression and ROC analysis results for sets A and B are shown in Appendix H. For Set A, the AUC statistic ranged from a high of 0.615 (3-band, $k = 35$) to a low of 0.513 (3-band, $k = 5$). The highest AUC statistic of 0.615 (significant at 0.001) had a Chi-square statistic of 9.374 (significant at 0.01). For Set B, the AUC statistic ranged from a high of 0.677 (shared between 4-band, $k = 5$; and 3-band, $k = 25$), to a low of 0.585 (3-band, $k = 5$).

The probability map (presence of Paterson's curse) for the Set B classification (4 bands, $k = 5$) is shown in Figure 5.10. There were no areas on the classified image that had a probability of Paterson's curse greater than 0.75, in contrast to the MLP probability image in Figure 5.8. The majority of the 0.5–0.75 probability range occurred in the north-west of the classified image, which had known infestations of Paterson's curse based on field knowledge. The range produced a salt and pepper pattern across the rest of the image.



Figure 5.10 Logistic regression model output (probability of presence) of Paterson's curse from two-class kNN classification (4-band, $k = 5$).

5.4 Discussion and Conclusion

The classification of DSMI imagery presented in this chapter used quantitative measures of accuracy, such as error matrices (Story and Congalton 1986) and the Kappa statistic (Congalton, *et al.* 1983), which had not been used in previous studies where image classification techniques had been used to map Paterson's curse (Bulman 2004; Ullah, *et al.* 1989b). The accuracy assessment result from the MLP and kNN classifications shows that Paterson's curse can be detected with high spatial resolution multispectral airborne imagery, but with low accuracy and a low Kappa statistic. The overall accuracy of the MLP and kNN classifiers was low ($< 66\%$), and in particular the omission and commission error of Paterson's curse was high. The

overall Kappa statistics of < 0.35 , and the corresponding per-class Kappa statistics for Paterson's curse were generally in the poor category (0.2 – 0.4) of Monserud and Leemans (1992) classification. The level of accuracy is not enough to satisfy the general standard of 85% for a thematic map output derived from remote sensing (Foody 2008).

The user's accuracy (23–73%) and producer's accuracy (40–73%) of Paterson's curse for the kNN and MLP classifications was similar to other remote sensing studies that have used high spatial resolution multispectral airborne imagery to map weeds in grassland and pasture (Carson, *et al.* 1995; Casady, *et al.* 2005; Lass and Callihan 1997). A higher user's accuracy (low omission error) is more desirable from a weed management perspective, as it minimises the likelihood that infestations are missed on the ground (Andrew and Ustin 2008; Mitchell and Glenn 2009). Omission error was reduced for both the MLP and kNN classifications by excluding crop; however there was no approach to similarly mask pasture, as it co-occurred with Paterson's curse across the property. Similarly there was no approach that could reduce commission error.

The limitations of the MLP and kNN classifiers and the resulting low accuracy of the detection of Paterson's curse with DMSI are attributable to the spectral resolution of the sensor (and the derived training signatures) and the environment. Artificial neural network classifiers have been shown to be generally more accurate than other classifiers (Kavzoglu and Mather 2003) but were dependent on choice of network architecture and training data that adequately represented the cover types of interest (Atkinson and Tatnall 1997). The network architecture used for the MLP was set by the number of input and output classes (training and mapped) classes; the training signatures for the classes were representative of the major cover types, but the high variance for the training classes most likely resulted in misclassification when applied to the entire image. The kNN classifier has been shown to be effective for forest inventory mapping in the northern hemisphere (e.g. Haapanen, *et al.* 2004), based on an assumption that forest types are similar across an image and differences in the radiometric properties of a particular type are due to differences in physical properties, e.g. stand volume (Franco-Lopez, *et al.* 2001). The majority of forest inventory applications of kNN used medium spatial resolution imagery (e.g. Landsat

5 and 7), which contributed to lower spectral variability within classes and across an image, compared to high spatial resolution imagery such as DMSI.

A minimum detection threshold is a desirable outcome for detecting weeds like Paterson's curse with remote sensing (Bulman 2004). However, the approach used in this chapter precluded the use of multiple density classes of Paterson's curse for training and validation, and subsequently a detection threshold could not be determined. Several studies using high spatial resolution data have used multiple density classes (Lass and Callihan 1997; Lass, *et al.* 1996) but percentage green cover was used rather than flower density, even where the flowers were the dominant spectral discrimination cue. The pasture species from those studies—yellow hawkweed (Lass and Callihan 1997) and yellow starthistle (Lass, *et al.* 1996) had a patchy distribution and tended to dominate an area with green cover, which were more amenable to multiple density classes. In contrast, Paterson's curse occurred in the study area as a fuzzy continuum of floral density, with few areas of high flowering density and was mixed with pasture (especially at lower densities).

The output probability maps produced by soft classification were a useful complement to the hard classifiers. A probability output allows a classification to be assessed on a location (pixel-by-pixel) basis, in contrast to a hard classification output where only the class or overall measure of accuracy is provided (Foody, *et al.* 1992). Combining the soft and hard classification outputs has potential utility for weed management, as it provides an option for end-users to interpret the hard classification based on the probability of a mapped infestation at a particular location being at that location when visited in the field. The main limitation of soft classifiers is that their accuracy is equivalent to their corresponding hard classification. This was demonstrated in the results of this chapter, where the best performing kNN and MLP soft classifications for Paterson's curse had AUC statistics of 0.677 and 0.656, but the corresponding per-class Kappa statistic for Paterson's curse were less than 0.32 for the kNN and in the range of 0.2 to 0.46 for the MLP. The overall and user accuracies of Paterson's curse need to be higher (i.e. > 70%) in order to produce equivalent soft classification output maps that would represent higher probabilities of

infestations across a study site and most importantly, include lower density infestations.

The results from this chapter indicate that spectral resolution may be more important than spatial resolution in order to accurately map Paterson's curse. This was demonstrated by the spectral confusion between Paterson's curse and pasture from the 1 m multispectral DMSI data, which was a similar result to previous studies (Bulman 2004; Ullah, *et al.* 1989b) that used medium spatial resolution multispectral imagery. The spectral contribution of the purple flowers of Paterson's curse within a DMSI pixel would have been less than that of green vegetative material, and is likely to produce a similar response within a larger pixel. This situation is similar for other weed species growing in agricultural settings, due to a limited spectral contrast of the species with green pasture (e.g. Carson, *et al.* 1995; Lass, *et al.* 1996). In contrast, high spatial resolution airborne multi-spectral applications have been successful for woody weed species because the pixel size was smaller than the vegetation canopy (e.g. Everitt and Yang 2007b; Robinson, *et al.* 2008). Another factor that benefited the delectability of the weed species in those applications was a non-weed background that produced a strong spectral contrast, e.g. green foliage against water or soil, or lighter or senescent vegetation.

6 DISCRIMINATING PATERSON'S CURSE WITH SATELLITE HYPERSPECTRAL IMAGERY

6.1 Introduction

Hyperspectral remote sensing from aerial and satellite platforms has contributed to knowledge on the ecology of weeds since the 1980s and has been a proven approach for mapping and modelling various species (He, *et al.* 2011). Airborne platforms in particular have been used to detect weeds at low densities (Glenn, *et al.* 2005; Lass, *et al.* 2002) and improve the mapping accuracy compared to multispectral sensors (Dehaan, *et al.* 2007; Mundt, *et al.* 2005). Despite this success, there are continuing issues with accurately geo-referencing imagery and matching field data (Aspinall, *et al.* 2002), which can affect the ability to quantitatively determine accuracy (Lawrence, *et al.* 2006; Mundt, *et al.* 2005). A major limitation of airborne hyperspectral remote sensing is the high expensive if weeds are to be mapped over a large area (He, *et al.* 2011).

Medium spatial resolution imagery is important for regional scale operational remote sensing, (Lawes and Wallace 2008; Rejmánek 2000), especially if the application of the technology is to be cost effective to management. Multispectral medium resolution sensors have been generally unsuccessful in detecting and mapping weeds (He, *et al.* 2011) except when they have distinctive characteristics for detection, are present in high densities, or cover large areas (Cuneo, *et al.* 2009; Lawes and Wallace 2008; Peterson 2005; Wilfong, *et al.* 2009). Multi-spectral remotely sensed imagery with medium spatial resolution (Landsat 5 and 7) have been shown in previous studies to lack the spectral resolution required to discriminate Paterson's curse from co-occurring vegetation (Bulman 2004; Ullah, *et al.* 1989b).

In Chapter 5, Paterson's curse was mapped at a low to medium accuracy from high spatial resolution multispectral imagery. The accuracy results demonstrated that high spatial resolution imagery may also be limited by spectral resolution, especially if there is a lack of spectral contrast between the weed species and co-occurring vegetation—as was the case with Paterson's curse and pasture. In Chapter 4, the field spectroscopy analysis showed that narrow discrete bands from a hyperspectral sensor could detect reflectance difference peaks between Paterson's curse and co-occurring

vegetation, and there was a good relationship between linear spectral unmixing, band ratios, indices and floral percentage cover. The results indicated that hyperspectral remote sensing could be a useful source of data for detecting and mapping Paterson's curse.

Satellite hyperspectral sensors represent the best of both worlds in spectral and spatial resolution: they can overcome the inherent spectral limitations of multi-spectral sensors and capture imagery over larger areas than airborne hyperspectral sensors. The Earth Observation 1 (EO-1) Hyperion sensor combines a hyperspectral resolution (196 unique bands) with the same 30 m spatial resolution as Landsat 8 (Jupp and Datt 2004). The large number of bands allows materials to be mapped with hyperspectral classification approaches such as mixture tuned matched filtering (MTMF) and linear spectral unmixing (LSU). The narrow spectral bandwidth of Hyperion is an advantage over multi-spectral sensors (e.g. DMSI), as the bands can be more closely matched with field spectroscopy data. Hyperion data are not used widely (operationally) because of processing and noise issues, but have been used in a number of studies to successfully map vegetation (e.g. Apan, *et al.* 2004; Datt, *et al.* 2003; Pu, *et al.* 2003) and weeds (Pengra, *et al.* 2007; Ramsey III and Nelson 2005; Ramsey III, *et al.* 2005b; Ramsey III, *et al.* 2005c). Given that Hyperion is currently the only operational hyperspectral satellite sensor, it provides an opportunity to foreshadow the performance of planned satellite hyperspectral sensors for mapping Paterson's curse.

The aim of this chapter is to investigate the utility of EO-1 Hyperion imagery to detect and map Paterson's curse. Two approaches are used: 1) a matched filter classification using image derived end-members; and 2) logistic regression, to determine the relationship between Paterson's curse and band ratios and indices from Chapter 4.

6.2 Methods

A Level 1R EO-1 Hyperion image was acquired on November 2 2006. A full description of the EO-1 Hyperion sensor and previous applications, as well as the acquisition process for the November 2 image and its properties is provided in Section 3.4.2.

The analysis of the Hyperion data was comprised of two main components 1) processing; and 2) classification and validation. The two components, and the major steps associated with each are shown as a flowchart in Figure 6.1.

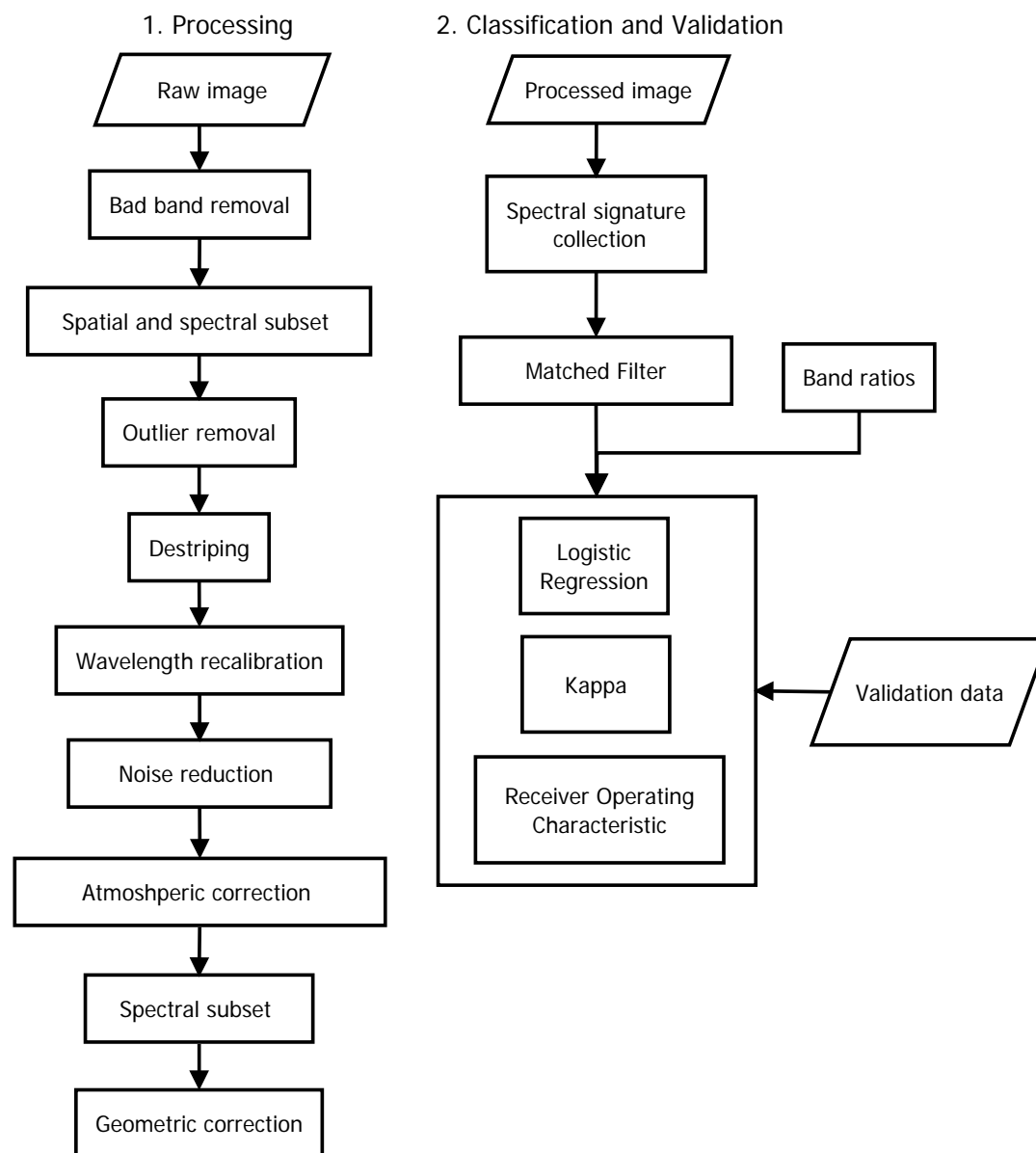


Figure 6.1 Flowchart of methodology for 1) processing and 2) classifying and validating Hyperion data.

6.2.1 Processing

Processing hyperspectral data is more specialised compared than multi-spectral, and the rigor of the processing can have a strong influence on the overall accuracy of a classification (Aspinall, *et al.* 2002). The large number of bands in hyperspectral data

necessitates noise reduction protocols and compensating for atmospheric attenuation. Hyperion data in particular can involve additional processing, due to the low signal-to-noise ratio, and detectors that are prone to malfunction (Jupp and Datt 2004).

6.2.1.1 Specialised Hyperion pre-processing

Hyperion level 1R images are pre-processed before delivery to users, however a number of artefacts are still present that require further processing. The following section describes the workflow to correct these image artefacts. A set of tools developed by the CSIRO during the Hyperion 2002–2004 validation experiments (Jupp and Datt 2004) were used for the processing in the ENVI software (ITT Visual Information Solutions 2006c).

Hyperion data have 44 bands that are non-calibrated, leaving 198 bands out of the original 242 (Pearlman, *et al.* 2003). Hyperion images can also have ‘bad’ pixels (columns) with zero values due to malfunctioning detectors in an array. A description of the types of abnormal or bad pixels that may be found in Hyperion data is provided by Han, *et al.* (2002). The CSIRO "Apply Bad Pixel List" tool was applied to the raw radiance image to correct instances of bad pixels. Image bands were selected for a mask that had either non-calibrated detectors (zero values) or bands that were visually assessed and considered very noisy. Each band was also inspected for abnormal columns, which were caused by malfunctioning detectors. These columns typically had zero values throughout, or very high or low values consistently throughout the length of the column. Appendix J lists the bad/noisy bands, along with the bad columns for selected bands.

The image was spatially subset to exclude areas outside the general locality of the study sites. The first and last columns of the image were removed, as these columns in Hyperion Level 1R datasets have zero values due to the process of pixel shifting the visible/near (VNIR) and short-wave infrared (SWIR) detectors to align them. A further spatial subset was made, where an along-track subset of 600 lines was selected from rows 1347–2047, which encompassed the along-track spatial extent of the validation data. A spectral subset of 158 bands was selected (Table 6.1). The bands 121–128, 167–178, and 224 were removed, as they were identified by Jupp and Datt (2004) as being deep water absorption areas. The bands removed were not

located in the water vapour areas (820, 940 and 1135 nm) used by the Fast Line-of-sight Atmospheric Analysis of Spectral Hypercubes (FLAASH) atmospheric correction module (see Section 6.2.1.2).

Table 6.1 Centre wavelengths of the 158 band image produced by spectral sub-setting for the visible/near infrared (VNIR) and the short-wave infrared (SWIR).

Array	Band	Wavelength (nm)
VNIR	8–57	428–927
SWIR	81–119	938–1322
	131–164	1442–1774
	182–184	1957–1977
	187–218	2007–2321

Hyperion data can contain outlier pixels with anomalous values, which appear as spikes and unnatural peaks in the band statistics. Although not ‘bad’, the presence of such pixels can compromise the results of the de-stripping procedure. The CSIRO ‘Remote Outliers’ tool identified outliers from the median threshold test of Datt, *et al.* (2003) and replaced them by taking the mean value from the five neighbouring columns.

Image striping occurs in Hyperion images when pixels (columns) have a different mean and standard deviation (gain and offset) to neighbouring pixels in the image (Datt, *et al.* 2003). Stripes can also occur in blocks, e.g. across two or more adjacent columns of data. There are two common methods for dealing with stripes: replacing column pixel values with the mean of the two neighbouring pixels, or using the global and local de-stripping method of Datt, *et al.* (2003). While the former method is simple, it has the tendency to smooth or even remove potentially valuable features by the averaging process, and does not deal effectively with instances where blocks of pixels have different gain and offset to the rest of the image (Datt, *et al.* 2003). The latter method was preferred, as it can restore the value of a pixel to match the gain and offset of the neighbouring pixels without fundamentally changing the value of the pixel (Datt, *et al.* 2003). The local de-stripping was applied separately on the VNIR and SWIR bands. The VNIR window was 4 pixels wide (9 pixels in total) and the SWIR window was 20 pixels wide (41 pixels in total). The parameters were

similar to those used by Datt, *et al.* (2003) for an agricultural application, where a local filter size of 5 pixels was used for VNIR striping and windows of up to 41 pixels for block striping in the SWIR.

6.2.1.2 Standard hyperspectral processing

A Minimum Noise Fraction (MNF) transform was applied to the de-striped image, followed by an inverse MNF. The entire image was used to generate the noise statistics rather than a homogeneous spatial subset, as it was found to be more visibly effective in reducing noise, compared to a homogeneous spatial subset recommended by Green, *et al.* (1988) The first 20 bands were retained, as they contained the least noise, and retained most of the image information. The cut-off was chosen according to where the curve levelled out for both the eigenvalue and the percentage of variance.

The image was atmospherically corrected using the FLAASH add-in for ENVI. FLAASH uses a physics-based algorithm to correct for atmospheric influence such as molecular and particulate scattering and absorption from an original 'radiance at detector' image (Felde, *et al.* 2003). The surface reflectance is calculated for each pixel in each band by a MODTRAN4 calculation that utilises user provided information such as viewing and solar angle, mean surface elevation, atmospheric model type, aerosol type and atmospheric visibility (ITT Visual Information Solutions 2006b).

A potential source of error during atmospheric correction is wavelength calibration uncertainty, which is caused by small misalignments of optical elements in the detector array, which can result in a constant spectral shift in all bands and wavelength errors of up to several nanometres (Felde, *et al.* 2003). Prior to atmospheric correction, the wavelength recalibration option in FLAASH was utilised to correct for the potential error. The recalibration used Normalized Optical Depth Derivative (NODD) and MODTRAN4, which compares radiance spectra from areas of atmospheric absorption bands to simulated spectra with correct atmospheric column densities in the same bands, and produces new calibrated band wavelength centres that showed a minimum root mean square area shift (Felde, *et al.* 2003). The

new band wavelength centres were applied to the Hyperion image by updating the image header information.

The original level 1R image radiance units of $W/m^2 * \mu m * sr$ were converted to the units of $\mu W/cm^2 * nm * sr$ required by FLAASH by dividing the original pixel values for the VNIR and SWIR bands by scaling factors of 400 and 800 respectively. The parameters used for the atmospheric correction in FLAASH are listed in Appendix K. A mid-latitude summer atmospheric model was used, which was the recommended model for the 30° S latitude of the study area, and for the month of November (ITT Visual Information Solutions 2006b). A default visibility option of 100 km was used, as previous attempts at atmospheric correction using the water vapour and aerosol options resulted in an output image with many negative values, especially in vegetated regions. Following atmospheric correction, a second spectral subset was conducted, to produce a 49 band image. The central (calibrated) wavelengths for the image are shown in Table 6.2. Bands 8 and 9 were retained despite residual noise, as spectral differences between Paterson's curse and other materials were prominent in the blue region of the electromagnetic spectrum (Chapter 4).

Table 6.2 Band centre wavelengths and full width half maximum (FWHM) for the 49 band subset.

Band	Centre (nm)	FWHM (nm)	Band	Centre (nm)	FWHM (nm)	Band	Centre (nm)	FWHM (nm)
8	428.44	11.39	25	601.19	10.56	42	774.23	10.79
9	438.61	11.39	26	611.34	10.48	43	784.43	10.88
10	448.79	11.39	27	621.50	10.41	44	794.64	10.99
11	458.96	11.39	28	631.66	10.36	45	804.84	11.10
12	469.14	11.39	29	641.83	10.32	46	815.04	11.20
13	479.31	11.39	30	652.00	10.29	47	825.24	11.26
14	489.49	11.38	31	662.17	10.29	48	835.42	11.28
15	499.65	11.35	32	672.35	10.30	49	845.59	11.28
16	509.82	11.31	33	682.53	10.33	50	855.77	11.28
17	519.98	11.26	34	692.72	10.39	51	865.94	11.28
18	530.13	11.19	35	702.92	10.46	52	876.12	11.28
19	540.29	11.11	36	713.11	10.53	53	886.29	11.28
20	550.44	11.02	37	723.30	10.60	54	896.47	11.28
21	560.59	10.93	38	733.49	10.66	55	906.64	11.28
22	570.74	10.84	39	743.68	10.69	56	916.82	11.28
23	580.89	10.74	40	753.86	10.71			
24	591.04	10.65	41	764.04	10.73			

The image was rectified to a base image comprised of a level 1G (terrain corrected) Landsat 5 image, captured on December 6 2006. The Landsat 5 base image was used instead of a higher resolution (0.5 m) ortho-rectified image due to coincident timing of the capture of the two images, and features were easier to identify and use as ground control points on the Landsat image compared to the high-resolution image. A total of 25 ground-control points were selected from easily identified and stable features, and an even coverage across the image was obtained. The rectification was performed with a second order polynomial function, and nearest neighbour re-sampling to maintain as much spectral fidelity as possible, resulting in an overall root mean square (RMS) error of 9.15 m (approximately one-third of a pixel).

6.2.2 Classification

A top-down hyperspectral classification approach was used, in which image derived end-members were input into the classification, rather than end-members derived from field or laboratory spectra of the target (Aspinall, *et al.* 2002).

6.2.2.1 Spectral sampling

An end-member representing dense flowering Paterson's curse was derived directly from the image. A sample size of 3 x 3 pixels (90 m x 90 m, or 0.81 ha) was used, as it allowed a representative end-member to be obtained whilst minimising the influence of mixed pixels from neighbouring cover types. There were three locations in the study area where a nine pixel sample of dense Paterson's curse was possible: one on the Morden Downs property, and two on the Bindarie property. The final end-member spectrum was derived from the mean of the three spectra.

Spectral samples of three non-Paterson's curse vegetation types were extracted from the image: 1) Senescent vegetation, which represented the condition of most pastures in the region during the time of year the image was captured; 2) Eucalypt woodland, since large areas of the image and part of the study site properties contained that land cover; and 3) Green vegetation, which represented areas of crop, irrigated areas, and riparian vegetation which was still green and lush, and with high reflectance in the near infrared region of the spectrum. Spectral samples from the five Paterson's curse density classes from the field survey sites described in Section 6.2.3 were also collected.

6.2.2.2 Matched filter classification

On the basis of the literature review in Chapter 2, the matched filter and MTMF methods were preferred over linear spectral un-mixing (LSU) and spectral angle mapper (SAM). These methods have been demonstrated to be superior over LSU when a single end-member is mapped and the extent of the other end-members is not known (Boardman 1998). In addition MTMF has been used in past studies to detect weed infestations at low densities (e.g. Mundt, *et al.* 2005), which is advantageous for Paterson's curse. In many applications, a region of high matched filter/low infeasibility pixels has been manually selected from a two-dimensional feature space plot of the matched filter and infeasibility output (Glenn, *et al.* 2005; Mitchell and Glenn 2009). However this procedure is arbitrary and may not represent the limits of detection of the target feature (Aspinall 2002). On this basis, the dense Paterson's curse end-member spectrum described in Section 6.2.2.1 was input into a matched filter.

6.2.2.3 Analysis of band ratios and indices

Band ratios and indices were selected from the field spectrometry analysis (Chapter 4) and from a search of the literature. The Hyperion bands were assigned to the nearest equivalent bands from the ratios and indices derived from the spectroradiometer data.

6.2.3 Validation

6.2.3.1 Data collection

A stratified random sampling approach was used for validation purposes, where a Geographic Information System (GIS) was used to stratify the study area according to where Paterson's curse was present or absent, and random plots were generated within the two strata. The area where Paterson's curse was absent was determined from field knowledge obtained from earlier reconnaissance with a handheld GPS and digital camera, and consisted predominantly of pasture and cropped areas. A 45 m-wide buffer was created around the extent of the stratified regions in the GIS, to reduce the likelihood of plots containing mixed pixels from nearby Eucalypt woodland and cleared areas. A total of 85 random plots were generated for the Paterson's curse class and 100 plots for the non-Paterson's curse class. The dimensions of the field plots were 90 m x 90 m (3 x 3 pixels) to account for geo-registration error.

A field survey of the Paterson's curse plots was conducted on October 18, 2006, between the daylight hours of 08:00 and 17:00. The non-Paterson's curse plots were not surveyed in the field as Paterson's curse was known to be absent. A handheld GPS (Lowrance Ifinder H²O) was used to locate the coordinates of each plot in the field. At each plot, four oblique digital photos were captured, each orientated towards one of the four cardinal compass directions. The approximate infestation density of Paterson's curse was visually estimated post-survey for each plot based on the oblique photographs. A classification key was used to assign a ranking to each plot (Table 6.3). Appendix I contains a list of the attributes for each plot.

Table 6.3 Density classes and description of Paterson's curse assessed from random field plots.

Density Class	Description
0	Paterson's curse absent
1	Isolated plants
2	Small patches of Paterson's curse, or up to total 25% Paterson's curse
3	Approx. 50% of plot covered by Paterson's cure
4	Up to 75% of plot covered by Paterson's curse
5	Plot nearly 100% Paterson's curse

The locations of the field plots are shown in Figure 6.2. The number of plots represented for each Paterson's curse density class was 24 for class 1, 26 for class 2, 13 for class 3, 10 for class 4, and 11 for class 5. All but one of the 85 plots contained Paterson's curse. Examples of different density classes for the plots from field photographs are shown in Figure 6.3.

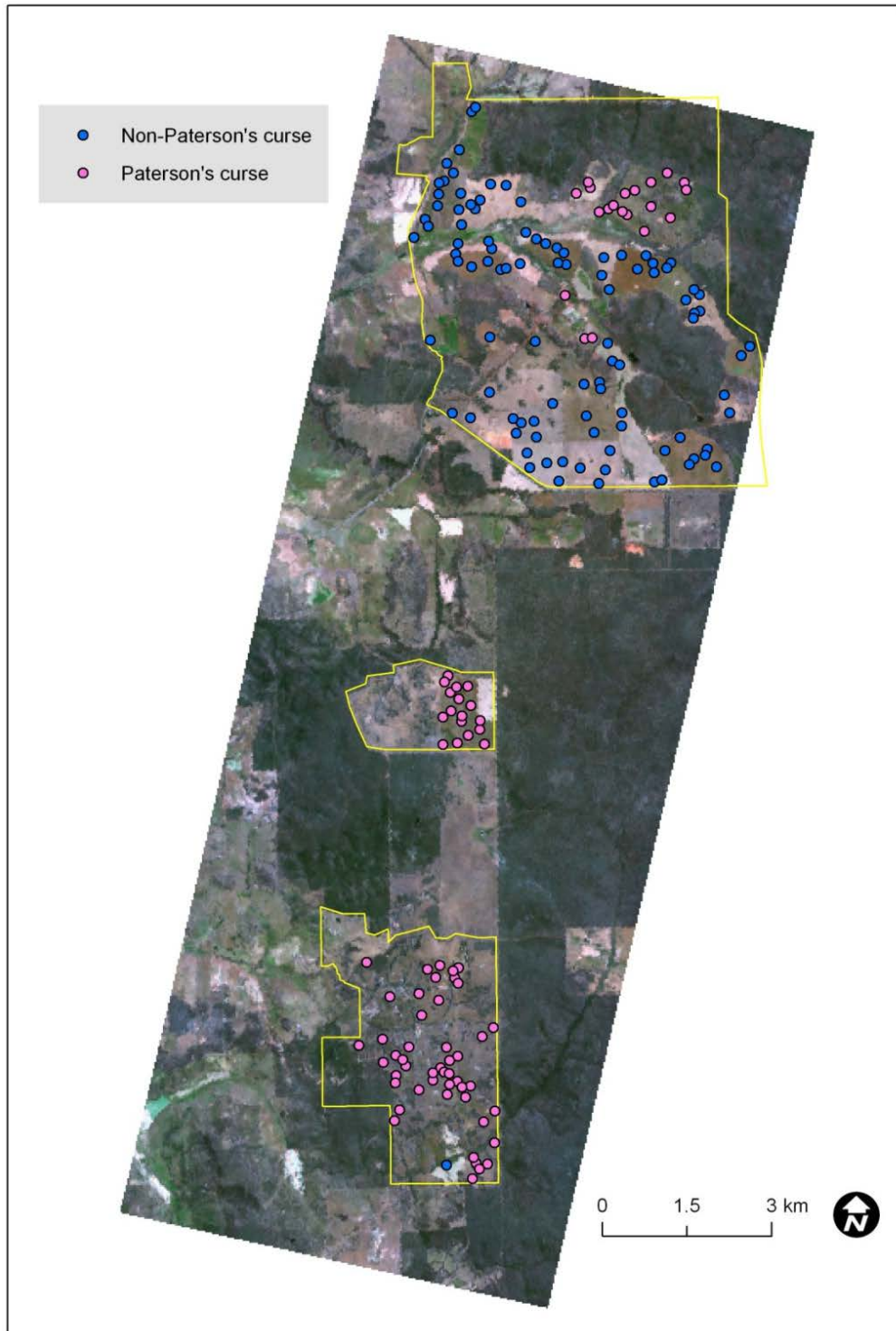


Figure 6.2 Location of sample sites for Paterson's curse, non-Paterson's curse. Bands 8 (428 nm), 20 (550 nm), and 30 (652 nm) are represented as blue, green, and red.

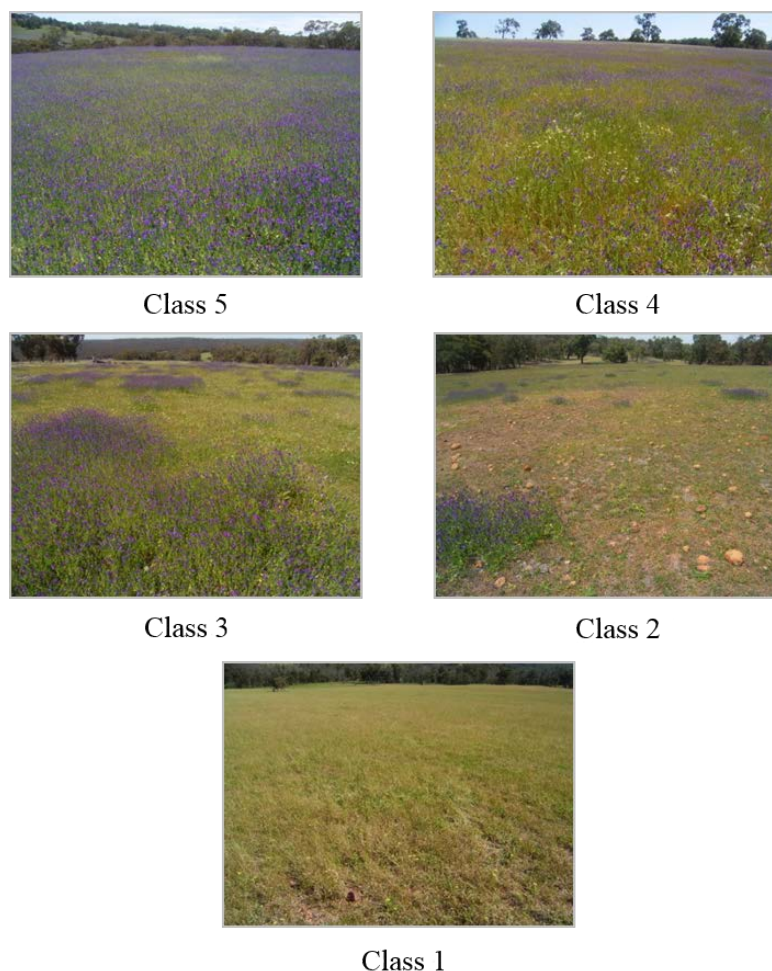


Figure 6.3 Examples of field plots representing the five density classes of Paterson's curse.

6.2.3.2 Quantitative accuracy assessment

The accuracy of the matched filter classification and band ratios/indices was assessed from the presence/absence field plots (Section 6.2.3.1), using both a threshold dependent and threshold independent approach. For the threshold dependent approach, a Kappa statistic was calculated for all possible thresholds of the matched filter scores from the field plots. The maximum Kappa statistic was used as a threshold value to convert the soft classification into a hard classification map (Liu, *et al.* 2005). For the threshold independent approach, logistic regression and receiver operating characteristic (ROC) statistics were generated from the SPSS (v.17) software package (SPSS Inc. 2007). For the former, a Chi-square statistic and predicted probabilities were generated. For the latter an area under curve (AUC) statistic (Equation 2.9) was calculated from the predicted probabilities of the logistic regression. The predicted probabilities were also used to produce a hard (binary)

image output based on the maximum efficiency method (Lippitt, et al. 2008): a threshold value was determined at the point where there was the greatest difference between the false positive rate and true positive rate across all possible threshold values of a validation dataset. This threshold value also corresponds to the closest point on the ROC curve to the top left-hand corner of the plot (Cantor, et al. 1999; Liu, et al. 2005).

6.3 Results

6.3.1 Processing

The de-stripping and minimum noise fraction resulted in an improvement to the aesthetic quality of the imagery, and a reduction in noise. In particular, noise and striping present in the VNIR bands was effectively removed, as shown in Figure 6.4. Striping effects were most apparent in bands 8 to 13 (428 nm–489 nm) from the blue region of the spectrum. Bands in the green, red and near infrared wavelengths were not visibly affected by striping.

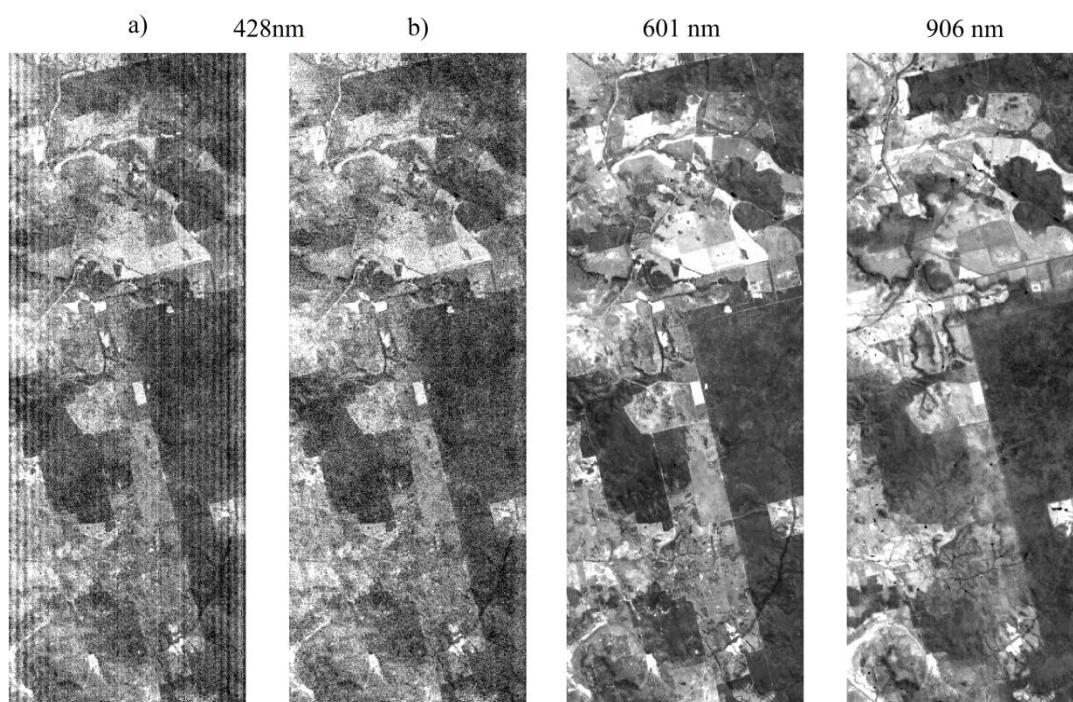


Figure 6.4 a) Before and b) after de-stripping and noise removal was applied to VNIR band 8 (428 nm). Bands 25 (601 nm) and 55 (906 nm) shown for comparison where no striping effect was apparent.

6.3.2 Classification

6.3.2.1 Spectral sampling

The locations of the sites from which Paterson's curse end-member spectra and the non-Paterson's curse spectral samples were derived are shown in Figure 6.5. Senescent vegetation was sampled from 6 sites (54 pixels), Eucalypt woodland from 10 sites (90 pixels), and green vegetation from 6 sites (54 pixels). The Eucalypt woodland class was spectrally heterogeneous across the image compared with the other two classes, and four additional sites were sampled to incorporate the variability.



Figure 6.5 Location of Paterson's curse non-Paterson's curse spectral samples.

The three spectral samples and the mean spectrum for dense Paterson's curse mean spectrum are shown in Figure 6.6. The general trend with all the spectra was a noise affected decrease in reflectance from 424 nm to 448 nm, then gradual increase through the rest of blue, and into the green and red. The spectra had similar reflectance in the blue, and became more separable in the green and beyond. The red-edge was located at approximately 662 nm (band 31), and the reflectance increased sharply into the near infrared until 733 nm (band 38). There was a gradual increase in reflectance from 733 nm until 815 nm (band 46). Spectrum 2 had a greater reflectance in the near infrared, compared to the other plots. Spectrum 3 had a similar reflectance trend to the mean plot.

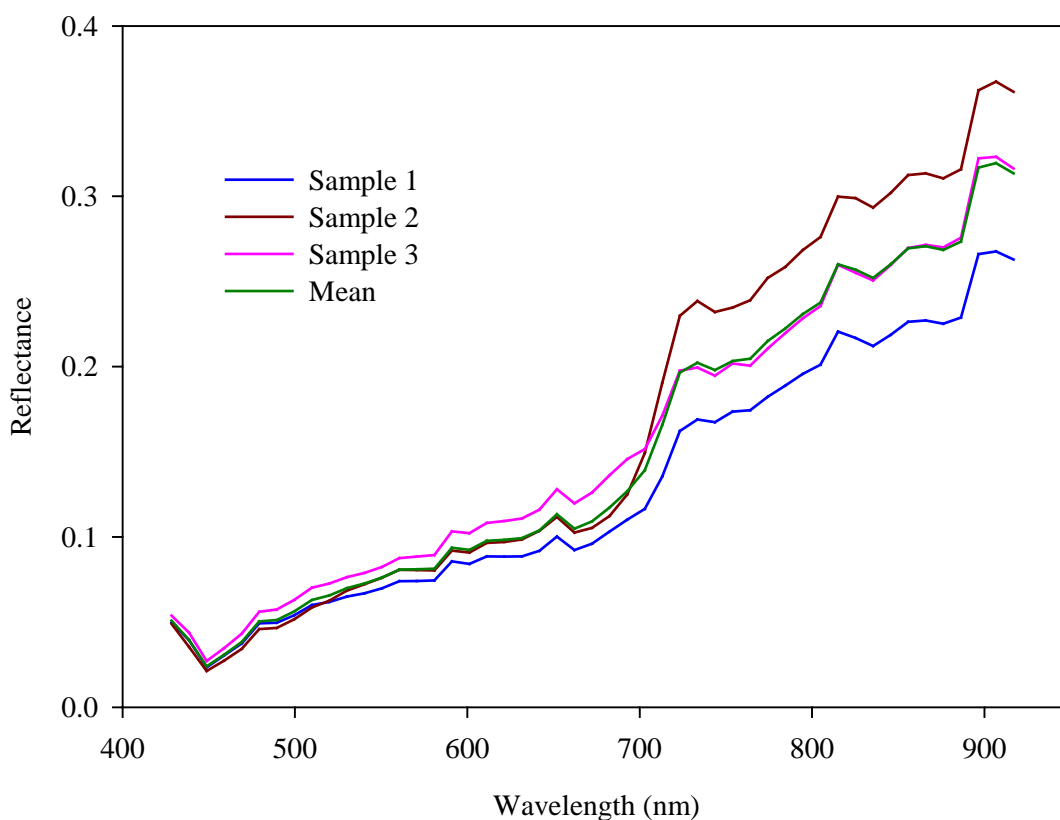


Figure 6.6 Spectral samples of dense Paterson's curse and the derived mean end-member spectrum.

The spectra of the Paterson's curse end-member and co-occurring vegetation types (senescent vegetation, Eucalypt woodland, and healthy vegetation) are shown in Figure 6.7. The red-edge for green vegetation was located at 741 nm (c.f. 662 nm for Paterson's curse) and showed a characteristic sharp increase into the near infrared, where it had the highest near infrared reflectance beyond 713 nm of all three classes.

Senescent vegetation showed the highest reflectance until 713 nm, and had the second highest reflectance to green vegetation for the remainder of the spectral range. The green vegetation, Paterson's curse and Eucalypt woodland had similar reflectance in the blue wavelengths. Senescent vegetation and Paterson's curse had a similar red-edge shift at approximately 662 nm.

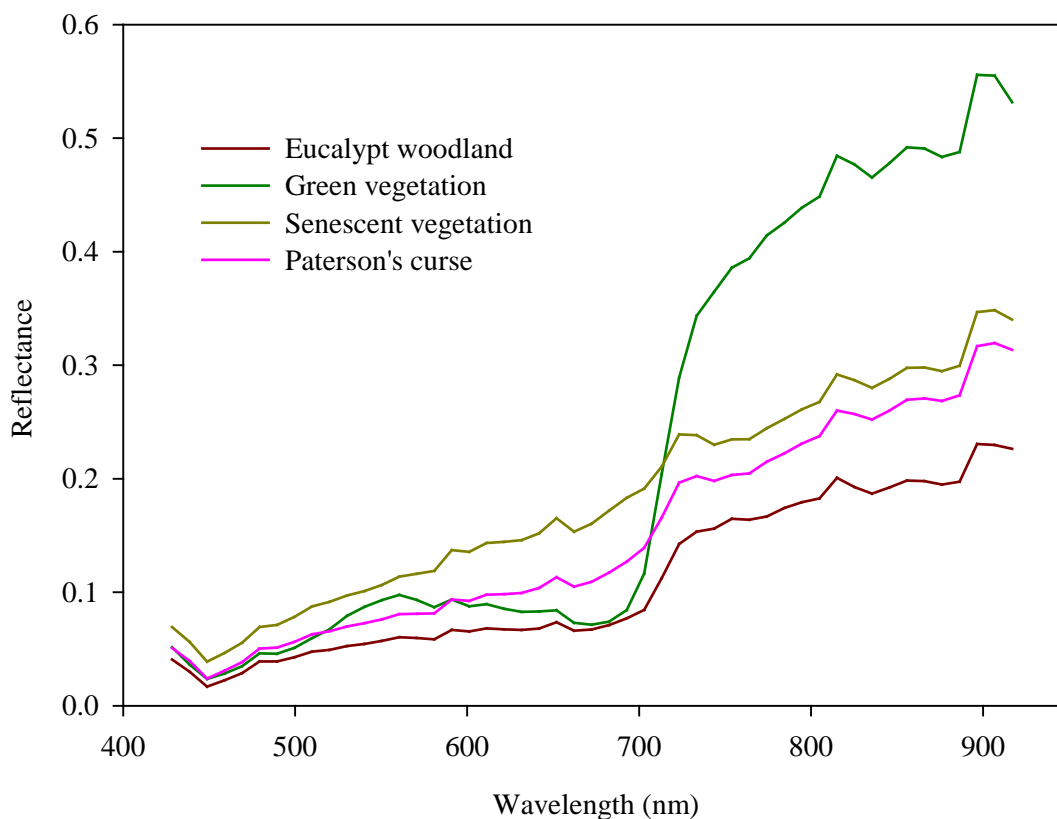


Figure 6.7 Spectra of the dense Paterson's curse end-member and co-occurring vegetation types.

The reflectance differences between the Paterson's curse end-member spectrum and the spectra for green vegetation, senescent vegetation and Eucalypt woodland are shown in Figure 6.8. For green vegetation and Paterson's curse, there was a small difference in blue and green until a small peak at 550 to 560 nm (bands 20 and 21). There was a negative peak at 682 to 692 nm (bands 33 and 34), followed by a sharp increase in the reflectance difference after the red-edge and a maximum difference in the near infrared at approximately 896 nm (band 54). Senescent vegetation and Paterson's curse showed a gradual increase in the reflectance difference through the visible and near infrared, with a peak at 693 nm, then a decrease from 703 to 765 nm, then a plateau through the remainder of the near infrared. Eucalypt woodland and Paterson's curse showed a similar trend to senescent vegetation and Paterson's curse,

with a gradual increase from blue into the near infrared, with a small plateau, and then a gradual increase through rest of the near infrared. Peaks in the reflectance difference for this pair occurred at bands 35 (703 nm) and 55 (907 nm).

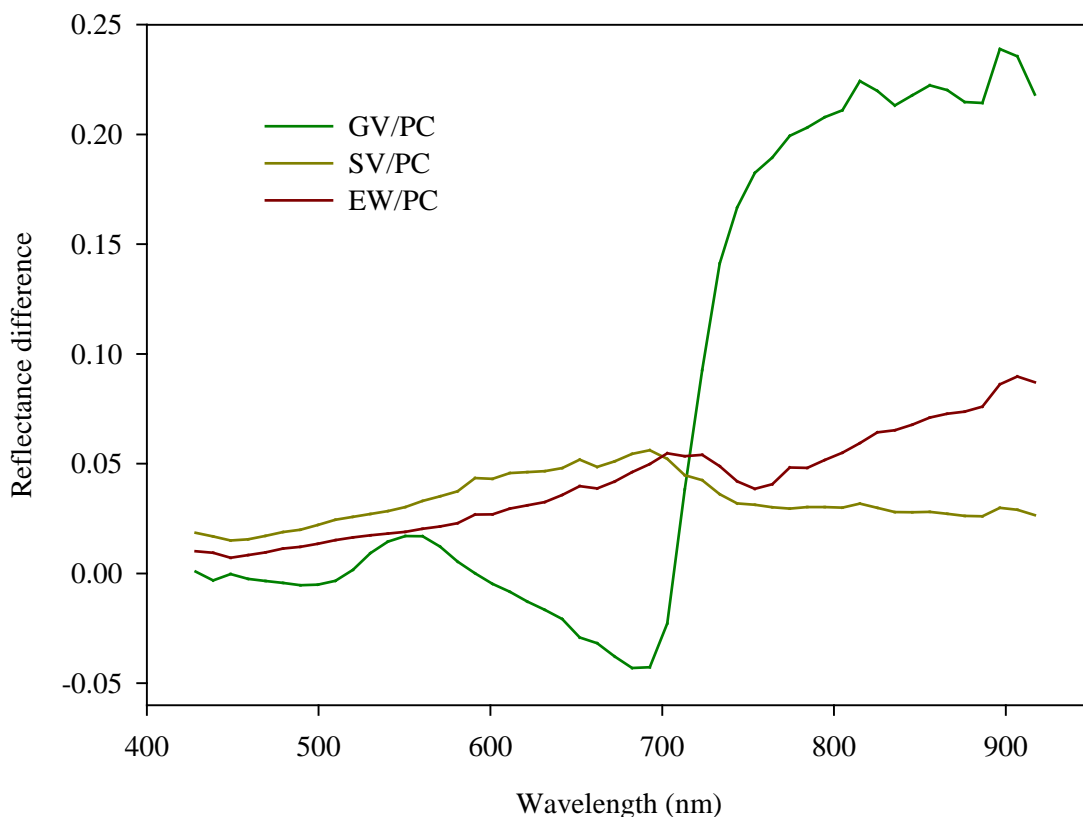


Figure 6.8 Reflectance differences between the dense Paterson's curse end-member spectrum (PC) and spectral samples representing green vegetation (GV), senescent vegetation (SV) and Eucalypt woodland (EW).

The spectra for Paterson's curse from the density class plots, along with green vegetation and senescent vegetation are shown in Figure 6.9. Class 1 had the lowest reflectance across the near infrared, and there was a general trend of higher near infrared reflectance as the density of the Paterson's curse classes increased. Generally all of the Paterson's curse classes had a similar reflectance across the full range.

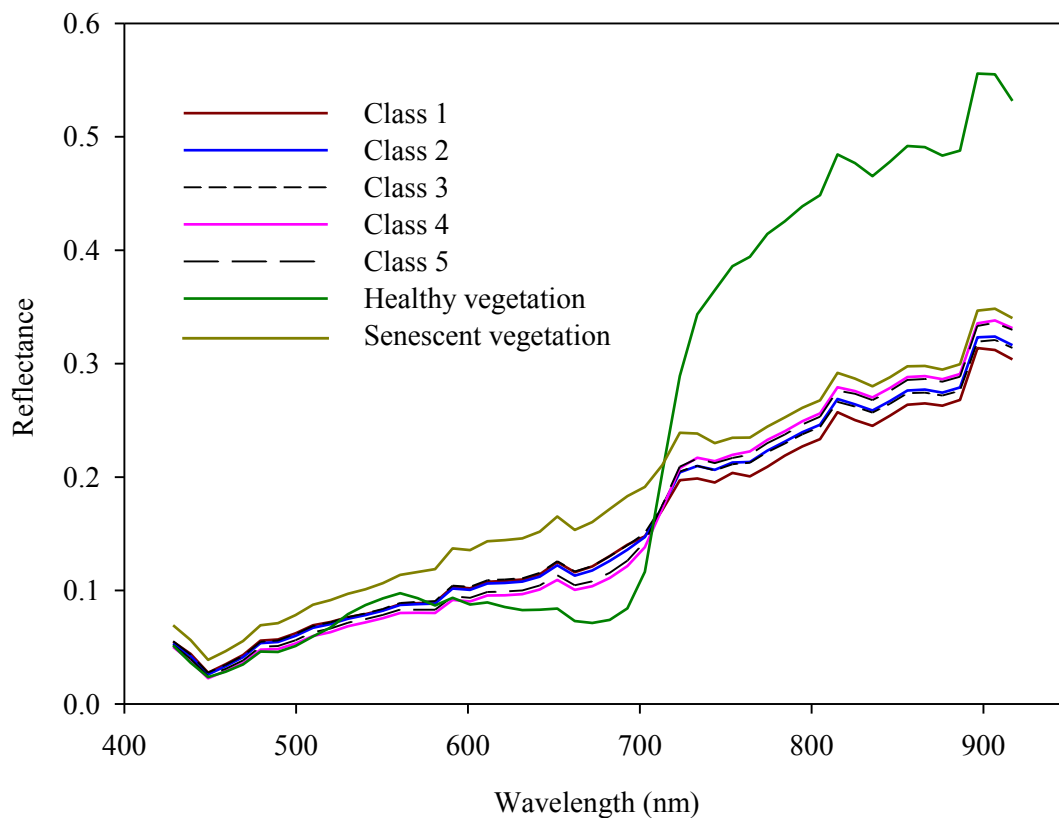


Figure 6.9 Spectra of the Paterson's curse density classes from the field validation plots, with green and senescent vegetation spectra shown for comparison.

6.3.2.2 Matched filter classification

The matched filter output (representing the abundance of the Paterson's curse end-member) for the matched filter classification is shown in Figure 6.10. Higher matched filter scores were generally present in pasture and cropped areas of the image (A) and areas infested by Paterson's curse. Matched filter scores were generally low for areas of Eucalypt woodland, water bodies, and fallow/cleared areas (B). Other areas of Eucalypt woodland had a 'speckle' effect caused by a large range of matched filter values (C).

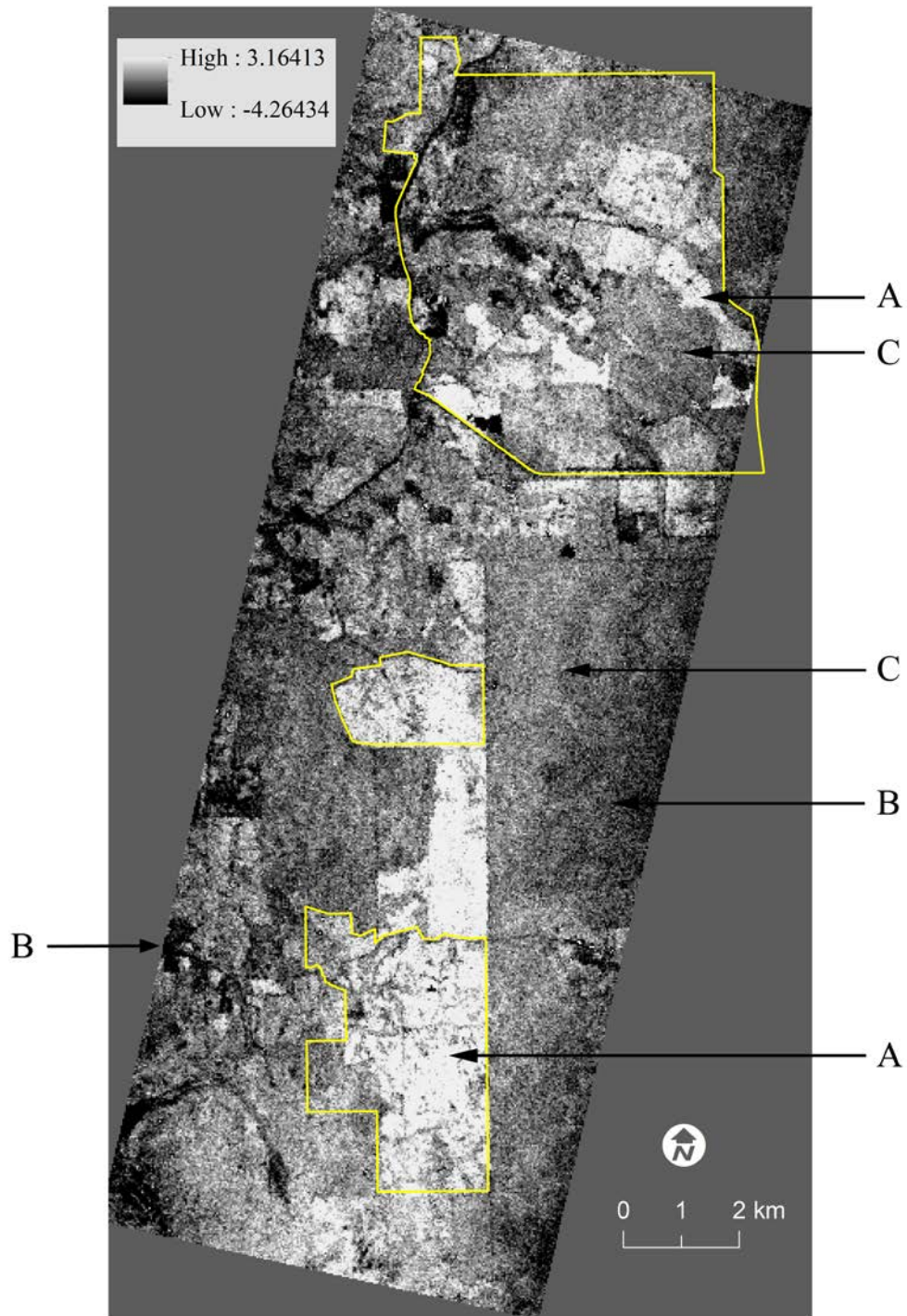


Figure 6.10 Matched filter image derived from Paterson's curse end-member.

6.3.2.3 Analysis of band ratios and indices

The Hyperion indices derived from the field spectroscopy analysis in Chapter 4 are shown in Table 6.4. Out of the eleven indices from Chapter 4, three were not used: SVPCF 1 due to the index containing a band that was not represented by the range of Hyperion (391 nm); SVDPC 2 (2007 nm and 1358 nm) and SVPCF 2 (2007 nm and

1415 nm) as the bands had been removed from the Hyperion image earlier due to noise. The spectral differences between spectra from Chapter 4 mostly translated well across to the equivalent Hyperion bands, and were within +/- 5 nm. For the green vegetation/Paterson's curse spectra, the Hyperion bands were similar to the bands identified from the radios derived from the spectroradiometer data in Chapter 4 (Table 6.5). For the senescent vegetation/Paterson's curse indices there were no similar wavelength peaks between the spectroradiometer indices and Hyperion spectra. The Normalised Difference Blue Index (NDBI) (Schut and McIntyre 2009) from Chapters 4 was used, as were four red-edge band ratios: the Red-Edge Normalised Difference Vegetation Index (NDVI) (RENDVI), Normalised Difference Red-Edge (NDRE), Red-Edge 2 (RE 2), and the Normalised Flower Red-Edge (NFRE).

Table 6.4 Hyperion indices derived from equivalent indices from Chapter 4.

Index	Formula	Reference
GVDPC 1	$\frac{(683 \text{ nm} - 550 \text{ nm})}{(550 \text{ nm} + 683 \text{ nm})}$	Chapter 4
GVDPC 2	$\frac{(866 \text{ nm} - 683 \text{ nm})}{(683 \text{ nm} + 866 \text{ nm})}$	Chapter 4
GVDPC 3	$\frac{(866 \text{ nm} - 550 \text{ nm})}{(550 \text{ nm} + 866 \text{ nm})}$	Chapter 4
GVPCF 1	$\frac{(550 \text{ nm} - 439 \text{ nm})}{(439 \text{ nm} + 550 \text{ nm})}$	Chapter 4
GVPCF 2	$\frac{(907 \text{ nm} - 693 \text{ nm})}{(693 \text{ nm} + 907 \text{ nm})}$	Chapter 4
GVPCF 3	$\frac{(896 \text{ nm} - 439 \text{ nm})}{(439 \text{ nm} + 896 \text{ nm})}$	Chapter 4
GVPCF 4	$\frac{(693 \text{ nm} - 439 \text{ nm})}{(439 \text{ nm} + 693 \text{ nm})}$	Chapter 4
NDBI	$\frac{(489 \text{ nm} - 428 \text{ nm})}{(428 \text{ nm} + 489 \text{ nm})}$	Schutt & McIntyre (2009)
RENDVI	$\frac{754 \text{ nm} - 713 \text{ nm}}{713 \text{ nm} + 754 \text{ nm}}$	Gitelson et al. (1994)
NDRE	$\frac{795 \text{ nm} - 723 \text{ nm}}{723 \text{ nm} + 795 \text{ nm}}$	Barnes et al. (2000)
RE 2	$\frac{713 \text{ nm} - 683 \text{ nm}}{683 \text{ nm} + 713 \text{ nm}}$	Cloutis et al. (1996)
NFRE	$\frac{723 \text{ nm} - 652 \text{ nm}}{652 \text{ nm} + 723 \text{ nm}}$	Chapter 4

Table 6.5 Comparison of peak spectral differences of green vegetation/Paterson's curse spectra derived from Hyperion image, and field spectroscopy in Chapter 4.

Hyperion Peaks (nm)	Spectroradiometer Peaks (nm)
550 - 561	555
683 - 693	684
896	865

6.3.3 Validation

6.3.3.1 Matched filter threshold independent

The Chi-square and ROC results for the matched filter image are shown in Table 6.6. The logistic regression model showed good agreement with the validation data. The model χ^2 of 86.95 rejects the null hypothesis that the matched filter score is not linearly related to the log-odds of presence/absence of Paterson's curse. The AUC statistic of 0.87 from the ROC analysis also indicated good agreement between the matched filter output and the validation data (Figure 6.11). The resulting matched filter cut-off value represented the top 54% of the dataset, in which 81% of Paterson's curse records were correctly identified (user's accuracy) and 17% of non-Paterson's curse records were misidentified (83% producer's accuracy).

Table 6.6 Chi-square results and ROC statistics from logistic regression of the matched filter classification output.

N	Chi-Square	Sig.	ROC	SE	Sig.	User's accuracy (%)	Producer's accuracy (%)
184	86.94	0.0001	0.870	0.027	0.01	81	83

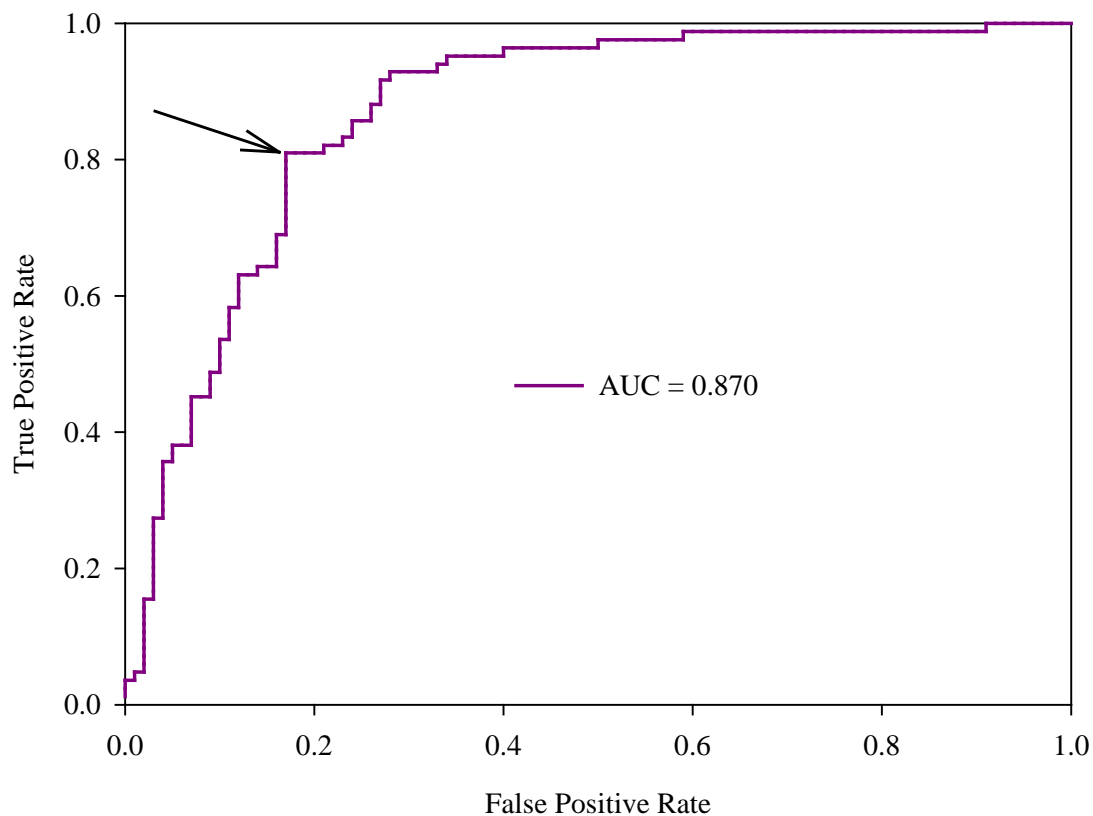


Figure 6.11 ROC plots for the matched filter validation result, with cut-off value indicated by arrow.

The probability image of Paterson's curse from the logistic regression is shown as Figure 6.12. There was a good association of the higher matched filter values with corresponding areas of high (> 0.70) probability, particularly in areas of pasture. Areas of Eucalypt woodland on the three properties had lower probability.

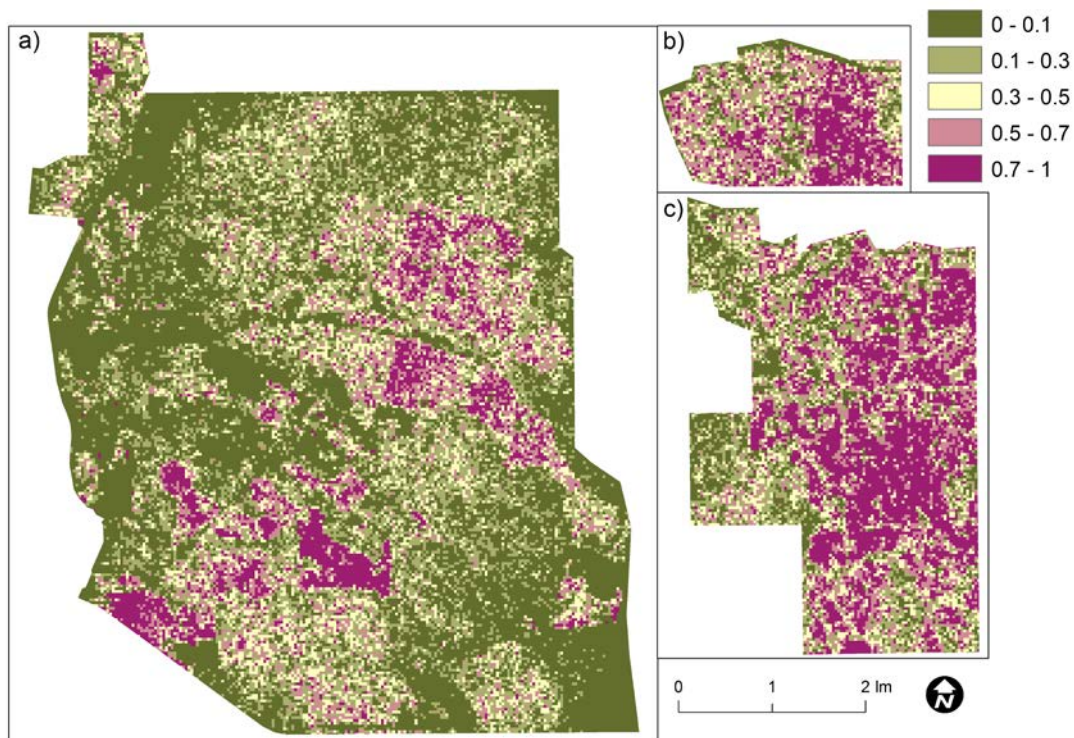


Figure 6.12 Paterson's curse model (probability of presence) derived from logistic regression.

The hard classification image from the ROC cut-off for the matched filter classification is shown in Figure 6.13 for the three properties. Small areas of sclerophyll woodland are incorrectly classified as Paterson's curse in the northern part of the CACB property (Figure 6.13a). Some areas of crop were misclassified in the eastern part of the property (A). In the south and south-west area of the property, some areas of pasture (B) were classified as Paterson's curse, where these areas are known not to contain Paterson's curse. The western portion of the Morden Downs property (Figure 6.13b) was not investigated on the ground, so it was not certain whether Paterson's curse was correctly classified. The main core areas of Paterson's curse found in the eastern section of the property was correctly classified (C). The areas on the Bindarie property (Figure 6.13c) classified as Paterson's curse were mostly open areas of pasture, although not all of these areas were surveyed on the ground, and could have contained some Paterson's curse. There were some instances of Eucalyptus woodland (D) being misclassified as Paterson's curse.

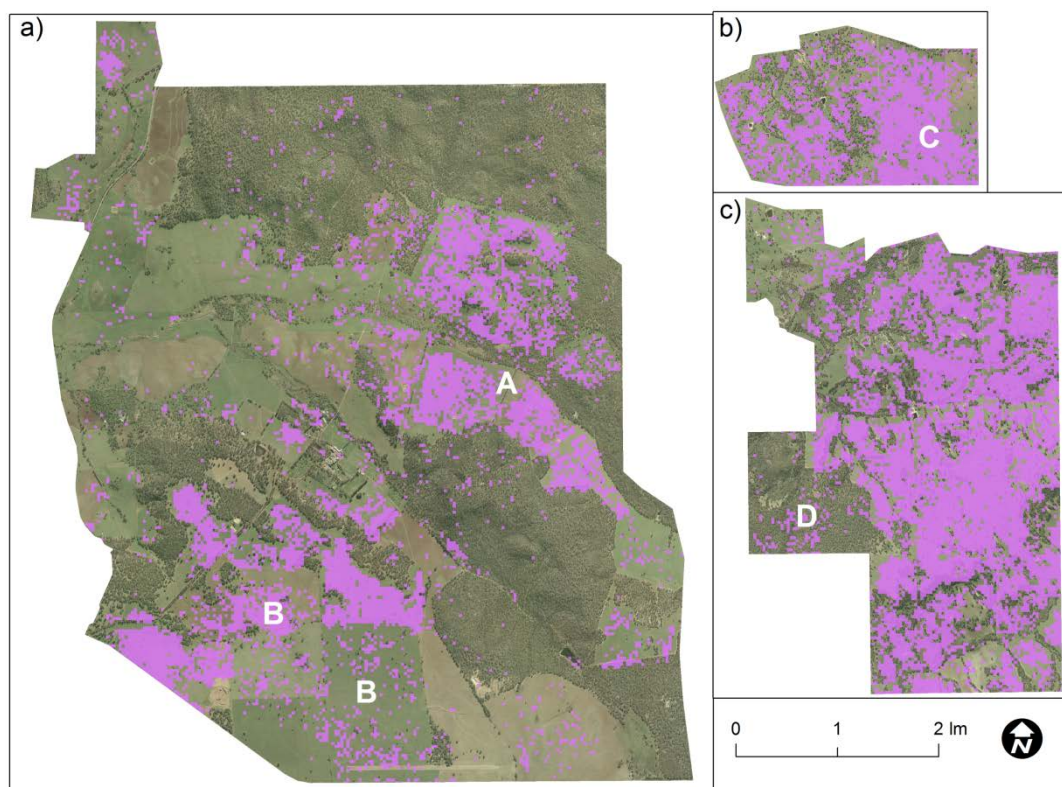


Figure 6.13 Threshold image showing Paterson's curse (purple) at a) Bindoon Catholic Agricultural College b) Morden Downs, and c) Bindarie.

6.3.3.2 Matched filter threshold dependent

The error matrix for the cut-off value (the top 46% of the dataset) of the matched filter classification (Table 6.7) shows a high overall accuracy (82%), and a high user's (80%) and producer's accuracy (81%) for Paterson's curse. The overall Kappa statistic of 0.64 was statistically significant ($z > 1.96$) and showed a good agreement with the validation data, based on the ranges proposed by Monserud and Leemans (1992). Similarly the per-class Kappa statistics for Paterson's curse from a user's and producer's perspective were above 0.6 and considered good.

Table 6.7 Threshold dependent accuracy results of matched filter classification with validation dataset (n = 184).

	Present	Absent	Totals	User's accuracy (%)	Kappa per-class (User's)
Present	68	17	85	80	0.632
Absent	16	83	99	84	
Totals	84	100	184		
Producer's accuracy (%)	81	83			
Kappa per-class (Producer's)			0.646		
Overall accuracy (%)			82		
Overall Kappa			0.640		

6.3.3.3 Band ratio/index threshold independent

The Chi-square results from the logistic regression and the ROC (AUC) statistics for the ratios/indices are shown in Table 6.8. The best performing indices in terms of the AUC statistic were the GVPCF 4 (0.756), GVPCF 1 (0.721) and GVDPC 1 (0.702). The cut-off value for these indices represented 30%, 50% and 52% of the top values of the datasets respectively. The model Chi-square values for the three indices (44.86, 33.09 and 9.69) rejects the null hypothesis that the range of values is not linearly related to the log-odds of presence/absence of Paterson's curse. The remaining ratios/indices had low AUC statistics, between 0.51 and 0.59 and non-significant Chi-square values. Of particular note was the low AUC statistic for the NDBI (0.565), which was the best performing index in the field spectroscopy analysis in Chapter 5.

The producer's accuracy was higher (70–96%) than that of user's accuracy (21–69%). This was due to a high prevalence of Paterson's curse being misclassified into non-Paterson's curse records, and a low amount of non-Paterson's curse being classified in Paterson's curse records. This trend is exemplified by the GVPCF 4 index, which had a low user's accuracy of 48%, but a higher producer's accuracy of 92%. Exceptions to this trend were the GVPCF 1 and GVDPC 1 indices, which had similar user's (66% and 69%) and producer's accuracy (70%).

Table 6.8 Chi-square, AUC and accuracy statistics from logistic regression of band ratios and indices with validation dataset (n = 184).

Ratio/Index	Threshold (%)	Chi-Square	Sig.	AUC	Sig.	User's accuracy (%)	Producer's accuracy (%)
GVPCF 4	30.43	44.861	0.001	0.756	0.001	48	92
GVPCF 1	50.00	30.09	0.001	0.721	0.001	66	70
GVDPC 1	51.63	9.694	0.002	0.702	0.001	69	70
GVPCF 2	34.78	3.224	0.073	0.592	0.031	48	82
GVDPC 2	22.83	2.349	0.125	0.585	0.048	35	93
NFRE	26.63	1.688	0.194	0.580	0.063	36	86
RENDVI	20.65	0.462	0.497	0.571	0.099	33	95
RE2	19.57	0.975	0.323	0.566	0.122	29	93
NDBI	14.67	4.064	0.044	0.565	0.127	22	95
GVPCF 3	36.41	2.062	0.151	0.562	0.147	46	76
NDRE	30.43	0.231	0.631	0.543	0.318	42	85
GVDPC 3	13.59	0.009	0.924	0.514	0.737	21	96

The ROC plots with cut-off values for the top ROC results (AUC > 0.7) are shown in Figure 6.12. The cut-off values were 50% for GVPCF 1, 30% for GVPCF 4, and 52% for GVDPC 1.

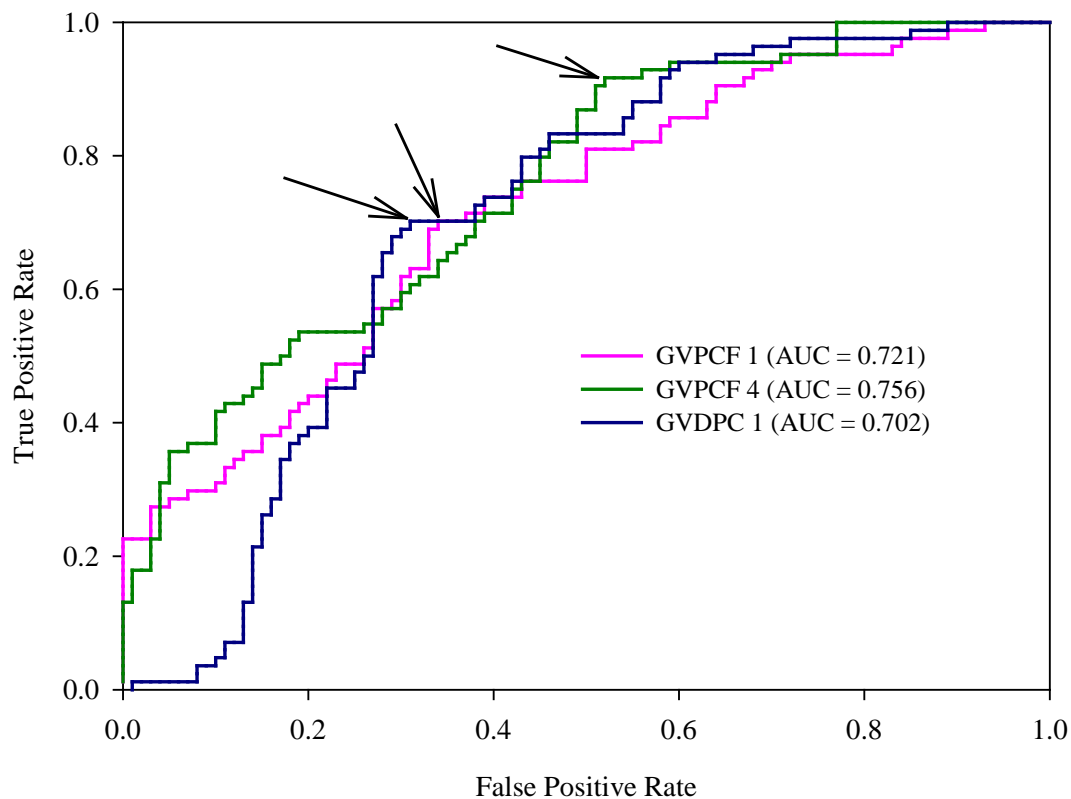


Figure 6.14 ROC plots for three best performing indices, with cut-off values indicated by arrows.

6.3.3.4 Band ratio/index threshold dependent

The threshold dependent results for the band ratios/indices are shown in Table 6.9. In terms of overall Kappa, the best performing ratios/indices were the same three as for the threshold independent method in Section 6.3.3.3: GVDPC 1, GVPCF 1 and GVPCF4. The Kappa statistic for GVDPC 1 (0.41) shows a fair agreement with the validation data, according to the ranges proposed Monserud and Leemans (1992); however the GVPCF 1 (0.36) and GVPCF 4 (0.35) had a poor agreement. The remaining band ratios had poor overall agreement, with Kappa statistics less than 0.3. The Kappa per class (user's and producer's) for GVDPC 1 and GVPCF 4 was between 0.29 and 0.45; whereas the per-class Kappa statistics for GVPCF 1 were < 0.1. The ratio with the least agreement with the validation dataset in terms of overall Kappa and Kappa per-class (user's) was the NDBI, which was the best performing ratio from the field spectroscopy analysis in Chapter 5.

The overall accuracy ranged from 49% for NDBI, to 71% for GVDPC 1. There was a general trend of the producer's accuracy increasing, with a corresponding decrease in the user's accuracy. This was due to a greater number of correctly identified Paterson's curse records in the lower Kappa ratios/indices, and a corresponding increase in the number of non-Paterson's curse records being mislabelled as Paterson's curse. An exception was the GVPCF 4 index, which had the highest user's accuracy (70%), but a low producer's accuracy, which resulted in a lower overall kappa and kappa per-class (user's).

Table 6.9 Threshold dependent accuracy results of band ratios and indices with validation dataset (n = 184).

Ratio/index	Kappa	Threshold (%)	UA (%)	PA (%)	OA (%)	KPC (U)	KPC (P)
GVDPC 1	0.412	48.91	66.67	71.43	70.65	0.387	0.441
GVPCF 1	0.359	50.54	47.2	70.24	50.54	0.028	0.072
GVPCF 4	0.352	34.78	70.31	53.57	68.48	0.454	0.288
GVPCF 2	0.291	65.76	57.03	82.14	63.59	0.209	0.478
RENDVI	0.266	79.89	54.42	95.24	61.41	0.161	0.763
GVDPC 2	0.264	77.71	54.55	92.86	61.41	0.164	0.679
NDRE	0.247	72.83	54.48	86.91	60.87	0.162	0.518
NFRE	0.207	65.76	53.72	77.38	59.24	0.148	0.339
RE2	0.206	80.98	52.35	92.86	58.15	0.123	0.624
GVDPC 3	0.150	85.33	50.32	94.05	54.89	0.086	0.594
GVPCF 3	0.117	90.76	49.1	97.62	52.72	0.063	0.742
NDBI	0.050	93.00	47.09	96.43	48.91	0.027	0.452

Key: UA – producer’s accuracy; PA – user’s accuracy; OA – overall accuracy; KPC (U) – Kappa per-class (user’s); KPC (P) – Kappa per-class (producer’s)

6.4 Discussion and Conclusion

The result from the matched filter classification indicates that Paterson’s curse can be accurately mapped with EO-1 Hyperion imagery. The user’s accuracy (81 and 80%) from the threshold independent and dependent validation methods was similar to other non-woody weeds that have been mapped from airborne hyperspectral imagery, such as musk thistle (Mirik, *et al.* 2013), hoary cress (Mundt, *et al.* 2005) and *Solidago altissima* (Ishii and Washitani 2013). Overestimation of weeds with hyperspectral remote sensing has been reported by a number of authors (e.g. Lass, *et al.* 2002; Mirik, *et al.* 2013; Parker-Williams and Hunt 2004) and is more likely to occur when images cover large areas (e.g. EO-1 Hyperion) and have correspondingly higher environmental variability (Andrew and Ustin 2008). The effect of this variability can be ameliorated by masking regions of the image prior to the classification that may cause spectral confusion with the target weed (Pengra, *et al.* 2007). For this research, overestimation was reduced by masking Eucalypt woodland; however additional sources of commission error are likely to include cropped areas, and pasture that retains greenness longer into the season.

The producer’s accuracy from the threshold independent and dependent validation methods (83 and 81%) was also similar to other airborne hyperspectral applications

and higher than the producer's accuracy of 69% obtained by Pengra, *et al.* (2007) from mapping the aquatic weed *Phragmites* with EO-1 Hyperion imagery. A likely source of omission error was lower density (patchy) areas of Paterson's curse that could not be reliably discriminated from senescent pasture. This result is indicative of the ongoing challenge amongst remote sensing practitioners to accurately detect low density weed infestations (refer Section 2.6), even with the enhanced spatial and spectral resolution of airborne hyperspectral sensors (Glenn, *et al.* 2005; Mundt, *et al.* 2005). A satellite hyperspectral sensor such as EO-1 Hyperion is further limited in its ability to detect weeds at low density due to the coarser spatial resolution and lower signal-to-noise ratio. Within the context of this research, the producer's accuracy is acceptable, given that the rationale for using EO-1 Hyperion data was to map the distribution of Paterson's curse over a larger area in a more cost effective manner than airborne sensors, and to highlight areas that can be further investigated in detail (e.g. airborne hyperspectral or field visit).

Quantitative measurements of weed density (or proportion cover) from hyperspectral imagery are a desirable output, given that a relationship between weed cover and estimated cover can be used to determine a detection threshold for a sensor (e.g. Parker-Williams and Hunt 2002). The main limitation with this approach is that the abundance measure from matched filter and MTMF are more representative of the presence of a material, rather than true abundance (Mitchell and Glenn 2009). In addition, only a small number of studies have related quantitative vegetation attributes to matched filter abundance with good correlations, and these studies mostly used airborne hyperspectral data with a higher signal to noise ratio than Hyperion (Andrew and Ustin 2008; Mitchell and Glenn 2009; Parker-Williams and Hunt 2002). Hyperion data was used by Ramsey III, *et al.* (2005c) to derive a good correlation between estimated cover of Chinese tallow (*Triadica sebifera*) and ground cover, but this approach required extensive field data and a rigorous calibration approach which is unlikely to be applicable to operational weed management.

The reduction in flower cover over the two week period between the fieldwork and image capture was not a limitation to detecting Paterson's curse with hyperspectral imagery. The feature that allowed Paterson's curse to be detected was the tendency

for Paterson's curse to retain living green material the end of spring when pasture is senescent (Piggin 1976). This result is similar to other studies that detected weeds with delayed senescence, for example para grass (Boyden, *et al.* 2013) and spotted knapweed (Lass, *et al.* 2002). In contrast, other studies could not reliably detect a weed species when in a reduced or absent flowering stage, due to spectral confusion with green co-occurring vegetation (Andrew and Ustin 2006; Everitt and Villarreal 1987; Lass and Callihan 1997). At the time of the image capture, most of the study area contained senescent pasture, except for irrigated cropped areas and pasture in wetter areas. In contrast, when the field data was collected there was more green pasture. If an image from that period was classified using a similar approach to this chapter, it is likely that despite the peak flowering condition, there would be spectral overlap between Paterson's curse and green pasture and a lower producer's accuracy.

The threshold dependent (maximum Kappa) and independent (ROC) methods produced similar user's and producer's accuracy for the matched filter classification. Similar accuracy results between different models are expected when there are equal numbers of presence and absence records (50% convergence) (Liu, *et al.* 2005). However for this research there was a convergence of 46% due to fewer presence records (85) than absence (100). The accuracy result indicates that the two methods may be sufficiently robust to compensate for moderately lower (or higher) convergence values; and that the two methods produce a complimentary measurement of accuracy, and it is advantageous to use them together when assessing the accuracy of a hardened classification.

A commonly cited advantage of the AUC statistic over threshold dependent approaches (e.g. maximum Kappa) is that all possible thresholds for a given model are incorporated (e.g. Fielding and Bell 1997; Zweig and Campbell 1993). However the statistic provides no information about the spatial distribution of errors, and most of the threshold values from the ROC curve used to derive the statistic are of no relevance to an end-user (Lobo, *et al.* 2008). Consequently, some authors have recommended the AUC statistic for stand-alone model assessment – but not as a comparative statistic for comparing the performance of different models (Robinson, *et al.* 2010; Termansen, *et al.* 2006). The main benefit of ROC (which was demonstrated from the current research) is the flexibility to determine an appropriate

threshold over a range of true positive and false positive values (Jiménez-Valverde and Lobo 2007; Lobo, *et al.* 2008; Robinson, *et al.* 2010).

One disadvantage of the maximum efficiency method is that omission and commission error are equally weighted (Lobo, *et al.* 2008). This is undesirable for predicting the distribution of weed with spatial models, because a higher user's accuracy is required to identify potential areas of invasion (Robinson, *et al.* 2010). Similarly for weed distribution maps derived from remote sensing, it is desirable to minimise weed infestations on the ground being misclassified into a non-weed class (omission error) (Andrew and Ustin 2008). To achieve this, a threshold value could be used that provides the highest user's accuracy possible whilst keeping commission error to an acceptable level. The output could be further optimised by masking the regions of the hardened classification where the weed species has been previously mapped, and attention focussed on the newly identified areas.

This study was the first to use quantitative statistical methods to measure the accuracy of Paterson's curse from remote sensing. Subsequently, the accuracy results cannot be directly compared to previous research (Bulman 2004; Ullah, *et al.* 1989b) that used qualitative methods (e.g. visual inspection) to determine the accuracy of mapped Paterson's curse from satellite imagery. Quantitative accuracy assessment is an important part of any product derived from remote sensing (Congalton and Green 1999) especially if the end purpose is to benefit weed management (McGowen 1998). Weed maps can be used to monitor the spread or reduction in weeds, or assist with locating specific infestations in the field. For the latter, soft classification maps akin to the probability maps derived from logistic regression from this study can complement the hard (threshold) classification map by providing a measure of certainty at each location on the map.

The poor accuracy of the Hyperion derived band ratios and indices was similar to the field spectroscopy analysis in Chapter 5, with the exception of the NDBI. There are three possible reasons for the poor performance of this index. First, there was a reduction in Paterson's curse flower density in the two week period between the collection of field data collection and image acquisition. This highlights the importance of concurrent field and image data collection, especially for annual

weeds species like Paterson's curse, in which the flowering is short-lived; however it also highlights the challenges of tasking sensors to capture satellite imagery during periods in which meteorological conditions are variable. Second, the low signal to noise ratio of Hyperion - particularly in the blue bands would have reduced the sensitivity of the NDBI to detect subtle differences between Paterson's curse and pasture. Third, the spatial resolution of the Hyperion imagery could not adequately measure the contribution of flowers, relative to the small spectral sampling area (0.45 m²) for the field spectroscopy. A mixture of Paterson's curse and senescent pasture within an area of ground covered by a Hyperion pixel will result in a low contribution of the flowers to the overall reflectance, especially given a reduction in flower density.

The presence/absence approach from this study was effective for accurately mapping Paterson's curse over a large area without a lengthy period of field validation. This result is similar to other remote sensing applications that have mapped the presence/absence of weeds from medium spatial resolution imagery (Bradley and Mustard 2005; Cuneo, *et al.* 2009; Dewey, *et al.* 1991; Pengra, *et al.* 2007). The approach is particularly suited to weed species such as Paterson's curse that have short phenological stages (e.g. flowering and delayed senescence) for detection with remote sensing, and is favourable from a management perspective as the fieldwork is less labour intensive (Lawes and Wallace 2008). In contrast, studies that have mapped proportion cover of a weed species conducted field surveys over longer periods (e.g. 1–2 months) (Wilfong, *et al.* 2009), or in the case of Ramsey III and Nelson (2005), required a helicopter to capture field data.

Despite the limitations of the Hyperion sensor (primarily the low signal-to-noise ratio), the previous limitations on detecting Paterson's curse with medium spatial resolution data were overcome to an acceptable extent by the higher spectral resolution of the Hyperion sensor. The application of Hyperion represents an improvement over the previous method of visual estimation on the ground, given that it could map the spatial distribution of Paterson's curse over a large area, with less field time. Next-generation sensors with a larger swath width (30 km) and a higher signal-to-noise ratio than Hyperion, such as EnMAP (Segal, *et al.* 2010) and Precursore Iperspettrale della Missione Applicativa (PRISMA) (Labate, *et al.* 2009)

will provide greater consistency in image quality and processing, and be more amenable with operational requirements for mapping Paterson's curse and other weeds over regional scales.

7 SUMMARY AND RECOMMENDATIONS

7.1 Introduction

The research presented in this thesis investigated the utility of remote sensing for mapping and monitoring Paterson's curse at study sites in the Wheatbelt Region of Western Australia. Three remote sensing data types at different spectral and spatial resolution were used to address the research objectives:

- (i) Field spectroscopy (Chapter 4);
- (ii) Airborne multispectral high spatial resolution imagery (Chapter 5); and
- (iii) Satellite hyperspectral imagery (Chapter 6).

The three objectives from Chapter 1 are evaluated below, with reference to the three remote sensing datasets.

7.2 The Optimum Spatial and Spectral Resolution

The results from Chapters 4, 5 and 6 indicate that spectral resolution may be more important than spatial resolution for detecting Paterson's curse. In Chapter 4, the characteristic reflectance peak of Paterson's curse flowers in the blue region of the electromagnetic spectrum resulted in a good relationship ($R^2 = 0.75$) between a Normalised Difference Blue Index (NDBI) derived from field spectroscopy and percentage floral cover of Paterson's curse. The relationship between linear spectral unmixing of Paterson's curse flowers and floral percentage cover produced an R^2 of 0.68. The relationship between the red-edge ratios in Chapter 4 and Paterson's curse floral cover were weak, and are most likely the result of an insufficient red-edge shift in the dense Paterson's curse spectrum, due to mixing between Paterson's curse flower material and green and dead plant material.

High spatial resolution multispectral imagery has the same detection limitations as medium spatial resolution imagery, due to spectral confusion between Paterson's curse and co-occurring vegetation (Chapter 5). The prevalence of green pasture resulted in spectral mixing within pixels and low classification accuracy, despite the imagery being captured in the peak flowering period for Paterson's curse. This outcome is similar to other studies that mapped weeds in pasture where co-occurring

vegetation caused confusion (Lass and Callihan 1997; Lass, *et al.* 1996). In contrast to pasture weeds, remote sensing applications to woody weeds have shown that higher spatial resolution improves classification accuracy when objects (discrete vegetation canopies) are larger than the pixel size (Everitt and Yang 2007b; Robinson, *et al.* 2008). The results from Chapter 5 indicate that reducing the pixel size of remotely sensed data is not sufficient for reliability detecting pasture weeds if matched with inadequate spectral resolution.

The results from the analysis of EO-1 Hyperion data in Chapter 6 showed that medium spatial resolution imagery (30 m) with hyperspectral resolution could accurately map Paterson's curse. The user's and producer's accuracy of Paterson's curse for the matched filter classification was 81 to 83% and 80 to 81% respectively, with a Kappa statistic of 0.64. The high spectral resolution of Hyperion mitigated the past limitations of medium spatial resolution imagery from other studies (Bulman 2004; Ullah, *et al.* 1989b) in which Paterson's curse was spectrally confused with pasture. The accuracy results in this research however could not be directly compared to these previous studies that mapped Paterson's curse with satellite multispectral imagery (Bulman 2004; Ullah, *et al.* 1989b) as they lacked quantitative accuracy assessment.

In Chapter 5, multiple density classes (and a detection limit) could not be determined for Paterson's curse from DMSI imagery. Paterson's curse occurred in the study area as a fuzzy continuum of floral density, with few areas of high flowering density, with a low mean floral cover, and was mixed with pasture in all densities, especially in lower density areas. In Chapter 6, the presence/absence classification approach was effective for mapping and validating Paterson's curse over a large area and favourable from a management perspective (i.e. cost effective).

7.2.1 Recommendations

The findings of the field spectroscopy analysis in Chapter 4, the Hyperion classification in Chapter 6, and previous studies (Bulman 2004; Mitchell, *et al.* 2006), demonstrate that airborne hyperspectral imagery has the potential to reliably detect and map Paterson's curse. Given the high cost of imagery, a practical approach could be to use maps of Paterson's curse from classified satellite

hyperspectral imagery to narrow down potential sites to capture airborne hyperspectral imagery. Airborne hyperspectral imagery could be used in those circumstances where the cost of acquisition, processing, and field time is justified; for example to evaluate biological control or in a research capacity.

The NDBI is shown by the field spectroscopy analysis in Chapter 4 to be a potentially useful index to apply to multispectral remote sensing. There are currently two multispectral satellite platforms with sensors that contain two blue bands (World View 2 and Landsat 8), which could be investigated for detecting Paterson's curse with the NDBI. Airborne multispectral sensors similar to DMSI could be used in a similar capacity, if an extra blue band could be included through a filter. The recommended band centres to be filtered, based on the NDBI from Chapters 4 are 430 nm and 480 to 490 nm respectively. When these two bands are used together in an index, atmospheric correction will be essential to reduce the noise from atmospheric attenuation, especially for satellite sensors such as Landsat 8.

The Hyperion classification results in Chapter 6 foreshadows the potential of future hyperspectral satellites such as EnMAP (Segal, *et al.* 2010) and PRISMA (Labate, *et al.* 2009) for providing accurate regional scale maps of Paterson's curse. Investigations into the utility of these data types could be conducted using appropriate classification methods such as MTMF, and validated using quantitative datasets derived from field survey. The Bindoon study sites (properties) used for this research represent an ideal location for such studies, due to the prevalence of Paterson's curse, close proximity to Perth, and active management of Paterson's curse by landowners. Future opportunities to assess the success of control of Paterson's curse are therefore possible with satellite hyperspectral data.

7.3 The Optimum Timing of Remote Sensing

The timing of remote sensing is an important factor for detecting and mapping Paterson's curse. The research highlights some important considerations about the temporal nature of Paterson's curse, and the most appropriate time to capture remote sensing imagery. In Chapter 4, there were good relationships between Paterson's curse and spectral values from field spectroscopy later in the season, when flower cover was lower than the peak period in October. In Chapter 5, airborne multispectral

imagery was captured during the peak flowering period in October, however the presence of green co-occurring pasture resulted in low accuracy results (user, producer, and Kappa) from the multi-layer perceptron (MLP) and k-nearest neighbour (kNN) classifiers (Section 7.4). In Chapter 6, satellite hyperspectral imagery was shown to accurately detect Paterson's curse later in the flowering season (November), due to the green material of Paterson's curse persisting longer than co-occurring pasture vegetation.

7.3.1 Recommendations

Remotely sensed imagery could be acquired during the peak flowering period of Paterson's curse (October), or later in the season when pasture is senescent (late October/early November). Which period is chosen will depend on the sensor and the environmental conditions during the course of a given year (e.g. rainfall), and the type of imagery. For airborne and satellite hyperspectral sensors, imagery from the either period may be suitable. For airborne multispectral sensors, imagery captured later in the season may be preferable from a detection perspective, when Paterson's curse retains its green material relative to pasture.

The influence of seasonal variability on the ability to detect and map Paterson's curse using remotely sensing is a potential area of investigation through landscape ecology studies. For example the flowering patterns of Paterson's curse and the spectral properties within individual seasons, and across several seasons could be analysed from field spectroscopy and digital field photography. It could be used to determine how the spectral separability of Paterson's curse changes with co-occurring vegetation such as pasture and crop. Such a study would benefit from several years of data, to capture seasonality trends, and over a larger area to capture geographic variability. An understanding of the influence of rainfall (amount and timing) on Paterson's curse (flowering intensity and timing, and retention of green material) over a given geographic area could be a useful guide to remote sensing.

7.4 Suitable Image Processing and Classification Techniques

The literature review in Chapter 2 ensured that the processing and classification methods used in the research were well matched to the remotely sensed imagery. In order to demonstrate the utility of image classification to Paterson's curse, a selection

of classifiers were used in the research, including both parametric and non-parametric.

In the field spectroscopy analysis in Chapter 4, band ratios and indices were useful for determining the relationship between floral proportion cover of Paterson's curse. Band ratios and indices were derived from the literature (e.g. red-edge and Paterson's Curse Index) and an analysis of spectral differences between Paterson's curse and pasture. The linear and non-linear regression technique was valuable for determining whether floral proportion cover could be predicted based on the ratio and index values.

In Chapter 5, the kNN and MLP non-parametric image classifiers were used to classify the DMSI image, as these classifiers have produced superior classification accuracy in past applications, compared to parametric classifiers. Despite this, the classification accuracy of Paterson's curse from the kNN and MLP classifiers was low. Overall classification accuracy was < 66%, with an overall Kappa statistics of < 0.35. The user's accuracy ranged from 23 to 73% and the producer's accuracy from 40 to 73%. The per-class Kappa statistic for Paterson's curse for the two classifiers was between 0.2 and 0.4.

A complex classifier (MLP) was shown not to provide any benefits over a simpler classifier (kNN) when there was spectral overlap between classes in the training data resulting from high within-class variance. The classification results demonstrate that the complexity of a classification algorithm will not compensate for the limitations of spectral resolution in multi-spectral sensors, and are unlikely to produce improvements in classification accuracy over traditional classifiers (e.g. maximum likelihood).

In Chapter 6, the Hyperion data required substantial processing to maximise the spectral information content whilst reducing the inherent noise, and remove artefacts such as striping. A minimum noise fraction combined with a matched filter was the best approach to classifying the data, as it reduced noise, and was suitable for cover types such as Paterson's curse that contribute a relatively small proportion of the reflected signal.

The receiver operating characteristic (ROC) analysis and logistic regression in Chapters 5 and 6 were shown to be a useful technique to assess the accuracy of soft classification output. The threshold approach generated a hard classification image in addition to the ‘soft’ probability image output. Hard and soft classification images were used as complimentary datasets, by attributing a measure of uncertainty (a probability value) to a particular location (pixel) on a map produced from a hard classification. This approach has value for weed managers, who can ‘screen’ a weed map for infestations with higher probabilities prior to a field visit. One limitation of soft classification is that the value of a soft classification output was only as good as its accompanying hard classification – shown in Chapter 5 by the relationships between the Kappa statistic and the ROC statistic for the MLP and kNN classifiers. A higher accuracy (e.g. > 70%) may be required to detect lower density infestations of Paterson’s curse with a corresponding higher probability in the image output.

7.4.1 Recommendations

In Chapter 5, the analysis of multispectral data suggested that using other image classification algorithms is not likely to overcome the spectral limitations for detecting Paterson’s curse. However a procedure to improve classification accuracy of existing classifiers could be implemented through stratification pre- and post-classification, as was done in Chapters 5 and 6 for crop and pasture areas. Another approach to improve accuracy could be to incorporate on-ground knowledge on the status of Paterson’s curse and other cover types. An example of such knowledge could be areas of a given property that were grazed or sprayed and free of Paterson’s curse at the time of image acquisition.

The Hyperion results in Chapter 6 shows that the matched filter is an effective classification method for detecting Paterson’s curse with satellite hyperspectral data. Such a method is likely to be equally effective for airborne hyperspectral imagery, given the higher signal-to-noise ratio. Appropriate processing techniques for maximising the information content, such as minimum noise fraction, should be part of a standard processing workflow.

7.5 Methods of Integrating Remotely Sensed Data and Field Data

Remotely sensed data and field data were integrated by deriving relationships between band ratios and indices with floral proportion cover (Chapter 4) and presence/absence data (Chapter 6), and using field data for training and validation (Chapters 5 and 6). In Chapter 4, the floral proportion cover from a systematic sampling grid was used to investigate relationships between band ratios/indices and linear spectral unmixing derived from field spectroscopy. In Chapter 5 training areas were selected from representative areas of Paterson's curse and associated cover types for input into MLP and kNN classifiers, and validation data were derived from stratified random point data collected in the field. ROC analysis and logistic regression were used to determine the accuracy of soft classification output; error matrices and Kappa were used to determine the accuracy of hard classification. In Chapter 6 a matched filter classification and band ratios and indices derived from Hyperion imagery were validated with stratified random presence/absence field data of Paterson's curse. As with Chapter 5, ROC analysis and logistic regression was used as well as error matrices and Kappa.

In Chapter 6 the poor performance of all Hyperion derived band ratios and indices was similar to the field spectroscopy analysis in Chapter 4, with the exception of the NDBI. The most likely factors that contributed to this were the reduction in flowering between the date of field data collection and image acquisition, the low signal-to-noise ratio of the data (Jupp and Datt 2004) and the spatial resolution of the sensor.

An important prerequisite for integrating field and image data in Chapters 4 and 5 was to derive floral proportion cover using a quantitative method (as recommended by Bulman (2004)) to reduce bias and maintain consistency. An object classification approach was used to derive floral proportion cover from digital field photographs captured at nadir (Appendix C). This method is a consistent and accurate way to derive floral percentage cover. The data were used to determine relationships between Paterson's curse and band ratios and indices in Chapter 4, and for accuracy assessment in Chapter 5.

7.5.1 Recommendations

If the relationship between floral proportional cover and band ratios and indices from high spatial resolution multispectral or hyperspectral imagery was to be investigated, high registration accuracy would be required. To obtain such accuracy, additional field work would be required to collect ground control points with a differential GPS. An alternative strategy might be to employ reflective markers at the start and end of transects, or employ a systematic grid. As an alternative, the top-down approach described in Aspinall, *et al.* (2002) may be more realistic, as it would negate the requirement for a rigorous geo-rectification. A disadvantage of this approach is that locations cannot be located on the ground with high accuracy.

Quantitative methods of assessing classification accuracy, such as Kappa and ROC analysis are suggested for future applications of remote sensing of Paterson's curse. In addition, statistically vigorous methods such as random sampling should be employed where possible as part of field validation.

Presence/absence is shown to be a robust and accurate method for mapping Paterson's curse with satellite hyperspectral data in Chapter 6. However an investigation of the relationship between Paterson's curse cover with band ratios/indices and matched filter output could be useful for determining a detection threshold. Green cover of Paterson's curse could be measured in addition to flower density, given that green material was shown in Chapter 6 to contribute more to the spectral signal late in the season than flowers. Field sampling would have to be conducted over a short period of time to take advantage of higher flower density and/or green material, and multiple field personnel may be required. A quantitative method similar to the one described in Appendix C could be used to determine cover in plots.

7.6 Contribution to Knowledge

This research made the following specific contributions to knowledge:

As far as the author is aware, this is first study to use airborne multispectral and satellite hyperspectral remotely sensing to detect and map Paterson's curse. The study shows that classification methods are secondary to the limitations imposed by

the spectral and spatial resolution of a sensor. It also shows that spectral resolution is more important than spatial resolution for mapping pasture weeds like Paterson's curse. This is demonstrated by the low-medium accuracy from the high spatial resolution multispectral imagery in Chapter 5, and from the high accuracy from the medium spatial resolution hyperspectral imagery in Chapter 6. The research in particular demonstrates that hyperspectral satellite data has the potential to produce accurate regional scale maps of Paterson's curse.

The study provides knowledge on the detection abilities of remote sensing for Paterson's curse during the peak flowering period—in particular that multispectral airborne remote sensing does not result in improvements over satellite multispectral imagery for mapping Paterson's curse if co-occurring pasture is green. It challenges the perception that highly visible pasture weed species on-ground (for instances where their detection features are most prominent) can be easily detected from air and space by remote sensing. This is exemplified by the purple flowers of Paterson's curse, which has a low measured cover (< 20%), when viewed from a sensor perspective (nadir), but the flower cover from a viewer's (oblique) perspective is higher (> 80%).

This research is the first remote sensing study to quantitatively measure the accuracy of maps of Paterson's curse derived from image classification. The research emphasises the importance of using quantitative measures of accuracy for mapping vegetation and weeds in remote sensing: to provide a statistically rigorous measure of accuracy that compliments a qualitative assessment. The research investigated optimum field sampling approaches that maintained statistical integrity while considering the limited time available to collect field data. This will benefit future remote sensing applications of Paterson's curse from the knowledge that acceptable levels of accuracy can be provided from satellite hyperspectral data with economical validation data (presence/absence).

7.7 Conclusion

The research demonstrated that despite some promising results from the datasets and methods employed, remote sensing is not a viable operational tool for routine mapping and monitoring Paterson's curse, especially at a regional scale. Regional

scale remote sensing of Paterson's curse is an assessment tool that could provide the greatest returns to land managers. The regional scale detection ability of satellite hyperspectral remote sensing could narrow down areas of Paterson's curse for further investigation, either from the ground, or using airborne hyperspectral data. However, until new-generation hyperspectral satellite sensors are available and can be evaluated, traditional methods of survey for Paterson's curse (e.g. field survey) will remain superior to remote sensing for making assessments of the extent and density of Paterson's curse.

REFERENCES

- Adair, R.J. and Groves, R.H. (1998) *Impact of environmental weeds on biodiversity: A review and development of a methodology*, Environment Australia, Canberra, A.C.T., p 52.
- Analytical Spectral Devices Inc. (1999) ASD technical guide. Analytical Spectral Devices Inc., Colorado USA.
- Anderson, G.L., Everitt, J.H., Richardson, A.J. and Escobar, D.E. (1993) 'Using satellite data to map false broomweed (*Ericameria austrotexana*) infestations on South Texas rangelands', *Weed Technology* 7 (4): 865-871.
- Andrew, M.E. and Ustin, S.L. (2006) 'Spectral and physiological uniqueness of perennial pepperweed (*Lepidium latifolium*)', *Weed Science* 54 (6): 1051-1062.
- Andrew, M.E. and Ustin, S.L. (2008) 'The role of environmental context in mapping invasive plants with hyperspectral image data', *Remote Sensing of Environment* 112 (12): 4301-4317.
- Apan, A., Held, A., Phinn, S.R. and Markley, J. (2004) 'Detecting sugarcane 'orange rust' disease using EO-1 Hyperion hyperspectral imagery', *International Journal of Remote Sensing* 25 (2): 489-498.
- Aplin, P. and Atkinson, P.M. (2001) 'Sub-pixel land cover mapping for per-field classification', *International Journal of Remote Sensing* 22 (14): 2853-2858.
- Arai, E., Shimabukuro, Y.E., Pereira, G. and Vijaykumar, N.L. (2011) 'A multi-resolution multi-temporal technique for detecting and mapping deforestation in the Brazilian Amazon rainforest', *Remote Sensing* 3 (9): 1943-1956.
- Archibald, S., Nickless, A., Govender, N., Scholes, R.J. and Lehsten, V. (2010) 'Climate and the inter-annual variability of fire in southern Africa: a meta-analysis using long-term field data and satellite-derived burnt area data', *Global Ecology and Biogeography* 19 (6): 794-809.
- Aspinall, R. and Veitch, N. (1993) 'Habitat mapping from satellite imagery and wildlife survey data using a Bayesian modelling procedure in a GIS', *Photogrammetric Engineering and Remote Sensing* 59 (4): 537-543.
- Aspinall, R.J. (2002) 'Use of logistic regression for validation of maps of the spatial distribution of vegetation species derived from high spatial resolution hyperspectral remotely sensed data', *Ecological Modelling* 157 (2-3): 301-312.
- Aspinall, R.J., Marcus, A.W. and Boardman, J.W. (2002) 'Considerations in collecting, processing, and analysing high spatial resolution hyperspectral data for environmental investigations', *Journal of Geographic Systems* 4 (1): 15-29.

- Atkinson, J.T., Ismail, R. and Robertson, M. (2014) 'Mapping bugweed (*Solanum mauritianum*) infestations in *Pinus patula* plantations using hyperspectral imagery and Support Vector Machines', *IEEE Journal of Selected Topics in Applied Earth Observations and Remote Sensing* 7 (1): 17-28.
- Atkinson, P.M. (1997) 'Selecting the spatial resolution of airborne MSS imagery for small-scale agricultural mapping', *International Journal of Remote Sensing* 18 (9): 1903-1917.
- Atkinson, P.M. and Aplin, P. (2004) 'Spatial variation in land cover and choice of spatial resolution for remote sensing', *International Journal of Remote Sensing* 25 (18): 3687-3702.
- Atkinson, P.M. and Tatnall, A.R. (1997) 'Neural networks in remote sensing', *International Journal of Remote Sensing* 18 (4): 699-709.
- Baatz, M., Benz, U., Dehghani, S., Heynen, M., Höltje, A., Hofmann, P., Lingenfelder, I., Mimler, M., Sohlbach, M., Weber, M. and Willhauck, G. (2004) eCognition Professional user guide 4. Definiens Imaging, Munich, Germany.
- Bachmann, C.M., Donato, T.F., Lamela, G.M., Rhea, W.J., Bettenhausen, M.H. and Fusina, R.A. (2002) 'Automatic classification of land cover on Smith Island, VA, using HyMAP imagery', *IEEE Transactions of Geoscience and Remote Sensing* 40 (10): 2313-2330.
- Ball, G.H. and Hall, D.J. (1967) 'A clustering technique for summarizing multivariate data', *Behavioral Science* 12 (2): 153-155.
- Bannari, A., Morin, D. and Bonn, F. (1995) 'A review of vegetation indices', *Remote Sensing Reviews* 13 (1-2): 95-120.
- Barano, S.S. and Hartono (2004). 'Mapping of *Mimosa pigra* on Maro River in Wasur National Park, Papua — Indonesia'. In: Julien, M, Flanagan, G, Heard, T, Hennecke, B, Paynter, Q & Wilson, C (eds.), *Research and Management of Mimosa pigra*, CSIRO Entomology, Canberra, Australia.
- Barnes, E.M., Clarke, T.R., Richards, S.E., Colaizzi, P.D., Haberland, J., Kostrzewski, M., Waller, P., Choi, C., Riley, E., Thompson, T., Lascano, R.J., Li, H. and Moran, M.S. (2000) 'Coincident detection of crop water status, nitrogen status, and canopy density using ground-based multispectral data', *Proceedings of the Fifth International Conference on Precision Agriculture, 16-19 July 2000*, Bloomington, Minnesota, American Society of Agronomy, Crop Science Society of America, Soil Science Society of America:
- Becker, R.H., Zmijewski, K.A. and Crail, T. (2013) 'Seeing the forest for the invasives: mapping buckthorn in the Oak Openings', *Biological Invasions* 15 (2): 315-326.
- Beeston, G.R., Hopkins, A.J.M. and Shepherd, D.P. (2001) *Land-use and vegetation in Western Australia*, Agriculture Western Australia, South Perth, p 59.

- Benediktsson, J.A., Swain, P.H. and Ersoy, O.K. (1990) 'Neural network approaches versus statistical methods in classification of multisource remote sensing data', *IEEE Transactions of Geoscience and Remote Sensing* 28 (4): 540-552.
- Benz, U.C., Hofmann, P., Willhauck, G., Lingenfelder, I. and Heynen, M. (2004) 'Multi-resolution, object-oriented fuzzy analysis of remote sensing data for GIS-ready information', *ISPRS Journal of Photogrammetry & Remote Sensing* 58 (3-4): 239-258.
- Bezdek, J.C., Ehrlich, R. and Full, W. (1984) 'FCM: The Fuzzy C-Means clustering algorithm', *Computers and Geosciences* 10 (3): 191-203.
- Birdsall, J.L., P.C., Q.J., Rees, N.E., Svejcar, T.J. and Sowell, B.F. (1997) 'Image analysis of leafy spurge (*Euphorbia esula*) cover', *Weed Technology* 11 (4): 798-803.
- Blaschke, T. (2010) 'Object based image analysis for remote sensing', *ISPRS Journal of Photogrammetry & Remote Sensing* 65 (1): 2-16.
- Blaschke, T. and Strobl, J. (2001) 'What's wrong with pixels? Some recent developments interfacing remote sensing and GIS', *GIS* 6: 12-17.
- Boardman, J.W. (1998) 'Leveraging the high dimensionality of AVIRIS data for improved subpixel target unmixing and rejection of false positives', *AVIRIS 1998 Proceedings*, JPL, California: 6pp.
- Bowman, D.M.J.S. and Dingle, J.K. (2006) 'Late 20th-century landscape-wide expansion of *Allosyncarpia ternata* (Myrtaceae) forest in Kakadu National Park, northern Australia', *Australian Journal of Botany* 54 (8): 707-715.
- Boyd, W.W. (1986) 'Correlation of rangelands brush canopy cover with Landsat MSS data', *Journal of Rangeland Management* 39 (3): 268-271.
- Boyden, J., Joyce, K.E., Boggs, G. and Wurm, P. (2013) 'Object-based mapping of native vegetation and para grass (*Urochloa mutica*) on a monsoonal wetland of Kakadu NP using a Landsat 5 TM Dry season time series', *Journal of Spatial Science* 58 (1): 53-77.
- Bradley, B.A. and Mustard, J.F. (2005) 'Identifying land cover variability distinct from land cover change: Cheatgrass in the Great Basin', *Remote Sensing of Environment* 94 (2): 204-213.
- Brando, V.E. and Dekker, A.G. (2003) 'Satellite hyperspectral remote sensing for estimating estuarine and coastal water quality', *IEEE Transactions of Geoscience and Remote Sensing* 41 (6): 1378-1387.
- Broge, N.H. and Mortensen, J.V. (2002) 'Deriving green crop area index and canopy chlorophyll density of winter wheat from spectral reflectance data', *Remote Sensing of Environment* 81 (1): 45-57.

- Broochs, F., Kupfer, G., Dockter, K. and Kuhbauch, W. (1990) 'Shape of the red edge as vitality indicator for plants', *International Journal of Remote Sensing* 11 (10): 1741-1753.
- Bulman, D. (2004) 'The application of remote sensing imagery to weed mapping: A case study for Paterson's curse (*Echium plantagineum* L.).' Monash University: Clayton.
- Bureau of Meteorology (2010) *Climate Data Online*. <<http://www.bom.gov.au/climate/data/>>. Viewed online: 12 August 2010.
- Campbell, J.B. (2008) *Introduction to Remote Sensing, Forth Edition*, 4 Ed., Guildford Press
- Canci, M., Wallace, J., Mattiske, E. and Malcolm, A. (2006) 'Evaluation of airborne multi-spectral imagery for monitoring the effect of falling groundwater levels on native vegetation', *The 13th Australasian Remote Sensing and Photogrammetry Conference*, Canberra:
- Canon, R.L., Dave, J.V., Bezdek, J.C. and Trivedi, M.M. (1986) 'Segmentation of a thematic mapper image using the fuzzy c-means clustering algorithm', *IEEE Transactions of Geoscience and Remote Sensing* 24 (3): 400-408.
- Cantor, S.B., Sun, C.C., Tortolero-Luna, G., Richards-Kortum, R. and Follen, M. (1999) 'A comparison of C/B ratios for studies using receiver operating characteristic curve analysis', *Journal of Clinical Epidemiology* 52 (9): 885-892.
- Carson, H.W., Lass, L.W. and Callihan, R.H. (1995) 'Detection of yellow hawkweed (*Hieracium pratense*) with high resolution multi-spectral digital imagery', *Weed Technology* 9 (3): 447-483.
- Carter, G.A. (1993) 'Responses of leaf spectral reflectance to plant stress', *American Journal of Botany* 80 (3): 239-243.
- Casady, G.M., Hanley, R.S. and Seelan, S.K. (2005) 'Detection of leafy spurge (*Euphorbia esula*) using multirate high-resolution satellite imagery', *Weed Technology* 19 (2): 462-467.
- Catholic Agricultural College Bindoon (2007) *On the Farm*. <<http://cacbindoon.wa.edu.au/farm.html>>. Viewed online: August 8 2007.
- Catt, P. and Thirarongnarong, K. (1992) 'An evaluation of remote sensing techniques for the detection, mapping, and monitoring of invasive plant species in coastal wetlands: A case study of Para grass (*Brachiaria mutica*).', *6th Australasian Remote Sensing Conference*, Wellington, New Zealand:
- Chavez, P.S. (1988) 'An improved dark-object subtraction technique for atmospheric scattering correction of multispectral data', *Remote Sensing of Environment* 24 (3): 459-479.

- Chen, J.M. and Cihlar, J. (1996) 'Retrieving leaf area index of boreal conifer forests using Landsat TM images', *Remote Sensing of Environment* 55 (2): 153-162.
- Cheng, Y.B., Tom, E. and Ustin, S.L. (2007) 'Mapping an invasive species, kudzu (*Pueraria montana*), using hyperspectral imagery in western Georgia', *Journal of Applied Remote Sensing* 1 (1): 013514.
- Cho, M.A., Mathieu, R., Asner, G.P., Naidoo, L., van Aardt, J., Ramoelo, A., Debba, P., Wessels, K., Main, R., Smit, I.P.J. and Erasmus, B. (2012) 'Mapping tree species composition in South African savannas using an integrated airborne spectral and LiDAR system', *Remote Sensing of Environment* 125: 214-226.
- Clark University (2006) IDRISI Andes. V 15.01 ed. Clark Laboratories, Worcester MA, USA.
- Clinton, N.E., Potter, C., Crabtree, B., Genovese, V., Gross, P. and Gong, P. (2010) 'Remote sensing-based time-series analysis of cheatgrass (*Bromus tectorum* L.) phenology', *Journal of Environmental Quality* 39 (3): 955-963.
- Cloutis, E.A., Connery, D.R., Major, D.J. and Dover, F.J. (1996) 'Airborne multi-spectral monitoring of agricultural crop status: effect of time of year, crop type and crop condition parameter', *International Journal of Remote Sensing* 17 (13): 2579-2601.
- Cochrane, M.A. (2000) 'Using vegetation reflectance variability for species level classification of hyperspectral data', *International Journal of Remote Sensing* 21 (10): 2075-2087.
- Cohen, J. (1960) 'A coefficient of agreement for nominal scales', *Educational and Psychological Measurement* 20 (1): 37-46.
- Congalton, R.G. (1988) 'A comparison of sampling schemes used in generating error matrices for assessing the accuracy of maps generated from remotely sensed data', *Photogrammetric Engineering and Remote Sensing* 54 (5): 593-600.
- Congalton, R.G. (1991) 'A review of assessing the accuracy of classifications of remotely sensed data', *Remote Sensing of Environment* 37 (1): 35-46.
- Congalton, R.G. and Green, K. (1999) *Assessing the accuracy of remotely sensed data: Principles and practices* Lewis Publishers, New York, p 137.
- Congalton, R.G., Oderwald, R.G. and Mead, R.A. (1983) 'Assessing Landsat classification accuracy using discrete multivariate analysis statistical techniques', *Photogrammetric Engineering and Remote Sensing* 49 (12): 1671-1678.
- Coops, N.C., Smith, M., Martin, M.E. and Ollinger, S.V. (2003) 'Prediction of eucalypt foliage nitrogen content from satellite-derived hyperspectral data', *IEEE Transactions of Geoscience and Remote Sensing* 41 (6): 1338-1346.
- Culvenor, C.C.J., Jago, M.V., Peterson, J.E., Smith, L.W., Payne, A.L., Campbell, D.G., Edgar, J.A. and Frahn, J.L. (1984) 'Toxicity of *Echium plantagineum*

- (Paterson's Curse). I Marginal toxic effects in Merino wethers from long-term feeding', *Australian Journal of Agricultural Research* 35 (2): 293-304.
- Cuneo, P., Jacobson, C.R. and Leishman, M.R. (2009) 'Landscape-scale detection and mapping of invasive African olive (*Olea europaea* L. ssp. *cuspidata* Wall ex G. Don Ciferri) in SW Sydney, Australia using satellite remote sensing', *Applied Vegetation Science* 12 (2): 145-154.
- Curran, P.J., Dungan, J.L. and Gholz, H.L. (1990) 'Exploring the relationship between reflectance red edge and chlorophyll content in slash pine', *Tree Physiology* 7 (1-4): 33-48.
- Curran, P.J. and Williamson, H.D. (1985) 'The accuracy of ground data used in remote-sensing investigations', *International Journal of Remote Sensing* 6 (10): 1637-1651.
- Curran, P.J. and Williamson, H.D. (1986) 'Sample size for ground and remotely sensed data', *Remote Sensing of Environment* 20 (1): 31-41.
- Curtiss, B. and Goetz, A.F.H. (1994) 'Field spectrometry: Techniques and instrumentation', *International Symposium on Spectral Sensing Research, 10-15 July 1994*, San Diego, California, National Aeronautics and Space Administration (NASA):
- Daniels, A.E. (2006) 'Incorporating domain knowledge and spatial relationships into land cover classifications: a rule-based approach', *International Journal of Remote Sensing* 27 (14): 2949-2975.
- Datt, B., McVicar, T.R., Van Niel, T.G., Jupp, D.L.B. and Pearlman, J.S. (2003) 'Preprocessing EO-1 Hyperion hyperspectral data to support the application of agricultural indexes', *IEEE Transactions of Geoscience and Remote Sensing* 41 (6): 1246-1259.
- Dawson, T.P. and Curran, P.J. (1998) 'Technical note: A new technique for interpolating the reflectance red edge position', *International Journal of Remote Sensing* 19 (11): 2133-2139.
- Dean, A.M. and Smith, G.M. (2003) 'An evaluation of per-parcel land cover mapping using maximum likelihood class probabilities', *International Journal of Remote Sensing* 24 (14): 2905-2920.
- Dehaan, R., Louis, J., Wilson, A., Hall, A. and Rumbachs, R. (2007) 'Discrimination of blackberry (*Rubus fruticosus* sp. agg.) using hyperspectral imagery in Kosciuszko National Park, NSW, Australia', *ISPRS Journal of Photogrammetry & Remote Sensing* 62 (1): 13-24.
- Delfosse, E.S. (1985) '*Echium plantagineum* in Australia: Effects of a major conflict of interest', *VI International Symposium on the Biological Control of Weeds, August 1984*, Vancouver, Canada: 293-299.

- Department of the Environment and Water Resources (2007) *Australia's Native Vegetation: A summary of Australia's Major Vegetation Groups, 2007*, Canberra, ACT, p 42.
- Dewey, S.A., Price, K.P. and Ramsey, D. (1991) 'Satellite remote sensing to predict potential distribution of dyers woad (*Isatis tinctoria*)', *Weed Technology* 5 (3): 479-484.
- Dixon, B. and Candale, N. (2008) 'Multispectral landuse classification using neural networks and support vector machines: one or the other, or both?', *International Journal of Remote Sensing* 29 (4): 1185-1206.
- Dodd, J., Martin, R.J. and Howes, M.K. (1993) Management of agricultural weeds in Western Australia. Department of Agriculture Western Australia, Perth, Western Australia.
- Dowling, P.M. and Wong, P.T.W. (1993) 'Influence of pre-season weed management and in-crop treatments on two successive wheat crops 1. Weed seedling numbers and wheat grain yield', *Australian Journal of Experimental Agriculture* 33 (2): 167-172.
- Dungan, J.L., Perry, J.N., Dale, M.R.T., Legendre, P., Citron-Pousty, S., Fortin, M.-J., Jakomulska, A., Miriti, M. and Rosenberg, M.S. (2002) 'A balanced view of scale in spatial statistical analysis', *Ecography* 25 (5): 626-640.
- Duro, D.C., Franklin, S.E. and Dube, M.G. (2012) 'A comparison of pixel-based and object-based image analysis with selected machine learning algorithms for the classification of agricultural landscapes using SPOT-5 HRG imagery', *Remote Sensing of Environment* 118: 259-272.
- Eastman, R.J. (2006) *IDRISI Andes: Guide to GIS and image processing* Clark Labs, Worcester, MA
- Eastman, R.J. and Laney, R. (2002) 'Soft classifiers for sub-pixel evaluation: A critical evaluation', *Photogrammetric Engineering and Remote Sensing* 68 (11): 1149-1154.
- Edwards, A., Hauser, P., Anderson, M., McCartney, J., Armstrong, M., Thackway, R., Allan, G., Hempel, C. and Russell-Smith, J. (2001) 'A tale of two parks: contemporary fire regimes of Litchfield and Nitmiluk National Parks, monsoonal northern Australia', *International Journal of Wildland Fire* 10 (1): 79-89.
- Elith, J., Graham, H., Anderson, R.P., Dudik, M., Ferrier, S., Guisan, A., Hijmans, R.J., Huttman, F., Leathwick, J.R., Lehmann, A., Li, J., Lohmann, L.G., Loiselle, B.A., Manion, G., Mortiz, C., Nakamura, M., Nakazawa, Y., Overton, J., Peterson, T.A., Phillips, S.J., Richardson, K., Scachetti-Pereira, R., Schapire, R.E., Soberon, J., Williams, S., Wisz, M.S. and Zimmermann, N.E. (2006) 'Novel methods improve prediction of species' distributions from occurrence data', *Ecography* 29 (2): 129-151.

- Erol, H. and Akdeniz (2005) 'A per-field classification method based on mixture distribution models and an application to Landsat Thematic Mapper data', *International Journal of Remote Sensing* 26 (6): 1229-1244.
- ESRI (2004) Environmental Systems Research Institute, ArcGIS Version 9. Environmental Systems Research Institute Incorporated, Redlands, California.
- Evangelista, P.H., Stohlgren, T.J., Morisette, J.T. and Kumar, S. (2009) 'Mapping Invasive tamarisk (*Tamarix*): A comparison of single-scene and time-series analyses of remotely sensed data', *Remote Sensing* 1: 519-533.
- Everitt, J.H., Alaniz, M.A., Escobar, D.E. and Davis, M.R. (1992) 'Using remote sensing to distinguish common (*Isocoma coronopifolia*) and drummond goldenweed (*Isocoma drummondii*)', *Weed Science* 40 (4): 621-628.
- Everitt, J.H., Anderson, G.L., Escobar, D.E., Davis, M.R., Spencer, N.R. and Andrascik, R.J. (1995) 'Use of remote sensing for detecting and mapping leafy spurge (*Euphorbia esula*)', *Weed Technology* 9 (3): 599-609.
- Everitt, J.H. and Deloach, C.J. (1990) 'Remote sensing of Chinese tamarisk (*Tamarix chinensis*) and associated vegetation', *Weed Science* 38 (3): 273-278.
- Everitt, J.H., Escobar, D.E., Villarreal, R., Alaniz, M.A. and Davis, M.R. (1993) 'Canopy light reflectance and remote sensing of shin oak (*Quercus havardii*) and associated vegetation', *Weed Science* 41 (2): 291-297.
- Everitt, J.H., Escobar, D.E., Villarreal, R., Noriega, J.R. and Davis, M.R. (1991) 'Airborne video systems for agricultural assessment', *Remote Sensing of Environment* 35 (2-3): 231-242.
- Everitt, J.H., Ingle, S.J., Gausman, H.W. and Mayeux Jr., H.S. (1984) 'Detection of false broomweed (*Ericameria austrotexana*) by aerial photography', *Weed Science* 32 (5): 621-624.
- Everitt, J.H. and Nixon, P.R. (1985) 'Video imagery: A new remote sensing tool for range management', *Journal of Range Management* 38 (5): 421-424.
- Everitt, J.H., Pettit, R.D. and Alaniz, M.A. (1987) 'Remote sensing of broom snakeweed (*Gutierrezia sarothrae*) and spiny aster (*Aster spinosus*)', *Weed Science* 35 (2): 295-302.
- Everitt, J.H., Richardson, J.V., Escobar, D.E., Alaniz, M.A., Villarreal, R. and Davis, M.R. (1994) 'Light reflectance characteristics and remote sensing of big bend loco (*Astragalus mollissimus* var. *earlei*) and wooton loco (*Astragalus wootonii*)', *Weed Science* 42 (1): 115-122.
- Everitt, J.H. and Villarreal, R. (1987) 'Detecting huisache (*Acacia farnesiana*) and Mexican palo-verde (*Parkinsonia aculeata*) by aerial photography', *Weed Science* 35 (3): 427-432.

- Everitt, J.H. and Yang, C. (2007a) 'Using QuickBird satellite imagery to distinguish two aquatic weeds in South Texas', *Journal of Aquatic Plant Management* 45 (1): 25-31.
- Everitt, J.H. and Yang, C. (2007b) 'Mapping broom snakeweed through image analysis of color-infrared photography and digital imagery', *Environmental Monitoring and Assessment* 134 (1-3): 287-292.
- Everitt, J.H., Yang, C., Alaniz, M.A., Davis, M.R., Nibling, F.L. and Deloach, C.J. (2004) 'Canopy spectra of giant reed and associated vegetation', *Journal of Range Management* 57 (5): 561-569.
- Everitt, J.H., Yang, C. and Drawe, D.L. (2007a) 'Mapping spiny aster infestations with QuickBird imagery', *Geocarto International* 22 (4): 273-283.
- Everitt, J.H., Yang, C., Escobar, D.E., Webster, C.F., Lonard, R.I. and Davis, M.R. (1999) 'Using remote sensing and spatial information technologies to detect and map two aquatic macrophytes', *Journal of Aquatic Plant Management* 37 (1): 71-80.
- Everitt, J.H., Yang, C. and Flores, D. (2003) 'Light reflectance characteristics and remote sensing of waterlettuce', *Journal of Aquatic Plant Management* 41 (1): 39-44.
- Everitt, J.H., Yang, C. and Johnson, H.B. (2007b) 'Canopy spectra and remote sensing of Ashe juniper and associated vegetation', *Environmental Monitoring and Assessment* 130 (1-3): 403-413.
- Everitt, J.H., Yang, C., Racher, B.J., Britton, C.M. and Davis, M.R. (2001) 'Remote sensing of redberry juniper in the Texas rolling plains', *Journal of Rangeland Management* 54 (3): 254-259.
- Fassnacht, K.S., Gower, S.T., MacKenzie, M.D., Nordheim, E.V. and Lillesand, T.M. (1997) 'Estimating the Leaf Area Index of north central Wisconsin forests using the Landsat Thematic Mapper', *Remote Sensing of Environment* 61 (2): 229-245.
- Felde, G.W., Anderson, G.P., Cooley, T.W., Matthew, M.W., Adler-Golden, S.M., Berk, A. and Lee, J. (2003) 'Analysis of Hyperion data with the FLAASH atmospheric algorithm', *IGARSS*, Toulouse, France: 90-92.
- Fensham, R.J., Fairfax, R.J. and Archer, S.R. (2005) 'Rainfall, land use and woody vegetation cover change in semi-arid Australian savanna ', *The Journal of Ecology* 93 (3): 596-606.
- Fielding, A.H. and Bell, J.F. (1997) 'A review of methods for the assessment of prediction errors in conservation presence/absence models', *Environmental Conservation* 24 (1): 38-49.
- Filella, I. and Penuelas, J. (1994) 'The red edge position and shape as indicators of plant chlorophyll content, biomass, and hydric status', *International Journal of Remote Sensing* 15 (7): 1459-1470.

- Fisher, P. (1997) 'The pixel: a snare and a delusion', *International Journal of Remote Sensing* 18 (3): 679-685.
- Fletcher, R.S., Everitt, J.H. and Elder, H.S. (2010) 'Evaluating airborne multispectral digital video to differentiate Giant Salvinia from other features in Northeast Texas', *Remote Sensing* 2 (10): 2413-2423.
- Foody, G.M. (1996) 'Fuzzy modelling of vegetation from remotely sensed imagery', *Ecological Modelling* 85 (1): 3-12.
- Foody, G.M. (2000) 'Estimation of sub-pixel land cover composition in the presence of untrained classes', *Computers and Geosciences* 26 (4): 469-478.
- Foody, G.M. (2004) 'Thematic map comparison: Evaluating the statistical significance of differences in classification accuracy', *Photogrammetric Engineering and Remote Sensing* 70 (5): 627-633.
- Foody, G.M. (2008) 'Harshness in image classification accuracy assessment', *International Journal of Remote Sensing* 29 (11): 3137-3158.
- Foody, G.M., Campbell, N.A., Trodd, N.M. and Wood, T.F. (1992) 'Derivation and applications of probabilistic measures of class membership from the maximum-likelihood classification', *Photogrammetric Engineering and Remote Sensing* 58 (9): 1335-1341.
- Foody, G.M. and Mathur, A. (2004) 'A relative evaluation of multiclass image classification by support vector machines', *IEEE Transactions of Geoscience and Remote Sensing* 42 (6): 1335-1343.
- Franco-Lopez, H., Ek, A.R. and Bauer, M.E. (2001) 'Estimation and mapping of forest stand density, volume, and cover type using the k-nearest neighbors method', *Remote Sensing of Environment* 77 (3): 251-274.
- Frazier, A.E. and Wang, L. (2011) 'Characterizing spatial patterns of invasive species using sub-pixel classifications', *Remote Sensing of Environment* 115 (8): 1997-2007.
- Frazier, P. (1998) 'Mapping blackberry thickets in the Kosciuszko National Park using airborne video data', *Plant Protection Quarterly* 13 (3): 145-148.
- Friedl, M.A. and Brodley, C.E. (1997) 'Decision tree classification of land cover from remotely sensed data', *Remote Sensing of Environment* 61 (3): 399-409.
- Furby, S., Caccetta, P., Wu, X. and Chia, J. (2008) 'Continental scale land cover change monitoring in Australia using Landsat imagery.', *International Earth Conference: Studying, Modeling and Sense Making of Planet Earth, June 2008*, Mytilene, Lesvos, Greece: 1-8.
- Galvao, L.S., Formaggio, A.R. and Tisot, D.A. (2005) 'Discrimination of sugarcane varieties in Southeastern Brazil with EO-1 Hyperion data', *Remote Sensing of Environment* 94 (4): 523-534.

- Galvao, L.S., Formaggio, A.R. and Tisot, D.A. (2006) 'The influence of spectral resolution on discriminating Brazilian sugarcane varieties', *International Journal of Remote Sensing* 27 (4): 769-777.
- Gates, D.M., Keegan, H.J., Schleter, J.C. and Weidner, V.R. (1965) 'Spectral properties of plants', *Applied Optics* 4 (1): 11-20.
- Gavier-Pizarro, G.I., Kuemmerle, T., Hoyos, L.E., Stewart, S.I., Huebner, C.D., Keuler, N.S. and Radeloff, V.C. (2012) 'Monitoring the invasion of an exotic tree (*Ligustrum lucidum*) from 1983 to 2006 with Landsat TM/ETM+ satellite data and Support Vector Machines in Córdoba, Argentina', *Remote Sensing of Environment* 122: 134-145.
- Gitelson, A.A. and Merzlyak, M.N. (1994) 'Quantitative estimation of chlorophyll-*a* using reflectance spectra: experiments with autumn chestnut and maple leaves', *Journal of Photocmemistry and Photobiology B: Biology* 22 (3): 247-252.
- Gitelson, A.A., Merzlyak, M.N. and Lichtenthaler, H.K. (1996) 'Detection of red edge position and chlorophyll content by reflectance measurements near 700 nm', *Journal of Plant Physiology* 148 (3-4): 501-508.
- Glenn, N.F., Mundt, J.T., Weber, K.T., Prather, T.S., Lass, L.W. and Pettingill, J. (2005) 'Hyperspectral data processing for repeat detection of small infestations of leafy spurge', *Remote Sensing of Environment* 95 (3): 399-412.
- Goetz, A.F.H., Vane, G., Solomon, J.E. and Rock, B.N. (1985) 'Imaging spectrometry for earth remote sensing', *Science* 228 (4704): 1147-1153.
- Government of Western Australia (1976) Agriculture and Related Resources Protection Act 1976. IN Australia, GoW (ed.) Government of Western Australia, Australia.
- Green, A.A., Berman, M., Switzer, P. and Craig, M.D. (1988) 'A transform for ordering multispectral data in terms of image quality with implications for noise removal', *IEEE Transactions of Geoscience and Remote Sensing* 26 (1): 65-74.
- Haapanen, R., Ek, A.R., Bauer, M.E. and Finley, A.O. (2004) 'Delineation of forest/nonforest land use classes using nearest neighbor methods', *Remote Sensing of Environment* 89 (3): 265-271.
- Haboudane, D., Miller, J.R., Pattey, E., Zarco-Tejada, P.J. and Strachan, I.B. (2004) 'Hyperspectral vegetation indices and novel algorithms for predicting green LAI of crop canopies: Modeling and validation in the context of precision agriculture', *Remote Sensing of Environment* 90 (3): 337-352.
- Haboudane, D., Miller, J.R., Tremblay, N., Zarco-Tejada, P.J. and Dextraze, L. (2002) 'Integrated narrow-band vegetation indices for prediction of crop chlorophyll content for application to precision agriculture', *Remote Sensing of Environment* 81 (2-3): 416-426.

- Han, T., Goodenough, D.G., Dyk, A. and Love, J. (2002) 'Detection and correction of abnormal pixels in Hyperion image', *IGARSS*, Toronto, ON, Canada: 1327-1330.
- Haralick, R.M., Shanmugam, K. and Dinstein, I. (1973) 'Textural features for image classification', *IEEE Transactions on Systems, Man, and Cybernetics* 3 (6): 610-621.
- Harris, R. (1980) 'Spectral and spatial image processing for remote sensing', *International Journal of Remote Sensing* 1 (4): 361-375.
- Hatfield, J.L., Gitelson, A.A., Schepers, J.S. and Walthall, C.L. (2008) 'Application of spectral remote sensing for agronomic decisions', *Agronomy Journal* 100 (S3): S117-S131.
- He, K.S., Rocchini, D., Neteler, M. and Nagendra, H. (2011) 'Benefits of hyperspectral remote sensing for tracking plant invasions', *Diversity and Distributions* 17 (3): 381-392.
- Heinz, D.C. and Chang, C.-I. (2001) 'Fully constrained least squares linear spectral mixture analysis method for material quantification in hyperspectral imagery', *IEEE Transactions of Geoscience and Remote Sensing* 39 (3): 529-545.
- Horler, D.N.H., Dockray, M. and Barber, J. (1983) 'The red edge of plant leaf reflectance', *International Journal of Remote Sensing* 4 (2): 273-288.
- Houborg, R., Soegaard, H. and Boegh, E. (2007) 'Combining vegetation index and model inversion methods for the extraction of key vegetation biophysical parameters using Terra and Aqua MODIS reflectance data', *Remote Sensing of Environment* 106 (1): 39-58.
- Huang, C., Davis, L.S. and Townshend, J.R.G. (2002) 'An assessment of support vector machines for land cover classification', *International Journal of Remote Sensing* 23 (4): 725-749.
- Huang, C., Geiger, E.L., Van Leeuwen, W.J.D. and Marsh, S.E. (2009) 'Discrimination of invaded and native species sites in a semi-desert grassland using MODIS multi-temporal data', *International Journal of Remote Sensing* 30 (4): 897-917.
- Hunt, E.R., McMurtrey III, J.E., Parker-Williams, A.E. and Corp, L.A. (2004) 'Spectral characteristics of leafy spurge (*Euphorbia esula*) leaves and flower bracts', *Weed Science* 52 (4): 492-497.
- Hunt, E.R. and Rock, B.N. (1989) 'Detection of changes in leaf water content using near- and middle-infrared reflectances', *Remote Sensing of Environment* 30 (1): 43-54.
- Hussey, B.M.J., Keighery, G.J., Cousens, R.D., Dodd, J. and Lloyd, S.G. (1997) *Western weeds: A guide to the weeds of Western Australia* The Plant Protection Society of Western Australia, Perth

- Ishii, J. and Washitani, I. (2013) 'Early detection of the invasive alien plant *Solidago altissima* in moist tall grassland using hyperspectral imagery', *International Journal of Remote Sensing* 34 (16): 5926-5936.
- ITT Visual Information Solutions (2006a) ENVI user's guide. ENVI version 4.3. Boulder Colorado.
- ITT Visual Information Solutions (2006b) FLAASH module user's guide. FLAASH Module Version 4.3. Boulder Colorado.
- ITT Visual Information Solutions (2006c) ENvironment for Visualizing Images (ENVI). 4.3 ed., Boulder, Colorado.
- Jensen, J.R. (1996) *Introductory digital image processing: a remote sensing perspective* Prentice-Hall, Upper Saddle River, NJ, p 318.
- Jiménez-Valverde, A. and Lobo, J.M. (2007) 'Threshold criteria for conversion of probability of species presence to either-or presence-absence', *Acta Oecologica* 31 (3): 361-369.
- Jones, H.G. and Vaughan, R.A. (2010) *Remote sensing of vegetation: Principles, techniques, and applications* Oxford University Press, New York
- Jones, R., Alemseged, Y., Medd, R. and Vere, D. (2000) *The distribution, density and economic impact of weeds in the Australian annual winter cropping system*, CRC for Weed Management Systems Technical Series, p 18.
- Jordan, C.F. (1969) 'Derivation of leaf area index from quality of light on the forest floor', *Ecology* 50 (4): 663-666.
- Jupp, D.L.B. and Datt, B. (2004) *Evaluation of the EO-1 Hyperion hyperspectral instrument and its applications at Australian validation sites 2001-2003*, CSIRO Earth Observation Centre Report 2004/06, CSIRO Earth Observation Centre - CSIRO Atmospheric Research, Canberra, p 189.
- Kadmon, R. and Harari-Kremer, R. (1999) 'Landscape-scale regeneration dynamics of disturbed Mediterranean maquis', *Journal of Vegetation Science* 10 (3): 393-402.
- Kanellopoulos, I. and Wilkinson, G.G. (1997) 'Strategies and best practice for neural network image classification', *International Journal of Remote Sensing* 18 (4): 711-725.
- Kasetkasem, T., Arora, M.K. and Varshney, P.K. (2005) 'Super-resolution land cover mapping using a Markov random field based approach', *Remote Sensing of Environment* 96 (3-4): 302-314.
- Kavzoglu, T. and Mather, P.M. (2003) 'The use of backpropagating artificial neural networks in land cover classification', *International Journal of Remote Sensing* 24 (23): 4907-4938.

- Kercher, S.M., Frieswyk, C.B. and Zedler, J.B. (2003) 'Effects of sampling teams and estimation methods on the assessment of plant cover', *Journal of Vegetation Science* 14 (6): 899-906.
- Kimothi, M.M., Anitha, D., Vasistha, H.B., Soni, P. and Chandola, S.K. (2010) 'Remote sensing to map the invasive weed, *Lantana camara* in forests', *Tropical Ecology* 51 (1): 67-74.
- Knipling, E.B. (1970) 'Physical and physiological basis for the reflectance of visible and near-infrared radiation from vegetation', *Remote Sensing of Environment* 1 (1): 155-159.
- Kokaly, R.J. and Clark, R.N. (1999) 'Spectroscopic determination of leaf biochemistry using band-depth analysis of absorption features and stepwise multiple linear regression', *Remote Sensing of Environment* 67 (3): 267-287.
- Kruse, F.A., Lefkoff, A.B., Boardman, J.W., Heidebrecht, K.B., Shapiro, A.T., Barloon, P.J. and Goetz, A.F.H. (1993) 'The Spectral Image Processing System (SIPS) interactive visualization and analysis of imaging spectrometer data', *Remote Sensing of Environment* 44 (2-3): 145-163.
- Labate, D., Ceccherini, M., Cisbani, A., De Cosmo, V., Galeazzi, C., Giunti, L., Melozzi, M., Pieraccini, S. and Stagi, M. (2009) 'The PRISMA payload optomechanical design, a high performance instrument for a new hyperspectral mission', *Acta Astronautica* 65 (9-10): 1429-1436.
- Lamb, D.W. (1998) 'Opportunities for satellite and airborne remote sensing of weeds in Australian crops', In: Medd, RW & Pratley, JE (eds.). *Precision Weed Management in Crops and Pastures*, Wagga Wagga. CRC for Weed Management Systems, pp. 48-54.
- Lass, L.W. and Callihan, R.H. (1997) 'The effect of phenological stage on detectability of yellow hawkweed (*Hieracium pratense*) and oxeye daisy (*Crysanthemum leucanthemum*) with remote multispectral digital imagery', *Weed Technology* 11 (2): 248-256.
- Lass, L.W., Carson, H.W. and Callihan, R.H. (1996) 'Detection of yellow starthistle (*Centaurea solstitialis*) and common St. John's wort (*Hypericum perforatum*) with multi-spectral digital imagery', *Weed Technology* 10 (3): 466-474.
- Lass, L.W., Prather, T.S., Glenn, N.F., Weber, K.T., Mundt, J.T. and Pettingill, J. (2005) 'A review of remote sensing of invasive weeds and example of the early detection of spotted knapweed (*Centaurea maculosa*) and babysbreath (*Gypsophila paniculata*) with a hyperspectral sensor', *Weed Science* 53 (2): 242-251.
- Lass, L.W., Thill, D.C., Shafii, B. and Prather, T.S. (2002) 'Detecting spotted knapweed (*Centaurea maculosa*) with hyperspectral remote sensing technology', *Weed Technology* 16 (2): 426-432.

- Lawes, R.A. and Wallace, J.F. (2008) 'Monitoring an invasive perennial at the landscape scale with remote sensing', *Ecological Management and Restoration* 9 (1): 53-59.
- Lawrence, R.L., Wood, S.D. and Sheley, R.L. (2006) 'Mapping invasive plants using hyperspectral imagery and Breiman Cutler classifications (RandomForest)', *Remote Sensing of Environment* 100 (3): 356-362.
- Leica Geosystems (2005) ERDAS Imagine. 9 ed. Leica Geosystems Geospatial Imaging,
- Liangyun, L., Tang, H., Caccetta, P., Lehmann, E.A., Hu, Y. and Wu, X. (2013) 'Mapping afforestation and deforestation from 1974 to 2012 using Landsat time-series stacks in Yulin District, a key region of the Three-North Shelter region, China', *Environmental Monitoring and Assessment* 185 (12): 9949-9965.
- Lillesand, T.M. and Kiefer, R.W. (2000) *Remote sensing and image interpretation*, Forth Ed., John Wiley & Sons, New York, p 724.
- Lippitt, C.D., Rogan, J., Toledano, J., Sangermano, F., Eastman, R.J., Mastro, V. and Sawyer, A. (2008) 'Incorporating anthropogenic variables into a species distribution model to map gypsy moth risk', *Ecological Modelling* 210 (3): 339-350.
- Liu, C.L., Berry, P.M., Dawson, T.P. and Pearson, R.P. (2005) 'Selecting thresholds of occurrence in the prediction of species distributions', *Ecography* 28 (3): 385-393.
- Lloyd, C.D., Berberoglu, S., Curran, P.J. and Atkinson, P.M. (2004) 'A comparison of texture measures for the per-field classification of Mediterranean land cover', *International Journal of Remote Sensing* 25 (19): 3943-3965.
- Lobo, A., Chic, O. and Casterad, A. (1996) 'Classification of Mediterranean crops with multisensor data: per-pixel versus per-object statistics and image segmentation', *International Journal of Remote Sensing* 17 (12): 2385-2400.
- Lobo, J.M., Jiménez-Valverde, A. and Real, R. (2008) 'AUC: a misleading measure of the performance of predictive distribution models', *Global Ecology and Biogeography* 17 (2): 145-151.
- Lu, D. and Weng, Q. (2007) 'A survey of image classification methods and techniques for improving classification performance', *International Journal of Remote Sensing* 28 (5): 823-870.
- Lu, M.-L., Huang, J.-Y., Chung, Y.-L. and Huang, C.-Y. (2013) 'Modelling the invasion of a Central American Mimosoid tree species (*Leucaena leucocephala*) in a tropical coastal region of Taiwan', *Remote Sensing Letters* 4 (5): 485-493.
- Luo, L. and Mountrakis, G. (2011) 'Converting local spectral and spatial information from a priori classifiers into contextual knowledge for impervious surface

- classification', *ISPRS Journal of Photogrammetry & Remote Sensing* 66 (5): 579-587.
- Luscier, J.D., Thompson, J.M., Wilson, J.M., Gorham, B.E. and Dragut, L.D. (2006) 'Using digital photographs and object-based image analysis to estimate percent ground cover in vegetation plots', *Frontiers in Ecology and the Environment* 4 (8): 408-413.
- Magnussen, S., Boudewyn, P. and Wulder, M. (2004) 'Contextual classification of Landsat TM images to forest inventory cover types', *International Journal of Remote Sensing* 25 (12): 2421-2440.
- Martin, M.P., Barreto, L., Riano, D., Fernandez-Quintanilla, C. and Vaughan, P. (2011) 'Assessing the potential of hyperspectral remote sensing for the discrimination of grassweeds in winter cereal crops', *International Journal of Remote Sensing* 32 (1): 49-67.
- Martinko, E.A. (1982). 'Remote sensing and integrated pest management: The case of musk thistle'. In: Johannsen, CJ & Sanders, JL (eds.), *Remote Sensing for Resource Management*, Soil Conservation Society of America, pp. 172-178.
- Mas, J.F. and Flores, J.J. (2008) 'The application of artificial neural networks to the analysis of remotely sensed data', *International Journal of Remote Sensing* 29 (3): 617-633.
- Maselli, F., Conese, C. and Petkov, L. (1994) 'Use of probability entropy for the estimation and graphical representation of the accuracy of maximum likelihood classifications', *ISPRS Journal of Photogrammetry & Remote Sensing* 49 (2): 13-20.
- Mather, P.M. and Koch, M. (2011) *Computer processing of remotely-sensed images: An introduction*, Forth Ed., Wiley-Blackwell, p 434.
- McDaniel, K., Gates, D.H., Findley, R. and Millter, G. (1975) 'An inventory of rangeland brush control projects from ERTS-1 space imagery', *Journal of Range Management* 28 (6): 499-500.
- McGowen, I.J. (1998) 'Remote sensing: background to the technology and opportunities for mapping pasture weeds', In: Medd, RW & Pratley, JE (eds.). *Precision Weed Management in Crops and Pastures*, Wagga Wagga, 5-6 May. CRC for Weed Management Systems, pp. 36-47.
- McIntyre, D.L. and Menges, C.H. (2004). 'A preliminary conceptual model of remote sensing for detecting small outbreaks of *Mimosa pigra*'. In: Julien, M, Flanagan, G, Heard, T, Hennecke, B, Paynter, Q & Wilson, C (eds.), *Research and Management of Mimosa pigra*, CSIRO Entomology, Canberra, Australia.
- McRoberts, R.E. (2008) 'Using satellite imagery and the k-nearest neighbors technique as a bridge between strategic and management forest inventories', *Remote Sensing of Environment* 112 (5): 2212-2221.

- Melgani, F. and Serpico, S.B. (2003) 'A Markov Random Field approach to spatio-temporal contextual image classification', *IEEE Transactions of Geoscience and Remote Sensing* 41 (11): 2478-2487.
- Menges, C.H., Hill, G.J.E. and Ahmad, W. (2001) 'Use of airborne video data for the characterization of tropical savannas in northern Australia: The optimal spatial resolution for remote sensing applications', *International Journal of Remote Sensing* 22 (5): 727-740.
- Miao, X., Gong, P., Swope, S., Pu, R., Carruthers, R., Anderson, G.L., Heaton, J.S. and Tracy, C.R. (2006) 'Estimation of yellow starthistle abundance through CASI-2 hyperspectral imagery using linear spectral mixture models', *Remote Sensing of Environment* 101 (3): 329-341.
- Milton, E.J. (1987) 'Principles of field spectroscopy', *International Journal of Remote Sensing* 8 (12): 1807-1827.
- Milton, E.J., Schaepman, M.E., Anderson, K., Kneubühler, M. and Fox, N. (2009) 'Progress in field spectroscopy', *Remote Sensing of Environment* 113 (S1): S92-S109.
- Mirik, M., Ansley, J.R., Steddom, K., Jones, D.C., Rush, C.M., Michels Jr., G.J. and Elliott, N.C. (2013) 'Remote distinction of A noxious weed (musk thistle: *Carduus Nutans*) using airborne hyperspectral imagery and the Support Vector Machine classifier', *Remote Sensing* 5 (2): 612-630.
- Mirik, M., Steddom, K. and Michels Jr., G.J. (2006) 'Estimating biophysical characteristics of musk thistle (*Carduus nutans*) with three remote sensing instruments', *Rangeland Ecology & Management* 59 (1): 44-54.
- Mitchell, A.L., McGowan, I., Roff, A. and Day, M. (2006) 'Remote sensing detection and mapping of Paterson's curse'. 13th ARSPC, Canberra, Australia
- Mitchell, J.J. and Glenn, N.F. (2009) 'Subpixel abundance estimates in mixture-tuned matched filtering classifications of leafy spurge (*Euphorbia esula* L.)', *International Journal of Remote Sensing* 30 (23): 6099-6119.
- Momani, B.A., McClean, S. and Morrow, P. (2006) 'Using Dempster-Shafer to incorporate knowledge into satellite image classification', *Artificial Intelligence Review* 25 (1-2): 161-178.
- Monserud, R.A. and Leemans, R. (1992) 'Comparing global vegetation maps with the Kappa statistic', *Ecological Modelling* 62 (4): 275-293.
- Moody, M.E. and Mack, R.N. (1988) 'Controlling the spread of plant invasions: the importance of nascent foci', *Journal of Applied Ecology* 25 (3): 1009-1021.
- Mountrakis, G., Im, J. and Ogole, C. (2011) 'Support vector machines in remote sensing: A review', *ISPRS Journal of Photogrammetry & Remote Sensing* 66 (3): 247-259.

- Müllerová, J., Pergl, J. and Pyšek, P. (2013) 'Remote sensing as a tool for monitoring plant invasions: Testing the effects of data resolution and image classification approach on the detection of a model plant species *Heracleum mantegazzianum* (giant hogweed)', *International Journal of Applied Earth Observation and Geoinformation* 25: 55-65.
- Mundt, J.T., Glenn, N.F., Weber, K.T., Prather, T.S., Lass, L.W. and Pettingill, J. (2005) 'Discrimination of hoary cress and determination of its detection limits via hyperspectral image processing and accuracy assessment techniques', *Remote Sensing of Environment* 96 (3-4): 509-517.
- Ngouajio, M., Lemieux, C., Fortier, J.-J., Careau, D. and Leroux, G.D. (1998) 'Validation of an operator-assisted module to measure weed and crop leaf cover by digital image analysis', *Weed Technology* 12 (3): 446-453.
- Nixon, P.R., Escobar, D.E. and Menges, R.M. (1985) 'A multiband video system for quick assessment of vegetal condition and discrimination of plant species', *Remote Sensing of Environment* 17 (2): 203-208.
- Noonan, M. and Chafer, C. (2007) 'A method for mapping the distribution of willow at a catchment scale using bi-seasonal SPOT5 imagery', *Weed Research* 47 (2): 173-181.
- Nordblom, T., Smyth, M., Swirepik, A., Sheppard, A. and Briese, D. (2001) 'Benefit-cost analysis for biological control of *Echium* weeds species (Paterson's curse/Salvation Jane)', *45 Annual Conference of the Australian Agricultural and Resource Economics Society (AARES), 23-25 January 2001*, Adelaide:
- Olmstead, M.A., Wample, R., Greene, S. and Tarara, J. (2004) 'Nondestructive measurement of vegetative cover using digital image analysis', *HortScience* 39 (1): 55-59.
- Osborne, P.E., Alonso, J.C. and Bryant, R.G. (2001) 'Modelling landscape-scale habitat use using GIS and remote sensing: a case study with great bustards', *Journal of Applied Ecology* 38 (2): 458-471.
- Otukei, J.R. and Blaschke, T. (2010) 'Land cover change assessment using decision trees, support vector machines and maximum likelihood classification algorithms', *International Journal of Applied Earth Observation and Geoinformation* 125 (S1): S27-S31.
- Pal, M. and Mather, P.M. (2003) 'An assessment of the effectiveness of decision tree methods for land cover classification', *Remote Sensing of Environment* 86 (4): 554-565.
- Paola, J.D. and Schowengerdt, R.A. (1995) 'A review and analysis of backpropagation neural networks for classification of remotely-sensed multi-spectral imagery', *International Journal of Remote Sensing* 16 (16): 3033-3058.

- Parker-Williams, A. and Hunt, R.E. (2002) 'Estimation of leafy spurge cover from hyperspectral imagery using mixture tuned matched filtering', *Remote Sensing of Environment* 82 (2-3): 446-456.
- Parker-Williams, A. and Hunt, R.E. (2004) 'Accuracy assessment for detection of leafy spurge with hyperspectral imagery', *Journal of Rangeland Management* 57 (1): 106-112.
- Parsons, W.T. and Cuthbertson, E.G. (2001) *Noxious weeds of Australia*, 2nd edition Ed., CSIRO Publishing
- Pearlman, J.S., Barry, P.S., Segal, C.C., Shepanski, J., Beiso, D. and Carman, S.L. (2003) 'Hyperion, a space-based imaging spectrometer', *IEEE Transactions of Geoscience and Remote Sensing* 41 (6): 1160-1173.
- Pengra, B.W., Johnston, C.A. and Loveland, T.R. (2007) 'Mapping an invasive plant, *Phragmites australis*, in coastal wetlands using the EO-1 Hyperion hyperspectral sensor', *Remote Sensing of Environment* 108 (1): 74-81.
- Peters, A.J., Reed, B.C., Eve, M.D. and McDaniel, K.C. (1992) 'Remote sensing of broom snakeweed (*Gutierrezia sarothrae*) with NOAA-10 spectral image processing', *Weed Technology* 6 (4): 1015-1020.
- Peterson, E.B. (2005) 'Estimating cover of an invasive grass (*Bromus tectorum*) using tobit regression and phenology derived from two dates of Landsat ETM+ data', *International Journal of Remote Sensing* 26 (12): 2491-2507.
- Phinn, S., Scarth, P., Gill, T., Roelfsema, C. and Stanford, M. (2008) *Field spectrometer and radiometer guide - version 4*. <http://ww2.gpem.uq.edu.au/CRSSIS/publications/CRSSIS_Field_Spectrometry_Guide_010508.pdf>. Viewed online: June 14 2009.
- Piggin, C.M. (1976) 'Factors affecting seedling establishment and survival of *Echium plantagineum* L., *Trifolium subterraneum* L. and *Lolium rigidum* Gaud.', *Weed Research* 16 (4): 267-272.
- Piggin, C.M. (1977) 'The nutritive value of *Echium plantagineum* L. and *Trifolium subterraneum* L.', *Weed Research* 17 (6): 361-365.
- Piggin, C.M. (1979) 'Control of *Echium plantagineum* L. with 2,4-D and grazing management', *Weed Research* 19 (1): 17-23.
- Piggin, C.M. and Sheppard, A.W. (1995). '*Echium plantagineum* L.'. In: Groves, RH, Shepherd, RCH & Richardson, RG (eds.), *The Biology of Australian Weeds Volume 1*, R.G. and F.J. Richardson, Frankston, pp. 87-110.
- Pitt, J.L. and Miller, I.L. (1988) 'A review of survey techniques for the detection of weeds with particular reference to *Mimosa pigra* L. in Australia and Thailand', *Plant Protection Quarterly* 3 (4): 149-155.
- Pohar, M., Blas, M. and Turk, S. (2004) 'Comparison of logistic regression and linear discriminant analysis: A simulation study', *Metodološki zvezki* 1 (1): 143-161.

- Pontius Jr., R.G. and Schneider, L.C. (2001) 'Land-cover change model validation by an ROC method for the Ipswich watershed, Massachusetts, USA', *Agriculture, Ecosystems, and Environment* 85 (1-3): 239-248.
- Pu, R., Gong, P., Biging, G.S. and Larrieu, M.R. (2003) 'Extraction of red edge optical parameters from Hyperion data for estimation of forest leaf area index', *IEEE Transactions of Geoscience and Remote Sensing* 41 (4): 916-921.
- Purevdorj, T.S., Tateishi, R., Ishiyama, T. and Honda, Y. (1998) 'Relationships between percent vegetation cover and vegetation indices', *International Journal of Remote Sensing* 19 (18): 3519-3535.
- Ramsey III, E. and Nelson, G. (2005) 'A whole image approach using field measurements for transforming EO1 Hyperion hyperspectral data into canopy reflectance spectra', *International Journal of Remote Sensing* 26 (8): 1589-1610.
- Ramsey III, E., Rangoonwala, A., Nelson, G. and Ehrlich, R. (2005a) 'Mapping the invasive species, Chinese tallow, with EO1 satellite Hyperion hyperspectral image data and relating tallow occurrences to a classified Landsat Thematic Mapper land cover map', *International Journal of Remote Sensing* 26 (8): 1637-1657.
- Ramsey III, E., Rangoonwala, A., Nelson, G. and Ehrlich, R. (2005b) 'Mapping the invasive species, Chinese tallow, with EO1 satellite Hyperion hyperspectral image data and relating tallow occurrences to a classified Landsat Thematic Mapper land cover map', *International Journal of Remote Sensing* 26 (8): 1637-1657.
- Ramsey III, E., Rangoonwala, A., Nelson, G., Ehrlich, R. and Martella, K. (2005c) 'Generation and validation of characteristic spectra from EO1 Hyperion image data for detecting the occurrence of the invasive species, Chinese tallow', *International Journal of Remote Sensing* 26 (8): 1611-1636.
- Ramsey III, E.W., Nelson, G.A., Sapkota, S.K., Seeger, E.B. and Martella, K.D. (2002) 'Mapping Chinese tallow with color-infrared photography', *Photogrammetric Engineering and Remote Sensing* 68 (3): 251-255.
- Rejmánek, M. (2000) 'Invasive plants: approaches and predictions', *Austral Ecology* 25 (5): 497-506.
- Robinson, T.P., van Klinken, R.D. and Metternicht, G. (2008) 'Spatial and temporal rates and patterns of mesquite (*Prosopis species*) invasion in Western Australia', *Journal of Arid Environments* 72 (3): 175-188.
- Robinson, T.P., van Klinken, R.D. and Metternicht, G. (2010) 'Comparison of alternative strategies for invasive species distribution modeling', *Ecological Modelling* 221 (19): 2261-2269.

- Roujean, J.L., Leroy, K. and Deschamps, P.Y. (1992) 'A bidirectional reflectance model of the earth's surface for the correction of remote sensing data', *Journal of Geophysical Research* 20 (D18): 455-468.
- Rouse, J.W., Haas, R.H., Schell, J.A. and Deering, D.W. (1973) 'Monitoring vegetation systems in the great plains with ERTS', *Third ERTS Symposium*, NASA 309-1317.
- Salazar, L., Kogan, F. and Roytman, L. (2008) 'Using vegetation health indices and partial least squares method for estimation of corn yield', *International Journal of Remote Sensing* 29 (1): 175-189.
- Schlerf, M., Atzberger, C. and Hill, J. (2005) 'Remote sensing of forest biophysical variables using HyMap imaging spectrometer data', *Remote Sensing of Environment* 95 (2): 177-194.
- Schoknecht, N., Tille, P. and Purdie, B. (2004) *Soil-landscape mapping in south-Western Australia: Overview of methodology and outputs*, Resource Management Technical Report November 2004.
- Schut, A.G.T., Gherardi, S.G. and Wood, D.A. (2010) 'Empirical models to quantify the nutritive characteristics of annual pastures in south-west Western Australia', *Crop and Pasture Science* 61 (1): 32-43.
- Schut, A.G.T. and McIntyre, D.L. (2009) 'Quantification of Paterson's curse infestation with remote sensing', *Proceedings of the Surveying & Spatial Sciences Institute Biennial International Conference, 2009*, Adelaide, Surveying & Spatial Sciences Institute: 915-924.
- Seaman, J.T. and Dixon, R.J. (1989) 'Investigations into the toxicity of *Echium plantagineum* in sheep 2. Pen feeding experiments', *Australian Veterinary Journal* 66 (9): 286-292.
- Seaman, J.T., Turvey, W.S., Ottaway, S.J., Dixon, R.J. and Gilmour, A.R. (1989) 'Investigations into the toxicity of *Echium plantagineum* in sheep 1, Field grazing experiments', *Australian Veterinary Journal* 66 (9): 279-285.
- Segal, K., Guanter, L. and Kaufmann, H. (2010) 'Simulation of spatial sensor characteristics in the context of the EnMAP hyperspectral mission', *IEEE Transactions of Geoscience and Remote Sensing* 48 (7): 3046-3054.
- Settle, J.J. and Drake, N.A. (1993) 'Linear mixing and the estimation of ground cover proportions', *International Journal of Remote Sensing* 14 (6): 1159-1177.
- Sharp, B.R. and Bowman, D.M.J.S. (2004) 'Patterns of long-term woody vegetation change in a sandstone-plateau savanna woodland', *Journal of Tropical Ecology* 20 (3): 259-270.
- Sheppard, A.W. and Smyth, M.J. (2002) 'Predicting seedbank decay rates: the effects of field conditions on seed longevity and seedling recruitment in *Echium plantagineum* L.', *Thirteenth Australian Weeds Conference*:

- Sheppard, A.W. and Smyth, M.J. (2012). '*Echium plantagineum* L. – Paterson's curse'. In: Julien, M, McFadyenand, R & Cullen, J (eds.), *Biological Control of Weeds in Australia*, CSIRO Publishing, Melbourne, pp. 211-226.
- Sheppard, A.W., Smyth, M.J. and Swirepik, A. (2001) 'The impact of a root-crown weevil and pasture competition on the winter annual *Echium plantagineum*', *Journal of Applied Ecology* 38 (2): 291-300.
- Silvan-Cardenas, J.L. and Wang, L. (2009) 'Sub-pixel confusion–uncertainty matrix for assessing soft classifications', *Remote Sensing of Environment* 112 (3): 1081-1095.
- Sinden, J., Jones, R., Hester, S., Odom, D., Kalisch, C., James, R. and Cacho, O. (2004) *The economic impact of weeds in Australia*, CRC for Australian Weed Management Technical Series no. 8, CRC for Australian Weed Management, Adelaide, p 55. <http://www.weeds.crc.org.au/documents/tech_series_.pdf>.
- Slater, P.N., Biggar, S.F., Holm, R.G., Jackson, R.D., Mao, Y., Moran, M.S., Palmer, J.M. and Yuan, B. (1987) 'Reflectance- and radiance-based methods for the in-flight absolute calibration of multispectral sensors', *Remote Sensing of Environment* 22 (1): 11-37.
- Slaton, M.R., Hunt, E.R. and Smith, W.K. (2001) 'Estimating near-infrared leaf reflectance from leaf structural characteristics', *American Journal of Botany* 88 (2): 278-284.
- Smith, G.M. and Fuller, R.M. (2001) 'An integrated approach to land cover classification: An example in the island of Jersey', *International Journal of Remote Sensing* 22 (16): 3123-3142.
- Smith, K.L., Steven, M.D. and Colls, J.J. (2004) 'Use of hyperspectral derivative ratios in the red-edge region to identify plant stress responses to gas leaks', *Remote Sensing of Environment* 92 (2): 207-217.
- Smyth, M.J., Sheppard, A.W. and Swirepik, A. (1997) 'The effect of grazing on seed production in *Echium plantagineum*', *Weed Research* 37 (2): 63-70.
- Somers, B. and Asner, G.P. (2013) 'Multi-temporal hyperspectral mixture analysis and feature selection for invasive species mapping in rainforests', *Remote Sensing of Environment* 136: 14-27.
- Somodi, I., Carni, A., Ribeiro, D. and Podobnikar, T. (2012) 'Recognition of the invasive species *Robinia pseudacacia* from combined remote sensing and GIS sources', *Biological Conservation* 150 (1): 59-67.
- Song, C. and Woodcock, C.E. (2003) 'Monitoring forest succession with multitemporal Landsat images: Factors of uncertainty.', *IEEE Transactions of Geoscience and Remote Sensing* 41 (11): 2557-2567.
- SPSS Inc. (2007) *SPSS Statistics Base 17.0 user's guide* SPSS Inc., Chicago, IL

- State Weed Plan Steering Group (2001) *A weed plan for Western Australia*, Bentley, Australia, October 2001, p 44.
- Stehman, S.V. (2009) 'Sampling designs for accuracy assessment of land cover', *International Journal of Remote Sensing* 30 (20): 5243-5272.
- Story, M. and Congalton, R.G. (1986) 'Accuracy assessment: A user's perspective', *Photogrammetric Engineering and Remote Sensing* 52 (3): 397-399.
- Stow, D., Hope, A., Richardson, D., Chen, D., Garrison, C. and Service, D. (2000) 'Potential of colour-infrared digital camera imagery for inventory and mapping of alien plant invasions in South African shrublands', *International Journal of Remote Sensing* 21 (15): 2965-2970.
- Su, L., Chopping, M.J., Rango, A., Martonchik, J.V. and Peters, D.P.C. (2007) 'Support vector machines for recognition of semi-arid vegetation types using MISR multi-angle imagery', *Remote Sensing of Environment* 107 (1-2): 299-311.
- Swain, P.H. and Hauska, H. (1977) 'The decision tree classifier: Design and potential', *IEEE Transactions on Geoscience Electronics* 15 (3): 142-147.
- Termansen, M., McClean, C.J. and Preston, C.D. (2006) 'The use of genetic algorithms and Bayesian classification to model species distributions', *Ecological Modelling* 192 (3-4): 410-424.
- Thenkabail, P.S., Enclona, E.A., Ashton, M.S. and Van der Meer, B. (2004) 'Accuracy assessments of hyperspectral waveband performance for vegetation analysis applications', *Remote Sensing of Environment* 91 (3-4): 354-376.
- Thenkabail, P.S., Smith, R.B. and De Pauw, E. (2000) 'Hyperspectral vegetation indices and their relationships with agricultural crop characteristics', *Remote Sensing of Environment* 71 (2): 158-182.
- Thessler, S., Sesnie, S., Ramos Bendaña, Z.S., Ruokolainen, K., Tomppo, E. and Finegan, B. (2008) 'Using k-nn and discriminant analyses to classify rain forest types in a Landsat TM image over northern Costa Rica', *Remote Sensing of Environment* 112 (5): 2485-2494.
- Thoonen, G., Hufkens, K., Vanden Borre, J., Spanhove, T. and Scheunders, P. (2012) 'Accuracy assessment of contextual classification results for vegetation mapping', *International Journal of Applied Earth Observation and Geoinformation* 15: 7-15.
- Tokola, T., Pitkanen, J. and Muinonen, E. (1996) 'Point accuracy of a non-parametric method in estimation of forest characteristics with different satellite materials', *International Journal of Remote Sensing* 17 (12): 2333-2351.
- Tomppo, E. and Halme, M. (2004) 'Using coarse scale forest variables as ancillary information and weighting of variables in k-NN estimation: a genetic algorithm approach', *Remote Sensing of Environment* 92 (1): 1-20.

- Tso, B. and Mather, P.M. (2001) *Classification methods for remotely sensed data* Taylor and Francis, London, p 332.
- Tucker, C.J. (1979) 'Red and photographic infrared linear combinations for monitoring vegetation', *Remote Sensing of Environment* 8 (2): 127-150.
- Turker, M. and Ozdarici, A. (2011) 'Field-based crop classification using SPOT4, SPOT5, IKONOS and QuickBird imagery for agricultural areas: a comparison study', *International Journal of Remote Sensing* 32 (24): 9735-9768.
- Ullah, E., Field, R.P., McLaren, D.A. and Peterson, J.A. (1989a) 'Use of airborne thematic mapper (ATM) to map the distribution of blackberry (*Rubus fruticosus* agg.) (Rosaceae) in the Strzelecki Ranges, south Gippsland, Victoria', *Plant Protection Quarterly* 4 (4): 149-154.
- Ullah, E., Shepherd, R.C.H., Baxter, J.T. and Peterson, J.A. (1989b) 'Mapping flowering Paterson's curse (*Echium plantagineum*) around Lake Hume, north eastern Victoria, using Landsat TM data', *Plant Protection Quarterly* 4 (4): 155-157.
- Underwood, E., Ustin, S. and DiPietro, D. (2003) 'Mapping non-native plants using hyperspectral imagery', *Remote Sensing of Environment* 86 (2): 150-161.
- Underwood, E.C., Mulitsch, M.J., Greenberg, J.A., Whiting, M.L.U., S.L. and Kefauver, S.C. (2006) 'Mapping invasive aquatic vegetation in the Sacramento-San Joaquin Delta using hyperspectral imagery', *Environmental Monitoring and Assessment* 121 (1-3): 47-64.
- Ungar, S.G., Pearlman, J.S., Mendenhall, J.A. and Reuter, D. (2003) 'Overview of the Earth Observing One (EO-1) mission', *IEEE Transactions of Geoscience and Remote Sensing* 41 (6): 1149-1159.
- United States Geological Survey (2014) *Data Acquisition Request (DAR) Information*. <<https://eo1.usgs.gov/dar/instructions>>. Viewed online: January 21 2014.
- Wang, L., Silván-Cárdenas, J.L., Yang, J. and Frazier, A.E. (2013) 'Invasive saltcedar (*Tamarisk* spp.) distribution mapping using multiresolution remote sensing imagery', *The Professional Geographer* 65 (1): 1-15.
- Whiteside, T.G., Boggs, G.S. and Maier, S.W. (2011) 'Extraction of tree crowns from very high resolution imagery over Eucalypt dominant tropical savanna', *Photogrammetric Engineering and Remote Sensing* 77 (8): 813-824.
- Wiegand, C.L., Richardson, A.J., Escobar, D.E. and Gerbermann, A.H. (1991) 'Vegetation indices in crop assessments', *Remote Sensing of Environment* 35 (2-3): 105-119.
- Wilfong, B.N., Gorchov, D.L. and Henry, M.C. (2009) 'Detecting an invasive shrub in deciduous forest understories using remote sensing', *Weed Science* 57 (5): 512-520.

- Woodcock, C.E. and Strahler, A.H. (1987) 'The factor of scale in remote sensing', *Remote Sensing of Environment* 21 (3): 311-332.
- Wyatt, B.K. (2000). 'Vegetation mapping from ground, air and space - Competitive or complimentary techniques?'. In: Alexander, R & Millington, C (eds.), *Vegetation mapping: From patch to planet*, John Wiley & Sons Ltd., pp. 3-15.
- Yang, C. and Everitt, J.H. (2007) 'Evaluating airborne hyperspectral imagery for mapping waterhyacinth infestations', *Journal of Applied Remote Sensing* 1 (1): 013546.
- Yang, C., Everitt, J.H. and Johnson, H.B. (2009) 'Applying image transformation and classification techniques to airborne hyperspectral imagery for mapping ashe juniper infestations', *International Journal of Remote Sensing* 30 (11): 2741-2758.
- Yang, C.C., Prasher, S.O., Landry, J.A., Perret, J. and Ramaswamy, H.S. (2000) 'Recognition of weeds with image processing and their use with fuzzy logic for precision farming', *Canadian Agricultural Engineering* 42 (4): 195-200.
- Zhang, X.Y., Friedl, M.A. and Schaaf, C.B. (2006) 'Global vegetation phenology from Moderate Resolution Imaging Spectroradiometer (MODIS): Evaluation of global patterns and comparison with in situ measurements', *Journal of Geophysical Research-Biogeosciences* 111 (G4): G04017.
- Zhao, Y., Zhang, L., Li, P. and Huang, B. (2007) 'Classification of high spatial resolution imagery using improved Gaussian Markov Random-Field-based texture features', *IEEE Transactions of Geoscience and Remote Sensing* 45 (5): 1458-1468.
- Zweig, M.H. and Campbell, G. (1993) 'Receiver-Operating Characteristic (ROC) plots: A fundamental evaluation tool in clinical medicine', *Clinical Chemistry* 39 (4): 561-577.

Every reasonable effort has been made to acknowledge the owners of copyright material. I would be pleased to hear from any copyright owner who has been omitted or incorrectly acknowledged.

APPENDIX A

CHARACTERISTICS OF WEEDS FOR DETECTION WITH REMOTE SENSING

(CHAPTER 2)



Table A.1 Summary of remote sensing applications of weeds with reference to detection characteristics.

Common Name	Scientific Name	Form/type	Characteristics	Distinguishing Features	References	Other Notes
Chinese tamarisk	<i>Tamarix sp.</i>	Deciduous shrub to 4.5 m in height	Foliage colour	Yellow-orange foliage - distinguished from native vegetation due to higher reflectance in visible (550 & 650 nm) wavelengths	Everitt and Deloach (1990)	Similar near infrared reflectance to co-occurring native vegetation
Broom snakeweed	<i>Gutierrezia sarothrae</i>	Deciduous shrub	Flower colour	Bright golden flowers, higher green and red reflectance compared to co-occurring vegetation	Everitt, <i>et al.</i> (1987); Peters, <i>et al.</i> (1992)	
Blackberry	<i>Rubus fruticosus</i>	Perennial, semi-deciduous, scrambling shrubs, up to several metres in height	Canopy reflectance	Higher near infrared reflectance compared to co-occurring vegetation due to higher canopy density	Dehaan, <i>et al.</i> (2007); Frazier (1998); Ullah, <i>et al.</i> (1989a)	
Paterson's curse	<i>Echium plantagineum</i>	Annual/bi-annual herb	Flower colour	Higher reflectance in visible (blue and red) compared to co-occurring pasture species; higher near infrared when co-occurring pasture species in senescent phase	Bulman (2004); Ullah, <i>et al.</i> (1989b)	
Leafy spurge	<i>Euphorbia esula</i>	Perennial herb to 1.2 m in height	Flower colour	Bright yellow-green bracts, higher visible reflectance than co-occurring vegetation	Everitt, <i>et al.</i> (1995); Hunt, <i>et al.</i> (2004)	
Spotted knapweed	<i>Centaurea maculosa</i>	Perennial herb to 1.2 m in high	Not provided	Nothing in paper to relate spectral distinctiveness to remote sensing results	Lass, <i>et al.</i> (2002)	

Common Name	Scientific Name	Form/type	Characteristics	Distinguishing Features	References	Other Notes
Babysbreath	<i>Gypsophila paniculata</i>	Shrub. Multiple branched stems up to 1 m in height	Not provided	Nothing in paper about spectral distinctiveness and relation to remote sensing	Lass, <i>et al.</i> (2005)	
Hoary cress	<i>Phragmites australis</i>	Perennial x; 30–60 cm in height; rhizomatous	Flower colour, arrangement	Dense white flowers forming a flat and mat-like structure	Mundt, <i>et al.</i> (2005)	
Chinese tallow	<i>Sapium sebiferum</i>	Deciduous tree to 8 m in height	Foliage colour	Bright red leaves during autumn	Ramsey III, <i>et al.</i> (2002)	
Ashe juniper	<i>Juniperus ashei</i>	Evergreen shrub/small tree; multi-stemmed; up to 6 m in height	Leaf arrangement	Erectophile leaves, lower visible & near infrared reflectance than co-occurring vegetation	Everitt, <i>et al.</i> (2007b); Yang, <i>et al.</i> (2009)	
Para grass	<i>Urochloa mutica</i>	Perennial grass	Canopy architecture		Boyden, <i>et al.</i> (2013); Catt and Thirarongnarong (1992)	
Mimosa	<i>Mimosa pigra</i>	Perennial shrub; spreading; up to 4 m in height	Canopy reflectance	Shrub structure against grass/sedge background; retains small green leaves when floodplain in senescent condition	Barano and Hartono (2004); McIntyre and Menges (2004)	
Perennial pepperweed	<i>Lepidium latifolium</i>	Perennial herb; up to 2 m in height	Flower colour	Many small white flowers in clusters at the end of leafy branches; Mostly occurs as monocultures; Flowering & fruiting phenology: canopy top panicle inflorescence of white flowers, produces high reflectance in the visible part of the spectrum	Andrew and Ustin (2006; 2008)	

Common Name	Scientific Name	Form/type	Characteristics	Distinguishing Features	References	Other Notes
Iceplant	<i>Carpobrotus edulis</i>	Succulent perennial	Not provided	Nothing in paper about spectral distinctiveness and relation to remote sensing	Underwood, <i>et al.</i> (2003)	
Jubata grass	<i>Cortaderia jubata</i>	Perennial tussock grass; can form mats up to 20 m wide, 50 cm in depth	Not provided	Nothing in paper about spectral distinctiveness and relation to remote sensing	Underwood, <i>et al.</i> (2003)	
False broomweed	<i>Ericameria austrotexana</i>	Perennial shrub to 1 m in height	Leaf arrangement	Has an erectophile canopy (erect leaf), compared with co-occurring species with planophile (horizontal leaf) canopies	Anderson, <i>et al.</i> (1993)	
Yellow starthistle	<i>Centaurea solstitialis</i>	Annual herb to 1 m in height	Foliage reflectance	Yellow flowers; lower near infrared reflectance than co-occurring vegetation, but confused with rock/soil	Lass, <i>et al.</i> (1996)	
Common St. Johnswort	<i>Hypericum perforatum</i>	Perennial	Foliage colour	Clusters of golden yellow flowers; lower radiance in the visible bands than co-occurring vegetation	Lass, <i>et al.</i> (1996)	
Yellow hawkweed	<i>Hieracium pratense</i>	Creeping perennial	Flower colour	Bright yellow flowers; spectrally separable from co-occurring vegetation in the visible wavelengths (yellow-green-red)	Lass and Callihan (1997)	
Huisache	<i>Acacia farnesiana</i>	Woody legume	Flower colour	Bright orange-yellow flowers, higher reflectance in green and red wavelengths	Everitt and Villarreal (1987)	

Common Name	Scientific Name	Form/type	Characteristics	Distinguishing Features	References	Other Notes
Mexican palo-verde	<i>Parkinsonia aculeata</i>	Woody legume	Flower colour	Dense yellow flowers; higher reflectance in green wavelength than co-occurring vegetation	Everitt and Villarreal (1987)	
Spiny aster	<i>Aster spinosus</i>	Perennial herb to 1.5 m in height	Canopy architecture	Less dense erectophile canopy, discriminated from co-occurring vegetation by lower near infrared reflectance	Everitt, <i>et al.</i> (1987)	Similar reflectance to co-occurring vegetation when flowering
Common goldenweed and Drummond goldenweed	<i>Isocoma coronopifolia</i> and <i>Isocoma drummondii</i>	Small shrub	Flower colour	Golden yellow flowers; higher visible reflectance than co-occurring vegetation, lower visible reflectance than soil	Everitt, <i>et al.</i> (1992)	
Big bend loco	<i>Astragalus mollissimus</i> var. <i>earlei</i>	Short lived perennial	Canopy reflectance	Higher near infrared reflectance compared to co-occurring vegetation due to higher canopy density	Everitt, <i>et al.</i> (1994)	
Wooton loco	<i>Astragalus wootonii</i>	Annual or biennial	Canopy reflectance	Higher near infrared reflectance compared to co-occurring vegetation due to higher canopy density	Everitt, <i>et al.</i> (1994)	Similar reflectance to co-occurring vegetation when not flowering
Redberry juniper	<i>Juniperus pinchotii</i>	Evergreen shrub/small tree; up to 3 m in height	Foliage colour	Higher vegetation density and darker green foliage than co-occurring vegetation in February	Everitt, <i>et al.</i> (2001)	
Giant reed	<i>Arundo donax</i> L.	Perennial grass; 2–8 m in height	Canopy reflectance	Forms dense stands with higher vegetation density; higher near infrared reflectance than co-occurring vegetation	Everitt, <i>et al.</i> (2004)	Spectrally distinctive from co-occurring vegetation in

Common Name	Scientific Name	Form/type	Characteristics	Distinguishing Features	References	Other Notes
						summer and autumn
Water lettuce	<i>Pistia stratiotes</i> L.	Free floating macrophyte	Foliage colour	Light green foliage colour results in higher green and red reflectance than darker green co-occurring vegetation	Everitt, <i>et al.</i> (2003)	
Hydrilla	<i>Hydrilla verticillata</i>	Submersed plant	Foliage colour	Very dark green foliage results in less green and red reflectance than lighter green co-occurring vegetation	Everitt, <i>et al.</i> (1999)	Not spectrally distinctive in green and red from dark green co-occurring vegetation
Kudzu	<i>Pueraria montana</i>	Herbaceous to semi-woody vine	Canopy reflectance	Produces large leaves and grows amongst and over native vegetation, resulting in high near infrared reflectance	Cheng, <i>et al.</i> (2007)	
Water hyacinth	<i>Eichhornia crassipes</i>	Emergent floating perennial macrophyte	Canopy reflectance	Dense dark green foliage results in higher near infrared reflectance than co-occurring vegetation	Everitt and Yang (2007a); Everitt, <i>et al.</i> (1999); Underwood, <i>et al.</i> (2006)	
Willow	<i>Salix</i> spp.	Large deciduous spreading shrub	Canopy reflectance	Leaf fall in winter reduces near infrared reflectance compared to native evergreen vegetation. Can be discriminated from native vegetation due to difference between seasonal leaf-on and leaf-off condition	Noonan and Chafer (2007)	Spectrally similar to pasture grass which has similar phenology (senescent in winter)
Amur honeysuckle	<i>Lonicera maackii</i>	Tall understory shrub	Canopy reflectance	The species retains green leaves longer into autumn than deciduous co-occurring over story species; Higher	Wilfong, <i>et al.</i> (2009)	

Common Name	Scientific Name	Form/type	Characteristics	Distinguishing Features	References	Other Notes
				near infrared reflectance		
Cheatgrass	<i>Bromus tectorum</i>	Annual grass	Canopy reflectance	Establishes earlier than co-occurring vegetation, and becomes senescent earlier. Can be discriminated due to seasonal differences of green and senescent	Clinton, <i>et al.</i> (2010); Peterson (2005)	
Prickly acacia	<i>Acacia nilotica</i>	Tree; 5–20 m in height with spreading canopy	Canopy reflectance	Dense stands of the species can be discriminated from background soil and vegetation due to higher near infrared reflectance	Lawes and Wallace (2008)	Medium and low density stands are less reliably discriminated from background soil and vegetation
African olive	<i>Olea europaea</i> L. <i>ssp. Cuspidata</i>	Evergreen small-medium tree	Canopy reflectance	Forms dense stands (> 80% cover) or as dominant understory of lower density Eucalyptus woodland; Spectrally discriminated from native vegetation by higher near infrared reflectance	Cuneo, <i>et al.</i> (2009)	
Shin Oak	<i>Quercus havardii</i>	Deciduous shrub	Foliage colour	Lower visible and near infrared reflectance than co-occurring vegetation	Everitt, <i>et al.</i> (1993)	
Mesquite	<i>Prosopis</i> spp.	Deciduous shrub/tree	Canopy architecture	Canopy distinctive against soil background	Robinson, <i>et al.</i> (2008)	

Common Name	Scientific Name	Form/type	Characteristics	Distinguishing Features	References	Other Notes
Hoary cress	<i>Lepidium draba</i>	Perennial herb	Flower colour	Spectrally distinct from co-occurring vegetation due to dense mats of white flowers	Mundt, <i>et al.</i> (2005)	
Brazilian waterweed	<i>Egeria densa</i>	Submerged aquatic perennial	Foliage reflectance	Green cover near surface has high near infrared reflectance, compared to water background with low near infrared reflectance	Underwood, <i>et al.</i> (2006)	Foliage in deeper water difficult to discriminate
Musk thistle	<i>Carduus nutans</i>	Biennial or Annual herb	Foliage reflectance	Lower NIR reflectance than native vegetation that persisted in June; Most native vegetation senescent in June	Mirik, <i>et al.</i> (2013); Mirik, <i>et al.</i> (2006)	
False acacia/black locust	<i>Robinia pseudacacia</i>	Deciduous tree to average height of 10 m with white flowers	Canopy reflectance/flower colour	More foliage than native vegetation species in spring	Somodi, <i>et al.</i> (2012)	
Late goldenrod	<i>Solidago altissima</i>	Erect perennial herb to 1.2 m. Single or multi-stemmed, with small yellow flowers on upper side of branches	Canopy reflectance	Can be detected in spring as understory before over-story grass species became dominant	Ishii and Washitani (2013)	
Lantana	<i>Lantana camara</i>	Thicket forming perennial shrub to height of 5 m or climbing to height of 15 m	Foliage reflectance	Retains foliage when the deciduous understory species shed their leaves	Kimothi, <i>et al.</i> (2010)	

Common Name	Scientific Name	Form/type	Characteristics	Distinguishing Features	References	Other Notes
Saltcedar	<i>Tamarisk</i> spp.	Tree or shrub that can form dense thickets	Foliage colour	Foliage turns a yellow-orange-brown colour in late autumn-early winter, and the spectral characteristics are different from the surrounding native vegetation	Evangelista, <i>et al.</i> (2009); Frazier and Wang (2011); Wang, <i>et al.</i> (2013)	
Coffee bush	<i>Leucaena leucocephala</i>	Shrub or tree to height of 10–20 m	Canopy shape and reflectance	Low NIR/high visible compared to native vegetation when defoliated in March dry period; opposite in July during monsoon	Lu, <i>et al.</i> (2013)	
Giant Salvinia	<i>Salvinia molesta</i>	Floating aquatic herb	Foliage reflectance	Dense coverage over surface of water	Fletcher, <i>et al.</i> (2010)	
Common and glossy buckthorn	<i>Frangula alnus</i> & <i>Rhamnus cathartica</i>	Deciduous woody shrub/small tree to height of 6–7.5 m	Foliage reflectance	Species form dense thickets; Produces foliage earlier in year than other vegetation species and remains green longer in the season.	Becker, <i>et al.</i> (2013)	
Giant hogweed	<i>Heracleum mantegazzianum</i>	Biennial or monocarpic perennial to height of 5 m	Foliage reflectance/flower cover	Distinctive texture from the flowers and properties such as shape, context (individual plants) allows accurate detection with high spatial resolution remote sensing	Müllerová, <i>et al.</i> (2013)	
Bugweed	<i>Solanum mauritianum</i>	Shrub or small tree 2–12 m in height; well-developed canopies of pale (yellow) to dark green foliage.	Foliage reflectance	A dominant understory species with green and yellow foliage. Can be detected when it grows in gaps in pine forest	Atkinson, <i>et al.</i> (2014)	

Common Name	Scientific Name	Form/type	Characteristics	Distinguishing Features	References	Other Notes
Fire tree	<i>Morella faya</i>	Tree to height of 20 m	Foliage reflectance	<i>Morella</i> experiences leaf flushing in summer (July, August, September) to produce a denser canopy (higher LAI) than native forest species <i>Metrosideros</i> ; <i>Morella</i> foliage yellows in summer-winter transition period and has lower NIR reflectance than native forest; Difference in water content between <i>Morella</i> and <i>Metrosideros</i> in winter.	Somers and Asner (2013)	
Glossy privet	<i>Ligustrum lucidum</i>	Evergreen tree to height of 10 m; dark green leaves	Foliage reflectance	Privet canopies are denser than native forest	Gavier-Pizarro, <i>et al.</i> (2012)	

APPENDIX B

DESCRIPTION OF LANDSCAPE UNITS OF THE STUDY AREA

(CHAPTER 3)



Table B.1 Landscape unit descriptions for units found on the Catholic Agricultural College Bindoon property.

Unit	Landscape	Dominant Soil	Dominant Vegetation	Area (ha)	% of Property
253Ju_2c	Very gentle to moderate hill slopes with some breakaways	Red and yellow duplex and some uniform fine soils which may be gravelly near crests	Dominated by <i>E. wandoo</i> woodland but with some <i>E. loxophleba</i> . <i>Acacia</i> spp. on the sandier topsoil areas	1458	39
253Ju_2a	Very gentle to moderate hill slopes (< 10–15%) and some breakaways on mid and upper slopes	Shallow rocky sandy gravelly earths with some uniform fine and duplex soils	Woodland of <i>E. loxophleba</i> , low <i>E. wandoo</i> with <i>E. calophylla</i> on soils with sandy topsoil. <i>E. marginata</i> on laterite	426	11
253Bn_2x	Very gentle to moderate (< 5–15%) middle and lower hill slopes	Mixed red and yellow duplex soils with some uniform fine and medium textured, structured soils.	Dominated by <i>E. wandoo</i> with a few <i>E. calophylla</i> on light textured topsoils with <i>E. marginata</i> and <i>E. accedens</i> on lateritic outcrops	398	11
253WnYA6	Very gentle to gentle hill slopes (< 10%)	Deep uniform medium textured and duplex pisolitic gravelly earths	Woodland of <i>E. marginata</i> , <i>E. calophylla</i> and <i>E. wandoo</i> with some <i>Dryandra</i> spp. and <i>E. accedens</i>	391	10
253Ju_3a	Gently to moderately sloping valleys	Alluvial red and yellow duplex and uniform fine soils which are often gravelly. Moderately saline	Dominated by <i>E. wandoo</i> but with some and <i>E. marginata</i> and small areas of <i>E. accedens</i> , <i>E. loxophleba</i> , <i>acacias</i> and <i>Casuarina obesa</i> in saline areas	180	5
253Ju_2cs	Gentle to moderate hill slopes with some breakaways	Red and yellow duplex and some uniform fine soils which maybe gravelly near crests	Dominated by <i>E. wandoo</i> woodland but with some <i>E. loxophleba</i> and <i>Acacia</i> spp. on the sandier topsoil areas	145	4
253WnA5	Very gentle to gentle hill slopes (< 10%)	Shallow pisolitic gravelly loams and clay loams over laterite	Mixed woodland and low woodland. Dominated by mixed <i>E. wandoo</i> , <i>E. loxophylla</i> associated with <i>E. marginata</i> and <i>E. accedens</i>	122	3

Unit	Landscape	Dominant Soil	Dominant Vegetation	Area (ha)	% of Property
253Ju_2d	Very gentle to gentle hillslopes	Shallow sandy loams overlying the country rock	Low woodland of <i>E.marginata</i> , <i>E.calophylla</i> and <i>dryandra</i> spp.	111	3
253Ju_3an	Saline gently to moderately sloping valleys	Alluvial red and yellow duplex and uniform fine soils which are often gravelly. Moderately saline	Dominated by <i>E. wandoo</i> but with some and <i>E. marginata</i> and small areas of <i>E. accedens</i>	99	3
253WnYA3	Very gentle to gentle upper slopes (< 10%) and crests	Shallow, pisolitic clayey sands of varying depths overlying laterite	Low woodland and shrubland with scattered trees. Dominated by <i>E. marginata</i> and with some <i>Banksia grandis</i> and <i>Nuytsia floribunda</i> in sandier areas	82	2
253Nn_2x	Very gently sloping valley floors of the upper Brockman river valley	Heavy grey clay alluvium often cracking and gleyed at depth. Not saline at the time of survey, but very prone to salinity	Varied vegetation with the major species <i>E. rudis</i> and <i>melaleucas</i> in the less salt prone areas and <i>E. loxophleba</i> and <i>C. obesa</i> in more salt prone areas	67	2
253Ju_2ds	Gentle to moderate hillslopes (1–15%)	Shallow sandy loams overlying the country rock	Low woodland of <i>E. marginata</i> and <i>Dryandra</i> spp.	57	2
253Bn_3x	Very gentle to gentle foot and lower slopes	Generally not gravelly. Colluvial soils accumulate to form sandy loam to med. clays with highly variable % of coarse fraction.	Varies greatly to <i>E. calophylla</i> on sandier soils to <i>E. loxophleba</i> and <i>E. wandoo</i> on the clays	51	1
253Nn_1x	Very gently sloping valley floors	Yellow gradational and duplex soils, occasionally with coarse, gleyed salty sandy clays and gravelly soils below a metre	<i>E. rudis</i> dominates with <i>E. camaldulensis</i> , <i>Melaleuca</i> spp. and occasionally <i>E. loxophleba</i> with <i>Casuarina obesa</i> in the most salt prone areas	32	< 1

Unit	Landscape	Dominant Soil	Dominant Vegetation	Area (ha)	% of Property
253Bn_1x	Very gentle to moderately sloping (< 15%) crests and hill slopes	Light to medium textured and shallow clay soils with varying percentages of coarse fraction	Dominated by <i>Eucalyptus marginata</i> , <i>E. calophylla</i> , <i>E. wandoo</i> , <i>E. accedens</i> and some <i>Allocasuarina huegeliana</i> (associated rock outcrops)	31	< 1
253Bn_4n	Saline very gently to gently sloping (< 10%) valley floors	Saline alluvial red and yellow duplex and uniform fine soils which are often gravelly	Dominated by acacias and <i>Casuarina obesa</i> . in saline areas and with <i>E. wandoo</i> , <i>E. marginata</i> and small areas of <i>E. accedens</i> , <i>E. loxophleba</i> in less salt	24	< 1
253Ju_2b	Gently to very gently sloping drainage depressions	Yellow and red duplex uniform fine and gradational soils	Mainly <i>E. wandoo</i> woodland but with some <i>E. calophylla</i> on sandy surfaced soils and <i>E. marginata</i> on lateritic soils	22	< 1
253Bn_1s	Gentle to moderately crests and upper hillslopes	Light to medium textured and shallow clay soils with varying percentages of coarse fraction	Dominated by <i>E. marginata</i> , <i>E. calophylla</i> , <i>E. wandoo</i> , <i>E. accedens</i> and some <i>Allocasuarina huegeliana</i>	20	< 1
253WnYA4	Very gentle to gentle upper slopes (< 10%) and summits	Deep pisolitic gravelly clayey sands	Low woodland to woodland to with some shrubland with scattered trees. Dominated by <i>E. marginata</i> and some <i>B. grandis</i>	16	< 1
253Ug_1a	Residual plateau, very gently to gently inclined (< 10%) undulating plain and hillslopes	loamy gravel, some shallow gravel and sandy gravels	Woodland, heath and some mallee spp. <i>E. wandoo</i> and <i>E. calophylla</i> , <i>D. polycephala</i> , <i>D. hewardiana</i> , <i>D. echinata</i> , <i>E. drummondii</i> , <i>E. eudesmioides</i>	12	< 1
253Bn_4x	Very gently to gently alluvial valleys	Alluvial soils are highly variable ranging from sandy loams to duplex red and yellow soils and may have pans underlying them. Not gravelly	Woodland of <i>E. rudis</i> , <i>E. camaldulensis</i> and low <i>Melaleucas</i> spp. With some <i>E. calophylla</i> and <i>Casuarina obesa</i> in the more salinity prone areas	1	< 1

Unit	Landscape	Dominant Soil	Dominant Vegetation	Area (ha)	% of Property
253Bn_2s	Gentle to moderate (3–25%) middle and lower hill slopes	Mixed red and yellow duplex soils with some uniform fine and medium textured, structured soils.	Dominated by <i>E. wandoo</i> , with a few <i>E. calophylla</i> on sandy textured soils and <i>E. marginata</i> and <i>E. accedens</i> on lateritic outcrops	< 1	< 1

Figure B.1 Map showing landscape units for CACB property.

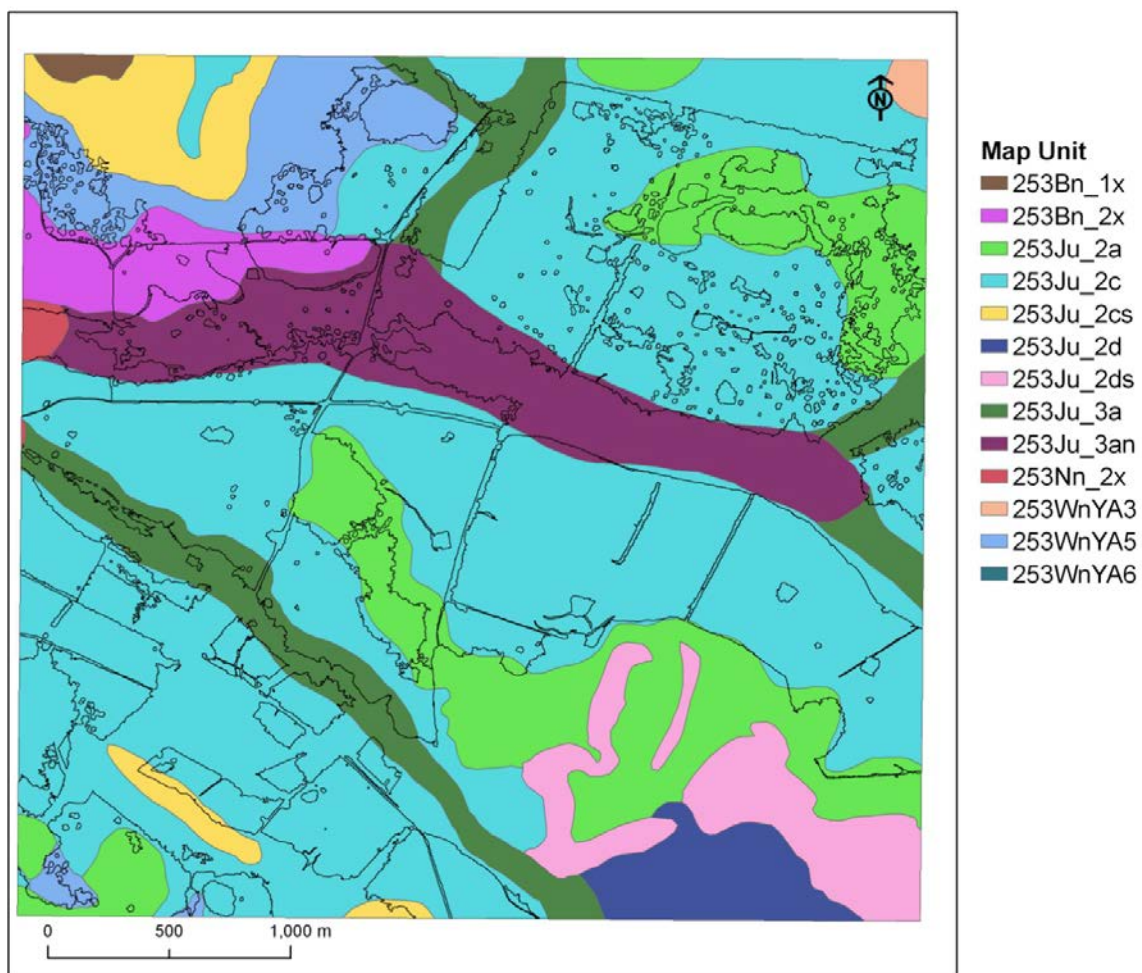


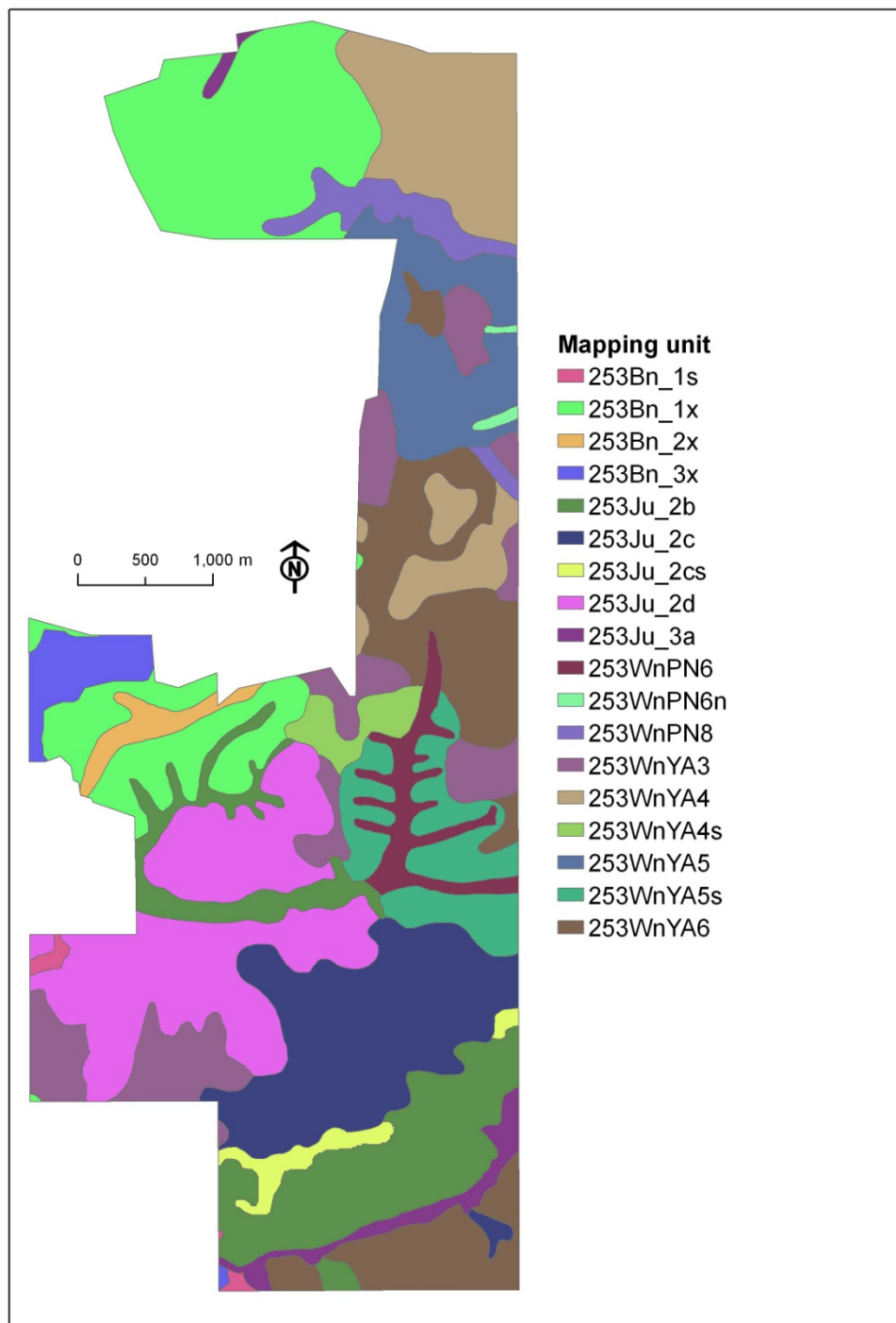
Table B.2 Landscape unit descriptions for the Bindarie and Morden Downs properties.

Unit	Landscape	Dominant Soil	Dominant Vegetation	Area	% of Properties
253Bn_1x	Very gentle to moderately sloping (< 15%) crests and hill slopes	Light to medium textured and shallow clay soils with varying percentages of coarse fraction	Dominated by <i>Eucalyptus marginata</i> , <i>E. calophylla</i> , <i>E. E. wandoo</i> , <i>E. accedens</i> and some <i>Allocasuarina huegeliana</i> (associated rock outcrops)	286	16
253Ju_2d	Very gentle to gentle hillslopes	Shallow sandy loams overlying the country rock	Low woodland of <i>E.marginata</i> , <i>E.calophylla</i> and <i>Dryandra</i> spp.	232	13
253WnYA6	Very gentle to gentle hill slopes (< 10%)	Deep uniform medium textured and duplex pisolitic gravelly earths	Woodland of <i>E. marginata</i> , <i>E. calophylla</i> and <i>E. wandoo</i> with some <i>Dryandra</i> spp. and <i>E. accedens</i>	197	11
253Ju_2c	Very gentle to moderate hill slopes with some breakaways	Red and yellow duplex and some uniform fine soils which may be gravelly near crests	Dominated by <i>E. wandoo</i> woodland but with some <i>E. loxophleba</i> . <i>Acacia</i> spp. on the sandier topsoil areas	195	11
253Ju_2b	Gently to very gently sloping drainage depressions	Yellow and red duplex uniform fine and gradational soils	Mainly <i>E. wandoo</i> woodland but with some <i>E. calophylla</i> on sandy surfaced soils and <i>E. marginata</i> on lateritic soils	191	10
253WnYA4	Very gentle to gentle upper slopes (< 10%) and summits	Deep pisolitic gravelly clayey sands	Low woodland to woodland to with some shrubland with scattered trees. Dominated by <i>E. marginata</i> and some <i>B. grandis</i>	160	9

Unit	Landscape	Dominant Soil	Dominant Vegetation	Area	% of Properties
253WnYA3	Very gentle to gentle upper slopes (< 10%) and crests	Shallow, pisolitic clayey sands of varying depths overlying laterite	Low woodland and shrubland with scattered trees. Dominated by <i>E. marginata</i> and with some <i>Banksia grandis</i> and <i>Nuytsia floribunda</i> in sandier areas	146	8
253WnYA5	Very gentle to gentle hill slopes (< 10%)	Shallow pisolitic gravelly loams and clay loams over laterite	Mixed woodland and low woodland. Dominated by mixed <i>E. wandoo</i> , <i>E. loxophylla</i> associated with <i>E. marginata</i> and <i>E. accedens</i>	102	6
253WnYA5s	Gentle to moderate hill slopes (3–15%)	Shallow pisolitic gravelly loams and clay loams over laterite	Mixed woodland and low woodland. Dominated by mixed <i>E. wandoo</i> , <i>E. loxophylla</i> associated with <i>E. marginata</i> and <i>E. accedens</i>	90	5
253WnPN6	Very gently to gently sloping, poorly drained floors and foot slopes of valleys of the central and eastern Darling Ranges	Alluvial red and yellow loams and clays that may be gravelly and are prone to salinity. Pans may underly these soils.	Dominated by <i>E. wandoo</i> , with <i>E. loxophleba</i> and <i>rudis</i> and <i>Acacia. Casuarina obesa</i> in saline areas	45	2
253WnPN8	Level to gently sloping valley floors and foot slopes of the upper reaches of streams	Lighter soils of loams and sandy duplexes	<i>E. wandoo</i> woodland, some <i>E. rudis</i> and <i>E. camaldulensis</i> . <i>E. marginata</i> where soils are sandy and gravelly. <i>Acacia</i> ssp., Teatree and reeds	40	2
253Bn_3x	Very gentle to gentle foot and lower slopes	Generally not gravelly. Colluvial soils accumulate to form sandy loam to medium clays with highly variable percentages of coarse fraction	Varies greatly to <i>E. calophylla</i> on sandier soils to <i>E. loxophleba</i> and <i>E. wandoo</i> on the clays	37	2

Unit	Landscape	Dominant Soil	Dominant Vegetation	Area	% of Properties
253Ju_3a	Gently to moderately sloping valleys	Alluvial red and yellow duplex and uniform fine soils which are often gravelly. Moderately saline	Dominated by <i>E. wandoo</i> but with some and <i>E. marginata</i> and small areas of <i>E. accedens</i> , <i>E. loxophleba</i> , acacias and <i>Casuarina obesa</i> in saline areas	29	2
253WnYA4s	Gentle to moderate hill slopes (3–15%)	Shallow pisolithic gravelly loams and clay loams over laterite	Mixed woodland and low woodland. Dominated by mixed <i>E. wandoo</i> , <i>E. loxophylla</i> associated with <i>E. marginata</i> and <i>E. accedens</i>	25	1
253Ju_2cs	Gentle to moderate hill slopes with some breakaways	Red and yellow duplex and some uniform fine soils which maybe gravelly near crests	Dominated by <i>E. wandoo</i> woodland but with some <i>E. loxophleba</i> and <i>Acacia</i> spp. on the sandier topsoil areas	21	1
253Bn_2x	Very gentle to moderate (< 5–15%) middle and lower hill slopes	Mixed red and yellow duplex soils with some uniform fine and medium textured, structured soils	Dominated by <i>E. wandoo</i> with a few <i>E. calophylla</i> on light textured topsoils with <i>E. marginata</i> and <i>E. accedens</i> on lateritic outcrops	21	1
253Bn_1s	Gentle to moderately crests and upper hillslopes	Light to medium textured and shallow clay soils with varying percentages of coarse fraction	Dominated by <i>E. marginata</i> , <i>E. calophylla</i> , <i>E. wandoo</i> , <i>E. accedens</i> and some <i>Allocasuarina huegeliana</i>	6	< 1
253WnPN6n	Very gently to gently sloping, poorly drained floors and foot slopes of valleys of the central and eastern Darling Ranges	Saline alluvial red and yellow loams and clays that may be gravelly and are prone to salinity. Pans may underly these soils	Dominated by <i>E. wandoo</i> , with <i>E. loxophleba</i> and rudis and <i>Acacia</i> . <i>Casuarina obesa</i> in saline areas.	4	< 1

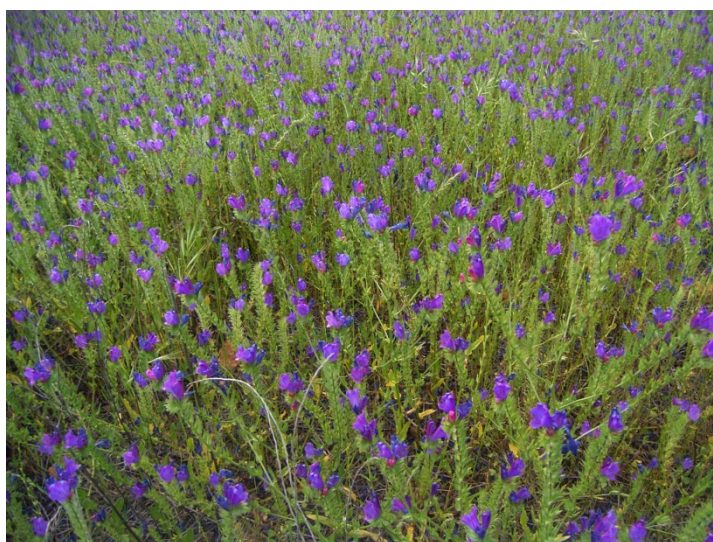
Figure B.2 Landscape units for Binarie and Morden Downs properties.



APPENDIX C

QUANTIFYING THE FLORAL COVER OF PATERSON'S CURSE FROM OBJECT-BASED CLASSIFICATION OF DIGITAL FIELD PHOTOGRAPHY

(CHAPTERS 4 & 5)



1 Introduction

There has been an emphasis in the remote sensing literature on optimum approaches for collecting validation data (Stehman 2009), and techniques for assessing the accuracy of products derived from remote sensed imagery (Congalton and Green 1999). However there has been less emphasis on how the training and validation data (e.g. percentage cover) are classified (Curran and Williamson 1985). Errors in field data have been shown to be as high as those from the processing and classification stage of the imagery, and can result from factors such as spatial variability in terrain, processing error, and variation between personnel due to bias or competency (Curran and Williamson 1985).

Most remote sensing applications for weeds have derived proportion cover of the target species (and other ground cover) either through in-situ visual estimation in the field by a human observer from an oblique perspective (e.g. Casady, *et al.* 2005; Lawrence, *et al.* 2006; Mitchell and Glenn 2009), or field photos have been assessed post-survey by a human interpreter (Andrew and Ustin 2008; Everitt, *et al.* 1994). Some published studies have used digital methods to classify field photography to derive cover estimates, including density slicing (Birdsall, *et al.* 1997), per-pixel classification algorithms (Yang, *et al.* 2000), object based classification (Luscier, *et al.* 2006), and manual classification of pixels from digital imagery (Ngouajio, *et al.* 1998). These applications however were stand-alone, and not used to classify or validate remotely sensed data.

Quantitative classification of field photographs can reduce the variance and error that results from visual estimation techniques (Kercher, *et al.* 2003). A per-pixel approach to classifying field photography can encounter similar problems to aerial and satellite imagery (Blaschke and Strobl 2001), especially when the field imagery is of a very high spatial resolution. A contextual classification approach (Refer Section 2.4.3.4) may be more desirable, as information other than the spectral properties of the target feature is used, such as shape, size, and association with other pixels or objects (Magnussen, *et al.* 2004).

This appendix describes an approach for classifying Paterson's curse floral cover from digital field photos using object based classification (Blaschke 2010) and decision trees (Friedl and Brodley 1997) at the Catholic Agricultural College Bindoon (CACB) study site. Object classification is a potentially useful type of contextual classification for extracting the floral percentage of Paterson's curse from the field data described in Section 3.5. Given that Paterson's curse flowers occur as discrete objects within a very high resolution field photograph, an object classification may be more effective than a pixel based approach. The overall objective was to address a recommendation of Bulman (2004) to derive an accurate quantitative method for determining floral percentage of Paterson's curse flowers from digital field photographs.

2 Methods

The approach consisted of four stages: 1) data collection; 2) image segmentation; 3) development of a classification hierarchy; and 4) accuracy assessment. These stages are described in the following sections.

2.1 Data collection

Transects were surveyed at the Catholic Agriculture College Bindoon (CACB) property between October 9 to 14, 2005, which coincided with the peak flowering period for Paterson's curse at the property for that year. A total of five transects were surveyed in areas where gradients of Paterson's curse densities were observed (Figure 1 and 2). The transects were pegged out prior to the survey using a real-time differential GPS (DGPS-Max). A series of digital photographs were taken at intervals of 4 metres along each transect. At each interval, three separate photographs were captured of a 1 m² quadrat: one quadrat positioned on the transect line, and a quadrat positioned to the immediate left and right of the first (Figure 3). A wide-angle lens (28 mm) digital camera (Ricoh Caplio 400G) was positioned approximately 1.7 m above the centre of each quadrat (nadir) on a modified camera tripod/lighting stand (Manfrotto 420b). The camera height was chosen to allow the operator to manually operate the timer delay for capturing photographs. The survey was conducted between the hours of 08:00 and 17:00, to maximise available time and to reduce the effects of shadow from low sun angle on images.

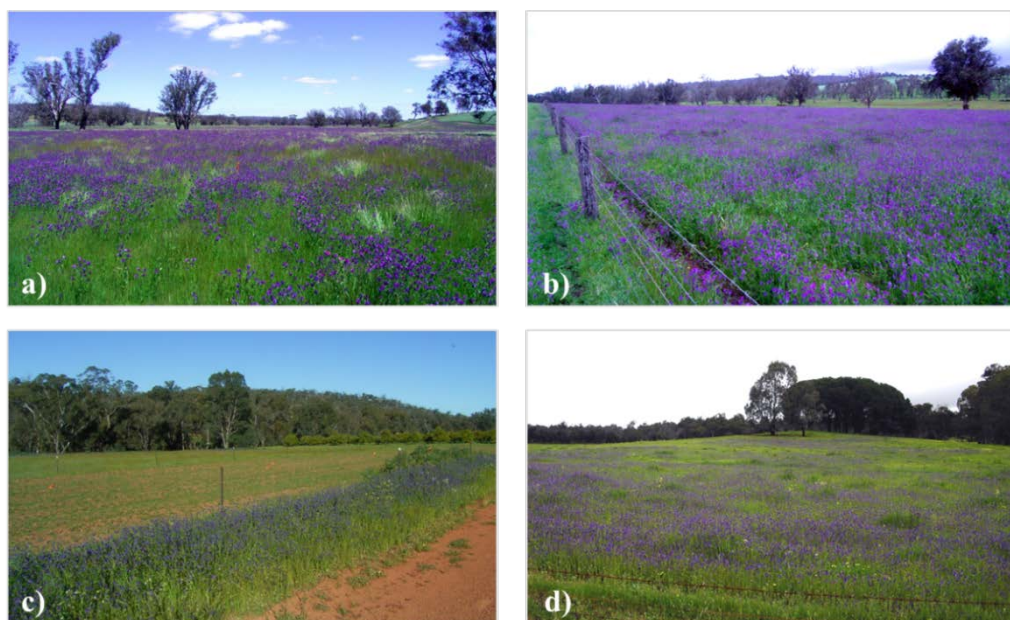


Figure 1 Photos showing representative conditions of the transects at the time of field survey: a) transect 1 b) transect 2; c) transect 3 and d) transects 4 and 5.



Figure 2 Location of transects at CACB overlaid on true-colour DMSI image. Non-relevant areas are masked in grey.

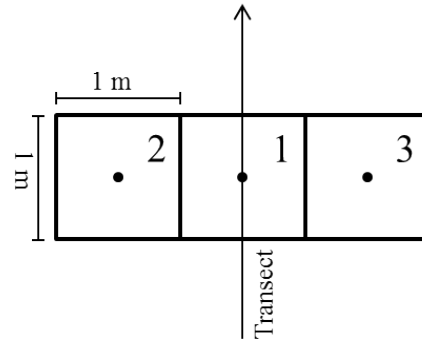


Figure 3 Schematic showing the arrangement of quadrats at each interval along a given transect. Dots denote centres of quadrats.

2.2 Image segmentation

A segmentation algorithm in the eCognition (version 4) software package (Baatz, *et al.* 2004) was used to derive objects for each image. The segmentation process used colour, shape, and a scale factor. The colour or spectral heterogeneity property (h) is the sum of the standard deviations of spectral values in each layer (Baatz, *et al.* 2004) and is given in Equation 1

$$h = \sum_c W_c \times \sigma_c \quad (1)$$

Where W_c is the weighting assigned to a given layer.

The shape property denotes the smoothness and compactness of generated image objects and is given in Equation 2.

$$h = \frac{l}{\sqrt{n}} \quad (2)$$

Where l is the perimeter of an object and n is the sum of pixels within the object.

The scale factor determined the average size of the created objects. The value of the factor was arbitrary and was not related to any quantitative measure of object size. The final output from the segmentation was determined from a combination of the scale factor (25), the heterogeneity colour and shape (both set at 0.5).

2.3 Development of classification hierarchy

A manual decision tree approach (Swain and Hauska 1977) was used to progressively reduce the number of misclassified objects, by dividing them into successive sub-classes in the hierarchy. An exploratory analysis was conducted with the features properties tool in the software, to determine which object features (spectral and spatial properties) were optimal for separating flowers from background. A summary of the properties and values used to derive each class is presented in Table 1, and are described in detail in the following section.

Image objects were classified first into two classes: ‘Flowers 1’ and ‘Non-flowers 1’ using the mean brightness property for band 1 (blue), given in Equation 3.

$$b = \frac{1}{n_L} \times \sum_{i=1}^{n_L} c_i \quad (3)$$

Where n_L is the number of pixels comprising a given image object, and c_i is the mean value for the pixels comprising a given image object for a given band.

The ‘Flowers 1’ class was separated into two sub classes: ‘Non flowers 2’ and ‘Flowers 2’ using the ratio property for band 2 (green). Two further sub-classes: ‘Non Flowers 3’ and ‘Flowers 3’ were derived from Flowers using the shape index property, given in Equation 4 (Baatz, *et al.* 2004):

$$S = \frac{e}{4 \times \sqrt{A}} \quad (4)$$

Where e is the border length of the image object and A is its area.

The property was used to filter out areas of shadow that were very spectrally similar to flowers in the image. These shadow areas typically occurred on the surface of the quadrat, where shadows from the vegetation were cast, and were typically long and elongated. To remove areas of high reflectance, the mean difference to scene property (Equation 5) for band 2 was used to create Non-flowers 4 and the final flowers class called ‘Final flowers’:

$$\Delta C_L = \bar{C}_{L,object} - \bar{C}_{L,scene} \quad (5)$$

Where $\bar{C}_{L,object}$ is the mean value for a given object for a given band, and $\bar{C}_{L,scene}$ is the mean value for the entire image for a given band.

Table 1 Summary of parameters and values used to derive classes in the classification hierarchy.

Class	Property	Band	Value
Non-Flowers 1/Flowers 1	Mean brightness value	1	> 61
Non-Flowers 2/Flowers 2	Mean brightness ratio	2	< 0.295
Non-Flowers 3/Flowers 3	Shape index	N/A	< 2.096
Non-flowers 4/Flowers final	Mean difference to scene	3	< -7

2.4 Accuracy assessment

The classification accuracy was assessed from a random sample of 50 photos from transect data (Section 2.1) that contained Paterson's curse. A traditional error matrix approach was not used as the small size of the classified images was conducive to a systematic assessment of misclassification, rather than using a randomly generated sample. The alternative approach to assessing the accuracy was done by calculating the percentage of pixels in each image that were correctly classified into the final flower class. Accordingly, two new classes were added to the class hierarchy: 'omission' and 'commission'. Omission referred to instances of error where objects that were flowers were not identified as such, and commission referred to instances of error where non-flower objects were classified as flowers. Misclassified objects were manually assigned into the correct class.

3 Results

The results of the transect survey are shown in Table 2. The lengths of individual transects ranged from 120 m to 348 m. There was a total of 264 sample points and Paterson's curse was present in 787 (94%) of the photos. There was high variability in floral cover across all transects, as indicated by the high ranges and standard deviation. Transect 2 had the highest mean floral cover of 7.25% (sd. 3.17%) compared with a mean of 4.02% (sd. 3.29%) for transect 2. The maximum floral

cover for all transects was 19.7%, and the mean floral cover was 2.96%. Figure 4 shows an example of an image where Paterson's curse flowers have been classified.

Table 2 Statistics for floral percentage data for each transect, and all transects combined.

	1	2	3	4	5	All
PC present	241	226	133	97	90	787
No. samples	81	76	46	31	31	264
Length (m)	348	300	188	144	120	N/A
Min (%)	< 1	< 1	< 1	< 1	< 1	< 1
Max (%)	12.76	16.53	12.80	14.43	19.65	19.65
Range (%)	12.73	16.08	12.79	14.42	19.62	19.64
Mean (%)	4.02	7.25	2.97	2.72	3.56	2.97
SD (%)	3.29	3.17	3.16	3.41	3.27	3.20

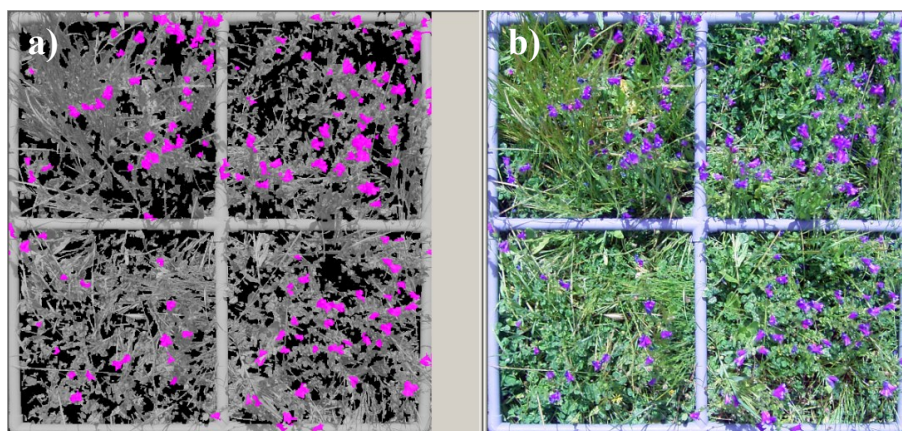


Figure 4 Digital images of a quadrat containing Paterson's curse, with a) classified image; and b) original image.

3.1 Accuracy assessment

The results of the accuracy assessment are summarised in Table 3. The mean floral percentage for the 50 classified validation photographs was 3.8% (SD = 3.2%) with a maximum cover of 11.4%. Omission errors were very low (< 1%) with a mean of 0.11% and a maximum of 0.92%. The maximum commission error was 4.64%, but the mean error was still less than 1%.

Table 3 Summary of floral cover, omission and omission errors from the random sample of field photographs.

	Floral Cover (%)	Omission Error (%)	Commission Error (%)
Mean	3.80	0.11	0.75
SD	3.24	0.12	1.02
Min	0	0	0
Max	11.40	0.92	4.64

The higher instances of commission error occurred due to areas of shadow in the quadrat being misclassified as flowers. There was a variable amount of shadow present in each image, depending on the amount of vegetation present. These shadow areas had very similar spectral properties to flowers where the misclassification occurred.

4 Discussion

The decision tree approach using object based classification was a robust quantitative method for classifying digital field photography, and represented an improvement over the visual estimate of Paterson's curse used by Bulman (2004). The generated cover values were suitable for statistical empirical methods, and classification error could be quantified. The two strengths of the method were that misclassified regions could be reclassified 'on the fly', and that the classification hierarchy could be run as a macro, therefore large numbers of images with variable illumination and ground conditions could be classified accurately and rapidly; The method did not rely on observer experience, and therefore did not produce variance or error within and between observers. The decision tree method has the potential to be successfully applied to other invasive plants and ground cover types, given appropriate discrimination cues.

The other published study which classified field imagery with object based classification was Lusier, *et al.* (2006), who used a nearest-neighbour algorithm rather than a decision tree, and classified multiple cover types rather than a single cover type. The advantage of the nearest neighbour method is that it is rapid and simple—a classification will progress through several iterations until an acceptable

level of accuracy is obtained (Batz, *et al.* 2004). A disadvantage of the method is that the iterative classification process may not be feasible for a large number of images. Another disadvantage of the nearest-neighbour approach is that the training areas are particular to a certain image, and cannot be applied across multiple images, unlike the classification hierarchy approach that was described in this Appendix.

Shadow was the dominant feature that was spectrally similar to Paterson's curse flowers in the images and caused the most spectral overlap. The impact of shadow varied according to the time of day (sun angle), the meteorological conditions at time of capture (e.g. clouds), and the colour and design of the quadrat. Olmstead, *et al.* (2004) minimised shadow in vertical photographs of crop cover by only capturing images during cloudy conditions and using a flash to ensure uniform lighting. However cloudy conditions are not common in the Bindoon study area in October and November. The light grey colour of the quadrat produced commission errors where shadow cast by vegetation on the quadrat surface was misclassified. To reduce or eliminate the problem, a wire quadrat, or painting the quadrat a darker colour, such as black, may be appropriate. The dark colour may also eliminate bands of haze along the periphery of the quadrat.

The influence of shadow across the entire range of field photos could not be fully addressed by the classification hierarchy. For example, when shadow was reduced in one image by modifying the class parameters, there was misclassification in subsequent images. The process of altering the parameters of classes should be done cautiously in order to maintain a stable and consistent hierarchy. Given the variability of the illumination and other conditions, it's unlikely that image based classification of field photos will ever be a fully automated process. Even if conditions are controlled as much as possible by the operator when capturing photos, there will always be misclassification, especially when large numbers of photos are captured.

APPENDIX D

NORMALITY TESTING OF VARIABLES FROM FIELD SPECTROSCOPY ANALYSIS

(CHAPTER 4)



Variable	Shapiro-Wilk	Sig.	Distribution	N
NDBI	0.913	0.001	NP	69
UNMIX	0.957	0.018	NP	65
NFRE	0.964	0.044	NP	69
reNDVI	0.965	0.051	N	69
GVDPC 3	0.972	0.124	N	69
RE 2	0.964	0.044	N	69
GVPCF 2	0.969	0.087	N	69
PCI	0.976	0.200	N	69
NDRE	0.970	0.098	N	69
SVDPC 1	0.968	0.075	N	69
SVDPC 2	0.979	0.287	N	69
SVPCF 1	0.985	0.568	N	69
GVDPC 2	0.965	0.048	NP	69
GVPCF 4	0.989	0.807	N	69
GVDPC 1	0.982	0.413	N	69
SVPCF 2	0.982	0.417	N	69
GVPCF 3	0.969	0.083	N	69
GVPCF 1	0.967	0.069	N	69
Floral % cover	0.940	0.003	N	69

N = normal distribution; NP = non-parametric

APPENDIX E

DMSI TRAINING CLASS STATISTICS

(CHAPTER 5)



Crop						
Band	N	Mean	SD	SE	Shapiro-Wilk	Sig.
1	839	702.51	26.57	0.92	0.992	0.001
2	839	1197.8	86.02	2.97	0.968	0.001
3	839	431.75	49.22	1.7	0.951	0.001
4	839	1667.17	110.42	3.81	0.990	0.001

Pasture						
Band	N	Mean	SD	SE	Shapiro-Wilk	Sig.
1	1081	775.54	48.82	1.49	0.946	0.001
2	1084	1487.23	134.53	4.09	0.973	0.001
3	1076	682.04	101.41	3.09	0.948	0.001
4	1084	1549.08	70.65	2.15	0.997	0.2

Fallow						
Band	N	Mean	SD	SE	Shapiro-Wilk	Sig.
1	369	906.22	41.30	2.15	0.909	0.001
2	372	1297.48	113.51	5.89	0.845	0.001
3	372	861.31	111.03	5.76	0.865	0.001
4	372	923.26	87.415	4.53	0.946	0.001

Paterson's curse						
Band	N	Mean	SD	SE	Shapiro-Wilk	Sig.
1	951	739.54	31.86	1.03	0.980	0.001
2	951	1274.29	117.72	3.82	0.979	0.001
3	951	549.35	76.92	2.49	0.977	0.001
4	951	1543.6	241.41	7.83	0.839	0.001

APPENDIX F

VALIDATION DATA SHEETS

(CHAPTER 5)



Table F.1 Random points for Paterson's curse class, with floral percentage cover (F) measured from field photographs. Coordinates in UTM GDA 94, zone 50.

ID	Easting	Northing	Floral % 1	Floral % 2	Floral % 3	Floral % 4	Floral % 5	Mean %
1	422204	6535466	4.24	0.02	3.69	4.70	2.68	3.07
2	422237	6535474	-	0.39	-	1.31	2.48	0.84
3	422259	6535519	4.02	0.79	1.45	-	0.56	1.37
4	422243	6535531	-	0.09	1.75	-	5.48	1.46
5	422209	6535545	2.40	5.32	4.18	4.74	5.25	4.38
6	422157	6535501	3.33	5.95	1.03	3.45	2.44	3.24
7	422030	6535548	1.87	1.19	0.83	2.82	-	1.68
8	422405	6537258	5.38	6.53	2.08	2.06	5.25	4.26
9	422425	6537204	0.03	1.20	-	-	-	0.25
10	422385	6537144	2.15	0.17	0.14	-	-	0.49
11	422349	6537066	-	-	0.11	-	-	0.02
12	422377	6537047	2.78	1.60	4.95	3.30	3.00	3.13
13	422437	6537129	0	0.66	0	0	0	0.13
14	422470	6537105	0.78	2.28	0	0.89	1.25	1.04
15	422467	6537137	2.87	5.34	2.62	4.04	7.47	4.47
16	422478	6537180	2.09	2.46	2.04	1.52	1.91	2.00
17	422543	6537145	0.30	1.48	0.12	0.17	-	0.52
18	422545	6537206	0.11	0	2.45	2.29	3.18	1.61
19	422563	6537184	2.42	4.22	4.07	0.88	-	2.90
20	422595	6537161	4.30	3.29	5.95	3.47	-	4.25
21	422687	6537138	7.59	5.51	6.25	8.42	5.24	6.60
22	422758	6537066	4.79	8.42	5.89	4.74	4.37	5.64
23	422797	6537042	0.20	0.25	0.24	0	3.55	0.85
24	422862	6537022	6.86	4.20	5.60	3.44	5.06	5.03
25	422874	6537003	5.02	2.97	7.61	2.43	5.50	4.70
26	422975	6536891	0	1.36	0.00	2.04	0	0.68
27	423010	6536898	1.19	2.62	2.68	1.78	2.68	2.19
28	422216	6536101	0	0.02	0.04	0.09	0.06	0.04
29	422253	6536122	1.19	0.72	1.21	1.19	0.49	0.96
30	422240	6536064	0.49	0	0	0.14	0.06	0.14
31	422154	6536050	0.52	0.61	0.46	1.61	0.29	0.70
32	422204	6536024	1.46	0.04	1.34	0.79	0.56	0.84
33	422180	6535992	0.99	0.34	0.97	0.32	1.38	0.80
34	422187	6535938	0.16	0.12	0.09	0.03	0.16	0.11
35	422261	6535871	0.09	0.07	0.55	0	0.05	0.15
36	422234	6535845	0.51	0	0	0	0	0.10
37	422331	6535787	0.62	1.18	0.61	1.12	0	0.71
38	422302	6535702	0.04	0	0	0	0	0.01

ID	Easting	Northing	Floral % 1	Floral % 2	Floral % 3	Floral % 4	Floral % 5	Mean %
39	422414	6535658	0	0.59	0	0.14	0	0.15
40	422408	6535540	0.05	0	0	0.55	0.47	0.21
41	422352	6535547	0	0	0.44	0.03	0.27	0.15
42	422301	6535611	0.23	0.13	3.61	0	0	0.79
43	422168	6535701	2.52	1.69	0.00	3.74	0.98	1.78
44	422142	6535688	0.19	0.62	0.13	0.07	0.52	0.30
45	422084	6535719	0.30	3.53	0.65	2.17	1.16	1.56
46	422062	6535763	0	0	0	0.02	0	0
47	422108	6535792	0.08	0	0.21	0	0.29	0.12
48	422072	6535819	1.23	1.57	1.93	0.48	0.39	1.12
49	422139	6535843	0.42	0	0.06	0	0.08	0.11
50	422171	6535850	0.09	0.06	0.11	0.40	0.06	0.14
51	422018	6535892	1.08	0.29	2.22	0.78	0.79	1.03
52	422059	6535930	0.64	0.99	0.07	0.18	0.25	0.42
53	422022	6535934	0.39	0	0.19	0.02	0.09	0.14
54	422039	6535964	0.32	0.04	0.06	0.18	0.04	0.13
55	422014	6535978	0.05	0	0.27	0.14	0.12	0.12
56	422054	6535996	1.11	0.11	0.19	0.55	0.15	0.42
57	422050	6536019	0.61	1.44	0.52	2.54	0.14	1.05
58	422351	6537460	0.08	0.05	0.05	0	0.17	0.07
59	422405	6537490	0.51	0.45	1.02	0.90	0.43	0.66
60	422423	6537521	0.44	0.03	0.34	0.13	0.34	0.26
61	422444	6537523	0.28	0.35	0.95	0.02	0.40	0.40
62	422428	6537565	0.28	0.14	0.45	0.21	1.12	0.44
63	422504	6537598	0.21	0.08	0.44	0.13	0.04	0.18
64	422515	6537607	0.03	0.19	3.31	0.09	0.03	0.73
65	422528	6537622	0.03	0.08	1.13	0.21	0.10	0.31
66	422554	6537705	0.41	0.95	0.17	0.10	2.00	0.73
67	422616	6537803	0.07	0.02	0.39	0.24	0.04	0.15
68	422524	6537732	0.03	0.28	0.00	0.01	0.28	0.12
69	422442	6537783	0.80	0.12	0.54	0.07	0.38	0.38
70	422417	6537742	0.09	0.02	0.17	0.08	0.03	0.08
71	422305	6537685	0.11	0.47	1.11	0.42	0.37	0.50
72	422296	6537655	0.30	0.08	0.20	0.08	0.04	0.14
73	422233	6537680	0.36	0.08	0.03	0.11	0.06	0.13
74	422208	6537650	0.07	0.10	0	0	0.21	0.08
75	422227	6537574	0.12	0.02	0	0.14	0	0.05
76	422329	6537592	0.06	0.09	0.34	0.65	0.44	0.32
77	422306	6537545	0	0	0	0	0.13	0.03
78	422264	6537508	0.04	0	0	0	0.22	0.05
79	422320	6537794	0.35	0.20	0.44	0.21	0.24	0.29

ID	Eastings	Northing	Floral % 1	Floral % 2	Floral % 3	Floral % 4	Floral % 5	Mean %
80	422288	6537465	0.59	0.35	0.09	0.71	0.34	0.41
81	422275	6537457	0.01	0.06	0.05	0.35	0.09	0.11
82	422219	6537427	0.02	0.09	0.11	0.07	5.60	1.18
83	422183	6537475	0.07	0.33	0.03	0.16	0.22	0.16
84	422113	6537465	0.03	0.03	0	0.04	0.05	0.03
85	422090	6537540	0.15	0.14	0.22	0.32	0.06	0.18
86	422123	6537603	0.31	0	0.10	0.34	0.17	0.18
87	422044	6537687	0.04	0	0.20	0	0	0.05
88	422037	6537644	0.07	0	0	0.03	0	0.02
89	421967	6537501	0.17	4.60	1.29	0.74	0.64	1.49
90	421962	6537477	0.15	0.60	0.33	0.14	0.03	0.25
91	421925	6537492	0.19	7.58	0.15	0.77	0.09	1.76
92	421932	6537467	0.58	0.43	0	0	0.19	0.24
93	421890	6537367	0.30	0	0	0	0	0.06
94	421833	6537116	2.52	2.26	1.79	2.20	4.81	2.72
95	421722	6537156	7.97	3.33	5.11	0.82	9.29	5.31
96	421699	6537093	0	22.89	0	0	4.17	5.41
97	421569	6536988	2.01	3.95	0.91	2.76	0.32	1.99
98	421585	6536969	0	0	5.21	0.17	0	1.08
99	421625	6537003	0.18	0.04	0	0.91	0	0.23
100	421840	6536894	3.61	2.87	4.29	1.90	3.97	3.33
101	421911	6536951	1.65	0.80	3.39	2.59	1.20	1.93
102	421804	6536950	2.88	5.44	7.38	6.94	4.87	5.50
103	421785	6536973	0.06	0	0.06	0	0.06	0.04
104	421848	6537010	0	0	0.28	0	0	0.06
105	421856	6537072	0.25	0	2.19	0	0.44	0.58
106	421934	6537043	0	0	2.32	0	1.43	0.75
107	422042	6537015	3.21	0	3.98	7.68	-	3.72
108	422007	6537063	4.23	6.28	4.94	2.05	4.07	4.32
109	421978	6537077	0.04	0.05	0.11	0	0	0.04
110	422063	6537157	10.30	0	2.95	0.24	11.47	4.99
111	422182	6537161	0	0	0	0.94	0	0.19
112	422183	6537118	9.79	3.27	8.31	3.34	10.97	7.14
113	422120	6537086	6.19	2.57	3.99	1.90	4.77	3.88
114	422191	6537075	0	0	0.14	0	0	0.03
115	422286	6537036	3.27	0	0	0	0.22	0.70

Table F.2

Random points for non-Paterson's curse classes. Key: F = derived from field survey; D = derived from desktop (GIS). Coordinates in UTM GDA 94, zone 50.

ID	Easting	Northing	Type	Class
116	421647	6537161	F	CROP
117	422092	6537220	F	CROP
118	422144	6537216	F	CROP
119	422207	6537217	F	CROP
120	422494	6534882	D	CROP
121	423229	6536053	D	CROP
122	424234	6535635	D	CROP
123	422960	6536309	D	CROP
124	422799	6536162	D	CROP
125	423431	6536281	D	CROP
126	423023	6536124	D	CROP
127	422659	6534633	D	CROP
128	424189	6535564	D	CROP
129	422765	6535884	D	CROP
130	421236	6536138	D	CROP
131	421542	6537277	D	CROP
132	421542	6537266	D	CROP
133	423010	6536049	D	CROP
134	422772	6536099	D	CROP
135	422002	6537336	D	CROP
136	423801	6535671	D	CROP
137	423258	6536045	D	CROP
138	422427	6534806	D	CROP
139	422726	6534801	D	CROP
140	423317	6535934	D	CROP
141	422019	6537384	D	CROP
142	421683	6537255	D	CROP
143	424110	6535433	D	CROP
144	423783	6536083	D	CROP
145	422551	6534776	D	CROP
146	424145	6535368	D	CROP
147	423315	6536162	D	CROP
148	421165	6536404	D	CROP
149	422241	6537302	D	CROP
150	424148	6535466	D	CROP
151	421839	6537216	D	CROP
152	423089	6536470	D	CROP
153	421500	6537068	D	CROP

ID	Easting	Northing	Type	Class
154	423504	6536028	D	CROP
155	423762	6536217	D	CROP
156	423364	6536412	D	CROP
157	422831	6536417	D	CROP
158	422732	6534833	D	CROP
159	423665	6536239	D	CROP
160	422001	6537278	D	CROP
161	421122	6536087	D	CROP
162	423999	6535831	D	CROP
163	424146	6535254	D	CROP
164	422999	6536560	D	CROP
165	424025	6535981	D	CROP
166	424212	6535474	D	CROP
167	423201	6535920	D	CROP
168	423281	6536029	D	CROP
169	421690	6537176	D	CROP
170	423102	6536498	D	CROP
171	421810	6537171	D	CROP
172	423177	6536314	D	CROP
173	423851	6536044	D	CROP
174	424165	6535412	D	CROP
175	422876	6536154	D	CROP
176	424203	6535710	D	CROP
177	421668	6537299	D	CROP
178	423092	6536158	D	CROP
179	423624	6536247	D	CROP
180	423812	6535833	D	CROP
181	421687	6537271	D	CROP
182	421525	6537309	D	CROP
183	423743	6535779	D	CROP
184	424256	6535600	D	CROP
185	423594	6535994	D	CROP
186	423207	6536029	D	CROP
187	424248	6535495	D	CROP
188	422451	6534891	D	CROP
189	422970	6536075	D	CROP
190	424144	6535516	D	CROP
191	422472	6534893	D	CROP
192	424120	6535264	D	CROP
193	423077	6536367	D	CROP
194	423090	6536511	D	CROP
195	423972	6535201	D	CROP

ID	Easting	Northing	Type	Class
196	424085	6535317	D	CROP
197	423995	6535920	D	CROP
198	423848	6535666	D	CROP
199	423009	6536306	D	CROP
200	423562	6536313	D	CROP
201	422121	6537205	D	CROP
202	421202	6536248	D	CROP
203	424290	6535811	D	CROP
204	422718	6534609	D	CROP
205	423702	6535881	D	CROP
206	421249	6536094	D	CROP
207	424038	6535525	D	CROP
208	422488	6534651	D	CROP
209	423888	6535873	D	CROP
210	423954	6535788	D	CROP
211	422758	6536298	D	CROP
212	422548	6534858	D	CROP
213	424029	6535731	D	CROP
214	421700	6537223	D	CROP
215	423386	6535976	D	CROP
216	423216	6536212	D	CROP
217	421224	6536153	D	CROP
218	422748	6536038	D	CROP
219	422866	6536234	D	CROP
220	424290	6535623	D	CROP
221	424084	6535593	D	CROP
222	422974	6535951	D	CROP
223	421137	6536303	D	CROP
224	422921	6536407	D	CROP
225	423574	6536259	D	CROP
226	422785	6534745	D	CROP
227	422761	6534647	D	CROP
228	424202	6535414	D	CROP
229	422514	6534835	D	CROP
230	422785	6534768	D	CROP
231	422065	6536139	F	PASTURE
232	422379	6535696	F	PASTURE
233	422412	6535644	F	PASTURE
234	422093	6535871	F	PASTURE
235	422327	6537431	F	PASTURE
236	422046	6537062	F	PASTURE
237	422261	6537200	F	PASTURE

ID	Easting	Northing	Type	Class
238	422292	6537184	F	PASTURE
239	422207	6537054	F	PASTURE
240	422282	6537022	F	PASTURE
241	422204	6537099	F	PASTURE
242	422718	6535843	D	PASTURE
243	421135	6537179	D	PASTURE
244	421410	6535826	D	PASTURE
245	422280	6536592	D	PASTURE
246	422754	6535835	D	PASTURE
247	421333	6537190	D	PASTURE
248	424117	6536338	D	PASTURE
249	422489	6536351	D	PASTURE
250	421211	6537169	D	PASTURE
251	422384	6536435	D	PASTURE
252	421301	6537467	D	PASTURE
253	421910	6535022	D	PASTURE
254	422028	6535193	D	PASTURE
255	424110	6536418	D	PASTURE
256	421268	6537620	D	PASTURE
257	422387	6536476	D	PASTURE
258	421490	6535739	D	PASTURE
259	422544	6535904	D	PASTURE
260	421622	6535966	D	PASTURE
261	421480	6536006	D	PASTURE
262	421147	6537528	D	PASTURE
263	421371	6537397	D	PASTURE
264	422626	6536500	D	PASTURE
265	421269	6534988	D	PASTURE
266	421309	6537249	D	PASTURE
267	421386	6535652	D	PASTURE
268	421870	6535072	D	PASTURE
269	421568	6534660	D	PASTURE
270	422546	6536241	D	PASTURE
271	421248	6537578	D	PASTURE
272	422631	6535752	D	PASTURE
273	421510	6535472	D	PASTURE
274	421415	6535071	D	PASTURE
275	422537	6536642	D	PASTURE
276	422379	6535272	D	PASTURE
277	422647	6536204	D	PASTURE
278	421217	6536859	D	PASTURE
279	421167	6535725	D	PASTURE

ID	Easting	Northing	Type	Class
280	421360	6536812	D	PASTURE
281	421347	6537448	D	PASTURE
282	422604	6536520	D	PASTURE
283	422591	6535809	D	PASTURE
284	421705	6534850	D	PASTURE
285	421250	6537504	D	PASTURE
286	422721	6536634	D	PASTURE
287	424235	6536348	D	PASTURE
288	421276	6535807	D	PASTURE
289	421286	6536758	D	PASTURE
290	421531	6537544	D	PASTURE
291	422543	6536427	D	PASTURE
292	424148	6536594	D	PASTURE
293	422354	6536426	D	PASTURE
294	421339	6537621	D	PASTURE
295	421220	6535107	D	PASTURE
296	421438	6535441	D	PASTURE
297	422501	6536385	D	PASTURE
298	421396	6534920	D	PASTURE
299	422501	6536417	D	PASTURE
300	422739	6535803	D	PASTURE
301	422866	6535806	D	PASTURE
302	422555	6536232	D	PASTURE
303	421906	6534625	D	PASTURE
304	422614	6536497	D	PASTURE
305	422881	6535777	D	PASTURE
306	421966	6534643	D	PASTURE
307	421444	6535412	D	PASTURE
308	421322	6536785	D	PASTURE
309	421289	6534730	D	PASTURE
310	421490	6534765	D	PASTURE
311	421645	6534639	D	PASTURE
312	421419	6534893	D	PASTURE
313	421316	6537083	D	PASTURE
314	421357	6535788	D	PASTURE
315	421275	6537177	D	PASTURE
316	421330	6535759	D	PASTURE
317	422563	6536640	D	PASTURE
318	421694	6535224	D	PASTURE
319	421340	6535030	D	PASTURE
320	421195	6535120	D	PASTURE
321	421841	6534755	D	PASTURE

ID	Easting	Northing	Type	Class
322	421253	6536846	D	PASTURE
323	421325	6534998	D	PASTURE
324	422722	6536326	D	PASTURE
325	424194	6536468	D	PASTURE
326	421422	6534757	D	PASTURE
327	422477	6536672	D	PASTURE
328	421989	6534665	D	PASTURE
329	421132	6535117	D	PASTURE
330	422073	6535317	D	PASTURE
331	421416	6535463	D	PASTURE
332	422673	6536166	D	PASTURE
333	422386	6535309	D	PASTURE
334	421678	6535167	D	PASTURE
335	421443	6534879	D	PASTURE
336	421158	6537546	D	PASTURE
337	421769	6535133	D	PASTURE
338	422622	6535798	D	PASTURE
339	421587	6535913	D	PASTURE
340	422863	6535675	D	PASTURE
341	422805	6535777	D	PASTURE
342	421341	6537096	D	PASTURE
343	422183	6536640	D	PASTURE
344	422530	6535935	D	PASTURE
345	421362	6534630	D	PASTURE

APPENDIX G

ERROR MATRICES FROM DMSI CLASSIFICATION RESULTS

(CHAPTER 5)



Appendix G.1 Error matrices for MLP classifications.

3-Class

	C	P	PC	Totals	UA	Kappa (U)
C	72	9	26	107	67	0.51
P	15	37	34	86	43	0.15
PC	28	69	55	152	36	0.04
Totals	115	115	115	345		
PA	63	32	48			
Kappa (P)	0.46	0.1	0.07		OA	48

2-Class

	P	PC	Totals	UA	Kappa (U)
P	62	38	100	62	0.24
PC	53	77	130	59	0.19
Totals	115	115	230		
PA	54	67			
Kappa (P)	0.19	0.28		OA	60

Appendix G.2 Error matrices from kNN classification (4 bands, 3 classes).

kNN = 5

	C	P	PC	Totals	UA	Kappa (U)
C	73	2	26	101	72	0.59
P	14	68	36	118	12	0.36
PC	24	44	49	117	42	0.13
Totals	111	114	111	336		
PA	66	60	44			
Kappa (P)	0.51	0.38	0.14		OA	57

kNN = 15

	C	P	PC	Totals	UA	Kappa (U)
C	73	3	27	103	71	0.57
P	14	70	40	124	57	0.34
PC	24	41	44	109	40	0.11
Totals	111	114	111	336		
PA	66	61	40			
Kappa (P)	0.51	0.39	0.11		OA	56

kNN = 25

	C	P	PC	Totals	UA	Kappa (U)
C	74	3	28	105	71	0.56
P	13	72	41	126	57	0.35
PC	24	39	42	105	40	0.1
Totals	111	114	111	336		
PA	67	63	38			
Kappa (P)	0.52	0.41	0.1		OA	56

kNN = 35

	C	P	PC	Totals	UA	Kappa (U)
C	73	3	28	104	70	0.56
P	14	73	40	127	58	0.36
PC	24	38	43	105	41	0.12
Totals	111	114	111	336		
PA	66	64	39			
Kappa (P)	0.50	0.42	0.11		OA	56

kNN = 45

	C	P	PC	Totals	UA	Kappa (U)
C	74	4	29	107	69	0.54
P	15	73	40	128	57	0.35
PC	22	37	42	101	42	0.13
Totals	111	114	111	336		
PA	67	64	38			
Kappa (P)	0.511	0.42	0.11		OA	56

kNN = 55

	C	P	PC	Totals	UA	Kappa (U)
C	74	4	29	107	69	0.54
P	16	74	41	131	57	0.34
PC	21	36	41	98	42	0.13
Totals	111	114	111	336		
PA	67	65	37			
Kappa (P)	0.51	0.43	0.11		OA	56

Appendix G.3 Error matrices from kNN classification (3 bands, 3 classes).

kNN = 5

	C	P	PC	Totals	UA	Kappa (U)
C	73	1	25	99	74	0.61
P	15	61	31	107	57	0.35
PC	23	52	54	129	42	0.13
Totals	111	114	110	335		
PA	66	54	49			
Kappa (P)	0.51	0.32	0.17		OA	56

kNN = 15

	C	P	PC	Totals	UA	Kappa (U)
C	72	2	26	100	72	0.58
P	14	60	31	105	57	0.35
PC	25	52	54	131	41	0.12
Totals	111	114	111	336		
PA	65	53	23			
Kappa (P)	0.50	0.31	0.16		OA	55

kNN = 25

	C	P	PC	Totals	UA	Kappa (U)
C	71	3	27	101	70	0.56
P	15	64	31	110	58	0.37
PC	25	47	52	124	42	0.14
Totals	111	114	110	335		
PA	64	56	47			
Kappa (P)	0.48	0.35	0.16		OA	56

kNN = 35

	C	P	PC	Totals	UA	Kappa (U)
C	70	3	27	100	70	0.55
P	14	62	31	107	58	0.36
PC	27	49	52	128	40	0.11
Totals	111	114	110	335		
PA	63	54	47			
Kappa (P)	0.47	0.33	0.15		OA	55

kNN = 45

	C	P	PC	Totals	U.A.	Kappa (U)
C	71	3	28	102	70	0.55
P	14	64	31	109	59	0.38
PC	26	47	52	125	42	0.13
Totals	111	114	111	336		
PA	64	56	47			
Kappa (P)	0.48	0.35	0.15		OA	56

kNN = 55

	C	P	PC	Totals	UA	Kappa (U)
C	70	3	28	101	69	0.54
P	14	65	31	110	59	0.38
PC	27	46	52	125	42	0.13
Totals	111	114	111	336		
PA	63	57	47			
Kappa (P)	0.47	0.36	0.15		OA	56

Appendix G.4 Error matrices from kNN classification (2 bands, 3 classes).

kNN = 5

	C	P	PC	Totals	UA	Kappa (U)
C	71	3	28	102	70	0.54
P	14	69	35	118	59	0.38
PC	25	38	46	109	42	0.14
Totals	110	110	109	329		
PA	65	63	42			
Kappa (P)	0.49	0.42	0.14		OA	57

kNN = 15

	C	P	PC	Totals	UA	Kappa (U)
C	68	3	27	98	69	0.54
P	14	67	32	113	59	0.39
PC	28	40	50	118	42	0.14
Totals	110	110	109	329		
PA	62	61	46			
Kappa (P)	0.46	0.41	0.16		OA	56

kNN = 25

	C	P	PC	Totals	UA	Kappa (U)
C	67	7	28	102	66	0.49
P	13	67	34	114	59	0.38
PC	30	36	48	114	42	0.13
Totals	110	110	110	330		
PA	61	61	44			
Kappa (P)	0.43	0.40	0.14		OA	55

kNN = 35

	C	P	PC	Totals	UA	Kappa (U)
C	70	5	28	103	68	0.52
P	13	67	32	112	60	0.4
PC	27	38	49	114	43	0.15
Totals	110	110	109	329		
PA	64	61	45			
Kappa (P)	0.47	0.41	0.16		OA	57

kNN = 45

	C	P	PC	Totals	UA	Kappa (U)
C	68	5	29	102	67	0.5
P	15	70	32	117	60	0.4
PC	27	35	48	110	45	0.16
Totals	110	110	109	329		
PA	62	64	44			
Kappa (P)	0.45	0.44	0.16		OA	57

kNN = 55

	C	P	PC	Totals	UA	Kappa (U)
C	67	4	30	101	66	0.49
P	15	68	33	116	59	0.38
PC	28	38	46	112	41	0.12
Totals	110	110	109	329		
PA	61	62	42			
Kappa (P)	0.43	0.41	0.12		OA	55

Appendix G.5 Error matrices from kNN classification (4 bands, 2 classes).

kNN = 5

	P	PC	Totals	UA	Kappa (U)
P	67	37	104	64	0.28
PC	47	74	121	61	0.23
Totals	114	111	225		
PA	59	67			
Kappa (P)	0.23	0.27		OA	63

kNN = 15

	P	PC	Totals	UA	Kappa (U)
P	71	43	114	62	0.24
PC	43	68	111	61	0.23
Totals	114	111	225		
PA	62	61			
Kappa (P)	0.24	0.23		OA	62

kNN = 25

	P	PC	Totals	UA	Kappa (U)
P	72	42	114	63	0.25
PC	42	69	111	62	0.25
Totals	114	111	225		
PA	63	62			
Kappa (P)	0.25	0.24		OA	63

kNN = 35

	P	PC	Totals	UA	Kappa (U)
P	73	43	116	63	0.25
PC	41	68	109	62	0.25
Totals	114	111	225		
PA	64	61			
Kappa (P)	0.26	0.24		OA	63

kNN = 45

	P	PC	Totals	UA	Kappa (U)
P	74	43	117	63	0.26
PC	40	68	108	63	0.26
Totals	114	111	225		
PA	65	61			
Kappa (P)	0.27	0.25		OA	63

kNN = 55

	P	PC	Totals	UA	Kappa (U)
P	73	42	115	64	0.26
PC	41	69	110	63	0.26
Totals	114	111	225		
PA	64	62			
Kappa (P)	0.26	0.25		OA	63

kNN = 65

	P	PC	Totals	UA	Kappa (U)
P	74	42	116	64	0.27
PC	40	69	109	63	0.27
Totals	114	111	225		
PA	65	62			
Kappa (P)	0.28	0.26		OA	64

Appendix G.6

Error matrices from kNN classification (3 bands, 2 classes).

kNN = 5

	P	PC	Totals	UA	Kappa (U)
P	62	30	92	67	0.34
PC	52	81	133	61	0.22
Totals	114	111	225		
PA	54	73			
Kappa (P)	0.23	0.32		OA	64

kNN = 15

	P	PC	Totals	UA	Kappa (U)
P	62	31	93	67	0.32
PC	52	80	132	61	0.22
Totals	114	111	225		
PA	54	72			
Kappa (P)	0.22	0.31		OA	63

kNN = 25

	P	PC	Totals	UA	Kappa (U)
P	63	30	93	68	0.34
PC	51	80	131	61	0.22
Totals	114	110	224		
PA	55	73			
Kappa (P)	0.24	0.31		OA	64

kNN = 35

	P	PC	Totals	UA	Kappa (U)
P	62	31	93	67	0.32
PC	52	79	131	60	0.21
Totals	114	110	224		
PA	54	72			
Kappa (P)	0.22	0.29		O.A.	63

kNN = 45

	P	PC	Totals	UA	Kappa (U)
P	64	31	95	67	0.34
PC	50	80	130	62	0.23
Totals	114	111	225		
PA	56	72			
Kappa (P)	0.24	0.32		OA	64

kNN = 55

	P	PC	Totals	UA	Kappa (U)
P	66	31	97	68	0.35
PC	48	80	128	63	0.25
Totals	114	111	225		
PA	58	72			
Kappa (P)	0.26	0.34		OA	65

kNN = 65

	P	PC	Totals	UA	Kappa (U)
P	65	31	96	68	0.35
PC	49	80	129	62	0.24
Totals	114	111	225		
PA	57	72			
Kappa (P)	0.25	0.33		OA	64

Appendix G.7

Error matrices from kNN classification (2 bands, 2 classes).

kNN = 5

	P	PC	Totals	UA	Kappa (U)
P	65	34	99	66	0.30
PC	49	76	125	61	0.22
Totals	114	110	224		
PA	57	69			
Kappa (P)	0.23	0.27		OA	63

kNN = 15

	P	PC	Totals	UA	Kappa (U)
P	66	32	98	67	0.34
PC	48	78	126	62	0.24
Totals	114	110	224		
PA	58	71			
Kappa (P)	0.25	0.31		OA	64

kNN = 25

	P	PC	Totals	UA	Kappa (U)
P	65	32	97	67	0.33
PC	49	78	127	61	0.23
Totals	114	110	224		
PA	57	71			
Kappa (P)	0.24	0.3		OA	64

kNN = 35

	P	PC	Totals	UA	Kappa (U)
P	66	32	98	67	0.34
PC	48	78	126	62	0.24
Totals	114	110	224		
PA	58	71			
Kappa (P)	0.25	0.31		OA	64

kNN = 45

	P	PC	Totals	UA	Kappa (U)
P	69	32	101	68	0.36
PC	45	78	123	63	0.27
Totals	114	110	224		
PA	60	71			
Kappa (P)	0.28	0.33		OA	66

kNN = 55

	P	PC	Totals	UA	Kappa (U)
P	66	33	99	67	0.32
PC	48	77	125	62	0.23
Totals	114	110	224		
PA	58	70			
Kappa (P)	0.25	0.29		OA	64

kNN = 65

	P	PC	Totals	UA	Kappa (U)
P	67	33	100	67	0.33
PC	47	77	124	62	0.24
Totals	114	110	224		
PA	59	70			
Kappa (P)	0.26	0.30		OA	64

APPENDIX H

LOGISTIC REGRESSION AND ROC ANALYSIS RESULTS

(CHAPTER 5)



Table H.1 Logistic regression and ROC analysis results for 3-class (Paterson's curse, crop, and pasture) subset (Set A). Records are order from highest to lowest AUC statistic.

Set	Bands	kNN	N	Chi-square	Sig.	AUC	Lower Value	Upper Value	SE	Sig.
A	3	35	327	9.374	0.002	0.615	0.552	0.677	0.032	0.001
A	4	55	328	6.621	0.01	0.613	0.552	0.674	0.031	0.001
A	3	25	323	9.125	0.003	0.613	0.55	0.676	0.032	0.001
A	3	55	331	8.73	0.003	0.612	0.55	0.674	0.032	0.001
A	2	55	333	8.434	0.004	0.612	0.55	0.673	0.031	0.001
A	3	45	328	8.834	0.003	0.611	0.548	0.674	0.032	0.001
A	3	15	316	8.241	0.004	0.607	0.543	0.671	0.033	0.002
A	4	45	327	6.589	0.01	0.606	0.543	0.668	0.032	0.002
A	2	25	323	7.133	0.008	0.606	0.543	0.668	0.032	0.002
A	2	45	332	7.62	0.006	0.606	0.543	0.668	0.032	0.002
A	4	5	294	6.165	0.013	0.604	0.538	0.669	0.033	0.003
A	4	25	322	6.375	0.012	0.601	0.537	0.664	0.032	0.003
A	2	35	327	6.933	0.008	0.601	0.539	0.664	0.032	0.003
A	4	15	316	6.168	0.013	0.6	0.536	0.664	0.033	0.004
A	4	35	325	6.198	0.012	0.6	0.537	0.663	0.032	0.003
A	2	15	316	6.072	0.014	0.599	0.535	0.663	0.032	0.004
A	2	5	300	4.506	0.034	0.585	0.52	0.651	0.033	0.015
A	3	5	297	5.179	0.023	0.58	0.513	0.647	0.034	0.022

Table H.2

Logistic regression and ROC analysis results for the 2-class (Paterson's curse and pasture) subset (Set B). Records are ordered from highest to lowest AUC statistic.

Set	Bands	kNN	N	Chi-square	Sig	AUC	Lower Value	Upper Value	SE	Sig.
B	4	5	197	18.108	> 0.01	0.677	0.603	0.752	0.038	> 0.01
B	3	25	214	19.615	> 0.01	0.677	0.605	0.749	0.037	> 0.01
B	3	35	217	20.001	> 0.01	0.675	0.604	0.747	0.036	> 0.01
B	2	25	215	19.054	> 0.01	0.673	0.601	0.745	0.037	> 0.01
B	3	15	207	16.156	> 0.01	0.67	0.597	0.743	0.037	> 0.01
B	3	55	221	19.167	> 0.01	0.67	0.599	0.741	0.036	> 0.01
B	2	55	222	19.247	> 0.01	0.67	0.599	0.741	0.036	> 0.01
B	3	45	218	18.943	> 0.01	0.669	0.597	0.741	0.037	> 0.01
B	3	65	221	19.187	> 0.01	0.669	0.598	0.74	0.036	> 0.01
B	4	55	217	19.615	> 0.01	0.668	0.596	0.741	0.037	> 0.01
B	4	15	208	17.362	> 0.01	0.667	0.593	0.74	0.038	> 0.01
B	4	25	212	18.431	> 0.01	0.667	0.595	0.74	0.037	> 0.01
B	4	45	216	19.24	> 0.01	0.667	0.595	0.74	0.037	> 0.01
B	2	45	221	18.488	> 0.01	0.667	0.596	0.739	0.036	> 0.01
B	2	15	208	15.718	> 0.01	0.666	0.593	0.739	0.037	> 0.01
B	2	5	200	14.499	> 0.01	0.665	0.59	0.74	0.038	> 0.01
B	2	65	223	18.193	> 0.01	0.665	0.594	0.736	0.036	> 0.01
B	4	35	214	17.974	> 0.01	0.662	0.589	0.736	0.037	> 0.01
B	2	35	217	17.204	> 0.01	0.662	0.59	0.735	0.037	> 0.01
B	3	5	201	13.372	> 0.01	0.66	0.585	0.736	0.038	> 0.01

APPENDIX I

FIELD DATA SHEET FROM 2006 HYPERION VALIDATION SURVEY

(CHAPTER 6)



Ranking Key

- 0: No Paterson's curse
- 1: Barely any Paterson's curse, except for isolated plants
- 2: Small patches of Paterson's' curse, or up to total 1/4 Paterson's curse
- 3: Approx. 1/2 of area covered by Paterson's curse
- 4: Up to 3/4 of area covered by Paterson's curse
- 5: Area nearly 100% covered by Paterson's curse

Property:

MORD: Morden Downs
BIND: Bindarie
CACB: Catholic Agricultural College
Bindoon

* Geocentric Datum of Australia 1994, UTM Zone 5

No.	Property	Easting*	Northing*	Direction & ranking				Mode	Median	Comments
				N	E	S	W			
1	CACB	422085	6537480	3	3	3	3	3	3	
2	MORD	419810	6528912	2	2	2	2	2	2	
4	BIND	419296	6521558	0	1	1	1	1	1	
5	CACB	423122	6537535	2	2	2	2	2	2	
6	CACB	422982	6537104	2	2	1	2	2	2	
7	CACB	422485	6537151	3	4	2	2	2	2.5	
10	BIND	419975	6521707	5	5	5	5	5	5	
11	CACB	421887	6535667	4	4	4	4	4	4	
12	BIND	420248	6519980	1	1	1	1	1	1	
13	CACB	422654	6537206	3	2	3	3	3	3	
14	BIND	419984	6522156	3	2	2	2	2	2	
15	BIND	419667	6523770	3	3	3	2	3	3	
16	BIND	418892	6521812	3	3	2	2	3	2.5	
18	BIND	419683	6521947	0	1	1	1	1	1	
19	BIND	420308	6520259	1	1	1	1	1	1	
20	BIND	419447	6523699	2	2	2	2	2	2	
21	BIND	418885	6522167	2	3	2	3	2	2.5	
22	MORD	420218	6528380	5	4	5	5	5	5	
23	MORD	419852	6528614	5	5	5	4	5	5	
24	MORD	420051	6528104	4	4	5	5	4	4.5	
25	MORD	419722	6527688	5	4	5	5	5	5	
26	MORD	419964	6528713	4	4	4	3	4	4	

No.	Property	Easting*	Northing*	Direction & ranking				Mode	Median	Comments
				N	E	S	W			
27	BIND	420214	6521629	3	3	3	3	3	3	
28	CACB	422896	6537153	2	2	2	3	2	2	
29	CACB	422328	6537582	2	2	2	3	2	2	
31	BIND	418956	6521204	2	2	2	2	2	2	Dry soil, senescent pasture
32	MORD	419721	6528178	4	3	4	4	4	4	
33	MORD	420008	6528497	5	5	4	5	5	5	
34	MORD	419748	6528800	2	3	3	3	3	3	
35	BIND	420370	6520153	1	1	0	0	1	0.5	
36	BIND	419593	6523557	2	N/A	N/A	N/A	2	2	
37	BIND	419997	6523727	1	1	1	1	1	1	
38	BIND	418235	6522347	5	3	3	4	3	3.5	Very dense mature PC, & clear patches
40	MORD	420063	6528196	4	4	4	4	4	4	Some crop species
41	CACB	423994	6537673	5	5	4	4	5	4.5	
42	BIND	420633	6520621	1	1	1	1	1	1	Dry paddock, some capeweed
43	CACB	422948	6537481	2	2	1	1	2	1.5	
44	BIND	418866	6521011	2	2	1	2	2	2	
45	BIND	420443	6520990	2	2	2	2	2	2	
46	BIND	419347	6522882	2	2	1	2	2	2	
47	CACB	423405	6537674	2	2	2	2	2	2	
48	MORD	420168	6527853	5	5	5	5	5	5	
51	BIND	419296	6523269	2	3	3	2	2	2.5	
53	BIND	419838	6521655	1	1	2	1	1	1	Rocky

No.	Property	Easting*	Northing*	Direction & ranking				Mode	Median	Comments
				N	E	S	W			
54	BIND	420263	6520355	0	1	1	1	1	1	Small tree in plot
55	BIND	420644	6521180	1	1	1	1	1	1	
56	BIND	419065	6521984	2	3	2	2	2	2	
57	CACB	423290	6536804	2	2	2	2	2	2	
59	CACB	423697	6537838	3	3	3	3	3	3	
60	BIND	420414	6522505	1	1	0	1	1	1	
61	BIND	418668	6522048	3	3	2	2	3	2.5	
62	CACB	423751	6537043	3	2	3	2	3	2.5	
63	BIND	419745	6521872	1	1	0	1	1	1	
64	BIND	420515	6520243	0	0	0	0	0	0	Dry paddock, no PC
65	BIND	420614	6522667	1	1	1	1	1	1	
66	BIND	418650	6522455	5	5	5	5	5	5	
67	BIND	420062	6521606	3	3	3	3	3	3	
68	CACB	422295	6537675	3	3	2	3	3	3	
69	BIND	419837	6522082	1	1	1	1	1	1	
70	BIND	420123	6521427	4	2	2	2	2	2	
71	BIND	419932	6523550	1	1	1	1	1	1	
72	CACB	422235	6534897	4	2	2	2	2	2	Dry paddock
73	MORD	420165	6528729	4	3	2	2	2	2.5	
76	MORD	420376	6527957	4	4	4	4	4	4	
77	CACB	424032	6537539	5	4	3	4	4	4	
78	BIND	419010	6522097	4	4	5	5	4	4.5	
80	BIND	419831	6521844	1	1	1	1	1	1	

No.	Property	Easting*	Northing*	Direction & ranking				Mode	Median	Comments
				N	E	S	W			
82	BIND	419651	6523147	1	1	1	1	1	1	
83	MORD	420385	6528117	5	5	5	4	5	5	Some crop
84	BIND	418880	6521679	2	2	2	2	2	2	
85	CACB	422364	6534913	1	1	2	1	1	1	Dry paddock, mature PC, but few flowers left
86	BIND	419117	6522321	2	2	2	2	2	2	
87	CACB	423407	6537245	4	5	4	5	4	4.5	
88	MORD	419870	6528291	3	3	4	3	3	3	
89	BIND	418784	6523209	4	4	4	4	4	4	
90	MORD	419975	6527718	2	2	3	3	2	2.5	
91	BIND	419546	6521729	1	0	1	1	1	1	Very rocky plot, dry
93	MORD	420460	6527694	5	4	4	5	5	4.5	
94	BIND	419785	6522314	1	1	1	2	1	1	
95	BIND	419546	6521863	1	1	1	0	1	1	Rocky plot, dry
96	BIND	419904	6523675	1	0	1	1	1	1	Awkward plot, on fence line near track
97	BIND	419796	6521474	1	1	1	1	1	1	
98	BIND	419989	6523453	1	1	1	1	1	1	
99	BIND	418371	6523822	5	5	5	5	5	5	Very dense mature PC
100	CACB	422742	6537268	2	2	1	2	2	2	

APPENDIX J

HYPERION BAD COLUMN LISTING

(CHAPTER 6)



Band Number	Bad Column Number
8	6, 68, 114, 246
9	6, 68, 114, 148, 229
10	6, 114, 199
11	114, 199
12	114
13	114
14	114
15	114
16	114
27	47
54	25
77	246, 247
78	246, 247
94	92
99	91
116	137
119	239
120	239
165	147
190	112
200	7
201	7
203	114

APPENDIX K

FLAASH ATMOSPHERIC CORRECTION PARAMETERS

(CHAPTER 6)



Attribute	Parameter
Visibility (km)	30
Scene Center Location	Lat -31 18 45.72, Long 116 10 58.80
Sensor Altitude (km)	705
Ground Elevation (km)	0.2
Pixel Size (m)	30
Flight Date	Nov 2 2006
Flight Time (GMT)	1:54:27
Atmospheric Model	Mid-Latitude Summer
Water Retrieval	None
Water Absorption Feature	N/A
Aerosol Model	Rural
Aerosol Retrieval	None
Initial Visibility (km)	100
Spectral Polishing	No
Wavelength Recalibration	No
Aerosol Scale Height (km)	2
CO2 Mixing Ratio (ppm)	390
Use Square Slit Function	No
Use Adjacency Correction	Yes
Reuse MODTRAN Calculations	No
Modtran Resolution (cm ⁻¹)	15
Modtran Multiscatter Model	Scaled DISTORT
Number of DISTORT Streams	8
Zenith Angle	180°
Azimuth Angle	0°
Output Reflectance Scale Factor	10000